Functional Neuroimaging of Cortical Plasticity in the Human Visual System

Dissertation

zur Erlangung des Grades eines
Doktors der Naturwissenschaften

der Mathematisch-Naturwissenschaftlichen Fakultät
und
der Medizinischen Fakultät
der Eberhard-Karls-Universität Tübingen

vorgelegt
von

Amalia Papanikolaou
aus Thessaloniki, Greece

May 2015

Tag der mündlichen Prüfung: 23/03/2015

Dekan der Math.-Nat. Fakultät: Prof. Dr. W. Rosenstiel

Dekan der Medizinischen Fakultät: Prof. Dr. I. B. Autenrieth

1. Berichterstatter: Prof. Dr. Nikos K. Logothetis

2. Berichterstatter: Prof. Dr. Ulrich Schiefer

Prüfungskommission: Prof. Dr. Nikos K. Logothetis

Prof. Dr. Dr. Hans-Otto Karnath

Dr. Stelios M. Smirnakis

Dr. Georgios A. Keliris

Erklärung / Declaration

Ich erkläre, dass ich die zur Promotion eingereichte Arbeit mit dem Titel:

"Functional Neuroimaging of Cortical Plasticity in the Human Visual System"

selbständig verfasst, nur die angegebenen Quellen und Hilfsmittel benutzt und wörtlich oder inhaltlich bernommene Stellen als solche gekennzeichnet habe. Ich versichere an Eides statt, dass diese Angaben wahr sind und dass ich nichts verschwiegen habe. Mir ist bekannt, dass die falsche Abgabe einer Versicherung an Eides statt mit Freiheitsstrafe bis zu drei Jahren oder mit Geldstrafe bestraft wird.

I hereby declare that I have produced the work entitled "Functional Neuroimaging of Cortical Plasticity in the Human Visual System", submitted for the award of a doctorate, on my own (without external help), have used only the sources and aids indi-cated and have marked passages included from other works, whether verbatim or in con-tent, as such. I swear upon oath that these statements are true and that I have not con-cealed anything. I am aware that making a false declaration under oath is punishable by a term of imprisonment of up to three years or by a fine.

Tübingen, den ....

Datum / Date Unterschrift / Signature

Abstract

Partial damage of the primary visual cortex (V1) and optic radiation lesions can cause visual field deficits restricted to specific regions of the contralateral visual hemifield. This thesis has explored the functional properties of the visual cortex and its capacity to reorganize in patients with chronic V1 or optic radiation lesions resulting in partial or complete homonymous quadrantanopia. We used functional magnetic resonance (fMRI) methods and quantitative population receptive field (pRF) analysis to investigate: i) how spared regions of the visual cortex cover the visual field following V1 injury, and ii) whether the retinotopic organization of the spared visual cortex changes as a result of reorganization. We demonstrate that the spared part of area V1 has at best a limited-degree of reorganization that manifests in some patients with a small shift of the pRF centers towards the border of the scotoma and by a slight increase in V1 pRF sizes near the border of the scotoma. Importantly, we show that responses in early and higher visual cortex are not always congruent with visual perception in subjects with visual cortical lesions. Several patterns of mismatch were identified: 1) visual field areas covered in both areas V1 and hV5/MT+, 2) visual field areas covered in hV5/MT+ but not V1 suggesting the existence of functional pathways that bypass area V1. Interestingly these areas overlap with dense regions of the perimetric scotoma, suggesting that activity in these areas does not contribute to visual awareness. Nevertheless, identifying and characterizing the patterns of activation seen in the visual cortex may help choose visual field locations with high potential for rehabilitation. Conversely, we found cases in which 3) spared area V1 failed to cover completely seeing visual field locations in the perimetric map, suggesting the existence of V1-bypassing pathways that are able to mediate useful vision. Understanding how the properties of visual areas change after injury, and how this correlates with perception is important in the effort to adopt new rational strategies for visual rehabilitation. Finally, we reviewed the literature and proposed a systematic approach to visual system rehabilitation using the combination of pRF mapping and real-time fMRI neuro-feedback methods.

Acknowledgements

All the great adventures one may encounter along the road of a long journey would be meaningless unless shared with great people. I was lucky enough to have many people by my side during the time of my PhD adventure who have deeply influenced me in many ways and I would like to thank all of them.

First of all, my thanks go to my parents for their love, their constant support, for teaching me to be strong, confident, to be patient and to love reading. Most importantly, I thank them for giving me the opportunity to follow my dreams.

I am especially grateful to my supervisor Stelios Smirnakis for his excellent guidance and advice throughout my PhD research studies. His sharp thinking, brilliant intuition and careful comments have contributed enormously to this work and have challenged me to always think out of the box. I particularly thank Nikos Logothetis for his great support and for giving me the opportunity to work in such a great and stimulating research environment. I would also like to thank the rest of my committee members Georgios Keliris and Andreas Bartels for all their help, encouragement and constructive comments.

Furthermore, I thank my colleagues Yibin Shao and Sangkyun Lee for their amazing help and support and for having a great as well as fun collaboration. I would also like to thank Natalia Zaretskaya for being extremely helpful, especially in my struggle with the German language. I am grateful to Ulrich Sciefer, Elke Krapp, Eleni Papageorgiou, Katarina Stingl and Anna Bruckmann from the Center of Ophthalmology for their help with the patients and their big contribution to this work. Special thanks to Dorina Papageorgiou for being both a coworker and a friend, for her advice, her great hospitality and for always supporting me when I most needed it.

I would also like to sincerely thank all the people who have participated in the experiments for this study. I am very grateful for all the patience and the genuine willingness to help.

Life in Tuebingen would never be tolerable without the support of my friends. I would like to thank all the people who have come and gone, shared a little bit of their lives with me and helped me to get to know myself a little better. In particular, I thank Eleni for being a fantastic flat mate, for all the amazing moments we have shared and for the long-lasting political, science and life related discussions. I owe a lot to my friend Takis; the first years of my PhD would not be easy without him.

My friends in Greece, Eleni, Eleni, Kiki, Dimitra and Athanasia, although far away have contributed a lot on keeping me as sane as possible. On this occasion I have to

thank Skype for not letting me loose contact with the outside world and the radio show "Rock the night" for keeping me company during some cold nights of the winter and making me laugh. Finally, I would like to thank Bill for being in my life and for always encouraging me to be my best.

To Giorgos and Anastasia

Contents

"When you have eliminated the impossible, whatever remains, however improbable, must be the truth."

Arthur Conan Doyle,
Sherlock Holmes in *The Sign of the Four*

1

Introduction

1.1 Visual field loss after cortical lesions

Cortical damage of the visual pathway occurs often as a result of posterior or middle cerebral artery infarcts and hemorrhages, traumatic brain injury, or vascular or neoplastic tumors. The most common visual cortical injuries involve the primary visual cortex (V1), which is the chief relay of visual information to higher visual areas. Damage to area V1 and/or its primary inputs leads to the loss of conscious vision in the corresponding region of the contralateral visual hemifield (dense contralateral scotoma). The visual impairment often involves a hemifield (hemianopia), a single visual field quadrant (quadrantanopia), or smaller homonymous scotomatous regions within the affected hemifield. Cortical blindness affects many activities on a patient's daily life such as driving, reading, and navigating complex visual environments. There are currently no widely accepted treatment options available for people with visual cortical damage. This is in sharp contrast with the physical therapy and motor retraining aggressively implemented to rehabilitate patients with damage to primary motor cortex.

However, hope is not entirely lost. Cortically blind individuals have been found to possess a small amount of residual sensitivity within their blind field. Unlike normal vision, however, this preserved sensitivity often occurs without consciousness, and as a result, it was originally termed "blindsight" [105]. Understanding brain repair processes is an important step in the effort to design treatments aimed at enhancing the ability of the nervous system to recover after injury. To make progress towards this goal, it is important to study in detail how the adult human brain reorganizes after injury.

1.2 Using fMRI to assess the properties of the visual system

The visual cortex is retinotopically organized, meaning that adjacent neurons in the brain have receptive fields that represent nearby and overlapping portions of the visual field. Receptive field properties of the visual cortex have been characterized in animals using extracellular or intracellular recordings [31, 43, 102]. In humans, functional magnetic resonance methods (fMRI) have provided us with the possibility to characterize noninvasively the retinotopic organization of the human visual cortex [19, 22, 24, 25, 96]. Moreover, new methods were recently introduced which allowed us to measure the population receptive field (pRF) properties of neuronal populations for each voxel in the visual cortex [3, 23, 36, 56, 110]. These methods provide an excellent tool for studying in detail the aggregate receptive field properties of human visual cortex and its capacity to reorganize following area V1 injury.

In parallel, the development of new approaches is also essential. The aforementioned studies capture the pRF shape using a predefined model which makes a priori assumptions about the receptive field structure. The pRF shape however may vary across the visual cortex and thus inaccurate assumptions about the pRF topography could lead to erroneous pRF property estimates. This requires the development of novel pRF methods which estimate the structure of the pRF directly from the fMRI data without assuming the pRF shape a priori (section 3, appendix A.2, A.3, [34, 60]). We have used these methods to study reorganization of the visual cortex following V1 injury in patients with homonymous visual field defects.

1.3 Reorganization of the visual cortex following injury

The ability of the visual cortex to reorganize following injury is a subject of much debate. Several studies in subjects suffering from macular degeneration and other retinal lesions report a remapping of area V1 in response to retinal lesions [4, 5, 12–14, 20, 30, 32, 37, 48, 90, 94]. The extent of this effect, however, has been questioned [8, 18, 41, 62, 68, 100, 101, 103].

Much less is known about visual cortex reorganization following cortical injury [35]. Animal studies report enhanced plasticity in the area surrounding experimentally induced V1 lesions [7, 26–28, 85, 95]. As expected, reorganization is more extensive in younger animals [72]. These studies provide important information but are less informative about large scale changes that may occur in spared visual cortex following injury.

Human literature on the topic is scant and inconclusive, consisting mainly of case reports. One problem is that naturally occurring cortical lesions show considerable variability, making it difficult to draw definite conclusions from isolated case studies. A recent study by Dilks and colleagues [21] in a subject with left upper quadrandanopia after damage to the optic radiation reported significant ectopic activity in area V1 six months after the ictus. However, it is unclear whether the ectopic V1 activity seen in [21] is the result of reorganization, versus simply the result of different visual stimulation between patient and controls. On the other hand, Baseler et al. [9] found that extrastriate visual areas retain their retinotopic organization following V1 damage when the stimulus is presented across the full visual field. However, abnormal maps were observed for the dorsal extrastriate visual areas when the stimulus was restricted inside the scotoma.

Since no systematic study existed in humans investigating how or whether spared V1 cortex reorganizes following chronic V1 injuries we first tried to tackle this question. We studied the functional properties of spared V1 cortex in five subjects suffering from chronic post-chiasmatic lesions resulting in homonymous visual field quadrantanopia. The results are presented in section 2 and in ([70], appendix A.1).

1.4 Activity in higher visual areas associated with blindsight

Activity that is independent of V1 input has been observed in higher visual areas of animals following V1 lesions [92]. Particularly, blindsight has been associated with activity observed in the middle temporal area (MT) after V1 damage. Experiments in monkeys showed that a significant proportion of MT cells remain visually responsive in the absence of area V1 input [11, 33, 81, 83]. However, other studies suggest that MT depends entirely on V1 for visual activation [15, 16, 47, 59]. The basis of this discrepancy is not yet understood. In the macaque, area V5/MT activation following V1 lesions is thought to be mediated by a V1-bypassing relay of visual information from the superior colliculus (SC) to the pulvinar and then to extrastriate cortex [82]. Rosa et al. [83] also showed that many area MT neurons acquire ectopic receptive fields responding to the visual field surrounding the scotoma suggesting reorganization. Other studies suggest that the Lateral Geniculate Nucleus (LGN) plays a significant role in transmitting visual information to the extrastriate cortex when V1 is damaged [63, 91, 92].

Visually driven activity was observed in human complex hV5/MT+ when moving stimuli were presented inside the blind visual field of a well-studied patient (G.Y.) with extensive area V1 injury [6, 29, 67]. Visual-motion related activity in hV5/MT+ was also observed

in a patient with homonymous hemianopia and Riddoch syndrome [93] and a patient with bilateral damage to the gray matter of V1 [10]. However, it is not known how the organization of hV5/MT+ changes following chronic deprivation of V1 input. We investigated this issue in five patients with homonymous visual field defects as a result of chronic V1 or optic radiation lesions. The results are presented in section 4 and in the article in preparation (appendix A.5).

1.5 Visual rehabilitation in cortically blind individuals

To date, there is no established method to effectively rehabilitate patients with visual field deficits as a result of damage in the primary visual cortex. Although several rehabilitative studies, based on a saccade-to-target task paradigm, have claimed to significantly shrink dense visual field scotomas [46, 50–55, 57, 58, 74–76, 86, 87, 106, 109], later studies implementing rigorous eye movement controls have failed to find a reduction of the visual field scotoma [39, 40, 73, 80].

However, rehabilitation of scotomas following V1 damage is not entirely without hope [2, 44, 77, 88, 91, 92]. In monkeys, visual training after V1 lesions restores the ability to detect and localize visual stimuli in their blind fields. These improvements do not occur spontaneously, but require training and they are largely restricted to visual field regions retrained [66, 104].

In general, behavioral training in healthy subjects can improve visual performance by inducing plastic changes in the physiology of visual networks [1, 49, 61, 108]. Several studies in subjects with V1 lesions suggest that visual performance in the scotoma can also improve with training [38, 79]. More recently, Huxlin and colleagues [44] have shown that when adult humans with stroke-induced V1 damage were retrained to perform a global direction discrimination task with random dot stimuli at a single location in their blind field, their performance progressed from a complete inability to discriminate global motion direction to normal direction integration thresholds. These data sparked renewed interest in studying visual rehabilitation strategies and provide important evidence for perceptual plasticity in the adult visual system after cortical damage. We proposed a systematic approach towards visual system rehabilitation that incorporates population receptive field mapping and fMRI neurofeedback methods (section 5 and appendix A.6)

1.6 Aim of the project

The ultimate goal of my project during these years as a Ph.D. candidate was to study the organization of the visual cortex in patients with post-chiasmatic lesions suffering from homonymous visual field defects and to understand what changes correlate with improved visual performance. This was divided into four individual but highly connected studies which are presented in the next sections and has led to four publications and two articles in preparation. These are:

1. Organization of the spared primary visual cortex in patients with homonymous visual field defects
2. A method for estimating population receptive field topography in the visual cortex
3. Organization of human area V5/MT+ in subjects with homonymous visual field defects
4. Visual rehabilitation in patients with visual cortical lesions

2

Organization of the spared primary visual cortex in patients with homonymous visual field defects

2.1 Motivation

As described in the introduction (section 1.3), little is known about the ability of the visual cortex to reorganize following cortical lesions affecting the primary visual cortex. The first step in understanding visual system plasticity after lesions that affect part of area V1 itself or part of its input is to i) study how to measure residual V1 function in vivo; and ii) to study how visual processing changes in the spared V1 regions. Understanding the ability of the visual cortex to process information post-lesion is important and it could help guide efforts at rehabilitation and recovery.

2.2 Methods

We studied five adult subjects with partial V1 or optic radiation lesions suffering from partial or complete homonymous quadrantanopia as a result of ischemic or hemorrhagic stroke 0.5-10 years before they enrolled in our study. We obtained functional magnetic resonance imaging (fMRI) during the presentation of a moving bar stimulus. The stimuli consisted of square-checkerboard bars, which travelled sequentially in 8 different directions spanning the visual field. The subjects were instructed to fixate a small dot at the center of the screen and respond to the color change by pressing a button. Five healthy participants were recruited as controls. The control subjects were asked to participate in a second session during which an isoluminant mask, covering the stimulus, was placed

in the upper left quadrant of the visual field trying to simulate an upper left quadrantanopia. This stimulus condition is called artificial scotoma (or AS) and is an adequate method in order to differentiate between changes that occur as a result of reorganization versus simple stimulus deprivation.

For the analysis we used the population receptive field (pRF) mapping method introduced by Dumoulin and Wandell [23]. Briefly, the pRF model estimates the region of the visual field that effectively elicits a response in a small region of visual cortex (voxel). The implementation of the pRF model is a circularly symmetric Gaussian receptive field in visual space, whose center and radius are estimated by fitting actual BOLD signal responses to estimated responses elicited by convolving the model with the moving bar stimuli. With this method we could derive reliable and reproducible retinotopic and pRF size maps.

In addition we calculated visual field coverage maps from all voxels in the spared V1 of each subject. The visual field coverage maps define the locations within the visual field that evoke a significant response from voxels within a region of interest (ROI) in the cortex. To estimate this we plot the pRF centers across all voxels within the ROI and the relative pRF size by fitting a 2D Gaussian with peak amplitude normalized to one. The map is estimated by plotting at each visual field location the maximum pRF amplitude between all Gaussian shaped pRFs that cover this location. We also estimate the non-normalized visual field coverage that weights the pRF Gaussians with their response amplitude.

We derived pRF properties, retinotopic maps and visual field coverage maps for all five patients examined and compared them with control subjects under the artificial scotoma condition.

2.3 Results

We found that the spared V1 region of the lesioned hemisphere can be visually modulated significantly and retains its coarse retinotopic organization. The borders between visual areas were found to be at similar locations as the AS controls and at the expected Talairach coordinates. Retinotopic maps had a monotonic progression of phase as expected. However, some finer changes in the pRF localization of the spared part of area V1 did occur suggesting that there is at best a limited degree of reorganization in adult humans with homonymous visual field defects. This reorganization is manifested in some (2/5) patients with a small shift of the pRF centers towards the border of the scotoma, and in most patients (4/5) by a slight increase in V1 pRF sizes near the border

of the scotoma as well as in the V1 of the contra-lesional hemisphere. Finding ways to expand further the pRF size in these patients may cover in part the visual field defect, inducing recovery.

Surprisingly, for 3 out of 5 patients we found a number of spared V1 voxels whose pRF centers lay well within the area of the visual field scotoma. Visual stimuli presented inside the scotoma can modulate neural activity in these voxels even though they generate no visual percept. These pRFs were found not to be ectopic as they fall at the correct anatomical locations. Two of these patients had lesions that included areas V2 and V3, making it possible that the information flow between area V1 and higher extrastriate areas has been cut off. Thus, in their case the lack of visual percept may happen because the retinotopically corresponding higher pathways are injured. However, the third patient had an optic radiation lesion and hence the pathways from area V1 to higher extrastriate areas are intact. Here, activity generated in area V1 may be too weak or too disorganized to elicit a percept. In any case, the region of overlap between a visual field coverage map and the corresponding perimetrically determined visual field scotoma identifies visual field locations that can still generate a level of V1 activity and therefore may have higher potential for visual rehabilitation. Visual rehabilitation studies may want to first focus training in these visual field locations, in order to optimize the chance of recovery.

On the contrary, the pRF maps of the remaining patients (2 out of 5) failed to cover completely seeing locations of the visual field suggesting that residual visual function may be mediated by V1 bypassing pathways (visual field coverage maps of one patient support this hypothesis) or perhaps through the contra-lesional hemisphere. The latter could be supported by a possible spread of the pRF coverage map across the vertical meridian. Although this occurs to a degree for one patient, it happens to a smaller degree than expected from the area of sparing seen in the perimetric map and therefore it cannot be stated with certainty.

2.4 Conclusions

Our study demonstrates that there is a limited-degree of reorganization in the spared part of area V1 following partial V1 injury. Importantly, we showed that area V1 population receptive field analysis is not fully congruent with the perceptual scotoma in subjects with cortical lesions. Studying the patterns of mismatch and understanding the capacity of early visual areas to reorganize after injury will allow us in the course of time to adopt more rational strategies for rehabilitation.

3

A method for estimating population receptive field topography in the visual cortex

3.1 Motivation

The retinotopic organization of the human visual cortex can be characterized noninvasively using fMRI [19, 22, 24, 25, 96]. New methods have been more recently introduced which allowed us to measure the population receptive field (pRF) properties of neuronal populations for each voxel in the visual cortex [3, 23, 36, 56, 110]. All these approaches, however, capture the pRF shape using a predefined model which makes a priori assumptions about the receptive field structure. The pRF shape though may vary across the visual cortex and thus inaccurate assumptions about the pRF topography could lead to erroneous estimations of the pRF properties. Especially, in subjects with lesions of the visual pathways the pRF properties may vary even more as a result of partial deprivation or reorganization. This required the development of a novel pRF method which estimates the structure of the pRF directly from the fMRI data without assuming the pRF shape a priori.

3.2 Methods

FMRI measurements were obtained from four healthy participants during the presentation of a moving checkerboard bar stimulus. The stimulus parameters were similar as described in the methods section 2.2.

We proposed a new method to estimate the pRF topography which predicts the fMRI time-series by solving a linear model for each voxel. In brief, the pRF structure p_i at voxel i is represented by a set of weights which predicts the BOLD signal $d_i(t)$ at voxel i and time t, using the stimulus protocol $s(t)$ and the hemodynamic response function $h(t)$ as:

$$d_i = h(t) * (p_i^T s(t)) = K p_i$$

The weight vector p is estimated by solving a linear model based on ridge regression with a bias:

$$J_i = y_i - K^+ p_i^{+2} + \lambda_1 {p_i}^2$$

where $K^+ = \begin{bmatrix} K & 1^{(M\times 1)} \end{bmatrix}$, $p_i^+ = \begin{bmatrix} p_i & \alpha \end{bmatrix}$, α is a constant value to account for the bias and λ_1 is a free parameter to control the extent to which the least-square function is regularized.

The central region of the pRF topography was then modelled using a 2-D Gaussian model:

$$exp\left(- \frac{1}{2(g-\mu)^T \Sigma^{-1} (g-\mu)} \right)$$

with center: $\mu = \begin{bmatrix} x_i, & y_i \end{bmatrix}^T$ and dispersion: $\Sigma = \begin{bmatrix} \cos\theta & -\sin\theta \\ \sin\theta & \cos\theta \end{bmatrix} \cdot \begin{bmatrix} \sigma_1^2 \\ \sigma_2^2 \end{bmatrix}$.

3.3 Results

We were able to derive reliably the structure of the pRF from voxels in the visual cortex. This allowed us also to derive pRF properties such as retinotopic location and pRF size by appropriately fitting a model to the structure of the data.

We compared our method with direct fitting methods [23, 36, 110] and found that i) it is computationally more efficient, and ii) it explains a higher proportion of the variance in the data than the direct fitting methods. Moreover, direct fitting methods are prompt to mislocalization of the pRF center near the border of the stimulus presentation space resulting in unreliable eccentricity maps. Our method overcomes this problem and

reflects more reliable estimations of the pRF center eccentricity. In addition, our method can capture characteristics of surround suppression in the pRF structure.

Most importantly, the pRF topography method allows us to observe the pRF shape and assess details of the pRF structure, making it ideal for our studies of the organization of the visual cortex in patients with visual cortical lesions, where the shape of the reorganized pRF cannot be anticipated. Particularly, extrastriate visual areas that are higher in the visual hierarchy, have large receptive fields that could be affected either by partial deafferentation or reorganization resulting in irregular shapes. Consequently, we applied this method to study the organization of area hV5/MT+ in patients with homonymous quadrantanopia as described in the next section.

4

Organization of human area V5/MT+ in subjects with homonymous visual field defects

4.1 Motivation

We showed that the early visual cortex has a limited capacity for reorganization (section 2 and [70]), yet fMRI methods providing information about spared activity in the cortex can help guide future visual rehabilitation strategies. Additionally, the functional organization of higher visual areas may provide important information about the mechanism associated with residual visual function. Finding ways to expand or strengthen this mechanism, may as well help in the effort of visual rehabilitation. Therefore, we studied the organization of area hV5/MT+ in five patients with injury of the visual pathway. In addition, we studied how responses in hV5/MT+ are affected by simulated visual field scotomas in healthy subjects. This step is critical in order to disguinsh between changes that occur as the result of true reorganization versus simple stimulus deprivation.

4.2 Methods

FMRI measurements were obtained from five healthy subjects after masking the stimulus in the left upper quadrant of the visual field to simulate a quadrantanopic visual field scotoma ("artificial scotoma" denoted as "AS"). The stimulus protocol consisted of moving checkerboard bars as described in the methods section 2.2.

For the analysis in AS subjects we used the pRF topography method as described in section 3. Because pRFs near the border of the artificial scotoma may not have a

circular shape we could not fit a Gaussian model to get an estimate of the pRF center and size. Instead we used the topography directly to get eccentricity and polar angle values corresponding to the center of the pRF as well as an estimate of the pRF size.

In addition, we studied five patients with V1 or optic radiation lesions resulting in partial or complete homonymous quadrantanopia. Four of these patients had also participated in the study presented in section 2. Because significant biases were observed in the BOLD time series of subjects with simulated artificial scotomas when using the drifting bar stimulus, a different approach in pRF mapping had to be implemented in order to compare responses in hV5/MT+ between patients and AS controls. In particular, the BOLD time series of each voxel were fitted separately for each bar direction. The pRF was then defined by its boundaries by marking the visual field locations where the BOLD signal rises above baseline for each direction.

4.3 Results

We found changes in the pRF location and size when healthy participants were scanned under the AS condition. Most voxels of area hV5/MT+ corresponding to locations within the AS responded to stimuli located in the surround of the AS, thereby effectively acquiring displaced pRFs. Surprisingly, a displacement of pRF center location towards the AS border occurred also for neurons whose pRF centers lied outside the AS area. In addition, we observed an increase in the pRF amplitude near the border of the AS and a decrease in the pRF size suggesting that significant nonlinearities influence the pRF estimation when using the truncated stimulus. These deviations from linearity do not reflect true reorganization, but rather properties of normal visual processing under different test-stimulus conditions. In addition, we found significant errors in pRF estimation which extend inside the artificial scotoma when we used the full bar stimulus model for predicting the pRF topography instead of the masked stimulus when the actual stimulus presented included the artificial scotoma. These biases are not the result of a trivial methodological artifact but appear to originate from asymmetric BOLD responses occurring when the stimulus moves from seeing to non-seeing locations of the visual field.

Given the biases observed in AS subjects when using the full bar stimulus to predict the pRF topography, a different approach had to be implemented for comparing responses between patients and AS controls. Specifically, we calculated directly the boundaries of the pRF from the BOLD time series of each voxel separately for each direction of motion of the visual stimulus. This way, the biases are eliminated and no activity arises within the area corresponding to the AS in healthy controls as expected. In patients, however, we found responses in hV5/MT+ of the lesioned hemisphere to stimuli presented within

the scotoma for all five patients. In 4/5 patients these responses might originate from the spared part of area V1, but they apparently do not contribute to visual awareness. In 2/5 patients there were visual field regions whose hV5/MT+ responses arose despite lack of significant corresponding V1 activation suggesting the existence of a potentially functional V1-bypassing pathway.

Given these findings, a natural question would be whether different regions of the scotoma have different capacity for recovery. If this turns out to be the case, characterizing the changes occurring in extrastriate visual areas following V1 lesions could help us develop better strategies for visual rehabilitation. We started to tackle the issue of visual rehabilitation, as described in the next and last section of this thesis.

5

Visual rehabilitation in patients with visual cortical lesions

5.1 Motivation

To date, no reliable method exists to effectively rehabilitate patients with visual field deficits as a result of V1 damage [39, 40]. However, hope is not entirely lost. Recent studies show that appropriate training strategies may be able to rehabilitate visual perception within the blind field [38, 44, 79, 88]. The mechanisms underlying this recovery are not yet understood. We reviewed the literature and proposed a visual rehabilitation strategy, which incorporates pRF mapping methods and real-time fMRI neuro-feedback training ([69], appendix A.6). We also work on studying the mechanisms which correlate with improved performance in the blind field following training. This work is currently in progress and only speculations about the expected results are presented here.

5.2 Using real-time fMRI neuro-feedback training to induce visual field recovery

Real-time fMRI neuro-feedback strategies allow subjects to voluntarily modulate activity in certain brain areas or, neural pathways. These methods can be used to promote plasticity [97]. In this regard, real-time fMRI neuro-feedback can be used to strengthen the neural pathways bypassing the V1 lesions and project to area hV5/MT+ in order to improve visual motion perception. Subjects can be trained to voluntarily upregulate

their hV5/MT+ activity. Whenever hV5/MT+ activity crosses a pre-set threshold, sub-threshold visual stimuli are presented. Repeated pairing of the top-down neurofeedback-driven activation with the "bottom-up" stimulus driven activation will engage Hebbian-like, association learning mechanisms, strengthening the response of hV5/MT+ to visual motion stimuli. Visual motion stimuli that were previously sub-threshold may then, rise above threshold following training, improving performance.

In addition, we have shown that pRF measurements can be used as an important tool to identify regions of the perimetric scotoma that are more amenable to rehabilitation. They can allow us to study the mechanism by which rehabilitation strategies improve visual performance and together with real-time fMRI neuro-feedback training we can induce plasticity in targeted pathways to promote successful rehabilitation.

5.3 Studying the mechanisms which mediate visual motion perception following training

Huxlin and colleagues [44] performed a well-controlled perceptual learning paradigm, which significantly improved the visual motion discrimination thresholds of patients with V1 lesions. The subjects were trained to perform a direction discrimination task with random dot kinematograms (RDKs) presented in their visual field bordering with their visual scotoma. We have trained three patients using the same paradigm and obtained fMRI measurements before and after training. Two out of three patients showed an increased performance within their blind field following visual training. The mechanism of this behavioral recovery though remains to be investigated.

One hypothesis is that following visual motion rehabilitation training the sensitivity to motion stimuli of hV5/MT+ increases. Initial results suggest that in some cases the contra-lesional hemisphere may take over, showing increasing activity in area hV5/MT+. Another hypothesis is that "higher" areas that receive input from hV5/MT+ may re-organize to process visual motion information more effectively. Understanding which pathways are involved in the recovery of visual motion perception may allow us to develop better rehabilitative strategies which will focus on strengthening these connections as described above. This work is still in progress and therefore could not be included in this thesis.

6

Discussion and Conclusions

This thesis has explored the functional properties of the visual cortex and the capacity to reorganize following chronic lesions of the primary visual cortex. We used quantitative population receptive field analysis to study the properties of the spared primary visual cortex and extrastriate cortex in subjects suffering from chronic post-chiasmatic lesions resulting in partial or complete homonymous visual field quadrantanopia. We investigated i) how spared regions of the visual cortex cover the visual field and how that correlates with the subjects perceptual scotoma, and ii) whether the retinotopic organization of the spared visual cortex changes as a result of reorganization. In parallel, we developed a new technique to model the pRF structure of voxels in the visual cortex in an unbiased way and we proposed ways how visual rehabilitation can improve performance and what might be the underlying mechanism.

6.1 How does spared visual cortex cover the visual field following a V1 lesion

We found that for three patients the visual field coverage maps of spared area V1 overlap significantly with the dense perimetric scotoma. In principle, lack of a percept in the presence of area V1 activity may happen because: i) retinotopically corresponding higher pathways or areas are injured, or ii) the activity generated in area V1 is too weak or too disorganized to elicit a percept. Two patients had lesions that included ventral areas V2/V3, making it possible that the information flow between area V1 and higher extrastriate areas has been cut off. One patient however had a lesion at the optic radiation, leaving the higher pathways intact. In this case it is likely that ii) dominates. Since the pathways from area V1 to higher extrastriate areas are intact, and there are

islands of activity in V1 cortex, it is reasonable to assume this patient would be a prime candidate for visual rehabilitation.

On the contrary we found that for two patients the visual field coverage maps of spared V1 do not cover completely seeing locations of the visual field. Presumably in this case, residual visual function is mediated by V1 bypassing pathways or perhaps through the contra-lesional hemisphere. Future research is needed to investigate this hypothesis.

Interestingly, for all patients visual field coverage maps of area hV5/MT+ overlap with areas of the perimetric scotoma. These findings are consistent with reports showing activity in hV5/MT+ after V1 lesions both in monkeys [11, 33, 81, 83, 91] and in humans [6, 10, 29, 67, 93]. In some patients, activity in hV5/MT+ may arise from responses in the spared part of area V1. In this case, although feedforward connections from area V1 to area hV5/MT+ may not have been interrupted, they are apparently not sufficient to mediate conscious vision. On the other hand for two patients there were visual field regions of the perimetric scotoma that were covered by area hV5/MT+ but not area V1 suggesting that there are V1-bypassing pathways capable of activating area hV5/MT+ in these patients. These results suggest that activation of hV5/MT+ alone is not sufficient for visual awareness. Some studies have pointed out the importance of feedback projections from V5/MT to V1 in visual awareness [17, 71, 98] supporting the idea that V1 is critical for conscious perception. However, it is unlikely that in our patients the lesion has selectively damaged the feedback connections and spared the feedforward connections. Our results suggest that extrastriate visual areas V2/V3 may play an important role in visual awareness [42, 64, 89, 99]. Another possibility is that activity is too disorganized or it needs to be in synchrony for awareness to arise [78].

In any case, knowing the region of overlap between a visual field coverage map and the corresponding perimetrically determined visual field scotoma is important as it identifies visual field locations that can still generate a level of activity in early and higher visual cortex and therefore may have higher potential for visual rehabilitation. For this reason we strongly suggest that pRF mapping should be incorporated in the design of visual rehabilitation studies in the future.

6.2 Does the spared visual cortex reorganize following a V1 lesion?

In general, we found that the early visual cortex of the lesioned hemisphere that is spared retains its coarse retinotopic organization in agreement with [92] and [9]. The

borders between early visual areas remained stable and retinotopic maps had a monotonic progression of phase as expected. However, finer changes in the pRFs of spared V1 do occur.

For two patients we found that pRF centers shift their location over short distances to locations near the scotoma border supporting the notion of reorganization. A possible mechanism behind this shift is that surviving portions of the pRF in voxels near the border of the scotoma become enhanced following injury, perhaps via a change in the balance of inhibition versus excitation [7, 45, 65, 85, 107]. The magnitude of the shift is on average only 1 degree consistent with, at best, a limited degree of reorganization. In addition, most patients showed a slight increase in V1 pRF sizes near the border of the scotoma. This may come about because of decreased inhibition in the surround of the lesion [27], or perhaps because subcortical inputs from LGN or the pulvinar may reorganize via strengthening existing connections or sprouting of cortical axons [84] and become able to contribute to the activation of area V1 surrounding the lesion. Finding ways to expand further the pRF size in these patients may cover in part the visual field defect, inducing recovery.

6.3 How can visual rehabilitation help improve performance in patients with visual field deficits following a V1 lesion?

Rehabilitating dense visual field scotomas requires adopting a systematic approach. Plasticity changes induced by new rehabilitation strategies should be mapped and their mechanism studied. We have presented evidence that pRF analysis is an excellent tool for this purpose, quantifying changes and providing rich data for formulating hypotheses about what regions of the visual field may be more amenable to rehabilitation and what pathways contribute to recovery.

We are also studying which mechanisms contribute to recovery of visual motion perception by training patients to perform a direction discrimination task with random dot kinematograms (RDKs). This perceptual learning paradigm has been shown to significantly improve the visual motion discrimination thresholds of patients with V1 lesions [44]. Understanding which pathways are involved in the recovery of visual motion perception may allow us to develop better rehabilitative strategies which will focus on strengthening these connections.

For example, appropriate training strategies may be able to strengthen pathways that bypass the V1 lesion and activate area hV5/MT+ to induce recovery. We propose

that this could be done using real-time fMRI neuro-feedback training. Real-time fMRI neuro-feedback strategies allow subjects to voluntarily modulate activity in certain brain areas or, neural pathways and can be used to promote plasticity [97]. One paradigm that could, in theory, be used to accomplish this is the following: Subjects are trained by real-time fMRI neuro-feedback to voluntarily upregulate their hV5/MT+ activity. Whenever hV5/MT+ activity crosses a pre-set threshold, sub-threshold visual stimuli are presented. Repeated pairing of the top-down neurofeedback-driven activation with the bottom-up stimulus driven activation will engage Hebbian-like, association learning mechanisms, strengthening the response of hV5/MT+ to visual motion stimuli. Visual motion stimuli that were previously sub-threshold may then, rise above threshold following training, improving performance.

6.4 Conclusions and future studies

Although inevitably each patient is different, our study was able to tackle several issues regarding visual cortex organization following partial V1 injury. We demonstrate that spared area V1 displays at best a limited degree of reorganization V1 injury. In addition, we showed that responses in early and higher visual cortex are not always congruent with visual perception and different locations of the visual field may have different capacity for rehabilitation. Clearly more studies are needed in this patient population in order to improve our understanding of visual processing in the context of injury. In addition, many important questions remain to be answered: 1) what visual attributes and types of lesions are amenable to recovery? 2) what is the optimal method for visual rehabilitative training? and 3) what is the underlying mechanism of recovery?

References

[1] Ahissar, M. and Hochstein, S. (1997). Task difficulty and the specificity of perceptual learning. *Nature*, 387(6631):401–6.

[2] Alexander, I. and Cowey, A. (2009). The cortical basis of global motion detection in blindsight. *Experimental brain research*, 192(3):407–11.

[3] Amano, K., Wandell, B. A., and Dumoulin, S. O. (2009). Visual field maps, population receptive field sizes, and visual field coverage in the human mt+ complex. *Journal of neurophysiology*, 102(5):2704–18.

[4] Baker, C. I., Dilks, D. D., Peli, E., and Kanwisher, N. (2008). Reorganization of visual processing in macular degeneration: replication and clues about the role of foveal loss. *Vision Res*, 48(18):1910–9.

[5] Baker, C. I., Peli, E., Knouf, N., and Kanwisher, N. G. (2005). Reorganization of visual processing in macular degeneration. *J Neurosci*, 25(3):614–8.

[6] Barbur, J. L., Watson, J. D., Frackowiak, R. S., and Zeki, S. (1993). Conscious visual perception without v1. *Brain : a journal of neurology*, 116 (Pt 6):1293–302.

[7] Barmashenko, G., Eysel, U. T., and Mittmann, T. (2003). Changes in intracellular calcium transients and ltp in the surround of visual cortex lesions in rats. *Brain Res*, 990(1-2):120–8.

[8] Baseler, H. A., Gouws, A., Haak, K. V., Racey, C., Crossland, M. D., Tufail, A., Rubin, G. S., Cornelissen, F. W., and Morland, A. B. (2011). Large-scale remapping of visual cortex is absent in adult humans with macular degeneration. *Nat Neurosci*, 14(5):649–55.

[9] Baseler, H. A., Morland, A. B., and Wandell, B. A. (1999). Topographic organization of human visual areas in the absence of input from primary cortex. *J Neurosci*, 19(7):2619–27.

[10] Bridge, H., Hicks, S. L., Xie, J., Okell, T. W., Mannan, S., Alexander, I., Cowey, A., and Kennard, C. (2010). Visual activation of extra-striate cortex in the absence of v1 activation. *Neuropsychologia*, 48(14):4148–54.

[11] Bruce, C. J., Desimone, R., and Gross, C. G. (1986). Both striate cortex and superior colliculus contribute to visual properties of neurons in superior temporal polysensory area of macaque monkey. *Journal of neurophysiology*, 55(5):1057–75.

[12] Calford, M. B., Schmid, L. M., and Rosa, M. G. (1999). Monocular focal retinal lesions induce short-term topographic plasticity in adult cat visual cortex. *Proc Biol Sci*, 266(1418):499–507.

[13] Chino, Y. M., Kaas, J. H., Smith, E. L., r., Langston, A. L., and Cheng, H. (1992). Rapid reorganization of cortical maps in adult cats following restricted deafferentation in retina. *Vision Res*, 32(5):789–96.

[14] Chino, Y. M., Smith, E. L., r., Kaas, J. H., Sasaki, Y., and Cheng, H. (1995). Receptive-field properties of deafferentated visual cortical neurons after topographic map reorganization in adult cats. *J Neurosci*, 15(3 Pt 2):2417–33.

[15] Collins, C. E., Lyon, D. C., and Kaas, J. H. (2003). Responses of neurons in the middle temporal visual area after long-standing lesions of the primary visual cortex in adult new world monkeys. *The Journal of neuroscience : the official journal of the Society for Neuroscience*, 23(6):2251–64.

[16] Collins, C. E., Xu, X., Khaytin, I., Kaskan, P. M., Casagrande, V. A., and Kaas, J. H. (2005). Optical imaging of visually evoked responses in the middle temporal area after deactivation of primary visual cortex in adult primates. *Proceedings of the National Academy of Sciences of the United States of America*, 102(15):5594–9.

[17] Cowey, A. and Walsh, V. (2000). Magnetically induced phosphenes in sighted, blind and blindsighted observers. *Neuroreport*, 11(14):3269–73.

[18] DeAngelis, G. C., Anzai, A., Ohzawa, I., and Freeman, R. D. (1995). Receptive field structure in the visual cortex: does selective stimulation induce plasticity? *Proc Natl Acad Sci U S A*, 92(21):9682–6.

[19] DeYoe, E. A., Carman, G. J., Bandettini, P., Glickman, S., Wieser, J., Cox, R., Miller, D., and Neitz, J. (1996). Mapping striate and extrastriate visual areas in human cerebral cortex. *Proceedings of the National Academy of Sciences of the United States of America*, 93(6):2382–6.

[20] Dilks, D. D., Baker, C. I., Peli, E., and Kanwisher, N. (2009). Reorganization of visual processing in macular degeneration is not specific to the "preferred retinal locus". *J Neurosci*, 29(9):2768–73.

[21] Dilks, D. D., Serences, J. T., Rosenau, B. J., Yantis, S., and McCloskey, M. (2007). Human adult cortical reorganization and consequent visual distortion. *J Neurosci*, 27(36):9585–94.

[22] Dougherty, R. F., Koch, V. M., Brewer, A. A., Fischer, B., Modersitzki, J., and Wandell, B. A. (2003). Visual field representations and locations of visual areas v1/2/3 in human visual cortex. *J Vis*, 3(10):586–98.

[23] Dumoulin, S. O. and Wandell, B. A. (2008). Population receptive field estimates in human visual cortex. *Neuroimage*, 39(2):647–60.

[24] Engel, S. A., Glover, G. H., and Wandell, B. A. (1997). Retinotopic organization in human visual cortex and the spatial precision of functional mri. *Cerebral cortex*, 7(2):181–92.

[25] Engel, S. A., Rumelhart, D. E., Wandell, B. A., Lee, A. T., Glover, G. H., Chichilnisky, E. J., and Shadlen, M. N. (1994). fmri of human visual cortex. *Nature*, 369(6481):525.

[26] Eysel, U. T. and Schmidt-Kastner, R. (1991). Neuronal dysfunction at the border of focal lesions in cat visual cortex. *Neurosci Lett*, 131(1):45–8.

[27] Eysel, U. T. and Schweigart, G. (1999). Increased receptive field size in the surround of chronic lesions in the adult cat visual cortex. *Cereb Cortex*, 9(2):101–9.

[28] Eysel, U. T., Schweigart, G., Mittmann, T., Eyding, D., Qu, Y., Vandesande, F., Orban, G., and Arckens, L. (1999). Reorganization in the visual cortex after retinal and cortical damage. *Restor Neurol Neurosci*, 15(2-3):153–64.

[29] ffytche, D. H., Guy, C. N., and Zeki, S. (1996). Motion specific responses from a blind hemifield. *Brain : a journal of neurology*, 119 (Pt 6):1971–82.

[30] Giannikopoulos, D. V. and Eysel, U. T. (2006). Dynamics and specificity of cortical map reorganization after retinal lesions. *Proc Natl Acad Sci U S A*, 103(28):10805–10.

[31] Gilbert, C. D. and Wiesel, T. N. (1985). Intrinsic connectivity and receptive field properties in visual cortex. *Vision research*, 25(3):365–74.

[32] Gilbert, C. D. and Wiesel, T. N. (1992). Receptive field dynamics in adult primary visual cortex. *Nature*, 356(6365):150–2.

[33] Girard, P., Salin, P. A., and Bullier, J. (1992). Response selectivity of neurons in area mt of the macaque monkey during reversible inactivation of area v1. *Journal of neurophysiology*, 67(6):1437–46.

[34] Greene, C. A., Dumoulin, S. O., Harvey, B. M., and Ress, D. (2014). Measurement of population receptive fields in human early visual cortex using back-projection tomography. *Journal of vision*, 14(1).

[35] Haak, K. V., Langers, D. R., Renken, R., van Dijk, P., Borgstein, J., and Cornelissen, F. W. (2012). Abnormal visual field maps in human cortex: A mini-review and a case report. *Cortex*.

[36] Harvey, B. M. and Dumoulin, S. O. (2011). The relationship between cortical magnification factor and population receptive field size in human visual cortex: constancies in cortical architecture. *The Journal of neuroscience : the official journal of the Society for Neuroscience*, 31(38):13604–12.

[37] Heinen, S. J. and Skavenski, A. A. (1991). Recovery of visual responses in foveal v1 neurons following bilateral foveal lesions in adult monkey. *Exp Brain Res*, 83(3):670–4.

[38] Henriksson, L., Raninen, A., Nasanen, R., Hyvarinen, L., and Vanni, S. (2007). Training-induced cortical representation of a hemianopic hemifield. *J Neurol Neurosurg Psychiatry*, 78(1):74–81.

[39] Horton, J. C. (2005a). Disappointing results from nova vision's visual restoration therapy. *The British journal of ophthalmology*, 89(1):1–2.

[40] Horton, J. C. (2005b). Vision restoration therapy: confounded by eye movements. *The British journal of ophthalmology*, 89(7):792–4.

[41] Horton, J. C. and Hocking, D. R. (1998). Monocular core zones and binocular border strips in primate striate cortex revealed by the contrasting effects of enucleation, eyelid suture, and retinal laser lesions on cytochrome oxidase activity. *J Neurosci*, 18(14):5433–55.

[42] Horton, J. C. and Hoyt, W. F. (1991). Quadrantic visual field defects. a hallmark of lesions in extrastriate (v2/v3) cortex. *Brain*, 114 (Pt 4):1703–18.

[43] Hubel, D. H. and Wiesel, T. N. (1974). Uniformity of monkey striate cortex: a parallel relationship between field size, scatter, and magnification factor. *The Journal of comparative neurology*, 158(3):295–305.

[44] Huxlin, K. R., Martin, T., Kelly, K., Riley, M., Friedman, D. I., Burgin, W. S., and Hayhoe, M. (2009). Perceptual relearning of complex visual motion after v1 damage in humans. *The Journal of neuroscience : the official journal of the Society for Neuroscience*, 29(13):3981–91.

[45] Imbrosci, B., Neubacher, U., White, R., Eysel, U. T., and Mittmann, T. (2013). Shift from phasic to tonic gabaergic transmission following laser-lesions in the rat visual cortex. *Pflugers Archiv : European journal of physiology*, 465(6):879–93.

[46] Julkunen, L., Tenovuo, O., Jaaskelainen, S., and Hamalainen, H. (2003). Rehabilitation of chronic post-stroke visual field defect with computer-assisted training: a clinical and neurophysiological study. *Restorative neurology and neuroscience*, 21(1-2):19–28.

[47] Kaas, J. H. and Krubitzer, L. A. (1992). Area 17 lesions deactivate area mt in owl monkeys. *Vis Neurosci*, 9(3-4):399–407.

[48] Kaas, J. H., Krubitzer, L. A., Chino, Y. M., Langston, A. L., Polley, E. H., and Blair, N. (1990). Reorganization of retinotopic cortical maps in adult mammals after lesions of the retina. *Science*, 248(4952):229–31.

[49] Karni, A. and Sagi, D. (1991). Where practice makes perfect in texture discrimination: evidence for primary visual cortex plasticity. *Proceedings of the National Academy of Sciences of the United States of America*, 88(11):4966–70.

[50] Kasten, E., Muller-Oehring, E., and Sabel, B. A. (2001). Stability of visual field enlargements following computer-based restitution training – results of a follow-up. *Journal of clinical and experimental neuropsychology*, 23(3):297–305.

[51] Kasten, E., Poggel, D. A., Muller-Oehring, E., Gothe, J., Schulte, T., and Sabel, B. A. (1999). Restoration of vision ii: residual functions and training-induced visual field enlargement in brain-damaged patients. *Restorative neurology and neuroscience*, 15(2-3):273–87.

[52] Kasten, E., Poggel, D. A., and Sabel, B. A. (2000). Computer-based training of stimulus detection improves color and simple pattern recognition in the defective field of hemianopic subjects. *Journal of cognitive neuroscience*, 12(6):1001–12.

[53] Kasten, E. and Sabel, B. A. (1995). Visual field enlargement after computer training in brain-damaged patients with homonymous deficits: an open pilot trial. *Restorative neurology and neuroscience*, 8(3):113–27.

[54] Kasten, E., Wuest, S., and Sabel, B. A. (1998a). Residual vision in transition zones in patients with cerebral blindness. *Journal of clinical and experimental neuropsychology*, 20(5):581–98.

[55] Kasten, E., Wust, S., Behrens-Baumann, W., and Sabel, B. A. (1998b). Computer-based training for the treatment of partial blindness. *Nature medicine*, 4(9):1083–7.

[56] Kay, K. N., Naselaris, T., Prenger, R. J., and Gallant, J. L. (2008). Identifying natural images from human brain activity. *Nature*, 452(7185):352–5.

[57] Kerkhoff, G., Munssinger, U., Haaf, E., Eberle-Strauss, G., and Stogerer, E. (1992). Rehabilitation of homonymous scotomata in patients with postgeniculate damage of the visual system: saccadic compensation training. *Restorative neurology and neuroscience*, 4(4):245–54.

[58] Kerkhoff, G., Munssinger, U., and Meier, E. K. (1994). Neurovisual rehabilitation in cerebral blindness. *Archives of neurology*, 51(5):474–81.

[59] Krubitzer, L. A. and Kaas, J. H. (1992). The somatosensory thalamus of monkeys: cortical connections and a redefinition of nuclei in marmosets. *The Journal of comparative neurology*, 319(1):123–40.

[60] Lee, S., Papanikolaou, A., Logothetis, N. K., Smirnakis, S. M., and Keliris, G. A. (2013). A new method for estimating population receptive field topography in visual cortex. *Neuroimage*, 81:144–57.

[61] Liu, Z. and Weinshall, D. (2000). Mechanisms of generalization in perceptual learning. *Vision research*, 40(1):97–109.

[62] Masuda, Y., Dumoulin, S. O., Nakadomari, S., and Wandell, B. A. (2008). V1 projection zone signals in human macular degeneration depend on task, not stimulus. *Cereb Cortex*, 18(11):2483–93.

[63] Maunsell, J. H., Nealey, T. A., and DePriest, D. D. (1990). Magnocellular and parvocellular contributions to responses in the middle temporal visual area (mt) of the macaque monkey. *The Journal of neuroscience : the official journal of the Society for Neuroscience*, 10(10):3323–34.

[64] Merigan, W. H., Nealey, T. A., and Maunsell, J. H. (1993). Visual effects of lesions of cortical area v2 in macaques. *The Journal of neuroscience : the official journal of the Society for Neuroscience*, 13(7):3180–91.

[65] Mittmann, T. and Eysel, U. T. (2001). Increased synaptic plasticity in the surround of visual cortex lesions in rats. *Neuroreport*, 12(15):3341–7.

[66] Mohler, C. W. and Wurtz, R. H. (1977). Role of striate cortex and superior colliculus in visual guidance of saccadic eye movements in monkeys. *Journal of neurophysiology*, 40(1):74–94.

[67] Morland, A. B., Le, S., Carroll, E., Hoffmann, M. B., and Pambakian, A. (2004). The role of spared calcarine cortex and lateral occipital cortex in the responses of human hemianopes to visual motion. *J Cogn Neurosci*, 16(2):204–18.

[68] Murakami, I., Komatsu, H., and Kinoshita, M. (1997). Perceptual filling-in at the scotoma following a monocular retinal lesion in the monkey. *Vis Neurosci*, 14(1):89–101.

[69] Papageorgiou, T., Papanikolaou, A., and Smirnakis, S. (2014). A systematic approach to visual system rehabilitation - population receptive field analysis and real-time functional magnetic resonance imaging neurofeedback methods. *InTech*.

[70] Papanikolaou, A., Keliris, G. A., Papageorgiou, T. D., Shao, Y., Krapp, E., Papageorgiou, E., Stingl, K., Bruckmann, A., Schiefer, U., Logothetis, N. K., and Smirnakis, S. M. (2014). Population receptive field analysis of the primary visual cortex complements perimetry in patients with homonymous visual field defects. *Proceedings of the National Academy of Sciences of the United States of America*, 111(16):E1656–65.

[71] Pascual-Leone, A. and Walsh, V. (2001). Fast backprojections from the motion to the primary visual area necessary for visual awareness. *Science*, 292(5516):510–2.

[72] Payne, B. R. and Lomber, S. G. (2002). Plasticity of the visual cortex after injury: what's different about the young brain? *Neuroscientist*, 8(2):174–85.

[73] Pleger, B., Foerster, A. F., Widdig, W., Henschel, M., Nicolas, V., Jansen, A., Frank, A., Knecht, S., Schwenkreis, P., and Tegenthoff, M. (2003). Functional magnetic resonance imaging mirrors recovery of visual perception after repetitive tachistoscopic stimulation in patients with partial cortical blindness. *Neuroscience letters*, 335(3):192–6.

[74] Poggel, D. A., Kasten, E., Muller-Oehring, E. M., Bunzenthal, U., and Sabel, B. A. (2006). Improving residual vision by attentional cueing in patients with brain lesions. *Brain research*, 1097(1):142–8.

[75] Poggel, D. A., Kasten, E., Muller-Oehring, E. M., Sabel, B. A., and Brandt, S. A. (2001). Unusual spontaneous and training induced visual field recovery in a patient with a gunshot lesion. *Journal of neurology, neurosurgery, and psychiatry*, 70(2):236–9.

[76] Poggel, D. A., Kasten, E., and Sabel, B. A. (2004). Attentional cueing improves vision restoration therapy in patients with visual field defects. *Neurology*, 63(11):2069–76.

[77] Poggel, D. A., Mueller, I., Kasten, E., Bunzenthal, U., and Sabel, B. A. (2010). Subjective and objective outcome measures of computer-based vision restoration training. *NeuroRehabilitation*, 27(2):173–87.

[78] Pollen, D. A. (1999). On the neural correlates of visual perception. *Cerebral cortex*, 9(1):4–19.

[79] Raninen, A., Vanni, S., Hyvarinen, L., and Nasanen, R. (2007). Temporal sensitivity in a hemianopic visual field can be improved by long-term training using flicker stimulation. *J Neurol Neurosurg Psychiatry*, 78(1):66–73.

[80] Reinhard, J., Schreiber, A., Schiefer, U., Kasten, E., Sabel, B. A., Kenkel, S., Vonthein, R., and Trauzettel-Klosinski, S. (2005). Does visual restitution training change absolute homonymous visual field defects? a fundus controlled study. *The British journal of ophthalmology*, 89(1):30–5.

[81] Rodman, H. R., Gross, C. G., and Albright, T. D. (1989). Afferent basis of visual response properties in area mt of the macaque. i. effects of striate cortex removal. *The Journal of neuroscience : the official journal of the Society for Neuroscience*, 9(6):2033–50.

[82] Rodman, H. R., Gross, C. G., and Albright, T. D. (1990). Afferent basis of visual response properties in area mt of the macaque. ii. effects of superior colliculus removal. *The Journal of neuroscience : the official journal of the Society for Neuroscience*, 10(4):1154–64.

[83] Rosa, M. G., Tweedale, R., and Elston, G. N. (2000). Visual responses of neurons in the middle temporal area of new world monkeys after lesions of striate cortex. *The Journal of neuroscience : the official journal of the Society for Neuroscience*, 20(14):5552–63.

[84] Rose, J. E., Malis, L. I., Kruger, L., and Baker, C. P. (1960). Effects of heavy, ionizing, monoenergetic particles on the cerebral cortex. ii. histological appearance of laminar lesions and growth of nerve fibers after laminar destructions. *J Comp Neurol*, 115:243–55.

[85] Rumpel, S., Hoffmann, H., Hatt, H., Gottmann, K., Mittmann, T., and Eysel, U. T. (2000). Lesion-induced changes in nmda receptor subunit mrna expression in rat visual cortex. *Neuroreport*, 11(18):4021–5.

[86] Sabel, B. A. and Kasten, E. (2000). Restoration of vision by training of residual functions. *Current opinion in ophthalmology*, 11(6):430–6.

[87] Sabel, B. A., Kenkel, S., and Kasten, E. (2004). Vision restoration therapy (vrt) efficacy as assessed by comparative perimetric analysis and subjective questionnaires. *Restorative neurology and neuroscience*, 22(6):399–420.

[88] Sahraie, A., Macleod, M. J., Trevethan, C. T., Robson, S. E., Olson, J. A., Callaghan, P., and Yip, B. (2010). Improved detection following neuro-eye therapy in patients with post-geniculate brain damage. *Experimental brain research*, 206(1):25–34.

[89] Salminen-Vaparanta, N., Koivisto, M., Noreika, V., Vanni, S., and Revonsuo, A. (2012). Neuronavigated transcranial magnetic stimulation suggests that area v2 is necessary for visual awareness. *Neuropsychologia*, 50(7):1621–7.

[90] Schmid, L. M., Rosa, M. G., Calford, M. B., and Ambler, J. S. (1996). Visuotopic reorganization in the primary visual cortex of adult cats following monocular and binocular retinal lesions. *Cereb Cortex*, 6(3):388–405.

[91] Schmid, M. C., Mrowka, S. W., Turchi, J., Saunders, R. C., Wilke, M., Peters, A. J., Ye, F. Q., and Leopold, D. A. (2010). Blindsight depends on the lateral geniculate nucleus. *Nature*, 466(7304):373–7.

[92] Schmid, M. C., Panagiotaropoulos, T., Augath, M. A., Logothetis, N. K., and Smirnakis, S. M. (2009). Visually driven activation in macaque areas v2 and v3 without input from the primary visual cortex. *PLoS One*, 4(5):e5527.

[93] Schoenfeld, M. A., Noesselt, T., Poggel, D., Tempelmann, C., Hopf, J. M., Woldorff, M. G., Heinze, H. J., and Hillyard, S. A. (2002). Analysis of pathways mediating preserved vision after striate cortex lesions. *Annals of neurology*, 52(6):814–24.

[94] Schumacher, E. H., Jacko, J. A., Primo, S. A., Main, K. L., Moloney, K. P., Kinzel, E. N., and Ginn, J. (2008). Reorganization of visual processing is related to eccentric viewing in patients with macular degeneration. *Restor Neurol Neurosci*, 26(4-5):391–402.

[95] Schweigart, G. and Eysel, U. T. (2002). Activity-dependent receptive field changes in the surround of adult cat visual cortex lesions. *Eur J Neurosci*, 15(10):1585–96.

[96] Sereno, M. I., Dale, A. M., Reppas, J. B., Kwong, K. K., Belliveau, J. W., Brady, T. J., Rosen, B. R., and Tootell, R. B. (1995). Borders of multiple visual areas in humans revealed by functional magnetic resonance imaging. *Science*, 268(5212):889–93.

[97] Shibata, K., Watanabe, T., Sasaki, Y., and Kawato, M. (2011). Perceptual learning incepted by decoded fmri neurofeedback without stimulus presentation. *Science*, 334(6061):1413–5.

[98] Silvanto, J., Lavie, N., and Walsh, V. (2005). Double dissociation of v1 and v5/mt activity in visual awareness. *Cerebral cortex*, 15(11):1736–41.

[99] Slotnick, S. D. and Moo, L. R. (2003). Retinotopic mapping reveals extrastriate cortical basis of homonymous quadrantanopia. *Neuroreport*, 14(9):1209–13.

[100] Smirnakis, S. M., Brewer, A. A., Schmid, M. C., Tolias, A. S., Schuz, A., Augath, M., Inhoffen, W., Wandell, B. A., and Logothetis, N. K. (2005). Lack of long-term cortical reorganization after macaque retinal lesions. *Nature*, 435(7040):300–7.

[101] Sunness, J. S., Liu, T., and Yantis, S. (2004). Retinotopic mapping of the visual cortex using functional magnetic resonance imaging in a patient with central scotomas from atrophic macular degeneration. *Ophthalmology*, 111(8):1595–8.

[102] Van Essen, D. C., Newsome, W. T., and Maunsell, J. H. (1984). The visual field representation in striate cortex of the macaque monkey: asymmetries, anisotropies, and individual variability. *Vision research*, 24(5):429–48.

[103] Wandell, B. A. and Smirnakis, S. M. (2009). Plasticity and stability of visual field maps in adult primary visual cortex. *Nat Rev Neurosci*, 10(12):873–84.

[104] Weiskrantz, L. and Cowey, A. (1963). Striate cortex lesions and visual acuity of the rhesus monkey. *Journal of comparative and physiological psychology*, 56:225–31.

[105] Weiskrantz, L., Warrington, E. K., Sanders, M. D., and Marshall, J. (1974). Visual capacity in the hemianopic field following a restricted occipital ablation. *Brain*, 97(4):709–28.

[106] Werth, R. and Moehrenschlager, M. (1999). The development of visual functions in cerebrally blind children during a systematic visual field training. *Restorative neurology and neuroscience*, 15(2-3):229–41.

[107] Yan, L., Imbrosci, B., Zhang, W., Neubacher, U., Hatt, H., Eysel, U. T., and Mittmann, T. (2012). Changes in nmda-receptor function in the first week following laser-induced lesions in rat visual cortex. *Cerebral cortex*, 22(10):2392–403.

[108] Yang, T. and Maunsell, J. H. (2004). The effect of perceptual learning on neuronal responses in monkey visual area v4. *The Journal of neuroscience : the official journal of the Society for Neuroscience*, 24(7):1617–26.

[109] Zihl, J. and von Cramon, D. (1985). Visual field recovery from scotoma in patients with postgeniculate damage. a review of 55 cases. *Brain : a journal of neurology*, 108 (Pt 2):335–65.

[110] Zuiderbaan, W., Harvey, B. M., and Dumoulin, S. O. (2012). Modeling center-surround configurations in population receptive fields using fmri. *Journal of vision*, 12(3):10.

List of papers and statement of contributions

1. **A Papanikolaou, GA Keliris, TD Papageorgiou, Y Shao, E Krapp, E Papageorgiou, K Stingl, A Bruckmann, U Schiefer, NK Logothetis, and SM Smirnakis. Population receptive field analysis of the primary visual cortex complements perimetry in patients with homonymous visual field defects. PNAS, 2014**

I designed the experiments together with SM Smirnakis and GA Keliris. I modified the stimuli, programmed and carried out the experiments, performed all data analysis, and wrote the paper. TD Papageorgiou and Y Shao helped in conducting some of the experiments and in data analysis. E Krapp, E Papageorgiou, K Stingl, A Bruckmann and U Schiefer performed the ophthalmological tests.

2. **S Lee, A Papanikolaou, NK Logothetis, SM Smirnakis, and GA Keliris. A new method for estimating population receptive field topography in visual cortex. NeuroImage, 2013**

S Lee, SM Smirnakis, and GA Keliris designed the experiments. I modified the stimuli, programmed and carried out all experiments. S Lee wrote the paper. I commented where appropriate and helped in the process of writing.

3. **S Lee, A Papanikolaou, GA Keliris and SM Smirnakis. Topographical estimation of visual population receptive fields by fMRI. Journal of Visualized Experiments, In press**

S Lee, SM Smirnakis, and GA Keliris designed the experiments. I modified the stimuli, programmed and carried out all experiments. S Lee wrote the paper. I commented where appropriate and helped in the process of writing.

4. **A Papanikolaou, GA Keliris, S Lee, NK Logothetis, and SM Smirnakis. Nonlinear population receptive field changes in human area V5/MT+ of healthy subjects with simulated visual field scotomas; In review**

I designed the experiments together with SM Smirnakis and GA Keliris. I modified the stimuli, programmed and carried the experiments, performed all data analysis, and wrote the paper.

5. **A Papanikolaou, GA Keliris, S Lee, TD Papageorgiou, U Schiefer, NK Logothetis, and SM Smirnakis. Organization of Area hV5/MT+ in Subjects with Homonymous Visual Field Defects; Under preparation**

I designed the experiments together with SM Smirnakis and GA Keliris. I modified the stimuli, programmed and carried the experiments, performed all data analysis, and wrote the paper. TD Papageorgiou and S Lee helped in conducting some of the experiments and in data analysis.

6. **TD Papageorgiou, A Papanikolaou, and SM Smirnakis. A Systematic Approach to Visual System Rehabilitation: Population Receptive Field Analysis and Real-time Functional Magnetic Resonance Imaging Neurofeedback Methods. InTech, 2014**

TD Papageorgiou and SM Smirnakis designed the experiments. I carried out the experiments and performed the data analysis of the population receptive field measurements. TD Papageorgiou carried out the experiments and performed the data analysis of the real-time fMRI neurofeedback. TD Papageorgiou, I and SM Smirnakis wrote the paper.

Appendix

A.1 "Population receptive field analysis of the primary visual cortex complements perimetry in patients with homonymous visual field defects"

Population receptive field analysis of the primary visual cortex complements perimetry in patients with homonymous visual field defects

Amalia Papanikolaou[a,b], Georgios A. Keliris[a,c,1], T. Dorina Papageorgiou[d], Yibin Shao[a], Elke Krapp[e], Eleni Papageorgiou[e,f], Katarina Stingl[e], Anna Bruckmann[e], Ulrich Schiefer[e,g], Nikos K. Logothetis[a,h], and Stelios M. Smirnakis[d,i]

[a]Max Planck Institute for Biological Cybernetics, 72076 Tuebingen, Germany; [b]Graduate School of Neural and Behavioural Sciences, International Max Planck Research School, 72076 Tuebingen, Germany; [c]Bernstein Center for Computational Neuroscience, 72076 Tuebingen, Germany; [d]Departments of Neuroscience and Neurology, Baylor College of Medicine, Houston, TX 77030; [e]Center for Ophthalmology, University Eye Hospital Tuebingen, 72076 Tuebingen, Germany; [f]Department of Ophthalmology, University of Leicester, Leicester Royal Infirmary, Leicester LE2 7LX, United Kingdom; [g]Competence Center "Vision Research," Faculty of Optics and Mechatronics, Aalen University of Applied Sciences, 73430 Aalen, Germany; [h]Division of Imaging Science and Biomedical Engineering, University of Manchester, Manchester M13 9PT, United Kingdom; and [i]Michael E. Debakey VA Medical Center, Houston, TX 77030

Edited by Brian A. Wandell, Stanford University, Stanford, CA, and approved February 25, 2014 (received for review September 13, 2013)

Injury to the primary visual cortex (V1) typically leads to loss of conscious vision in the corresponding, homonymous region of the contralateral visual hemifield (scotoma). Several studies suggest that V1 is highly plastic after injury to the visual pathways, whereas others have called this conclusion into question. We used functional magnetic resonance imaging (fMRI) to measure area V1 population receptive field (pRF) properties in five patients with partial or complete quadrantic visual field loss as a result of partial V1+ or optic radiation lesions. Comparisons were made with healthy controls deprived of visual stimulation in one quadrant ["artificial scotoma" (AS)]. We observed no large-scale changes in spared-V1 topography as the V1/V2 border remained stable, and pRF eccentricity versus cortical-distance plots were similar to those of controls. Interestingly, three observations suggest limited reorganization: (*i*) the distribution of pRF centers in spared-V1 was shifted slightly toward the scotoma border in 2 of 5 patients compared with AS controls; (*ii*) pRF size in spared-V1 was slightly increased in patients near the scotoma border; and (*iii*) pRF size in the contralesional hemisphere was slightly increased compared with AS controls. Importantly, pRF measurements yield information about the functional properties of spared-V1 cortex not provided by standard perimetry mapping. In three patients, spared-V1 pRF maps overlapped significantly with dense regions of the perimetric scotoma, suggesting that pRF analysis may help identify visual field locations amenable to rehabilitation. Conversely, in the remaining two patients, spared-V1 pRF maps failed to cover sighted locations in the perimetric map, indicating the existence of V1-bypassing pathways able to mediate useful vision.

cortical blindness | quadrantanopia | plasticity | retinotopy | hemianopia

Cortical damage of the visual pathway often results from posterior or middle cerebral artery infarcts, hemorrhages, and other brain injuries. The most common visual cortex lesions involve the primary visual cortex (V1), the chief relayer of visual information to higher visual areas. Damage to area V1 or its primary inputs leads to the loss of conscious vision in the corresponding region of the contralateral visual hemifield, producing a dense contralateral scotoma that often covers a hemifield (hemianopia) or a single visual field quadrant (quadrantanopia).

A much-debated issue is whether the adult V1 is able to reorganize after injury. Reorganization refers to long-term changes in the neuronal circuit (1) and generally requires the growth of new anatomic connections or a permanent change in the strength of existing connections. Several studies report significant remapping in area V1 of patients suffering from macular degeneration and other retinal lesions (2–12). The extent of this remapping has recently been called into question, however (1, 13–19). Less is known about how the visual system remaps to cover the visual field after injury to area V1 or its input projection from the lateral geniculate nucleus (LGN). Enlarged receptive fields have been found in areas surrounding chronic V1 lesions in cats (20–22), and visual point spread functions were seen to enlarge over time in the areas surrounding focal V1 lesions in kittens (23). Smaller, short-term changes (2 d after the lesion) have been reported as well (24). As expected, reorganization is more extensive in young animals (23, 25) compared with adults (26). A change in the balance between excitation and inhibition may underlie this functional reorganization (27–31).

In humans, V1 injury is typically followed by a brief period of spontaneous recovery, which rarely lasts beyond 6 mo (32). Whether this recovery is the result of true visual system plasticity or is related to the gradual resolution of perilesional edema and general clinical improvement of the patients is unclear. A recent study in an adult human subject suggested that large-scale reorganization occurs in area V1 after partial deafferentiation by an optic radiation lesion (33); however, quantitative measurements were not performed. To date, there has been no systematic study in humans investigating how spared V1 cortex covers the visual field after chronic V1 injury. The present work is an effort in this direction.

Significance

Partial damage of the primary visual cortex (V1), or damage to the white matter inputs to V1 (optic radiation), cause blindness in specific regions of the visual field. We use functional MRI to measure responses in individual patients with a localized, chronic V1 injury that resulted in blindness in a quarter of the visual field. The fMRI responses of patients and controls are generally similar, but in some patients differences from controls can be measured. Importantly, responses in spared early visual cortex are not always congruent with visual perception. Understanding how the properties of early visual areas respond to injury will lead to better strategies for visual rehabilitation.

Author contributions: A.P., G.A.K., U.S., N.K.L., and S.M.S. designed research; A.P., G.A.K., T.D.P., Y.S., E.K., E.P., K.S., A.B., and S.M.S. performed research; A.P. and T.D.P. analyzed data; and A.P., G.A.K., and S.M.S. wrote the paper.

Conflict of interest statement: U.S. serves as a consultant for Haag-Streit Inc., Köniz, Switzerland.

This article is a PNAS Direct Submission.

Freely available online through the PNAS open access option.

[1]To whom correspondence should be addressed. E-mail: georgios.keliris@tuebingen.mpg.de.

This article contains supporting information online at www.pnas.org/lookup/suppl/doi:10.1073/pnas.1317074111/-/DCSupplemental.

We used the population receptive field (pRF) mapping method (34) to study how spared area V1 covers the visual field after chronic injury in five adult human subjects suffering from partial or complete quadrantanopia. Our findings suggest that there is at best a limited degree of reorganization in the spared part of area V1 after partial V1 injury. Interestingly, the pattern of coverage of the visual field measured in spared V1 cortex by functional magnetic resonance imaging (fMRI) typically does not match predictions derived from perimetry maps. Identifying the patterns of mismatch and how they relate to the capacity of early visual areas to reorganize after injury will eventually allow the adoption of more rational strategies for visual rehabilitation.

Results

Retinotopic Mapping of Spared Area V1. We studied five patients with partial V1 or optic radiation lesions resulting in partial or complete quadrantanopia (Table S1) and examined how the adjacent spared area V1 organization changes after the injury. We expected that in the absence of significant reorganization, retinotopic organization in the spared-V1 cortex would remain unchanged compared with controls. The patient's lesions are described in detail in Fig. 1. In brief, patient P1 had a lesion of the right inferior calcarine cortex (Fig. 1 *A*, *a*), resulting in a superior quadrantanopic defect of the left visual field (Fig. 2 *A*, *b*). Patient P2 had a right superior quadrantanopia (Fig. 2 *A*, *c*) after sustaining a temporal optic radiation infarct of the left hemisphere. Patient P3 had a lesion of the left inferior calcarine region resulting in a central (<10° radius) right superior quadrantanopia (Fig. 2 *A*, *d*), which spread slightly into the inferior right quadrant. Patient P4 had a lesion of the left inferior calcarine cortex, resulting in a right superior quadrantanopia (Fig. 2 *A*, *e*). Patient P5 had a partial left superior quadrantanopia extending to the inferior quadrant across the horizontal meridian (Fig. 2 *A*, *f*), resulting from an infarct in the right midposterior temporoparietal region (Fig. 1 *A*, *e*).

We observed two general patterns in the five patients examined. In patients P1, P2, and P3, spared (i.e., not completely deafferented) area V1 seems to retain its "coarse" retinotopic

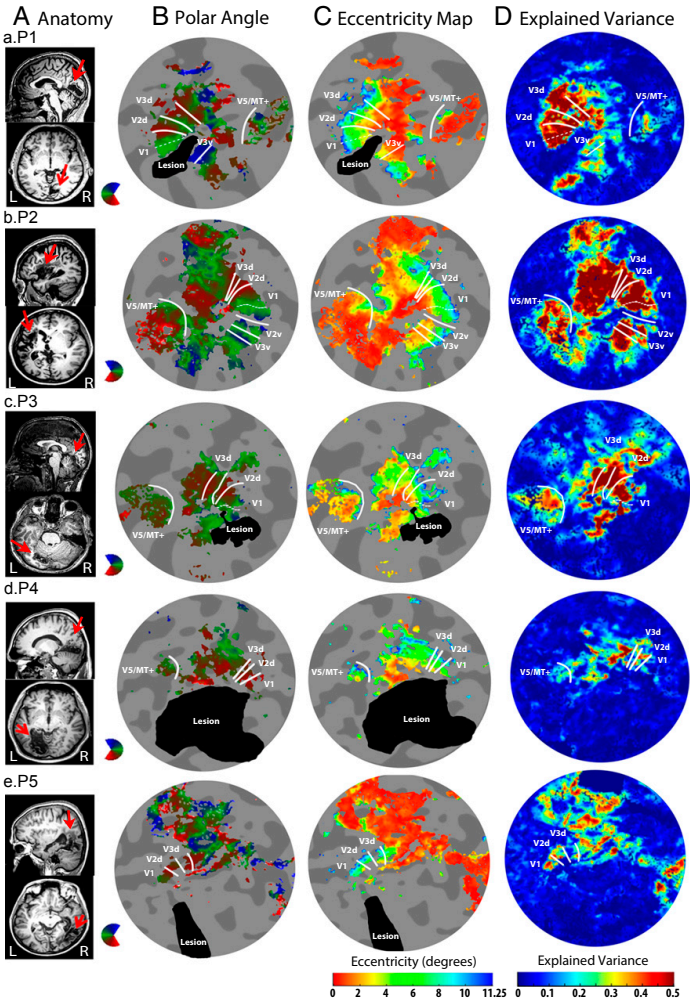

Fig. 1. Anatomic location of the lesion and retinotopic mapping. (*A*) Sagittal (*Upper*) and axial (*Lower*) slice showing each patient's anatomic lesion (a red arrow points to the lesion). Patient P1 had a lesion of the right inferior calcarine cortex involving the part of the V1 area inferior to the calcarine sulcus and the part of the extrastriate cortex corresponding to the ventral visual areas V2 and V3, with the foveal part of the vertical meridian at the border of ventral V3 and V4 spared. Patient P2 had a temporal optic radiation infarct of the left hemisphere located along the territory of the middle cerebral artery, sparing the gray matter of area V1 but deafferenting a significant portion of it by injuring the optic radiation. Patient P3 had a lesion of the left inferior calcarine cortex as a result of an ischemic event at the left inferior territory of the posterior cerebral artery, resulting in a right upper quadrantanopia. This lesion also involves part of the peripheral (>10° radius) area V1 superior to the calcarine, as well as extrastriate cortex corresponding to ventral visual areas V2, V3, and V4. Patient P4 had a lesion of the left inferior calcarine cortex caused by an infarct to the lower bank of the calcarine fissure. It involves left ventral area V1, left ventral extrastriate areas V2, V3, and V4, as well as part of the cortex near the fovea. Patient P5 had an infarct of the right midposterior temporoparietal lobes that damaged the temporal optic radiation and part of the parietal optic radiation. White matter tracts in the temporal lobe were affected, but deafferented V1 gray matter remained intact; the area corresponding to the anatomic lesion does not include early visual areas. (*B* and *C*) Polar angle (*B*) and eccentricity maps (*C*) overlaid on the flattened occipital lobe of the lesioned hemisphere for each patient. The lesioned area is colored black (Fig. S4 and *SI Materials and Methods*). (*D*) As expected, no significant activity was found inside the area of the lesion, as shown in the explained variance map. White contour lines indicate borders between visual areas. The dashed white line indicates the middle of the calcarine sulcus as identified by its anatomic localization (i.e., bottom of the calcarine sulcus).

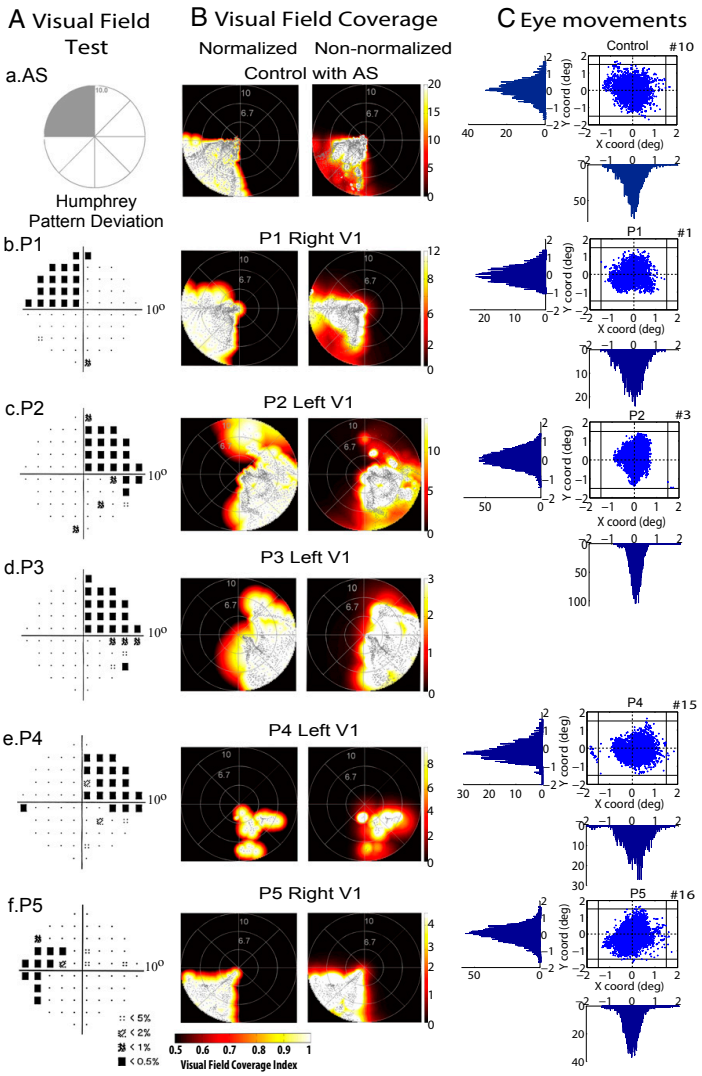

Fig. 2. Perimetry maps versus visual field coverage maps of spared area V1. (*A*) (*a*) Sketch of the visual field indicating the location of the artificial scotoma (shaded gray area). (*b–f*) Pattern deviation probability plots of the 10° Humphrey type (10, 2) visual field test for patients P1, P2, P3, P4, and P5. The small black dots show the locations in the visual field that are normal, and the black squares indicate a visual field defect at a $P < 0.5\%$ level according to the pattern probability plot (meaning that <0.5% of normal subjects would be expected to have such a low sensitivity at this visual field location). Pattern deviation numeric plots for patients P1, P2, P3, and P4 had a visual sensitivity of <−20 dB, indicating absolute visual field scotoma (56), at all visual field locations within the affected quadrants. Black squares outside the affected quadrants had a visual sensitivity of <−10 dB (most still <−20 dB) for these patients. Patient P5 had a visual sensitivity of <−20 dB (absolute scotoma) in all of the black square locations. (*B*) Visual field coverage maps of area V1 for a control subject with AS in the upper left quadrant and for each patient. The color map indicates the maximum pRF amplitude at each visual field location of all of the pRFs covering that location. The pRF centers across all voxels within the spared V1 are plotted with gray dots. In the normalized maps (*Left*), values range between 0 and 1, because the fitted Gaussian model is normalized to 1. In the nonnormalized maps (*Right*), the maximum pRF amplitude of the nonnormalized Gaussian pRFs is plotted. The nonnormalized color map is plotted with the maximum color value taken at the median pRF amplitude across all pRFs (*SI Materials and Methods*) to maintain sensitivity to relatively low values. The V1 coverage maps of patients P1, P2, and P3 overlap significantly with locations of the perimetric map that show an absolute scotoma (black squares with decibel deviations of <−20 dB). Only a few pRFs (~6%) of patient P2's spared-V1 overlap with locations of the perimetric map (black squares) that have a lower decibel deviation, between −10 dB and −20 dB. (*C*) Eye positions plotted at 60 Hz for each subject for one entire session (6.4 min). The number of eye deviations, defined as excursions >1.5° from the fixation point, is indicated next to the graphs with #. Patient P3 was scanned without eye-tracking while performing a task at fixation. All other patients were able to maintain fixation.

organization, similar to control subjects. In particular, the pRF center eccentricity maps (Fig. 1 *C*, *a–c*) show that the foveal representation was in the occipital pole, as expected, and that increasingly anterior locations responded to increasingly eccentric stimuli. In addition, the representation of the visual field in the dorsal spared V1 corresponding to the sighted quadrant extended from the horizontal meridian to the lower vertical meridian, as shown on the pRF polar angle maps (Fig. 1 *B*, *a–c*), similar to controls. Surprisingly, in these patients, the polar angle map shows significant activity in locations ordinarily corresponding to the inferior part of the calcarine (separated by the dotted line; Fig. 1 *B*, *a–c*), a region normally activated by stimuli presented in the superior part of the visual field, where the perimetry shows a dense scotoma (Fig. 2 *A*, *b–d*). We investigated this pattern in more depth, as discussed in the next section.

Patients P4 and P5 exhibited a different pattern. In these patients, the extent of the retinotopic topography of area V1 that was activated was considerably less than would be predicted from the visual field maps. Specifically, for patient P4, the organization of spared area V1 was severely disrupted, and almost the entire dorsal V1, except for a sliver near the lower vertical meridian, was devoid of activity (Fig. 1 *B–D*, *d*). Nevertheless, the perimetry map of this patient closely conforms to a superior quadrantanopia, with only a slight extension below the horizontal meridian. The relatively well-preserved perimetry map of the right lower visual field quadrant (Fig. 2 *A*, *e*) suggests either the presence of sufficient intact dorsal V1 islands to compensate (even though they are not visible on the retinotopic map) or the presence of functional V1-bypassing pathways to higher areas that may have more complete retinotopic coverage maps (35).

Similarly, patient's P5 visual cortex inferior to the calcarine was severely affected, with no visually driven functional activity present in the ventral occipital region as a whole (Fig. 1 *B–D*, *e*). However, this subject shows a sparing along the left upper vertical meridian in the perimetry map (Fig. 2 *A*, *f*). Presumably, preserved visual function in the left upper visual field is mediated by V1-bypassing pathways, likely involving areas beyond V3 (*Discussion*), or perhaps via the contralesional hemisphere (left area V1). We explore this in more details in the next section.

In summary, we observed two different patterns in the five patients that we examined. Patients P1, P2, and P3 had visually driven activity in spared V1 regions that corresponded to dense locations of their perimetric scotoma. In contrast, patients P5 and P4 had intact perimetric maps in locations corresponding to area V1 regions, with an absence of visually driven activity. We analyzed these patterns further using the concept of visual field coverage maps.

Correspondence Between Visual Field Coverage Maps and Perimetric Scotomas. To estimate how the visual field is represented in spared area V1, we superimposed appropriately normalized pRFs arising from all of the spared V1 voxels to derive visual field coverage maps (Fig. 2*B* and *SI Materials and Methods*). The visual field coverage maps define the locations within the visual field that evoke a significant response from voxels within a region of interest (ROI) in the cortex. Determining the degree to which visual field coverage maps match perimetric maps, which indicate the patients' perceptual scotoma, is of interest.

To ensure that the patients' visual field coverage maps are not an artifact of poor pRF estimation caused by the presence of the visual field scotomas, we tested the effect of an "artificial scotoma" (AS) on normal subjects. We measured responses in five control subjects while masking the left superior quadrant of the visual field, thereby simulating a left upper quadrantanopia. As expected, the visual field coverage maps of the right V1 hemisphere in AS controls reveal visually driven activity only for stimuli presented in the left inferior visual field quadrant (Fig. 2 *B*, *a*). No activity was observed in the left upper visual field quadrant in any of the five AS control subjects.

In contrast, the visual field coverage maps of spared V1 in patients P1, P2, and P3, who had a quadrantic visual field defect similar to AS controls, contain pRF centers that extend well beyond the border of the perimetric scotoma into the superior (anopic) visual field quadrant (Fig. 2 *B*, *b–d*). The pRFs, whose centers fall inside the area of the scotoma, belong to voxels at the correct anatomic location, inferior to the calcarine, which do not appear to be grossly ectopic (Fig. 3). Thus, the observed activity likely reflects islands of V1 that were spared or only partially damaged. Interestingly visually driven activity in this spared V1 region is not sufficient to guarantee visual awareness, as measured by standard perimetry.

One possibility is that the blood oxygen level-dependent (BOLD) signal amplitude is lower at V1 locations covering the interior of the scotoma and thus cannot mediate visual perception. However, for patients P1 and P3, the mean amplitude of the pRF centers that fall inside the perimetric scotoma was similar to the mean amplitude of pRF centers located outside the scotoma, as shown in the nonnormalized visual field coverage maps (Fig. 2 *B*, *b* and *d*). In this case, the dense perimetric defect near the horizontal meridian might be explained by injury in downstream extrastriate areas, such as V2/V3 (36, 37), or the interruption of V1 projections to extrastriate areas. In fact, the lesion of these patients involves areas V2v and V3v, supporting the first possibility.

On the other hand, for patient P2, who had an optic radiation lesion, the loss of visual perception cannot be attributed to a lesion downstream from area V1, because the visual cortex remained intact. Responses in ventral areas V2 and V3 overlapped with the area of the scotoma, similar to V1 (Fig. S1*A*). In this case, the nonnormalized visual field coverage maps showed a significantly lower mean amplitude of pRF centers falling inside the scotoma compared with those in the inferior (sighted) quadrant (Fig. 2 *B*, *c* and Fig. S1*A*). Thus, it is possible, at least in principle, that this decreased level of visually driven activity is responsible for the loss of visual perception as measured by perimetry. Interestingly, scattered pRF centers with high amplitude remained inside the scotoma. One possible explanation for this finding is that intact islands of spared, partial axonal tracts in the optic radiation survived after the ischemic event and activate corresponding locations in area V1. Despite being visually driven, however, these islands were unable to mediate visual perception as measured on perimetric maps and cannot be detected even with the relatively sophisticated perimetry mapping methods used here (*SI Materials and Methods*).

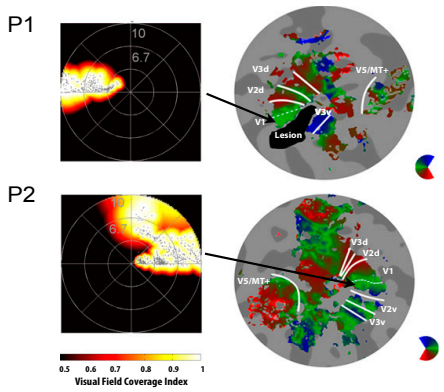

Fig. 3. Anatomic localization of area V1 population receptive fields within the scotoma. (*Left*) Visual field coverage maps obtained from the region of spared V1 inferior to the bottom of the calcarine sulcus (anatomic location of the horizontal meridian) for patients P1 and P2. (*Right*) Anatomic location of the bottom of the calcarine sulcus indicated by a dashed line on the polar angle flat maps. Note that pRFs with centers falling within the scotomatous area in these patients map to the correct anatomic location, inferior to the calcarine (black arrow).

The mismatch between the visual field coverage map and perimetric scotoma does not manifest in the same way in every individual. For example, the visual field coverage of the spared V1 in patient P4 shows pRF centers within the inferior quadrant, outside the visual field scotoma (Fig. 2 *A* and *B*, *e*). In patient P5, a few pRF centers below the horizontal meridian seemed to fall in areas where the perimetry test showed a dense defect, as in patients P1, P3, and P2 (Fig. 2 *A* and *B*, *f*). However, the more striking observation in both these patients is the smaller than expected (based on the perimetry map) activated area in V1. In patient P4, the activation pattern seen in area V1 (Fig. 2 *B*, *e*) was patchy and smaller than expected based on the perimetric map. The visual field coverage map of the right inferior (sighted) quadrant contained significantly fewer pRF centers compared with controls, although the corresponding pRFs cover most, but not all, of the quadrant.

It is possible that pRFs in surviving islands of area V1 enlarged over time, producing a confluent visual field coverage map that partially mediated the residual visual function. However, even taking this into account, the pRF coverage map appeared to miss portions of the visual field where the perimetric map showed normal vision. This finding suggests that part of the residual visual function may be mediated through spared V1-bypassing pathways. In fact, dorsal areas V2 and V3 showed full coverage of the lower visual field quadrant, supporting this hypothesis

(Fig. S1*B*). Similarly, the perimetry map of patient P5 showed a significant area of sparing along the vertical meridian and beyond, within the left upper visual field quadrant (Fig. 2 *A*, *f*). Surprisingly, there was no contralateral V1 activation corresponding to that quadrant, despite the fact that a significant portion of the quadrant was essentially normal on the perimetry map (Fig. 2 *A*, *f*). One possibility is that visual perception near the vertical meridian might arise from V1-bypassing pathways providing direct input to extrastriate areas beyond V3 (35), or perhaps from ectopic V1 activation in the contralesional hemisphere.

The differences in visual field coverage maps between patients and AS controls cannot be explained by eye movements. Subjects were able to maintain fixation within a 1.5° radius from the center of fixation as measured with our eye-tracking system (Fig. 2*C* and *SI Materials and Methods*), except for very occasional excursions beyond this range (Fig. 2). The results remained unchanged after the epochs in which the patients had eye deviations (>1.5°) from the fixation point were removed from the analysis. Patient P3's eye movements were not recorded, but he performed a challenging detection task at fixation, and his performance was always >80% correct. The retinotopic maps of his healthy hemisphere were well organized, suggesting that he did not make large, confounding eye movements. In addition, to ensure intrasubject reproducibility, we repeated the experiment on another day for patients P2 and P5 and confirmed the findings across days. Patients P1, P3, and P4 could not repeat the session; however, we analyzed each scan separately before averaging and confirmed the reliability across different scans obtained on the same day.

In summary, our comparison of perimetric maps and pRF coverage maps of the visual field confirmed the two patterns of mismatch noted in the previous section. In three of the five patients, spared area V1 pRF maps overlapped significantly with the scotoma, suggesting remaining visually responsive islands of V1 that cannot contribute to visual perception, perhaps because of damage to downstream areas or damage to the inputs that they receive from area V1. In the remaining two patients, spared V1 pRF maps failed to completely cover locations that were found to have intact thresholds on perimetry. In these patients, the observed mismatch might indicate the existence of V1-bypassing pathways able to mediate useful vision. The information obtained from pRF analysis complements that obtained by standard perimetry maps, and can be used to further characterize the underlying etiology of cortical visual field defects.

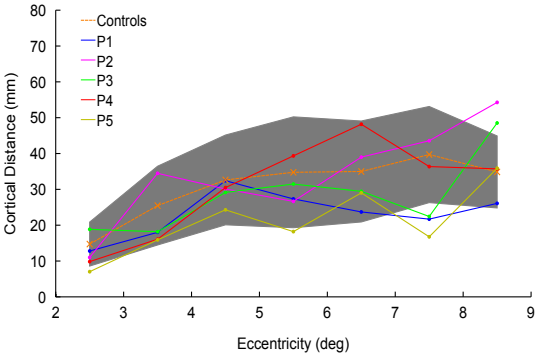

Fig. 4. Cortical distance between the V1 horizontal meridian and dorsal V1/V2 border for patients P1–P5. The cortical distance is calculated by measuring the surface area of seven isoeccentric ROIs (range of eccentricities, 2–9°; bin size, 1°) and dividing by the cortical magnification factor (mm/°) at each eccentricity. The mean cortical distance of the controls (mm) is plotted as an orange dotted line. The gray shaded area indicates the SD (n = 16 hemispheres).

pRF Center Distributions in Spared Area V1 Show at Best Limited Reorganization. A general finding in all five patients was that the retinotopic representation of the spared V1 remained grossly unaffected (Fig. 1). The borders between visual areas, as marked by polar angle reversals, were detected at the expected locations. We measured the cortical distance from the V1 horizontal meridian to the dorsal V1/V2 border along isoeccentricity contours, and plotted it as a function of eccentricity. Plots for all patients were within the range of controls (Fig. 4). Furthermore, the Talairach coordinates at an eccentricity of 8° along the horizontal meridian of V1 and the dorsal V1/V2 border were similar to those of controls (Table S2), and consistent with previous reports (38). In addition, the eccentricity maps exhibited a monotonic progression of phase, as expected (Fig. 1*C*). These results reveal that large-scale retinotopic distortions do not occur; however, the possibility of fine changes in the retinotopic structure of spared V1 cortex cannot be excluded and merits quantitative assessment.

To do so, we compared the distributions of pRF center locations between patients and AS controls. The AS serves as a baseline to control for pRF changes that may arise from reorganization versus simple stimulus deprivation. This control might not always be completely adequate, however, given that partial deafferentiation of the visual pathways may affect the pRFs corresponding to visual field locations that do not belong to the scotoma. Thus, a case-by-case evaluation of whether pRF differences between patients and AS controls are result of partial deafferentiation as opposed to remapping or true reorganization is needed.

pRF center distribution as a function of distance from the scotoma border. In two of the five patients (P1 and P2), the distribution of pRF centers as a function of distance from the horizontal border of the scotoma (elevation) differed significantly from that of AS controls [two-sample Kolmogorov–Smirnov test; significance is reported as $P = a < b$, where b is the value selected to reject the null hypothesis (*Materials and Methods*); P1: $P = 8.09 \times 10^{-63} < 10^{-27}$; P2: $P = 7.62 \times 10^{-42} < 10^{-27}$]. Specifically, pRF centers were seen to cluster near the border of the scotoma, that is, the horizontal meridian (Fig. 5*A*). In fact, in these patients, a number of pRF centers crossed the scotoma border to lie inside the scotoma (i.e., with elevation > 0°), as seen in the visual field coverage maps (Fig. 5*A*, *Insets*). These pRFs belonged to voxels that were not anatomically ectopic but mapped roughly at the correct anatomic location, the lower bank of the calcarine sulcus (Fig. 3). One may then wonder whether they are the reason that pRF centers cluster more strongly near the border of the scotoma in patients compared with AS-controls. However, the distribution of pRFs of the spared dorsal V1, defined by its anatomic location, was also significantly shifted toward the scotoma border, with voxels clustering near the border (0° elevation) (Fig. 5*B*; P1: $P = 8.09 \times 10^{-38} < 10^{-26}$; P2: $P = 8.09 \times 10^{-38} < 10^{-26}$). This finding suggests that the observed shift in the distribution of pRF centers likely corresponds to a slight reorganization of the visual field coverage map in unlesioned portions of area V1 that are located close to the scotoma border, perhaps because of a change in local excitation/inhibition balance as a result of the lesion.

This effect was not seen in every patient. The distribution of pRFs in the dorsal V1 of patient P3 did not show significant clustering near the border of the scotoma compared with AS controls ($P = 1.4 \times 10^{-15} > 10^{-28}$) (Fig. 5*B*). Patients P4 and P5 had fewer voxels with pRFs inside the sighted quadrant compared with AS controls, and P4 also showed a trend toward clustering of pRF centers at the scotoma border, but this did not reach significance under our relatively strict comparison criterion (P4: $P = 1.48 \times 10^{-04} > 10^{-07}$; P5: $P = 9.6 \times 10^{-04} > 10^{-11}$) (Fig. 5*A*). Regardless, the lesions of patients P4 and P5 extended to

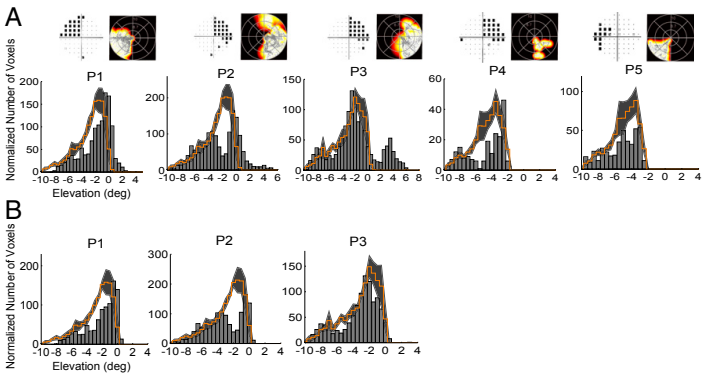

Fig. 5. pRF center distribution as a function of distance from the scotoma border. (*A*) Histograms (gray bars) showing the number of voxels as a function of the pRF center elevation, that is, the distance of the pRF center from the horizontal meridian border of the scotoma (coordinate Y), for patients P1–P5. Units are degrees of visual angle. The mean distribution of voxels in the control subjects with AS is overlaid as a step histogram in orange. To adjust for V1 size, the distributions of the controls were normalized according to the relative size of the retinotopically corresponding V1 regions that were activated in patients versus controls under the full stimulation condition (*SI Materials and Methods*). The shaded area represents the SEM for the control group ($n = 5$). The pRF center elevation distributions of patients P1, P2, and P3 show pRFs within the area of the scotoma (elevation >0), as also shown in the visual field coverage maps (*Insets* and Fig. 2 *B*, *b*–*d*). However, for patients P1 and P2, there was also a clustering of voxels near the scotoma border. The pRF center elevation distributions of patients P4 and P5 show fewer voxels within the sighted quadrant compared with AS controls and a clustering near the scotoma border for P4, but the effect did not reach significance. The observed differences between these patients and AS controls are likely related to partial deafferentiation of the voxels plotted. (*B*) pRF center elevation distributions of the significantly activated voxels in the anatomically defined intact dorsal V1 of patients P1, P2, and P3. For patients P1 and P2, pRFs clustered significantly near the scotoma border, suggesting reorganization. This effect was not seen in patient P3.

partially involve dorsal V1 or its inputs (Fig. 1 *A*, *d* and *e*), making it difficult to determine whether observed changes are related to true reorganization or to partial deafferentiation.

In summary, these results suggest that in some patients with partial lesions of area V1 or its inputs (here P1 and P2), the pRF centers of spared V1 cortex cluster near the border of the scotoma. This clustering is seen primarily within 1–2° of the scotoma border. The magnitude of the shift is small, suggesting a limited degree of reorganization. One patient (P3) did not exhibit this effect; however, this patient's injury occurred only 6 mo before recruitment, compared with the chronic lesions of the other patients, and we cannot exclude the possibility that time may affect the degree of the observed reorganization. In patients P4 and P5, the observed differences are more likely related to partial deafferentiation or partial injury of the corresponding voxels.

Population receptive field size. We found a larger mean pRF size in the spared V1 area in patients compared with AS controls (Fig. 6). Specifically, the mean pRF size in the spared V1 of patients P1, P2, P4, and P5 was increased by ∼25% compared with AS controls. A larger increase was seen in patient P3, ∼90% compared with AS controls. The pRF size distributions of patients P1, P2, and P3 were significantly shifted toward larger sizes compared with the AS controls ($P = 1.4 \times 10^{-76} < 10^{-63}$, $P = 1.67 \times 10^{-78} < 10^{-70}$, and $P = 1.13 \times 10^{-165} < 10^{-66}$, respectively) (Fig. 6*A*). The same trend was seen for patients P4 and P5, but it did not reach significance ($P = 7.4 \times 10^{-09} > 10^{-39}$ and $P = 1.19 \times 10^{-33} > 10^{-62}$) (Fig. 6*A*). V1 lesions were larger in these patients (Fig. 1 *B*, *d* and *e*), leading to few visually modulated area V1 voxels and thus more measurement variability. In addition, in these patients, the pRFs were located at higher eccentricities, where pRF sizes are larger. In general, the mean pRF size for each patient was greater than the corresponding mean of the distribution of pRF sizes of the AS controls (Table S3).

We examined whether the pRF size increase depends on eccentricity and distance of the voxel from the scotoma border. To do so, we divided voxels in the spared V1 of patients and AS controls into two categories: voxels with pRF centers within 2° of the horizontal scotoma border and voxels with pRF centers >2° from this border, and plotted mean pRF size versus eccentricity (Fig. 6 *B* and *C*). We found that for all patients, mean pRF size was increased for voxels located within 2° of the scotoma border (Fig. 6*B*), with increases of ∼40% for patients P2, P4, and P5; ∼75% for patient P1; and ∼120% for patient P3. For patients P1, P2, P3, and P5, the increase occurred across almost the whole range of eccentricities, whereas for P4, it was more profound for large eccentricities (>6°). In contrast, the mean pRF size of voxels >2° away from the scotoma was more similar in patients P1, P2, P4, and P5 and AS controls (Fig. 6*C*). For P3, the mean pRF size was increased for voxels away from the scotoma as well, but to a lesser degree (∼40%) compared with voxels near the scotoma. The larger increase observed in this patient might be attributed to the relatively recent lesion compared with the other patients, but we cannot exclude the possibility that small eye movements might have affected the pRF size, considering that this patient was not eye-tracked. However, eye movements would be expected to increase pRF size in higher areas in a comparable way as in V1 (39). In patient P3, pRF size in areas V2d and V3d was slightly larger (∼15%) compared with that in AS controls, but the magnitude of the increase was considerably less than observed in area V1 and did not occur for all eccentricities (Fig. S2). Thus, eye movements cannot be the sole explanation for the pRF size increase observed in area V1 of this patient.

In summary, the pRF size distribution in the spared V1 regions of patients with partial quadrantanopia appeared to shift toward larger values compared with the AS controls, particularly near the scotoma border.

Contralesional Hemisphere. Previous reports have suggested that in some cases, residual vision in the blind hemifield might be mediated by visual areas in the intact hemisphere (40–43). It is then possible that after area V1 injury, reorganization might occur in the contralateral, healthy hemisphere. Because in primates, callosal projections are concentrated along the V1/V2 boundary (44), the vertical meridian is the most natural place in the contralesional hemisphere to look for potential reorganization. We compared pRF sizes between the dorsal and ventral V1 and

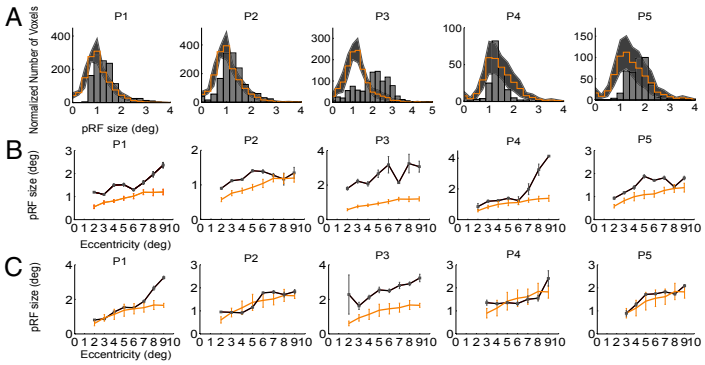

Fig. 6. pRF size in spared V1 areas. (*A*) Histograms of the distribution of pRF size from the spared V1 of all patients (gray bars) compared with the mean distribution of AS controls (orange stairs). The shaded area indicates the SEM across the AS controls. The pRF size distribution of all patients is shifted toward larger pRF sizes compared with the AS controls. (*B*) Mean pRF size versus eccentricity for voxels located near the scotoma border (<2°) in patients (black) and AS controls (orange). The orange error bars indicate the SEM across AS control subjects ($n = 5$). The gray error bars indicate the SEM across voxels within an eccentricity bin (bin size, 1°) for each patient. Mean pRF size is larger in patients compared with AS controls across eccentricities. pRFs within the area of the scotoma of patients P1, P2, and P3 were not included in the plots; however, results remain the same when these voxels are included. (*C*) Mean pRF size versus eccentricity for voxels located away from the scotoma border (>2°) in patients (black) and AS controls (orange). Mean pRF size was similar in patients P1, P2, P4, and P5, and AS controls across eccentricities, with only P1 having a slightly increased pRF size for eccentricities >7°. For P3, the mean pRF size was larger than that of AS controls for all eccentricities. Eye movements cannot explain the observed differences for patients P1, P2, P4, and P5, given that the distribution of eye movements was similar in patients and controls (Fig. 2*B*) and eye movements would have caused an increase in pRF size at low eccentricities irrespective of distance from the scotoma border. Patient P3 was not eye-tracked, and thus we cannot completely exclude that possibility. However, pRF sizes in areas V2d and V3d did not increase similarly to those in V1, suggesting that eye movements might not be responsible for the large increase observed in V1 (Fig. S2).

between the vertical and horizontal V1 meridians of the hemisphere ipsilateral (contralesional) to the visual field scotoma in patients and in AS controls. Patients P1, P2, P3, and P4 showed no significant difference in mean pRF size between contralesional dorsal and ventral V1 or between vertical and horizontal V1 meridians (Fig. S3); however, the pRF size distribution of the entire contralesional V1 in each patient showed a significant shift to larger pRF sizes in patients P2, P5, and P3 compared with AS controls ($P = 1.63 \times 10^{-64} < 10^{-62}$, $P = 2.55 \times 10^{-167} < 10^{-70}$, and $P = 4.93 \times 10^{-236} < 10^{-63}$ respectively) (Fig. 7*A*). The increase occurred across all eccentricities in patients P3 and P5 and mainly for eccentricities >5° in patient P2 (Fig. 7*B*). Patients P1 and P4 had a pRF size distribution more similar to that of AS controls, with differences that did not reach significance (P1: $P = 8.34 \times 10^{-34} > 10^{-64}$; P4: $P = 7.53 \times 10^{-18} > 10^{-55}$) (Fig. 7*A*); however, these patients had a larger pRF size for eccentricities >7° compared with AS controls (Fig. 7*B*).

Only patient P5 had significantly larger pRFs in the ventral contralesional V1 than in the dorsal contralesional V1, particularly along the upper vertical meridian (Fig. S3). This finding is intriguing, and it is tempting to associate it with the sparing seen in the perimetric map of this patient along the left upper vertical meridian (Fig. 2 *A*, *f*). This association is not certain, however, for several reasons: (*i*) Although larger, patient P5′s pRFs along the vertical meridian crossed only modestly (~1–2°) into the contralateral visual field, and this cannot readily explain the relatively larger sparing seen on perimetric maps; (*ii*) the degree of crossover was commensurate with the size of patient P5′s eye movements (~1.3°); and (*iii*) we cannot completely exclude the possibility that area V1 of the lesioned hemisphere could be mediating visual perception in the spared region seen on visual perimetry while being too weakly visually driven to be evident on the pRF maps.

Discussion

The few published studies of human visual system organization in the setting of area V1 injury are mainly case reports (33, 45). Naturally occurring cortical lesions show considerable variability, making it difficult to draw definite conclusions from isolated case studies. Dilks et al. (33) studied a subject with left upper quadrantanopia after damage to the optic radiation and report significant ectopic activity in area V1 at 6 mo after the ictus. Specifically, activity elicited by stimuli presented in the sighted left lower visual field quadrant mislocalized to V1 regions ordinarily corresponding to the blind left upper quadrant, suggesting the occurrence of large-scale reorganization. Whether the ectopic V1 activity that Dilks et al. reported is the result of reorganization or simply the result of a different pattern of visual input between patient and controls is unclear, however. The authors attempted to control for this by removing stimulation epochs corresponding to the left upper quadrant from their analysis in the controls, but this was not necessarily definitive, because the stimulus was in fact presented there. A more appropriate control would have been to mask the stimulus presentation space in the controls to simulate a quadrantic scotoma (AS condition). Given the high intersubject variability, further studies are needed to characterize how the functional properties of the visual cortex change in the context of injury.

Here we used quantitative pRF analysis (34, 46–48) to study the properties of spared V1 cortex in five patients with chronic postchiasmatic lesions resulting in homonymous visual field quadrantanopia. We derived detailed retinotopic maps and visual field coverage maps of spared area V1 for each patient and made the following observations: (*i*) The spared V1 region of the lesioned hemisphere retained its coarse retinotopic organization, as described previously (35, 45), the V1/V2 border remained stable, and retinotopic maps showed a monotonic progression of phase, as expected; and (*ii*) visual field coverage maps of the spared V1 area generally did not exactly match the area of the dense perimetric scotoma (Fig. 2). Two main patterns of mismatch were identified.

Pattern 1: Visual Field Coverage Maps of Spared-V1 Overlapped Significantly with the Dense Perimetric Scotoma in Three of the Five Patients. pRFs activated inside the scotoma were found in the proper anatomic locations. Thus, in patient P2, whose scotoma

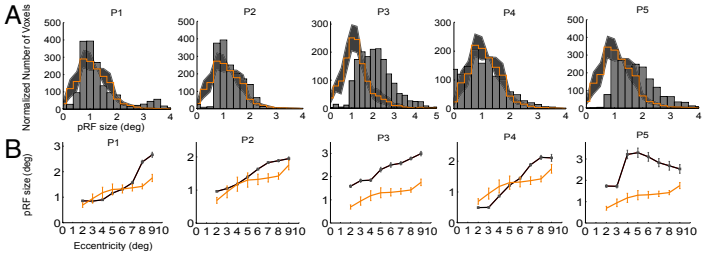

Fig. 7. pRF size of the contralesional V1. (*A*) Histograms of the distribution of pRF sizes from the contralesional V1 of all patients (gray bars) compared with the mean distributions of AS controls (orange stairs). The shaded area indicates the SEM across AS controls ($n = 5$). The distributions show a significant shift to larger pRF sizes for patients P2, P3, and P5. Patients P1 and P4 showed a significant increase in pRF size only for eccentricities >7°. (*B*) Mean pRF size versus eccentricity for voxels in the contralesional V1 of patients (black) and AS controls (orange). The orange error bars indicate the SEM across AS control subjects ($n = 5$). The gray error bars indicate the SEM across voxels within an eccentricity bin (bin size, 1°) for each patient. For patients P1, P2, and P4, pRF size was larger compared with that in AS controls for eccentricities >6–7°. For patients P3 and P5, pRF size was increased across all eccentricities. As shown in Fig. 2*C*, patients P1, P2, P4, and P5 were able to ensure fixation. The amplitude of the eye movements did not differ between patients and controls (Fig. 2*C*), and epochs of significant deviation from fixation were excluded from the analysis; thus, the findings for these patients are unlikely to be attributed to eye movements. Patient P3 was not eye-tracked, however, and even though he was performing a challenging detection task at fixation, in his case we cannot completely exclude that possibility.

resulted from optic radiation injury, residual islands of V1 activity likely received inputs from axonal tracts that are only partially affected by the lesion. These tracts were able to elicit area V1 activity, but were not strong enough to elicit a visual percept (Fig. 2 *B*, *c*). In principle, lack of a percept in the presence of area V1 activity may occur because retinotopically corresponding higher pathways or areas are injured, or because the activity generated in area V1 is too weak or too disorganized to elicit a percept. Patient P2 had no lesion in higher pathways, and so the latter mechanism likely dominates. Given that the pathways from area V1 to higher extrastriate areas were intact and islands of activity were present in the V1 cortex, it is reasonable to view this patient as a prime candidate for visual rehabilitation. In theory, the capacity for recovery would be maximal in the portion of the scotoma that overlaps with the visual field coverage map of area V1.

The two other patients in this category, P1 and P3, had lesions that included ventral areas V2/V3, raising the possibility that the information flow between area V1 and higher extrastriate areas had been cut off. In that event, knowing the region of overlap between the visual field coverage map of area V1 and the scotoma might still be helpful if the projection from spared V1 cortex to extrastriate areas was not completely cut off. Regardless, the region of overlap between a visual field coverage map and the corresponding perimetrically determined visual field scotoma identifies visual field locations that can still generate some level of V1 activity and thus may have greater potential for visual rehabilitation. This strongly suggests that pRF mapping (34, 49) should be incorporated into the design of future visual rehabilitation studies.

Pattern 2: Visual Field Coverage Maps of Spared-V1 Did Not Cover Completely the Sighted Quadrant of the Perimetric Map. Two out of five patients exhibited this pattern of activity. Presumably in this case, residual visual function is mediated by V1-bypassing pathways (as supported by the visual field coverage maps of areas V2/V3 in patient P4; Fig. S1) or perhaps through the contralesional hemisphere. The latter possibility would be supported by a spreading of the pRF coverage map across the vertical meridian, as occurred to some degree in patient P5 (Fig. S3), who exhibited an area of sparing near the vertical meridian in the perimetry map. This occurred to a lesser degree than expected from the area of sparing seen in the perimetric map, however, and thus this hypothesis cannot be verified here; more research is needed. Another possible explanation that we cannot completely exclude here is that in some cases, fMRI mapping might not be sufficiently sensitive to detect weak visually induced activity in early visual areas. This is probably not the complete explanation, however, for several reasons: (*i*) We calculated the BOLD signal-to-noise ratio (SNR) in the areas of interest in all patients and found them to be within the range obtained in controls with AS; (*ii*) the variance explained of voxels corresponding to these visual field locations is within the range obtained in nonvisually responsive areas; and (*iii*) previous studies have shown that BOLD signal amplitude correlates well with visual stimulus perception (50, 51), and in some cases even subthreshold stimuli elicit significant modulation in early visual areas (52).

Do (Spared) Area V1 pRFs Change After the Lesions? pRF measurements provide a way to gauge the degree of reorganization that occurs in early visual areas. The pRF depends on both the size and the position scatter of individual receptive fields within a voxel (53). It thus might be affected by partial deafferentiation of V1 inputs, or may reflect reorganization, that is, sprouting or strengthening of anatomic connections after V1 injury. Incomplete stimulus presentation itself might alter pRF size measurements and result in apparent remapping even in the absence of true reorganization (54). For this reason, changes can be reasonably attributed to cortical reorganization only if they are significantly different than changes observed in controls under the AS condition. Thus, we compared pRF center and size distributions between patients and AS controls.

Does the Position of pRF Centers Reorganize? One important question is whether the pRFs of spared area V1 in patients emerge from voxels that are at the correct anatomic locations versus voxels that are ectopic, suggesting possible reorganization. We have not found voxels with grossly ectopic V1 pRFs in any patient. pRFs fall in approximately correct anatomic locations; that is, pRFs located in the upper visual field belong to voxels located below the calcarine sulcus and vice versa. Finer changes in pRF localization do occur, however.

We found that for two of the five patients (P1 and P2), pRF center elevation (i.e, distance from the scotoma border) distributions differed significantly from that of the AS controls, with clustering near the scotoma border (horizontal meridian). Moreover, this occurred even when we restricted the analysis to the intact part of V1 that corresponds to a normal perimetry (dorsal V1; Fig. 5*B*). This suggests that for these patients, some pRF centers shift their location over short distances to locations near the scotoma border, supporting the notion of reorganization. A

possible mechanism behind this shift is enhancement of surviving single-cell pRFs in voxels near the border of the scotoma after injury, perhaps via a change in the balance of inhibition versus excitation (27–31). The magnitude of the shift is on average only 1°, consistent with at most a limited degree of reorganization.

In contrast, patients P4 and P5 exhibited patchy activation of spared V1. The difference in pRF center distributions between these patients and AS controls may be the result of partial deafferentiation. The remaining patient, P3, had similar pRF center location distributions as AS controls. A possible important difference in this patient is that V1 injury occurred only 6 mo before recruitment, whereas all other patients had been lesioned for years. None of the patients who participated in this study, including the two patients with optic radiation lesions, had ectopic pRF centers over distances comparable to those suggested by Dilks et al. (33).

Does pRF Size Change in Spared-V1 Cortex? pRF size measurements in the spared V1 cortex of patients showed pRF size increases of ∼25% for patients P1, P2, P4, and P5 and ∼90% for patient P3 compared with AS controls. The pRF size difference reached ∼40% for patients P2, P4, and P5, ∼75% for patient P1, and ∼120% for patient P3 near (<2°) the scotoma border, whereas it was correspondingly smaller far (>2°) from the scotoma border (Fig. 6 *B* and *C*). As mentioned earlier, this may stem from decreased inhibition in the area surrounding the lesion (21), or perhaps because subcortical inputs from LGN or the pulvinar may reorganize via sprouting of cortical axons (55) and contribute to the activation of area V1 areas surrounding the lesion.

pRF size in area V1 of the intact hemisphere also increased in patients compared with healthy AS controls. The relative magnitude of the increase was ∼20% for patient P2 and ∼90% for patients P3 and P5. pRFs for patients P1 and P4 increased by ∼30% but only for eccentricities 6–10°. The relative increase in pRF size seen in the contralesional hemisphere may be attributed to loss of input from interhemispheric connections (40–42), although the expectation that these would affect mainly pRFs along the vertical meridian is not well born out.

Conclusions

Although each patient is unique, several themes emerge from our study:

1. Area V1 displays at best a limited degree of reorganization in adult humans with homonymous visual field defects due to postchiasmatic lesions of the visual pathway.
2. This reorganization is manifested in some patients by a small shift in the pRF centers toward the border of the scotoma and in most patients by a slight increase in V1 pRF sizes near the border of the scotoma, as well as in the V1 of the contralesional hemisphere. Finding ways to further expand pRF size in these patients may increase coverage of the visual field defect, inducing recovery.
3. Importantly, pRF measurements in patients with cortical lesions yield information on the functional properties of spared visual cortex that complements the information provided by standard perimetry maps.
4. We identified two different patterns of mismatch between responses in early visual areas and visual perception as measured by perimetry mapping, and examined possible underlying mechanisms.
5. Understanding how surviving visual areas process visual information post-lesion could potentially help guide visual rehabilitation efforts to induce recovery. Future studies of this patient population incorporating pRF measurements are clearly warranted to improve understanding of visual processing in the context of injury.

Materials and Methods

Patients. Four adult patients (age 27–64 y; two females and two males) with visual cortical lesions were recruited at the Center for Ophthalmology of the University Clinic in Tuebingen. One patient (male, age 33 y) was recruited at the Center for Advanced MR Imaging at Baylor College of Medicine. Four of the participants had homonymous visual field defects as a result of ischemic or hemorrhagic stroke at 7–10 y before enrollment in this study, and one patient had sustained an ischemic stroke at 0.5 y before recruitment (Table S1). Nine participants (age 26–65 y; eight males and one female) were recruited as controls. All patients had normal or corrected-to-normal visual acuity. The experiments were approved by the Ethical Committee of the Medical Faculty of the University of Tuebingen and the Institutional Review Board of Baylor College of Medicine.

Scanning. At least two T1-weighted anatomic volumes and a minimum of five fMRI scans were acquired for each patient and averaged to increase the SNR.

Stimuli. The patients were presented with moving square-checkerboard bars that traveled sequentially in eight different directions spanning a circular aperture with a radius of 11.25° around the fixation point. The bar width was 1.875°, and it was moved in a step of half its size (0.9375°) at each image volume acquisition (repetition time, 2 s). Five control subjects were asked to participate in a second session, during which an isoluminant mask was placed in the upper left quadrant of the visual field. The mask covered the area of the stimulus and created an AS.

Data Analysis. Data analysis was performed in MATLAB using the mrVista toolbox (http://white.stanford.edu/software/). Reliable pRF measurements and visual field coverage maps were derived using the direct isotropic Gaussian pRF method (Fig. S5) (34).

Normalization of pRF Center Voxel Distributions. To test for significant differences between individual patients and the mean distribution from controls (38), we normalized the distributions derived from the AS controls separately for each patient. To do so, we scaled these distributions by the ratio of active spared voxels in V1 of each patient divided by the number of active voxels in the retinotopically corresponding V1 regions of the control subjects during full stimulation (i.e., without AS).

Statistical Analysis. We used a two-sample Kolmogorov–Smirnov test to compare pRF center locations and size distributions between the patients and AS controls. The significance level selected to reject the null hypothesis (same distributions) was estimated by comparing each of the control distributions with the mean control distribution. The minimum P value of these comparisons was then used to test for significance differences in the mean distribution between patients and controls. We report significance as $P = a < b$, where b is the value selected to reject the null hypothesis.

Detailed descriptions of the methodology used in this study are provided in *SI Materials and Methods*.

ACKNOWLEDGMENTS. We thank Natalia Zaretskaya and Andreas Bartels for their help with MRI scanning and eye-tracking. This work was supported by National Eye Institute Grants R01 EY019272 and R01 EY024019, Department of Defense Contract W81XWH-08-2-0146, a Howard Hughes Medical Institute Early Career Award (to S.M.S.), the Deutsche Forschungsgemeinschaft, the Plasticise Consortium (Project HEALTH-F2-2009-223524), a McNair Foundation award (to T.D.P.), a McNair Medical Institute award and a Fight for Sight grant (to T.D.P.), and the Max Planck Society.

1. Wandell BA, Smirnakis SM (2009) Plasticity and stability of visual field maps in adult primary visual cortex. *Nat Rev Neurosci* 10(12):873–884.
2. Kaas JH, et al. (1990) Reorganization of retinotopic cortical maps in adult mammals after lesions of the retina. *Science* 248(4952):229–231.
3. Chino YM, Kaas JH, Smith EL, 3rd, Langston AL, Cheng H (1992) Rapid reorganization of cortical maps in adult cats following restricted deafferentation in retina. *Vision Res* 32(5):789–796.
4. Chino YM, Smith EL, 3rd, Kaas JH, Sasaki Y, Cheng H (1995) Receptive-field properties of deafferentated visual cortical neurons after topographic map reorganization in adult cats. *J Neurosci* 15(3 Pt 2):2417–2433.
5. Gilbert CD, Wiesel TN (1992) Receptive field dynamics in adult primary visual cortex. *Nature* 356(6365):150–152.
6. Schmid LM, Rosa MG, Calford MB, Ambler JS (1996) Visuotopic reorganization in the primary visual cortex of adult cats following monocular and binocular retinal lesions. *Cereb Cortex* 6(3):388–405.
7. Calford MB, Schmid LM, Rosa MG (1999) Monocular focal retinal lesions induce short-term topographic plasticity in adult cat visual cortex. *Proc Biol Sci* 266(1418):499–507.
8. Baker CI, Dilks DD, Peli E, Kanwisher N (2008) Reorganization of visual processing in macular degeneration: Replication and clues about the role of foveal loss. *Vision Res* 48(18):1910–1919.

9. Baker CI, Peli E, Knouf N, Kanwisher NG (2005) Reorganization of visual processing in macular degeneration. *J Neurosci* 25(3):614–618.
10. Giannikopoulos DV, Eysel UT (2006) Dynamics and specificity of cortical map reorganization after retinal lesions. *Proc Natl Acad Sci USA* 103(28):10805–10810.
11. Schumacher EH, et al. (2008) Reorganization of visual processing is related to eccentric viewing in patients with macular degeneration. *Restor Neurol Neurosci* 26(4-5):391–402.
12. Dilks DD, Baker CI, Peli E, Kanwisher N (2009) Reorganization of visual processing in macular degeneration is not specific to the "preferred retinal locus." *J Neurosci* 29(9): 2768–2773.
13. DeAngelis GC, Anzai A, Ohzawa I, Freeman RD (1995) Receptive field structure in the visual cortex: Does selective stimulation induce plasticity? *Proc Natl Acad Sci USA* 92(21):9682–9686.
14. Murakami I, Komatsu H, Kinoshita M (1997) Perceptual filling-in at the scotoma following a monocular retinal lesion in the monkey. *Vis Neurosci* 14(1):89–101.
15. Horton JC, Hocking DR (1998) Monocular core zones and binocular border strips in primate striate cortex revealed by the contrasting effects of enucleation, eyelid suture, and retinal laser lesions on cytochrome oxidase activity. *J Neurosci* 18(14): 5433–5455.
16. Sunness JS, Liu T, Yantis S (2004) Retinotopic mapping of the visual cortex using functional magnetic resonance imaging in a patient with central scotomas from atrophic macular degeneration. *Ophthalmology* 111(8):1595–1598.
17. Smirnakis SM, et al. (2005) Lack of long-term cortical reorganization after macaque retinal lesions. *Nature* 435(7040):300–307.
18. Masuda Y, Dumoulin SO, Nakadomari S, Wandell BA (2008) V1 projection zone signals in human macular degeneration depend on task, not stimulus. *Cereb Cortex* 18(11): 2483–2493.
19. Baseler HA, et al. (2011) Large-scale remapping of visual cortex is absent in adult humans with macular degeneration. *Nat Neurosci* 14(5):649–655.
20. Eysel UT, Schmidt-Kastner R (1991) Neuronal dysfunction at the border of focal lesions in cat visual cortex. *Neurosci Lett* 131(1):45–48.
21. Eysel UT, Schweigart G (1999) Increased receptive field size in the surround of chronic lesions in the adult cat visual cortex. *Cereb Cortex* 9(2):101–109.
22. Eysel UT, et al. (1999) Reorganization in the visual cortex after retinal and cortical damage. *Restor Neurol Neurosci* 15(2-3):153–164.
23. Zepeda A, Vaca L, Arias C, Sengpiel F (2003) Reorganization of visual cortical maps after focal ischemic lesions. *J Cereb Blood Flow Metab* 23(7):811–820.
24. Schweigart G, Eysel UT (2002) Activity-dependent receptive field changes in the surround of adult cat visual cortex lesions. *Eur J Neurosci* 15(10):1585–1596.
25. Payne BR, Lomber SG (2002) Plasticity of the visual cortex after injury: What's different about the young brain? *Neuroscientist* 8(2):174–185.
26. Yinon U, Shemesh R, Arda H, Dobin G, Jaros PP (1993) Physiological studies in deafferented visual cortex cells of cats following transplantation of fetal xenografts from the rat's cortex. *Exp Neurol* 122(2):335–341.
27. Rumpel S, et al. (2000) Lesion-induced changes in NMDA receptor subunit mRNA expression in rat visual cortex. *Neuroreport* 11(18):4021–4025.
28. Mittmann T, Eysel UT (2001) Increased synaptic plasticity in the surround of visual cortex lesions in rats. *Neuroreport* 12(15):3341–3347.
29. Barmashenko G, Eysel UT, Mittmann T (2003) Changes in intracellular calcium transients and LTP in the surround of visual cortex lesions in rats. *Brain Res* 990(1-2): 120–128.
30. Yan L, et al. (2012) Changes in NMDA-receptor function in the first week following laser-induced lesions in rat visual cortex. *Cereb Cortex* 22(10):2392–2403.
31. Imbrosci B, Neubacher U, White R, Eysel UT, Mittmann T (2013) Shift from phasic to tonic GABAergic transmission following laser-lesions in the rat visual cortex. *Pflugers Arch* 465(6):879–893.
32. Zhang X, Kedar S, Lynn MJ, Newman NJ, Biousse V (2006) Natural history of homonymous hemianopia. *Neurology* 66(6):901–905.
33. Dilks DD, Serences JT, Rosenau BJ, Yantis S, McCloskey M (2007) Human adult cortical reorganization and consequent visual distortion. *J Neurosci* 27(36):9585–9594.
34. Dumoulin SO, Wandell BA (2008) Population receptive field estimates in human visual cortex. *Neuroimage* 39(2):647–660.
35. Schmid MC, Panagiotaropoulos T, Augath MA, Logothetis NK, Smirnakis SM (2009) Visually driven activation in macaque areas V2 and V3 without input from the primary visual cortex. *PLoS ONE* 4(5):e5527.
36. Horton JC, Hoyt WF (1991) Quadrantic visual field defects: A hallmark of lesions in extrastriate (V2/V3) cortex. *Brain* 114(Pt 4):1703–1718.
37. Slotnick SD, Moo LR (2003) Retinotopic mapping reveals extrastriate cortical basis of homonymous quadrantanopia. *Neuroreport* 14(9):1209–1213.
38. Dougherty RF, et al. (2003) Visual field representations and locations of visual areas V1/2/3 in human visual cortex. *J Vis* 3(10):586–598.
39. Levin N, Dumoulin SO, Winawer J, Dougherty RF, Wandell BA (2010) Cortical maps and white matter tracts following long period of visual deprivation and retinal image restoration. *Neuron* 65(1):21–31.
40. Ptito M, Dalby M, Gjedde A (1999) Visual field recovery in a patient with bilateral occipital lobe damage. *Acta Neurol Scand* 99(4):252–254.
41. Raninen A, Vanni S, Hyvärinen L, Näsänen R (2007) Temporal sensitivity in a hemianopic visual field can be improved by long-term training using flicker stimulation. *J Neurol Neurosurg Psychiatry* 78(1):66–73.
42. Henriksson L, Raninen A, Näsänen R, Hyvärinen L, Vanni S (2007) Training-induced cortical representation of a hemianopic hemifield. *J Neurol Neurosurg Psychiatry* 78(1):74–81.
43. Reitsma DC, et al. (2013) Atypical retinotopic organization of visual cortex in patients with central brain damage: congenital and adult onset. *J Neurosci* 33(32):13010–13024.
44. Hubel DH, Wiesel TN (1967) Cortical and callosal connections concerned with the vertical meridian of visual fields in the cat. *J Neurophysiol* 30(6):1561–1573.
45. Baseler HA, Morland AB, Wandell BA (1999) Topographic organization of human visual areas in the absence of input from primary cortex. *J Neurosci* 19(7):2619–2627.
46. Amano K, Wandell BA, Dumoulin SO (2009) Visual field maps, population receptive field sizes, and visual field coverage in the human MT+ complex. *J Neurophysiol* 102(5):2704–2718.
47. Harvey BM, Dumoulin SO (2011) The relationship between cortical magnification factor and population receptive field size in human visual cortex: Constancies in cortical architecture. *J Neurosci* 31(38):13604–13612.
48. Winawer J, Horiguchi H, Sayres RA, Amano K, Wandell BA (2010) Mapping hV4 and ventral occipital cortex: The venous eclipse. *J Vis* 10(5):1.
49. Lee S, Papanikolaou A, Logothetis NK, Smirnakis SM, Keliris GA (2013) A new method for estimating population receptive field topography in visual cortex. *Neuroimage* 81: 144–157.
50. Boynton GM, Demb JB, Glover GH, Heeger DJ (1999) Neuronal basis of contrast discrimination. *Vision Res* 39(2):257–269.
51. Avidan G, et al. (2002) Contrast sensitivity in human visual areas and its relationship to object recognition. *J Neurophysiol* 87(6):3102–3116.
52. Watanabe M, et al. (2011) Attention, but not awareness, modulates the BOLD signal in the human V1 during binocular suppression. *Science* 334(6057):829–831.
53. Haak KV, Cornelissen FW, Morland AB (2012) Population receptive field dynamics in human visual cortex. *PLoS ONE* 7(5):e37686.
54. Pettet MW, Gilbert CD (1992) Dynamic changes in receptive-field size in cat primary visual cortex. *Proc Natl Acad Sci USA* 89(17):8366–8370.
55. Rose JE, Malis LI, Kruger L, Baker CP (1960) Effects of heavy, ionizing, monoenergetic particles on the cerebral cortex, II: Histological appearance of laminar lesions and growth of nerve fibers after laminar destructions. *J Comp Neurol* 115:243–255.
56. Heijl A, Patella VM, Bengtsson B (2012) *The Field Analyzer Primer: Effective Perimetry* (Carl Zeiss Meditec, Dublin, CA), 4th Ed.

Supporting Information

Papanikolaou et al. 10.1073/pnas.1317074111

SI Materials and Methods

Visual Field Tests. The visual field tests for the Tuebingen patients were carried out at the Center for Ophthalmology in Tuebingen. All patients received a Humphrey type (10, 2) visual field test (1, 2), with a background luminance level of 10 cd/m^2. Humphrey pattern deviation perimetry results for all patients are shown in Fig. 2*A*.

Scanning. Structural magnetic resonance imaging (MRI) and functional MRI (fMRI) experiments were performed at the Max Planck Institute for Biological Cybernetics, Tuebingen, Germany, using a 3.0-T Siemens Trio high-speed echo-planar imaging unit with a quadrature head coil. Two T1-weighted anatomic volumes were acquired for each subject with a 3D magnetization-prepared rapid acquisition gradient echo (T1 MPRAGE scan) and averaged to increase the signal-to-noise ratio [matrix size, 256 × 256; voxel size, 1 × 1 × 1 mm^3; 176 partitions; flip angle, 9°; repetition time (TR), 1,900 ms; echo time (TE), 2.26 ms; inversion time (TI), 900 ms]. The structural and functional scans of the patient recruited at Baylor College of Medicine's Center for Advanced MR Imaging were acquired on a 3.0-T Siemens TIM Trio scanner. Seven T1-weighted anatomic volumes were acquired by MPRAGE with a pulse sequence (matrix size, 256 × 256; voxel size, 0.5 × 0.5 × 0.75 mm^3; flip angle, 9°; TR, 2,600 ms; TE, 3.53 ms; TI, 900 ms; 256 measurements) and averaged. The averaged structural data were used for segmentation of anatomic data into white and gray matter, and for registering different functional scanning sessions to the subject's anatomy.

Blood oxygen level-dependent (BOLD) image volumes were acquired using gradient echo sequences of 28 contiguous 3-mm-thick slices (matrix size, 64 × 64; voxel size, 3 × 3 × 2.6 mm^3; flip angle, 90°; TR, 2,000 ms; TE, 40 ms) at Tuebingen, and 29, 3.6 mm-thick slices covering the entire brain (matrix size, 64 × 64; voxel size, 3.46 × 3.46 × 3.6 mm^3; flip angle, 90°; TR, 2,000 ms; TE, 30 ms) at Baylor College of Medicine.

Stimuli. The stimuli were presented using VisuaStim MRI-compatible digital goggles (Resonance Technology) with a 30° horizontal and 22.5° vertical field of view (800 × 600 resolution; minimum luminance, 0.3 cd/m^2; maximum luminance, 12.2 cd/m^2). The subjects were presented with moving square-checkerboard bars (100% contrast) that traveled sequentially (with no gap) in eight different directions spanning a circular aperture with a radius of 11.25° around the fixation point. The bar width was 1.875°, and it was moved by a step of half its size (0.9375°) for each image volume acquisition (TR, 2 s). Stimuli were generated in MATLAB (Mathworks), using Psychtoolbox (3) and an open toolbox (Vistadisp). The subjects were instructed to fixate a small dot in the center of the screen (radius, 0.0375°; 2 pixels) and respond to the color change by pressing a button. The color was changed at random, with an average frequency of 1 every 6.25 s.

At Tuebingen, an infrared eye tracker was used to record eye movements (iView X; SensoMotoric Instruments). The patient at Baylor College of Medicine was not eye-tracked. Five control subjects were asked to participate for a second session, during which an isoluminant mask was placed in the upper left quadrant of the visual field. The mask covered the stimulus' area and created a so-called "artificial scotoma" (AS). All other stimulus' parameters remained the same.

Data Analysis. Data analysis was performed in MATLAB using the mrVista toolbox (http://white.stanford.edu/software/). For the analysis of anatomic data, a segmentation of the white matter was performed manually using itkGray (4). Gray matter was grown to form a 3-mm layer covering the white matter surface. The cortical surface was represented as a mesh, and was used to render an inflated 3D cortical surface and to flatten the cortical representation within a chosen distance from a starting point. A point in cortex near the fovea was selected as the starting point, and a radius of 80 mm cortical distance was used.

A minimum of five repeated scans were obtained for each subject. Each functional scan consisted of 195 image volumes, the first three of which were discarded. The functional images were corrected for motion in between and within scans (5). Scans with movements that exceeded 1 voxel (3 mm) were excluded. Functional data were averaged across scans for each subject. The functional images were aligned to the high-resolution anatomic volume using a mutual information method (6).

To compute the Talairach coordinates, we identified the following anatomic landmarks manually in the T1 anatomic images: the anterior commissure, posterior commissure, midsagittal plane, and boundaries of the brain along the three axes. Using these points the voxel coordinates can be transformed to Talairach coordinates (7–9).

Flattening of the Lesioned Hemisphere. One problem arising in the analysis of functional patterns and their spatial extents in patients with cortical visual lesions is the lack of cortical tissue in the injury site. To address this issue, we developed a method that approximates reconstruction of the damaged territory based on information from the healthy hemisphere. This method involves reflecting the corresponding cortical region from the intact hemisphere of each subject and aligning it to the lesioned hemisphere using the SPM8 realign algorithm (www.fil.ion.ucl.ac.uk/spm). Using the aligned image as a reference, we manually reconstructed the affected region and connected it to the healthy parts of that hemisphere using the itkGray program. The "hybrid" hemisphere generated can be flattened with minimal distortion, while largely preserving the relationships between the visual areas and various anatomic landmarks (Fig. S4).

Population Receptive Field Mapping. We derived reliable population receptive field (pRF) estimates as described previously (10). In brief, the pRF model estimates the region of the visual field that effectively elicits a response in a small region of the visual cortex (i.e., voxel). The implementation of the pRF model is a circularly symmetric Gaussian receptive field in visual space, whose center and radius are estimated by fitting actual BOLD signal responses to estimated responses elicited by convolving the model with the moving bar stimuli. We retained only those voxels in the visual area for which the fitting model explained more than 10% of the variance. This threshold was set after measuring the mean explained variance (3% ± 2%) in a non-visually responsive area and setting the value of the threshold at 3 SD above the mean. Using this method, we derived reliable and reproducible retinotopic and pRF size maps (Fig. S5).

Furthermore, to confirm that the fMRI signal strength does not differ between patients and controls, we calculated the BOLD signal-to-noise ratio (SNR) in area V1. We calculated the mean SNR from the time series in V1 as the common logarithm of the mean signal change divided by the SD and found it to be 1.98 ± 0.2 for the patients and 1.85 ± 0.2 for AS controls.

Visual Field Coverage Maps. The visual field coverage maps define the locations within the visual field that evoke a significant re-

sponse from voxels within a region of interest (ROI) in the cortex. To estimate this, we plotted the pRF centers across all voxels within the ROI (gray dots in Fig. 2*B*) and the relative pRF size by fitting a 2D Gaussian with peak amplitude normalized to 1 (Fig. 2*B*, first column). We estimated the color map by plotting at each visual field location the maximum normalized pRF amplitude between all Gaussian- shaped pRFs that cover this location. We also plotted the nonnormalized visual field coverage (Fig. 2*B*, second column) that weights the pRF Gaussians with their response amplitude. The color map was plotted with the maximum color value taken at the median pRF amplitude over all voxels within the map, to allow better visualization by preventing the masking of weak visual responses by very large outlier pRF amplitudes.

Normalization of the pRF Center Voxel Distributions. To test for significant changes in the pRF center distributions, we compared the distributions between the patients and AS controls. To control for the different sizes of activated visual areas in subjects (7), we normalized the distributions derived from the AS controls separately for each patient. To do so, we scaled these distributions by the ratio of active spared voxels in V1 of each patient divided by the number of active voxels in the retinotopically corresponding V1 regions of the control subjects during full stimulation (i.e., without AS). This normalization was possible given our finding that the coarse retinotopic organization was similar in patients, AS controls, and controls under the full stimulus condition. As a result of this normalization, to a first approximation, a mere size difference in the V1 area activated in patients compared with AS controls would not result in differing pRF distributions.

We defined retinotopically corresponding regions in controls as the V1 voxels corresponding to the same part of the visual field as the spared-V1 regions of patients. To do so, we defined for each patient the range of polar angles and eccentricities of the significantly activated voxels (i.e., voxels with explained variance >0.1) and selected regions within these ranges in area V1 of controls. We ensured by visual inspection that single voxel outliers did not influence the retinotopic range used for normalization. Because the simulated AS was in the left upper quadrant, we reflected right-hemisphere data of the AS control subjects into a left hemisphere format for comparison with the patients with a scotoma in the right quadrant. Eccentricities <2° were excluded from this analysis, because foveal voxels were not strongly activated by the stimulus the we used, and because pRF estimates near the fovea were limited by the stimulus (bar) size and step. Eccentricities at the border of the stimulus presentation field (>10°), which could be prone to pRF estimation biases were excluded as well (11).

We measured visual field polar angle counterclockwise from the upper vertical meridian (0°), with the horizontal meridian corresponding to 90° and the lower vertical meridian to 180°. Thus, for the comparison with patient P1, we selected pRF centers from the right V1 area of control subjects with polar angles ranging from 70° to 180° and eccentricities ranging from 2° to 10°. Similarly, for patients P2, P3, P4, and P5, we selected voxels in controls with pRF centers at polar angles 180–290°, 180–320°, 180–240°, and 110–180° and corresponding eccentricities of 2–10°, 2–10°, 3.5–10°, and 3–10°.

Statistical Analysis. A two-sample Kolmogorov–Smirnov test was used to compare the pRF center location and size distributions between the patients and the AS controls. The significance level selected to reject the null hypothesis (same distributions) was estimated by comparing each of the control distributions with the mean control distribution. The minimum P value of these comparisons was then used to test for significance between the mean control distribution and the patients. We report significance in the format of $P = a < b$, where b is the value selected to reject the null hypothesis as described above. We note that this is a conservative choice that may hinder the identification of small differences; however, it is difficult to argue for the significance of small differences, given the limited number of patients. More studies including larger numbers of patients and controls are needed to more precisely assess the statistical significance of the changes observed in this study.

1. Beck RW, Bergstrom TJ, Lichter PR (1985) A clinical comparison of visual field testing with a new automated perimeter, the Humphrey Field Analyzer, and the Goldmann perimeter. *Ophthalmology* 92(1):77–82.
2. Trope GE, Britton R (1987) A comparison of Goldmann and Humphrey automated perimetry in patients with glaucoma. *Br J Ophthalmol* 71(7):489–493.
3. Brainard DH (1997) The Psychophysics Toolbox. *Spat Vis* 10(4):433–436.
4. Yushkevich PA, et al. (2006) User-guided 3D active contour segmentation of anatomical structures: Significantly improved efficiency and reliability. *Neuroimage* 31(3):1116–1128.
5. Nestares O, Heeger DJ (2000) Robust multiresolution alignment of MRI brain volumes. *Magn Reson Med* 43(5):705–715.
6. Maes F, Collignon A, Vandermeulen D, Marchal G, Suetens P (1997) Multimodality image registration by maximization of mutual information. *IEEE Trans Med Imaging* 16(2):187–198.
7. Dougherty RF, et al. (2003) Visual field representations and locations of visual areas V1/2/3 in human visual cortex. *J Vis* 3(10):586–598.
8. Cox RW (1996) AFNI: Software for analysis and visualization of functional magnetic resonance neuroimages. *Comput Biomed Res* 29(3):162–173.
9. Talairach J, Tournoux P (1998) *Co-Planar Stereotaxic Atlas of the Human Brain* (Thieme, New York).
10. Dumoulin SO, Wandell BA (2008) Population receptive field estimates in human visual cortex. *Neuroimage* 39(2):647–660.
11. Lee S, Papanikolaou A, Logothetis NK, Smirnakis SM, Keliris GA (2013) A new method for estimating population receptive field topography in visual cortex. *Neuroimage* 81: 144–157.

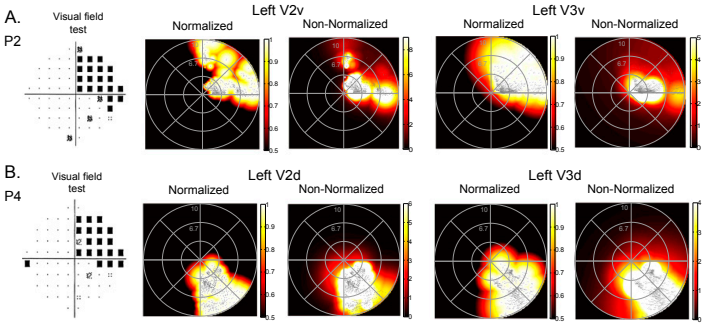

Fig. S1. Visual field coverage maps of extrastriated areas. (*A*) Normalized and nonnormalized visual field coverage maps of areas V2v and V3v from the left hemisphere of patient P2. The color map indicates the maximum pRF amplitude at each visual field location of all of the pRFs covering this location. The pRF centers across all voxels within each area are indicated by gray dots. The coverage maps overlap significantly with locations on the perimetric map showing an absolute scotoma (*Left*). (*B*) Normalized and nonnormalized visual field coverage maps of areas V2d and V3d from the left hemisphere of patient P4. The maps show full coverage of the lower visual field quadrant except for a small area inferior to the peripheral horizontal meridian, consistent with the perimetry map. The fact that areas V2d and V3d show more complete coverage of the sighted visual field quadrant than area V1 (Fig. 2 *B*, *e*) suggests that V1-bypassing pathways may play a role in preserving this patient's visual perception in the sighted quadrant.

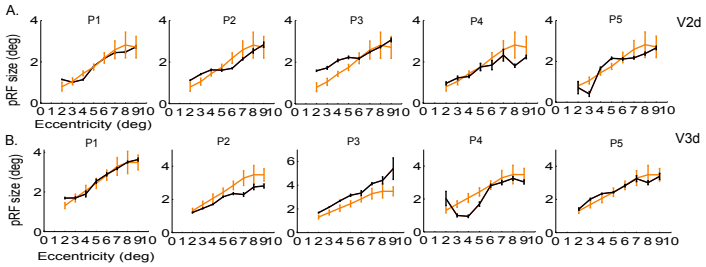

Fig. S2. Mean pRF size versus eccentricity for voxels in V2d (*A*) and V3d (*B*) of the lesioned hemisphere of all patients (black) and AS controls (orange). The orange error bars indicate the SEM across AS controls ($n = 5$), and the gray error bars indicate the SEM across voxels within an eccentricity bin (bin size, 1°) for each patient. pRF sizes of areas V2d and V3d are similar for patients P1, P2, P4, and P5 and AS controls. For patient P3, the pRF size of these areas is slightly increased compared with AS controls, but not to the same degree as the large increase observed in V1 and not occurring for all eccentricities. Thus, the pRF size increase near the border of the scotoma in V1 cannot be explained by eye movements.

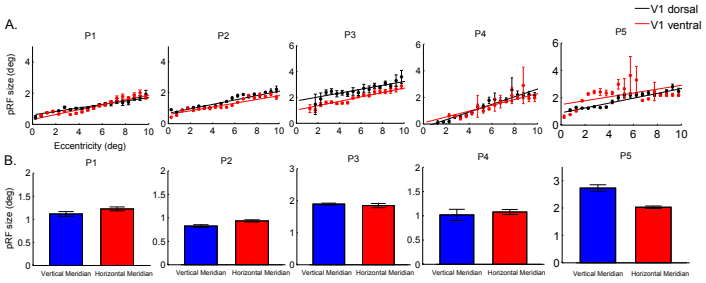

Fig. S3. pRF size in the dorsal and ventral contralesional V1. (*A*) pRF size as a function of eccentricity in the dorsal (black) and ventral (red) V1 of the intact hemisphere of all patients. (*B*) Mean pRF size of voxels located within 2–10° of eccentricity along the vertical meridian (blue) versus the horizontal meridian (red) in the ventral V1 of the contralesional hemisphere for all patients. Error bars indicate SEM. Patients P1, P2, P3, and P4 showed no significant difference in mean pRF size between contralesional dorsal and ventral V1 (*A*) or between the vertical and horizontal meridian (*B*). Patient P5 had significantly larger pRFs in the ventral contralesional V1 compared with the dorsal V1 (*A*), particularly along the upper vertical meridian (*B*) ($P < 10^{-8}$, paired t test).

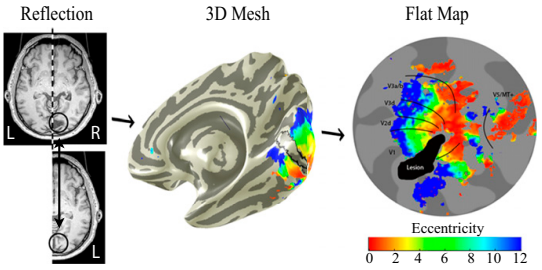

Fig. S4. Reconstruction of the lesioned hemisphere. (*Left*) Axial plane of the anatomy of a patient with a V1 lesion in the right hemisphere. In this patient, the left intact hemisphere was reflected and aligned to the right hemisphere as shown at the bottom. The area of the lesion indicated by the circle was manually reconstructed after the region reflection and subsequent alignment. The reconstruction of the lesioned area is shown on the 3D mesh (*Center*) and on the flat map (*Right*). The ROI representing the lesion was manually selected on the anatomy and projected on the 3D mesh, the territory of which is drawn. This region was then drawn in black on the flattened representation. This limits distortions introduced by the lesion to the nearby, spared cortex at a minimum. Our pRF measurements were all performed in the spared areas of the lesioned hemisphere and were not affected by the reflection procedure.

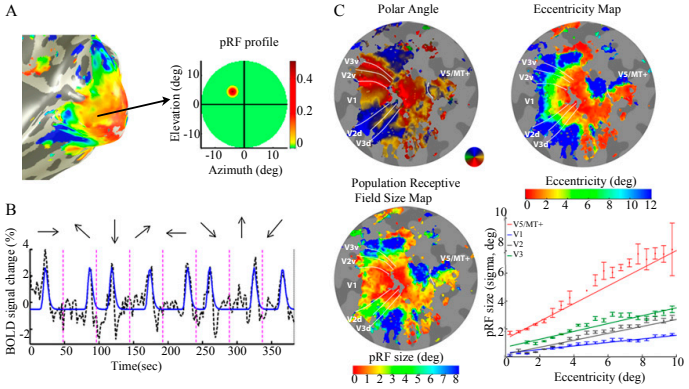

Fig. S5. pRF mapping method. (*A*) Estimated position and size of the pRF of a voxel located in area V1 of the right hemisphere of a control subject. The color-coded pRF size parametric map (see color key) is overlaid on the inflated mesh of the right hemisphere. The pRF profile plot on the right shows the amplitude of the predicted pRF model at each visual field location. (*B*) Raw BOLD time series (black dashed line) averaged over five scans and the predicted model (blue solid line) of the voxel presented in *A*. Arrows at the top show the direction of the bar motion during the scan. As the model predicted, the BOLD time series peaked for every direction each time the bar passed on top of the pRF center. In this case, the model explains 79% of the variance in the time series. (*C*) Statistical parametric maps of polar angle, eccentricity, and pRF size overlaid on the flattened left occipital lobe of a control subject. The color-coding of the polar angle and eccentricity maps indicate the visual field angle and eccentricity, respectively, corresponding to the peak of the pRF at each cortical location. The borders of the early visual areas were defined according to the vertical meridian reversals on the polar angle map and are represented on all three maps as white contours. (*Lower*, *Right*) The relationship between eccentricity and pRF size for areas V1, V2, V3, and V5/MT+. In agreement with previous electrophysiological recordings in macaques (1) and studies in humans (2), pRF size increased from early visual areas (V1) to higher-level visual areas (V2, V3, and V5/MT+). As expected, within each visual area, pRF size increased linearly with eccentricity (2–4).

1. Zeki SM (1978) Uniformity and diversity of structure and function in rhesus monkey prestriate visual cortex. *J Physiol* 277:273–290.
2. Smith AT, Singh KD, Williams AL, Greenlee MW (2001) Estimating receptive field size from fMRI data in human striate and extrastriate visual cortex. *Cereb Cortex* 11(12):1182–1190.
3. Burkhalter A, Van Essen DC (1986) Processing of color, form and disparity information in visual areas VP and V2 of ventral extrastriate cortex in the macaque monkey. *J Neurosci* 6(8): 2327–2351.
4. Felleman DJ, Van Essen DC (1987) Receptive field properties of neurons in area V3 of macaque monkey extrastriate cortex. *J Neurophysiol* 57(4):889–920.

Table S1. Clinical data of patients ($n = 5$)

ID	Sex	Age,	Δt, y	Etiology	Hemisphere	Area	Defect
P1	M	49	7	Ischemia	Right	Occipital	LUQ
P2	F	27	10	Ischemia	Left	Parieto-occipital	RUQ
P3	M	33	0.5	Ischemia	Left	Occipital	RUQ
P4	M	54	7	Ischemia	Left	Occipital	RUQ
P5	F	64	9	Hemorrhage	Right	Temporo-occipital	LUQ

Age, age at time of examination; Δt, interval between brain lesion and examination; etiology, pathogenesis of brain lesion; hemisphere, side of brain lesion; area, cortical area affected by the lesion; defect, type of homonymous visual field defect; LUQ, left upper quadrantanopia; RUQ, right upper quadrantanopia.

Table S2. Location of the V1/V2 border in patients and controls

		V1 HM			Dorsal V1/ V2		
ID	Hemisphere	X	Y	Z	X	Y	Z
Patients							
P1	RH	8	−87	−9	0	−95	−1
P2	LH	−10	−79	−3	2	−97	11
P3	LH	−3	−86	−17	−5	−96	−9
P4	LH	—	—	—	−6	−93	8
P5	RH	11	−84	−1	2	−93	1
Controls							
Mean	LH	−7	−84	−6	6	−88	2
	RH	9	−84	−4	−3	−95	5
SD	LH	5	3	6	2	5	8
	RH	4	3	7	3	7	7

RH, right hemisphere; LH, left hemisphere.

Shown are the Talairach coordinates (X, left/right; Y, anterior/posterior; Z, inferior/superior) for an 8° eccentricity point along the horizontal meridian of V1 (V1 HM) and along the dorsal V1/ V2 border in patients and controls. Control data show the average coordinates in each hemisphere across nine healthy subjects.

Table S3. pRF size measurements

		Lesioned hemisphere V1 pRF		
ID	pRF measures	Patients	AS controls	Controls
P1	Mean ± SD	1.36	1.06 ± 0.19	1.29 ± 0.26
	Median ± SD	1.26	0.99 ± 0.18	1.13 ± 0.14
	Stdev ± SD	0.52	0.55 ± 0.12	0.74 ± 0.22
	Area size ± SD	1187	1,303 ± 262	1,179 ± 250
P2	Mean ± SD	1.55	1.06 ± 0.19	1.29 ± 0.26
	Median ± SD	1.2	0.99 ± 0.18	1.13 ± 0.14
	Stdev ± SD	0.56	0.55 ± 0.12	0.74 ± 0.22
	Area size ± SD	1463	1,303 ± 262	1,179 ± 250
P3	Mean ± SD	1.83	1.01 ± 0.19	1.31 ± 0.29
	Median ± SD	1.97	0.98 ± 0.18	1.14 ± 0.17
	Stdev ± SD	1.01	0.54 ± 0.12	0.79 ± 0.21
	Area size ± SD	1291	1,304 ± 261	1,493 ± 367
P4	Mean ± SD	2.23	1.36 ± 0.46	1.58 ± 0.45
	Median ± SD	1.33	1.31 ± 0.45	1.44 ± 0.39
	Stdev ± SD	0.61	0.55 ± 0.13	0.62 ± 0.18
	Area size ± SD	195	633 ± 202	391 ± 162
P5	Mean ± SD	1.94	1.4 ± 0.53	1.57 ± 0.44
	Median ± SD	1.75	1.36 ± 0.5	1.47 ± 0.41
	Stdev ± SD	0.46	0.55 ± 0.13	0.58 ± 0.11
	Area size ± SD	414	545 ± 185	362 ± 160

Measurements derived from the spared-V1 area of patients and the retinotopically corresponding area of control subjects with and without AS: mean pRF size (radius σ), median pRF size (radius σ), SD of the pRF size distribution across area V1 activated voxels, and surface area of the significantly activated V1 region. For controls with and without the AS, the SD is reported across subjects. All measurements are in degrees except area size, which is in millimeters squared.

A.2 "A new method for estimating population receptive field topography in visual cortex"

NeuroImage 81 (2013) 144–157

Contents lists available at SciVerse ScienceDirect

NeuroImage

journal homepage: www.elsevier.com/locate/ynimg

A new method for estimating population receptive field topography in visual cortex

Sangkyun Lee [a,*], Amalia Papanikolaou [a], Nikos K. Logothetis [a,c], Stelios M. Smirnakis [b,1], Georgios A. Keliris [a,d,1]

[a] Max Planck Institute for Biological Cybernetics, Spemannstr. 38, 72076 Tübingen, Germany
[b] Department of Neuroscience and Neurology, Baylor College of Medicine, Houston, USA
[c] Division of Imaging Science and Biomedical Engineering, University of Manchester, Manchester M13 9PT, UK
[d] Bernstein Center for Computational Neuroscience, Tübingen, Germany

ARTICLE INFO

Article history:
Accepted 5 May 2013
Available online 16 May 2013

Keywords:
Retinotopic mapping
Population receptive field
Visual field mapping
fMRI

ABSTRACT

We introduce a new method for measuring visual population receptive fields (pRF) with functional magnetic resonance imaging (fMRI). The pRF structure is modeled as a set of weights that can be estimated by solving a linear model that predicts the Blood Oxygen Level-Dependent (BOLD) signal using the stimulus protocol and the canonical hemodynamic response function. This method does not make *a priori* assumptions about the specific pRF shape and is therefore a useful tool for uncovering the underlying pRF structure at different spatial locations in an unbiased way. We show that our method is more accurate than a previously described method (Dumoulin and Wandell, 2008) which directly fits a 2-dimensional isotropic Gaussian pRF model to predict the fMRI time-series. We demonstrate that direct-fit models do not fully capture the actual pRF shape, and can be prone to pRF center mislocalization when the pRF is located near the border of the stimulus space. A quantitative comparison demonstrates that our method outperforms the direct-fit methods in the pRF center modeling by achieving higher explained variance of the BOLD signal. This was true for direct-fit isotropic Gaussian, anisotropic Gaussian, and difference of isotropic Gaussians model. Importantly, our model is also capable of exploring a variety of pRF properties such as surround suppression, receptive field center elongation, orientation, location and size. Additionally, the proposed method is particularly attractive for monitoring pRF properties in the visual areas of subjects with lesions of the visual pathways, where it is difficult to anticipate what shape the reorganized pRF might take. Finally, the method proposed here is more efficient in computation time than direct-fit methods, which need to search for a set of parameters in an extremely large searching space. Instead, this method uses the pRF topography to constrain the space that needs to be searched for the subsequent modeling.

Introduction

One of the great achievements of fMRI is the in-vivo characterization of the functional organization of the human visual cortex. Early methods for the retinotopic mapping of the visual cortex (DeYoe et al., 1996; Dougherty et al., 2003; Engel et al., 1994, 1997; Sereno et al., 1995) used ring and wedge stimuli, and reported a strong coherence between the blood oxygen level-dependent (BOLD) signal arising in a voxel and particular stimulus locations in the visual field. From these measurements, the eccentricity and azimuth visual angle of each voxel can be estimated and this information can be used to define the borders between early visual areas (Sereno et al., 1995; Wandell et al., 2007).

Recently, Dumoulin and Wandell (2008) introduced a new method to model population receptive fields (pRFs) and quantitatively assess their properties. This seminal approach allowed us for the first time to measure quantitatively, in vivo, basic population receptive field properties in human visual areas. Like any method, however, this approach also has its limitations. For example, it assumed that the pRF has an isotropic Gaussian topography while the potentially suppressive surround is not modeled. There have been subsequent approaches (Harvey and Dumoulin, 2011; Zuiderbaan et al., 2012) which have used the same principles with different pRF models, but in general any assumptions about the receptive field structure puts some *a priori* constraints on the ability to extract the pRF topography without necessarily strong experimental justification. Inaccurate assumptions about the pRF topography could lead to the wrong model and to potentially erroneous estimation of pRF characteristics such as location and size. It would therefore be useful to have a method that can provide information about pRF topography in an unbiased manner.

To overcome these problems, we propose a new data-driven method that estimates the structure of the pRF. Without assuming the pRF shape *a priori*, we model the pRF as a vector of weights which can be estimated

* Corresponding author.
E-mail address: lee.sangkyun@gmail.com (S. Lee).
[1] These authors contributed equally to this work.

1053-8119/$ – see front matter © 2013 Elsevier Inc. All rights reserved.
http://dx.doi.org/10.1016/j.neuroimage.2013.05.026

from the fMRI time-series by solving a set of linear equations for each voxel. This approach is similar to linear reverse correlation methods applied in electrophysiology (Ringach, 2004; Simoncelli et al., 2004). By avoiding a-priori assumptions, our method enables us to visualize pRF features such as surround suppression, or the anisotropic shape of the pRF. Visual inspection of the pRF topography can then guide the development of more appropriate models for fitting the pRF weights. This is particularly important in regions where the pRF shape is unknown. Even in early visual cortex, exploring the pRF topography reveals that pRF centers would be best modeled by an anisotropic Gaussian, in contrast to prevailing methods (Dumoulin and Wandell, 2008; Harvey and Dumoulin, 2011; Zuiderbaan et al., 2012). This approach yields an estimate of the orientation and elongation of the pRF center in addition to an estimate of its location and size.

In order to evaluate the method we proposed, we compared its performance to that of direct pRF model fitting methods. Our method of estimating the pRF center outperforms the direct-fit isotropic Gaussian (DIG) (Dumoulin and Wandell, 2008), the direct-fit anisotropic Gaussian (DAG), and the direct-fit difference of isotropic Gaussians (DDoIG) (Harvey and Dumoulin, 2011; Zuiderbaan et al., 2012) models by i) explaining a larger part of the BOLD signal variance, and by ii) providing more accurate eccentricity maps. In addition, visualizing the pRF topography as proposed here can make the subsequent modeling more efficient in computation time by constraining the pRF shape prior to the modeling. In contrast, direct-fit methods need considerably longer computation time as they have to select the best set of parameters in a much larger searching space.

Material and methods

Subjects

FMRI data were acquired from 4 participants (2 females, ages 23–26). All participants had normal or corrected-to-normal visual acuity. Experiments were conducted with the informed written consent of each participant and were approved by the Ethical Committee of the Medical Faculty of the University of Tübingen.

Stimulus

While scanning, participants fixated a central spot (radius: 0.0375°; 2 pixels) while a moving bar aperture exposed a moving square-checkerboard pattern with 100% contrast travelling across the visual field. The checkerboard pattern aligned to the longitudinal axis of the bar aperture moved in orthogonal directions of the bar movement. The stimulus was presented only over the central part of the visual field within a circular disk with radius 11.25°. The bar was moved sequentially in 8 different directions according to the following sequence [0, 135, 270, 315, 180, 45, 90, 225°] (Fig. 1A), where angles are reported counter-clockwise from the horizontal (0°) direction of the right visual hemifield. The long axis of the bar was orthogonal to the drifting direction. In each direction, the bar drifted 24 steps with each moving step being 0.9375°. The bar width was 1.875°. The position of the bar was updated for every image volume acquisition. The visual stimuli were generated with an adaptation of an open toolbox (VISTADISP), and PsychToolbox (Brainard, 1997) in MATLAB (The Mathworks, Inc.). The stimuli were presented through an MR-compatible goggle system (VisuaStimDigital, Resonance Technology Inc., Northridge, CA, USA) with min luminance = 0.39 cd/m^2, mean luminance = 6.27 cd/m^2, and max luminance = 12.15 cd/m^2 (lower photopic vision).

Data acquisition and preprocessing

All subjects participated in scanning sessions to obtain T1-weighted anatomical volume and functional volume data. FMR and structural MR imaging were performed using a 3T whole body scanner (Trio Tim, Siemens, Erlangen, Germany) with a 12-channel head coil. Two T1-weighted anatomical volumes (T1 MPRAGE scan) were acquired for each subject and averaged to increase signal to noise ratio [matrix size = 256 × 256, voxel size = 1 × 1 × 1 mm^3, 176 partitions, flip angle = 9°, TR = 1900 ms, TE = 2.26 ms, TI = 900 ms]. The structural data were used for segmentation of anatomical data into white and gray matter (Teo et al., 1997). Functional BOLD image volumes were acquired using gradient echo sequences of 28 contiguous 3 mm-thick slices covering the entire brain (repetition time [TR] = 2,000 ms, echo time [TE] = 40 ms, matrix size = 64 × 64, voxel size = 3 × 3 × 3 mm^3, flip angle = 90°).

We performed 5–9 identical scanning sessions. In each functional session, 195 image volumes were acquired, the first 3 of which were discarded to allow for signal stabilization. Motion artifacts within and between runs were corrected (Nestares and Heeger, 2000). The functional images were co-registered with the averaged anatomical image using a mutual information method (Maes et al., 1997). All these preprocessing steps were performed using VISTA software (http://white.stanford.edu/software/). After detrending fMRI data in each scan with a cut-off frequency of 1 cycle per scan, all functional images across scans were averaged to formulate a volume series of 192 images.

Estimation of pRF topography based on linear system analysis

To predict the fMRI signals, we used a linear model for the fMRI response (Birn et al., 2001; Boynton et al., 1996; Friston et al., 1995; Hansen et al., 2004; Worsley and Friston, 1995). As opposed to the pRF model which directly uses a Gaussian model with a single sigma (Dumoulin and Wandell, 2008) to fit the BOLD data, we first use the BOLD data to estimate a weight vector representing the detailed topography of the pRF. Then, in a second step, we select an appropriate model to fit the observed pRF structure. The "stimulus presentation space" corresponding to a circular disk in the visual field, is represented as M pixels with size of 0.0187 × 0.0187 degrees per pixel. The stimulus at time t is denoted as $\mathbf{s}(t)\in\Re^M$ and the pRF at voxel i is denoted as $\mathbf{p}_i\in\Re^M$. Under the linear model, the presentation of the effective stimulus to the pRF of voxel i causes the following response:

$$r(t) = p_i^T s(t) \tag{1}$$

After convolving with the canonical hemodynamic response function (HRF) $h(t)$, the prediction of the BOLD response $d_i(t)$ at voxel i and time t is obtained:

$$d_i(t) = h(t) * \left(p_i^T s(t)\right) \tag{2}$$

The convolution in Eq. (2) is reformulated into:

$$d_i = Kp_i = HSp_i \tag{3}$$

where $\mathbf{H}$ is a matrix form for the convolution of $h(t)$ and $\mathbf{S} = [\mathbf{s}(1),\cdots, \mathbf{s}(t),\cdots, \mathbf{s}(N)]^T$, (N: the number of volume instances). In our study, a two-gamma function (Friston et al., 1998; Glover, 1999; Worsley et al., 2002) with the default parameters in the VISTA software was used as the canonical HRF as follows:

$$h(t) = (t/d_1)^{\alpha_1}\exp(-(t-d_1)/\beta_1) - c(t/d_2)^{\alpha_2}\exp(-(t-d_2)/\beta_2), \tag{4}$$

where $d_1 = 5.4, \alpha_1 = 5.98, \beta_1 = 0.90, c = 0.35, d_2 = 10.8, \alpha_2 = 11.97$, and $\beta_2 = 0.90$.

Then, when the observed signal vector $\mathbf{y}_i$ at voxel i is given, the pRF $\mathbf{p}_i$ can be estimated via a least-square fit:

$$J_i = \|y_i - d_i\|^2 = \|y_i - Kp_i\|^2. \tag{5}$$

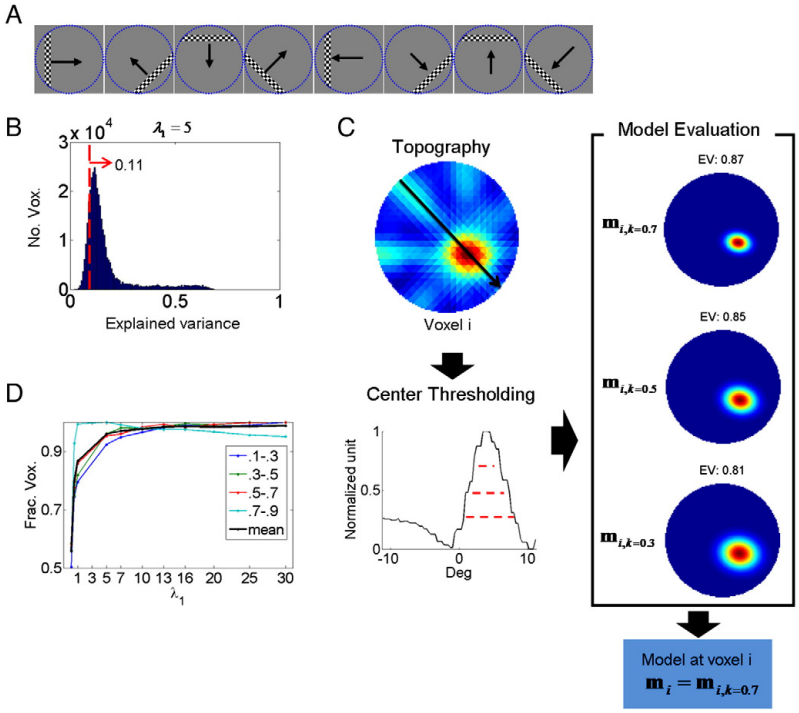

Fig. 1. Illustration of the stimulus presentation protocol and the modeling of the pRF central region. (A) Stimulus presentation sequence. Checkerboard patterns were presented through a bar aperture within the stimulus presentation space, which is a circular disk of radius 11.25°. The stimulation presentation space is marked with a blue dot circle (not shown during the actual experiments). The bar moved sequentially in 8 different directions as indicated by the arrows. (B) Histogram of voxels as a function of the explained variance (EV) of each voxel's pRF topography, illustrated here for $\lambda_1 = 5$. At a region of interest from non-visually responsive voxels, the mean of explained variance (0.11) of pRF topographies was calculated and used as threshold to select visually responsive voxels. In the histogram, the area above the threshold (dashed red line) corresponds to visually responsive voxels. (C) Process followed in modeling of the pRF central region. The left upper, left bottom, and right panels show the pRF topography, thresholding at the cross-section (black arrow in the pRF topography) of the topography (only for illustration purposes), and model evaluation, respectively. In the pRF topography of a visually responsive voxel, 3 central patches are obtained by thresholding at $k = [0.3, 0.5, 0.7]$, which are denoted by the dashed red lines. Then, among these patches, the best model is selected by assessing the explained variance (EV) of each model. In this example voxel, the model with threshold, $k = 0.7$, is selected as the best model, $\mathbf{m}_i$. The text contains a more detailed account of the modeling process with the mathematical formulae and the calculation of explained variance. Note that the appearance of bar patterns across the pRF center originates not from the pRF structure but from the use of the bar aperture. See the Results section for a more detailed explanation. (D) Fraction of voxels that achieve a certain level of explained variance, across different λ_1 choices, in one subject. These graphs show the distribution of only the visually responsive voxels. The data from the other subjects behaved very similarly (not shown). The fraction is defined as the ratio of the number of voxels for a certain λ_1 to the maximum number of voxels across λ_1 s that belong in the same EV bin (e.g., 0.1–0.3). At each EV bin, the fraction of voxels is plotted across $\lambda_1 = [0.1\ 0.5\ 1\ 5\ 7\ 10\ 13\ 16\ 20\ 25\ 30]$.

However, as this problem is underdetermined (i.e., $N \ll M$), it is necessary to exploit a mathematical trick and implement reasonable constraints in order to solve this problem. The first solution is to use the Moore–Penrose pseudoinverse (Haykin, 1999):

$$p_i = \left(K^T K\right)^{-1} K^T y_i \tag{6}$$

While this technique provided the solution of Eq. (6), it did not reveal a smooth or clear topography for the pRF. The reason for this derives from the fact that the linear problem is underdetermined and fMRI signals are usually contaminated with various artifacts and noise. The underdetermined problem can be solved by introducing additional constraints on the receptive field structure via a regularization technique such as the ridge regression (using L2-norm minimization) (Hastie et al., 2001; Hoerl, 1970; Jain, 1985), the lasso regression (using L1-norm minimization) (Hastie et al., 2001; Tibshirani, 1996, 2011), and the elastic-net regression (using combinations of L2-norm and L1-norm minimizations) (Zou and Hastie, 2005). Generally, the lasso regression and the elastic-net provide a sparser solution than the ridge regression, but they are computationally expensive as they are not differentiable. An appropriate method was selected as follows: a reasonable assumption for the pRF shape is that it should be localized in the visual space (i.e., sparseness in the distribution of weights; sparseness in the distribution does not guarantee localization in space, yet localization in space implies sparseness in the distribution) and it should change smoothly in space due to the fact that the pRF reflects aggregate properties of large numbers of single units with different receptive fields. In our investigation, the ridge regression yielded pRF shapes that satisfy the assumption. The lasso regression provided a sparse solution but not a reasonable pRF topography (i.e., not localized and smooth). The elastic-net yields a similar pRF shape to the one obtained by ridge regression since it also includes the L2-norm minimization. Based on the above, we elected to use the ridge regression technique for the estimation of the pRF vectors discussed in this paper. Therefore, the model we use is based on the ridge regression with a bias and is written as:

$$J_i = \|y_i - K^+ p_i^+\|^2 + \lambda_1 \|p_i\|^2 \tag{7}$$

where $\mathbf{K}^+ = \left[\mathbf{K} \quad \mathbf{1}^{M\times 1}\right]$, $p_i^+ = [p_i \quad \alpha]$ (α is a constant value introduced to account for the bias), and λ_1 is a free parameter to control the extent to

which the least-square function is regularized. The solution of Eq. (7) is given:

$$p_i^+ = \left(K^{+T}K^+ + \lambda_1 I^+\right)^{-1} K^{+T} y_i \tag{8}$$

$$\text{Where } \mathbf{I}^+ = \begin{bmatrix} \mathbf{I} & \mathbf{0}^{M\times 1} \\ \mathbf{0}^{1\times M} & 0 \end{bmatrix}, \mathbf{I} = \begin{bmatrix} 1 & 0 & \cdots & 0 \\ 0 & 1 & \ddots & \vdots \\ \vdots & \ddots & \ddots & 0 \\ 0 & \cdots & 0 & 1 \end{bmatrix} = \Re^{M\times M}$$

In our experiments, the screen resolution was 800 × 600 pixels, and a circular disk circumscribed within a central square area composed of 360,000 (600 × 600) pixels was used to present the stimulus. The stimulus size corresponding to the square was down-sampled to 101 × 101 to increase the computation efficiency (This value is the default setting in the VISTA software; implementations of our algorithm were carried out using VISTA software by replacing Dumoulin's method (Dumoulin and Wandell, 2008)).

Modeling the central region of the pRF

Here, we define pRF center, pRF central region, and pRF center model. The pRF center is the point which exhibits the maximum positive peak in the receptive field and the pRF central region is the area that is positive, surrounding the center point. These notions parallel the classical receptive field terminology commonly used in physiology. The pRF center model denotes the model we apply to fit the pRF central region.

In our model, there are two free parameters: the regularization parameter, λ_1, and the cut-off threshold to define the pRF central region, k. For each value of λ_1, topographies of pRFs were estimated for all gray matter voxels and visually responsive voxels were identified (Fig. 1B). For this, a region of interest (ROI) of a sphere with a radius of 10 mm was created in a non-visually responsive area. Then, explained variance (EV) was computed as:

$$EV(p_i) = 1 - \frac{||y_i - K^+ p_i^+||^2}{||y_i||^2} \text{ at voxel i} \tag{9}$$

The mean EV (**<EV> ≈ 0.1**) in a non-visually responsive ROI (e.g. a sphere of diameter 10 mm from the lower medial prefrontal cortex) was used as a threshold to select voxels that visually respond. The mean explained variance in a visually non-responsive area corresponds to the portion of the explained variance that could be due to noise. This is a reasonable choice for setting the threshold for identifying voxels that visually respond, since we want to err on the side of caution, i.e. not exclude any visually responsive voxels from the initial pRF estimate. After estimating the full pRF topography ($\mathbf{p}_i$) we need to define a strategy for extracting the pRF central region. Typically, the structure of the pRF has a dominant region while more distant visual field locations have much smaller, potentially suppressive, contributions. Fig. 1C illustrates the strategy we use to identify and model the central part of the pRF topography, which presents the dominant excitatory field (Fig. 1C). First, the components of the pRF vector $\mathbf{p}_i$ are normalized to lie between 0 and 1. Then, three regions of the pRF vector (corresponding to more or less restrictive estimates of the pRF central region) at each voxel are obtained by thresholding the topography at three values, k = [0.3, 0.5, 0.7]. The pRF topography patch remaining after thresholding (i.e., each topography of the pRF central region) was fitted with a 2D-Gaussian model:

$$\exp\left(-1/2(\mathbf{g}-\mu)^T \Sigma^{-1} (\mathbf{g}-\mu)\right) \tag{10}$$

whose center and dispersion are

$$\mu = [x_i, y_i]^T \tag{11-1}$$

and

$$\Sigma = \begin{bmatrix} \cos\theta & -\sin\theta \\ \sin\theta & \cos\theta \end{bmatrix} \cdot \begin{bmatrix} \sigma_1^2 \\ \sigma_2^2 \end{bmatrix}. \tag{11-2}$$

To find the optimal parameters for each pRF central patch, we applied a nonlinear curve-fitting method at voxel i and threshold k:

$$\min_{a,b,\mu,\Sigma} ||\mathbf{p}_i^{>k} - a\exp\left(-1/2\left(\mathbf{g}^{>k}-\mu_i\right)^T \Sigma_i^{-1}\left(\mathbf{g}^{>k}-\mu_i\right)\right) + b||^2, \tag{12}$$

where $\mathbf{p}_i^{>k}$ is the topography patch for the pRF central region at voxel i and threshold k, and $\mathbf{g}^{>k}$ the corresponding stimulus space, and a and b are a scale and a bias, respectively. This implementation was performed via the optimization toolbox of MATLAB. After determining the parameters of the 2D-Gaussian model, the EV of each model at each voxel was obtained:

$$EV\left(m_i^k\right) = 1\frac{||y_i - \beta_1 K m_{i,k} + \beta_2||^2}{||y_i||^2}, \tag{13}$$

where $\mathbf{m}_{i,k} = \exp(-1/2(\mathbf{g}-\mu_i)^T \sum_i^{-1}(\mathbf{g}-\mu_i))$ at voxel i and threshold k, β_1 and β_2 are a scale factor and a bias, respectively. That is, each voxel has 3 different models according to the threshold, k, defining the pRF central region. Among the three different models, the best one was selected with respect to the EV (Fig. 1C). Hereafter $\mathbf{m}_i$ indicates the model with the best threshold among the candidates.

To select the best λ_1 across the range λ_1 = [0.1–30], we considered the distribution of voxels with EVs ranging from 0.1 to 0.9 binned in intervals of size 0.2, (Fig. 1D). As λ_1 increases, the fraction of voxels with lower and intermediate EV values (0.1-0.7) was quickly saturated (Fig. 1D), suggesting that it was insensitive to high values of λ_1. However, at the EV bin (0.7–0.9), the number started decreasing after reaching a maximum (Fig. 1D). From this pattern, to maximize the mean EV in low EV bins while minimizing the loss of the EV in the high EV bins, we chose the lambda for which the mean fraction (thick black line in Fig. 1D) of voxels across all of the EV bins reached 0.95. Data from all other subjects showed similar results (not shown here). Hereafter, we used the selected lambda for all the following analyses.

Estimates from the direct-fit models

Direct-fit methods first model the pRF shape as a certain parametric model, and then find optimal parameters for the model to minimize the residual between the observed fMRI signal and the signal predicted from the model (Dumoulin and Wandell, 2008). This approach used a two-stage coarse-to-fine search to reduce the computation time. In the coarse search, sparsely sampled voxels were used to estimate parameters in the grid fitting after spatial smoothing. That is, the grid fitting had hundreds of thousands of sets of different parameters (e.g., 2-location and 1-dispersion parameters per voxel in the DIG model), which were assessed with respect to the explained variance to find the best parameter set at an individual voxel. Then, after interpolating the parameters of all gray voxels from the parameters of the sparsely sampled voxels, the fine search was applied in unsmoothed raw data to further optimize the parameter set.

The grid-search method in this approach requires a long computation time. Even though this approach permits the use of various models such as the anisotropic Gaussian model and the difference of Gaussians model, its applicability to testing models composed of more parameters is limited because the search space increases exponentially with the number of parameters.

Comparison between methods

We compared our method with the previously described method that directly fits isotropic Gaussian (DIG) models (Dumoulin and Wandell, 2008). Even though many recent studies only tested DIG models (Dumoulin and Wandell, 2008; Levin et al., 2010; Winawer et al., 2010), to be fair, we further compared our method with the directly fitting anisotropic Gaussian (DAG) method.

For a quantitative comparison, we used a cross-validation strategy by using a 'leave-one-scan-out' method. That is, for each turn, data from a single fMRI scan were left out for testing while data from all remaining scans were used to estimate the model. This process was repetitively performed for all scans. Since we collected a different number of scans in subjects, 'x'-fold cross validation was performed, where 'x' indicates the number of scans in each subject. Each time, the comparison test was performed by measuring the amount of variance accounted for by the estimated model.

For the model estimation in the training data, we considered only patches covering the central region of the pRF model that were modeled as two-dimensional Gaussians because the main aim of our modeling here was to estimate the pRF central area. Note that this comparison used patches from the models rather than the extracted area from the topography since the direct fitting methods cannot provide the topography. The patch $\mathbf{m}^{>thr}$ which covered the central region of the pRF model was obtained by thresholding the normalized Gaussian models (i.e. a magnitude of 0-1) with a range of $thr = \{0.1, 0.3, 0.5, 0.7\}$ after building the models (i.e., $\exp(-1/2(\mathbf{g}-\mu)^T \sum^{-1}(\mathbf{g}-\mu))$ in our and DAG approaches and $\exp\left(-\frac{1}{2\sigma^2}(\mathbf{g}-\mu)^T(\mathbf{g}-\mu)\right)$ in the DIG approach (Dumoulin and Wandell, 2008) with the estimated parameters. We call this value the threshold for the pRF central region. The threshold value of 0 indicates a complete stimulus area. Then, we assessed how much variance the patch from each method explains in the testing data:

$$EV\left(m_i^{>thr}\right) = 1 - \frac{||y_i - \left(\beta_1 d_i^{>thr} + \beta_2\right)||^2}{||y_i||^2} \quad (13)$$

Where $\mathbf{d}_i^{>thr} = \mathbf{H}\mathbf{S}^{>thr}\mathbf{m}_i^{>thr}$, $\mathbf{S}^{>thr}$ is the stimulus area corresponding to $\mathbf{m}_i^{>thr}$ (central patch after thresholding the best model, $\mathbf{m}_i$, at *thr*), and β_1 and β_2 are a scale factor and a bias, respectively.

This comparison was performed at the voxels where the EV of either the proposed model, *or* the DIG/DAG model was above 0.2 (small enough to include all early visual areas). The use of the union set means that voxel selection was not biased to either method. To avoid penalizing the direct-fit methods that completely miss pRF parameters in some voxels (leading to EV = 0 despite EV from the proposed >0.2) we excluded those voxels. On the contrary, we did not exclude any voxels estimated by our method; therefore this gives an advantage to the direct-fit methods in the comparison. More specifically, in the first stage of computation the direct-fit method performs pRF estimation only in the sampled voxels after spatial smoothing and the subsequent interpolation process derives the model parameters along all cortical voxels from the parameters of the sampled voxels. This interpolation process might sometimes provide completely different parameter values from the actual ones by estimating model parameters from sampled poor BOLD signals. Therefore, good signals could be excluded in the later optimization stage (see Appendix A for more details).

To avoid potential errors of pRF center estimation near the border of the stimulus space, the comparison was performed only on pRFs whose center resides within the stimulus space for both methods, and which have EV above 0.2. This is also a relative disadvantage for our method that provides more accurate estimates of the pRF centers near the border of stimulus space (see Results section).

In order to compare the models we evaluated their ability to estimate the pRF center over the central region of the receptive field as defined by the thresholded topography. This is a fair comparison, particularly since the DIG and DAG models intrinsically assume that the pRF consists only of a strong excitatory field without any surround inhibition and therefore will be prone to errors arising from the existence of the surround. On the other hand, Zuiderbaan et al. (2012) used the direct-fit difference of isotropic Gaussians (DDoIG) to account for the surround inhibition as well as the excitatory center. Therefore, we also compared the proposed and DDoIG methods for the pRF center modeling as above.

Results

PRF topographies and comparison between pRF center models

We ensured that our model could estimate reasonable pRF structures based on the assumption of localization and smoothness in space (Fig. 2A), enforced by regularization (see Material and methods section). In the typical topography, we observe one strong positive peak and weaker bar patterns crossing the peak (Fig. 2A). The strong positive peak corresponds to the pRF center since it is located in the most responsive position. The appearance of bar patterns in the topography is associated with the fact that areas along directions of the bar movements across the pRF center are stimulated at the same time as the pRF central region. That is, while the pRF central region evokes a robust BOLD response eight times (from 8 bar sweeps), the non-central bar areas along each orientation that are simultaneously stimulated with the center induce a BOLD response twice (from 2 sweeps in each orientation) and thus crossing bar patterns appear appropriately weaker in the topography.

The central region of the pRF topography was modeled with an anisotropic Gaussian in our method. This model was qualitatively compared to direct-fit methods (Dumoulin and Wandell, 2008). As shown in Fig. 2B, the DIG method could not capture anisotropy in the pRF by definition (being isotropic), while direct-fit anisotropic models (DAG) can capture anisotropies better. However, even the introduction of anisotropy in the model, i.e. DAG, could not capture the pRF orientation as well as the proposed method (see voxel 141960 in Fig. 2B). Furthermore, either direct-fit method could not localize the pRF center as well as the proposed method (see voxels 129112 and 321775 in Fig. 2B). This is probably because the direct-fit methods minimize the residual between their prediction and the observed fMRI signal regardless of the actual location of the pRF center region (Fig. 2B).

For a quantitative comparison, we used cross-validation tests by employing a 'leave-one-scan-out' method (see Material and methods section). Specifically, after obtaining the mean explained variance (mEV) at each voxel from the testing data, the distributions of the mEV difference between the two methods were plotted at each voxel. EVs were obtained only taking into account the pRF center regions, which were determined using the thresholds [0.1–0.7] for each method. This comparison showed that the method we propose performs better as threshold increases, leading more voxel EVs to be positive and greater than EVs estimated with the DIG or DAG models (Fig. 3; EV-diff > 0.05 with $p > 0.5$ at thr = 0.1, and EV-diff > 0.05 with $p < 1e-10$ for thr = 0.3, 0.5, 0.7 for both DIG and DAG models; one-tailed *t*-test.). This implies that the proposed method models the pRF center region better than direct-fit methods. As expected, the difference between the two methods is smaller at lower thresholds. This is because direct-fit methods optimize the parameters in the full stimulus space, while the topography-based method selects the local area of the pRF center prior to model optimization. Since the pRF center resides in the local stimulus space (narrowing its localization to within a few degrees of visual angle) compared to a range of ~11° (stimulus space radius) for the full stimulus space, optimizing the pRF parameters in the full stimulus space leads to a less accurate estimate, and lower EVs.

The direct-fit methods sometimes yield pRF models with centers at higher eccentricity than the radius of the stimulus presentation area (i.e., the pRF center can be located outside the stimulus presentation space; see Fig. 4). Since our method estimates the topography it can

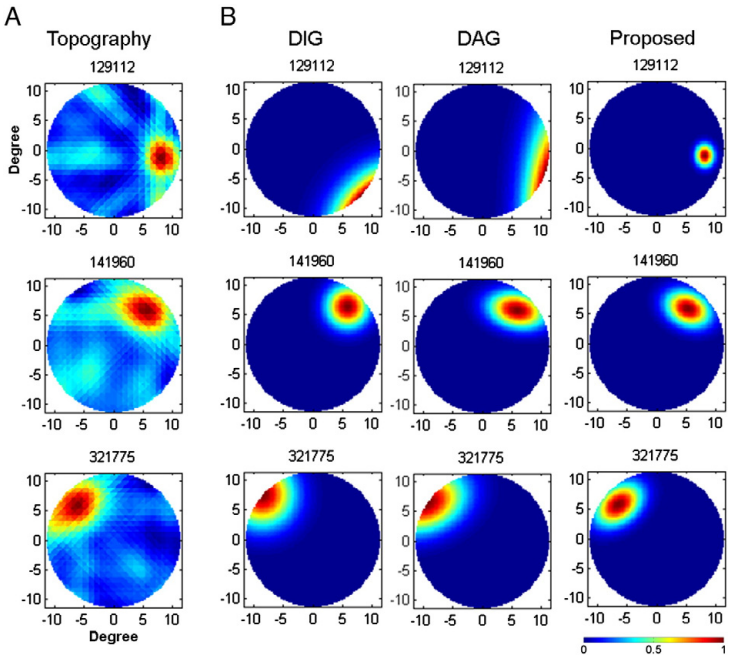

Fig. 2. Topography of the pRFs and model fitting the pRF center region. (A) Examples of the pRF topography at 3 different voxels. (B) The left, middle, and right columns show the corresponding pRF models with the direct-fit isotropic Gaussian (DIG) (Dumoulin and Wandell, 2008), the direct-fit anisotropic Gaussian (DAG), and the proposed (topography based anisotropic Gaussian) approaches, respectively. Normalized pRF weights are plotted in the range between [0 and 1].

better optimize the model fit for voxels whose pRF center falls outside the stimulus space outperforming the direct-fit methods there. To ensure that this is not the only reason we outperformed the DIG and DAG methods, we performed the same analysis restricted to voxels for which the eccentricity of the pRF center from both models falls within the stimulus space. This comparison also shows that the method we propose performs better as threshold increases, leading to more voxel EVs to be positive and greater than EVs estimated with the DIG and DAG models (Supplementary Fig. 1; EV-diff > 0.01 with $p > 0.5$ at thr = 0.1, and EV-diff > 0.01 with $p < 1e-10$ for thr = 0.3, 0.5, 0.7 for both DIG and DAG models; one-tailed *t*-test.). These results show that the proposed method is more robust in estimation of pRF center parameters both within and outside the stimulus presentation space than direct-fit methods. Note that this is the case despite the fact that this comparison was chosen to be biased in favor of direct-fit methods: i.e. we excluded voxels that could not be reliably modeled with the direct-fit methods because of their proximity to the stimulus border.

Eccentricity and polar angle maps

We compared the eccentricity maps for the three methods. Differences between the maps were mainly observed at high eccentricities (Fig. 4A). The proposed method yielded more voxels than the DIG and DAG methods with centers at 8–11.25° eccentricity, but fewer voxels

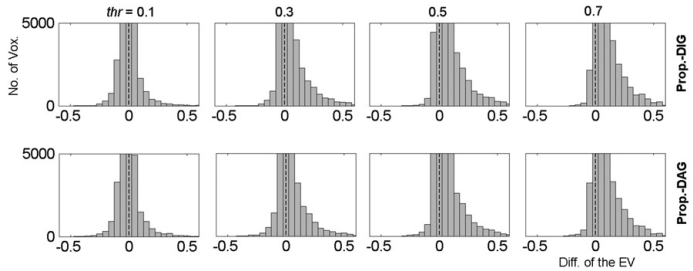

Fig. 3. Histograms of the differences in mean explained variance between the proposed, and the DIG (top row) and the DAG (bottom row) methods obtained by cross validation (see methods). In each subject, after 'x'-fold cross validation according to the number of scans (i.e., 'x' is the number of scans acquired in each subject; it produced 'x' explained variances for each voxel), the mean explained variance (mEV) at each single voxel was obtained. The explained variance (EV) from the direct-fit isotropic Gaussian (DIG) (Dumoulin and Wandell, 2008) and the direct-fit anisotropic Gaussain (DAG) method were subtracted from the EV from the proposed method voxel by voxel and data were pooled over all 4 subjects. In the figures, the EVs for each model were obtained only taking into account the pRF center region, and the pRF center regions were determined by thresholding the models at [0.1, 0.3, 0.5, 0.7], respectively (see methods). The black vertical broken lines indicate an EV difference of 0, and the Y-axis (number of voxels) is truncated above 5000 for ease of visualization. This examination shows larger differences between the proposed, and the DIG and the DAG methods with the threshold increase (for both methods, EV-diff > 0.05 with $p > 0.5$ at thr = 0.1, and EV-diff > 0.05 with $p < 1e-10$ at thr = 0.3, 0.5, 0.7; one-tailed t-test).

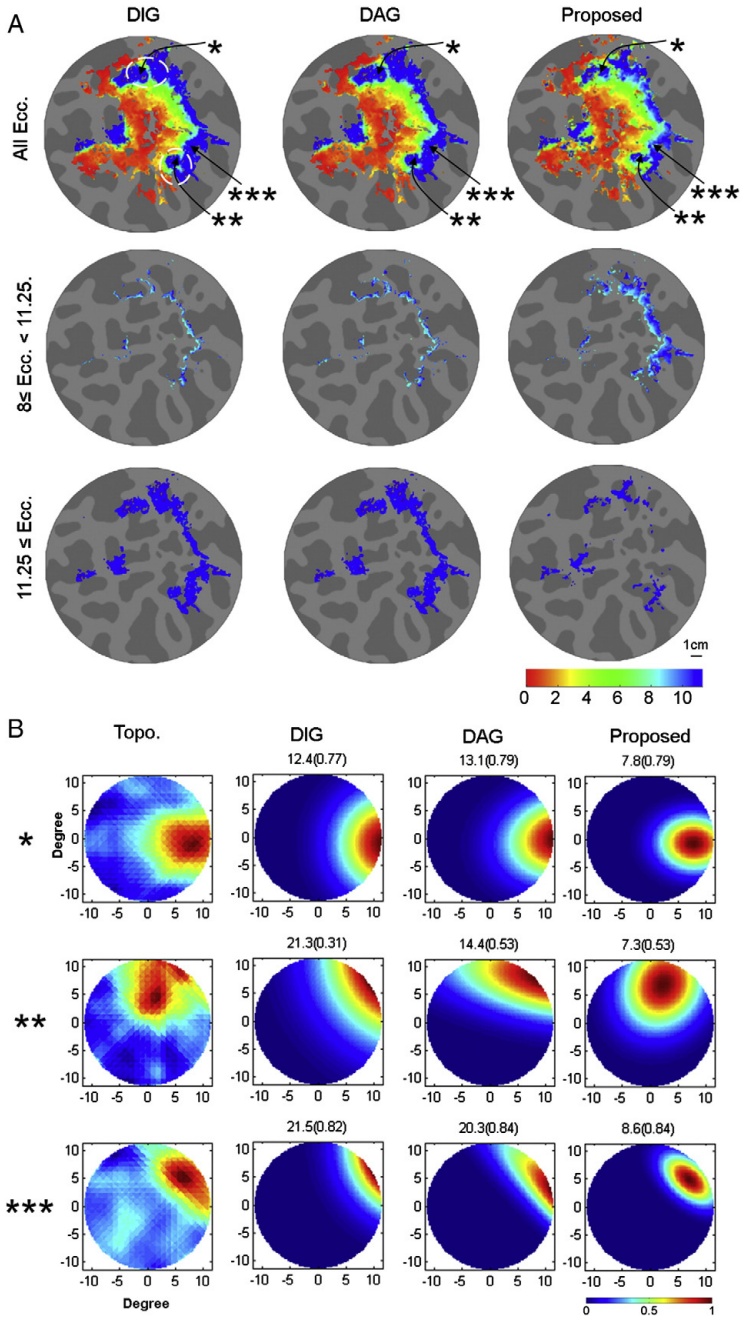

Fig. 4. Comparison of eccentricity maps derived from the proposed method versus direct-fit models. (A) Eccentricity maps from one subject are illustrated. From the top to the bottom row, eccentricity maps are shown for the full eccentricity range, for 8–11.25°, and for >11.25° of eccentricity, respectively. The panels left to right show eccentricity maps from the DIG (direct-fit isotropic Gaussian), the DAG (direct-fit anisotropic Gaussian), and the proposed methods, respectively. (B) PRF topographies from the 3 locations shown in (A). In panel (A), the locations are indicated by *, **, and ***, respectively. On the top of each panel, the pRF center eccentricity in degrees and the corresponding explained variance is shown. Normalized pRF weights are plotted in the range between [0-1].

with centers beyond the border of the stimulus presentation space, i.e. >11.25° (Fig. 4A). In addition, the eccentricity maps derived from the direct-fit models exhibit discontinuities by showing some regions where distant eccentricities intermingle (areas outlined by the white dashed lines in Fig. 4A). This differs from the results of our method, which leads to relatively gradual changes in the eccentricity map. For example, in Fig. 4, the non-physiological distinct eccentricity "island" patterns (inside the dashed circles) seen with the direct-fit methods are far less prominent using the method we propose here. To illustrate the difference, we examined the pRF topography at the voxels marked with * and ** in Fig. 4A. In the first voxel (*), the DIG, the DAG, and the proposed method estimated the pRF center to lie at 12.4°, 13.1°, and 7.8° eccentricity with explained variances of 0.77, 0.79, and 0.79, respectively (Fig. 4B). In the second voxel (**), the corresponding numbers are 21.3°, 14.4°, and 7.3° with explained variances of 0.31, 0.53, and 0.53, respectively. For both voxels, the pRF topographies (Fig. 4B) clearly show that the pRF center is well within the stimulus space indicating that our method provides more accurate results in this range of eccentricities. This is even more striking for voxels whose pRF centers, as estimated by the direct-fit models, lie at eccentricities >11.25°. Markedly fewer voxels are estimated to have centers that lie in this eccentricity range using our method compared to estimates derived from the direct-fit models (Fig. 4A). An example is the voxel marked with *** in Figs. 4A and B. Note again that its center is estimated erroneously to lie at 21.5° and 20.3° with the DIG and DAG methods, as compared to 8.6° with the method proposed here. Inspired by these examples, we examined the relation between the difference in eccentricity and the difference in explained variance of the pRF-center estimates derived from the proposed versus the direct-fit methods (see Supplementary Fig. 2). Supplementary Fig. 2 shows that pRF center estimates derived by direct fit methods that lie in high (non-physiologic) eccentricities do not typically lead to higher explained variance as compared to the proposed method. These results would originate from the fact that direct-fit methods minimize the residual between the actual BOLD signal and their prediction without first constraining the location of the pRF center. Therefore, noisy or suppressive surround regions distant from the true pRF center can contribute significantly to explained variance estimates and lead to erroneous or biased fitting of the pRF center. On the other hand, the proposed method first suppresses low SNR responses in the pRF topography via regularization (see Eq. (7)) and then fits a model to the high SNR peak of the pRF topography.

We then examined the distribution of the voxels' eccentricity estimated by the 3 different methods (Fig. 5). A strong bias is observed at high eccentricities in the histogram of the two direct-fit methods, seen at ~22.5°. This is particularly evident in the DIG method, but does not appear at all in the proposed method. This bias is not physiological, given the known properties of population receptive field size as a function of eccentricity, particularly for early visual areas (Burkhalter and Van Essen, 1986; Felleman and Van Essen, 1987; Gattass et al., 1981, 1987; Newsome et al., 1986). Moreover, this result is inconsistent with the previous finding that the number of voxels gradually decreases with increase of eccentricity (Daniel and Whitteridge, 1961; Hubel and Wiesel, 1974). For the proposed method, another bias was observed at eccentricities near the border of the stimulus presentation space. This happens particularly when voxels with low explained variance (EV > 0.2) are included (Fig. 5). This bias manifests as a sharp drop in the histogram peak as pRF center eccentricity crosses the stimulus space border. This happens because the proposed method tends to map the center of pRFs that are truncated by the stimulus space border inside that border, even though sometimes they may be located outside the stimulus space (see Fig. 6C). The proposed method models pRFs with centers just outside the stimulus presentation space with a smaller error than direct-fit methods because it calculates the model based on the thresholded excitatory fields observed in the pRF topography. PRFs with centers far outside the border of the stimulus presentation space are unlikely to yield strong excitatory fields within the stimulus presentation space in the pRF topography. As the threshold for the explained variance increases both biases are degraded by removing inaccurate estimates arising from low SNR signals (Fig. 5 and Supplementary Fig. 3). Nonetheless, the direct-fit methods still result in many voxels whose pRF center resides far outside the stimulus space, e.g., greater than 5° distant to the stimulus space border, whereas the proposed method does not.

In addition, the proposed method identified more voxels with higher explained variance (e.g., 0.4) in all visually responsive voxels (Fig. 5), as well as in the visual field maps of areas V1-3 specifically (Supplementary Fig. 3). Since pRF centers lying at eccentricities 6–8° are unlikely to be truncated by the border of the stimulus presentation aperture (11.25°), the superior performance of the proposed method in explaining variance results at least in part from the accurate capture of pRF center shapes.

We examined the relationship between eccentricity and explained variance (Supplementary Fig. 4). Given the relationship between pRF size and eccentricity (Burkhalter and Van Essen, 1986; Felleman and Van Essen, 1987; Gattass et al., 1981, 1987; Newsome et al., 1986), pRF centers lying far beyond the stimulus presentation area are expected to yield lower explained variances than those just outside the stimulus presentation area. Our methods of pRF center estimation obeys this expectation. In contrast, direct-fit methods yield high explained variance even for voxels whose pRF centers lie far beyond the stimulus presentation space. This further suggests that pRF centers estimated by the direct-fit method to lie far beyond the stimulus space are unlikely to be correct.

In Figs. 6A, B, and C we illustrate the conditions under which different pRF estimation methods could potentially misbehave. When the pRF center is inside the stimulus space, an anisotropic Gaussian model can reliably identify the pRF properties (Fig. 6A) regardless of whether the true pRF is isotropic or anisotropic. If the true pRF center is outside the stimulus space and the pRF central region is isotropic, an isotropic model may, in principle, better estimate the true pRF center (Fig. 6B). Regardless of the pRF actual shape, however, the DIG and DAG methods tend to mis-localize the pRF center when it lies near the stimulus space border leading to the large, non-physiologic, bias seen at large eccentricities (Fig. 5). This is because these methods minimize the residual between the actual BOLD signal and its prediction without constraining the stimulus space over which the optimization is done. This bias is stronger in the DIG method in part because pRFs are not necessarily isotropic, and in part because errors in pRF localization from models assuming isotropy can be large and biased towards high eccentricities (see pRF C2 in Fig. 6C).

For the proposed method, the pRF center modeling can be successfully performed only for the pRF center located within the stimulus space. On the other hand, when the pRF center is outside the stimulus space, the subsequent modeling process is prone to identify one location of the stimulus space border as the pRF center (pRF C1 in Fig. 6C). These qualifications notwithstanding, the method proposed here results in more accurate positioning of the pRF center than the directly-fitting models (Dumoulin and Wandell, 2008). This is because having access to the pRF topography allows us to constrain the central region of the pRF prior to fitting, and because even for pRF topographies that are in part outside the stimulus presentation space, the actual pRF centers are likely to lie close to the border of the stimulus presentation space as mentioned above. This is because the typical pRF size at corresponding eccentricities in early visual areas remains restricted below 5° (Burkhalter and Van Essen, 1986; Felleman and Van Essen, 1987; Gattass et al., 1981, 1987; Newsome et al., 1986). Regardless of what shape the pRF structure is outside the stimulus presentation space, direct-fit methods are subject to large errors in localizing the pRF center when it lies outside the stimulus presentation space (e.g., C2 of Fig. 6C). In contrast, even when it is unable to precisely identify the exact pRF center location, the proposed method can at least give us an approximate estimate of the pRF center location by extrapolating from the portion of the true pRF topography that lies within the stimulus presentation space.

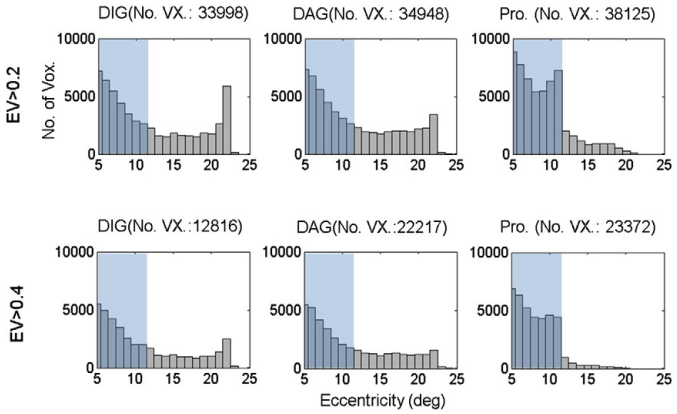

Fig. 5. Histogram of eccentricity derived by 3 different methods (DIG, DAG, and the proposed). Histograms of voxels with explained variance above 0.2 (top) and above 0.4 (bottom) are shown. This distribution was obtained from all 4 subjects. Panels from the top and bottom rows show the number of voxels with explained variance above 0.2 and 0.4, respectively. Blue shaded regions denote the stimulus presentation space, and the Y-axis (number of voxels) is truncated above 10,000 for ease of visualization. The direct-fit methods have many more voxels whose pRF center lies at eccentricities much greater than the border of stimulus space, as compared to the proposed method. Direct-fit methods show a strong non-physiologic peak at the highest eccentricity (~22°), which is particularly evident for the direct-fit isotropic Gaussian (DIG) model when voxels with EV > 0.2 are considered. On the other hand, the proposed method maps the pRF center of many voxels near or just inside the stimulus space border. For voxels with EV above 0.4, the direct-fit methods (particularly DIG) still show many voxels with eccentricities beyond the stimulus space, while the bias of the proposed method is much reduced and it shows much fewer voxels with centers outside the stimulus space.

On the contrary, comparing polar angle maps showed no discernible difference between the models (Fig. 7). As shown in Figs. 6 A and B, even when the pRF center is outside the stimulus space, similar polar angles are estimated with both methods if the dominant peak (i.e., a part of the pRF center) is at least observable near the border of stimulus space. In other words, the polar angle of the pRF center is dependent on the location of its peak, and thus estimates from both methods are likely to be similar (Figs. 6A and B). Even though the direct-fit models are not constrained by pre-calculating the pRF topography, all the methods provided polar angle estimates similar to those of the actual pRF centers (as determined by the topography).

pRF size estimates using different methods

We also examined whether the proposed method yielded different relationships between pRF size and eccentricity in comparison with the DIG and DAG methods (Fig. 8). For this analysis, the pRF size was defined as the single Gaussian dispersion parameter σ for the DIG and $(\sigma_1 + \sigma_2)/2$ from Eq. (11-2) for the DAG and the proposed methods. The comparison was performed in the visual field maps V1-3 of the left hemisphere of all 4 subjects. For this comparison, we selected voxels with explained variance above 0.4 in the visual field maps of areas V1-3 and then plotted the relationship between pRF size and eccentricity for eccentricities 2–9°. For these eccentricities modeling of the pRF centers was reliable for all three methods given the bar aperture size, sweep step, and stimulus space extent that we have used (see Fig. 8 and also Figs. 4–5). This comparison showed that while all the 3 methods showed similar linear relationships between pRF size and eccentricity, the proposed method modeled pRFs across V1-3 more reliably than the DIG and DAG methods as it identified more voxels with EV > 0.4. These results support that the higher explained variance obtained with our method did not originate from arbitrary capturing of the pRF shape.

Presence of surround suppression in the pRF

The visualization of pRF topographies allowed us to observe evidence of surround suppression. To examine whether the proposed method can capture characteristics of surround suppression, we carefully examined the pRF topographies and the raw BOLD signals. Surround suppression

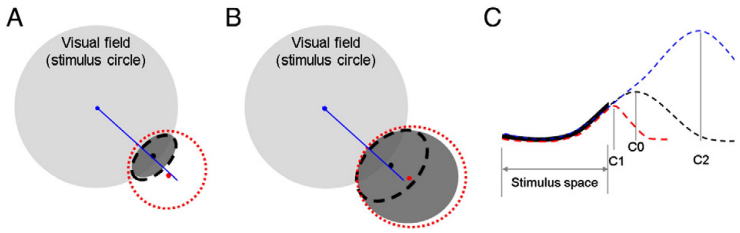

Fig. 6. Schematic illustrations comparing anisotropic and isotropic models, and direct-fit models. (A-B) Illustrations of anisotropic and isotropic models. The light gray disk delineates the stimulus space. The dark gray ellipsoid/circle represents the true pRF. The black and the red dashed lines contrast fits obtained by an anisotropic and an isotropic model, respectively. The blue dot and line denote the origin and the polar angle of the pRF center. The black and red dots denote the corresponding pRF centers. In a pRF which has an anisotropic topography located near the edge but inside the stimulus space, the anisotropic model would correctly identify the location of the center, but the isotropic model would not (A). When the true pRF center is outside the stimulus space and the true pRF center has circular topography, the anisotropic model would fail, but the isotropic model would succeed (B). In panels A–B, different models provide different eccentricities but similar polar-angles. (C) Illustration of potential pitfalls of the direct-fit and the proposed methods. The thick black line indicates a cross-section from the topography, where the pRF center is outside the stimulus space. The red- and blue- dashed curves denote two different models that can properly model the cross-section within the stimulus space. C0, C1, and C2 denote the actual pRF center and the centers of two models, respectively. When actual center C0 is given, the proposed and the direct-fit methods are prone to estimate C1 and C2 as the center respectively, illustrating that differences can occur between models fitting similar data.

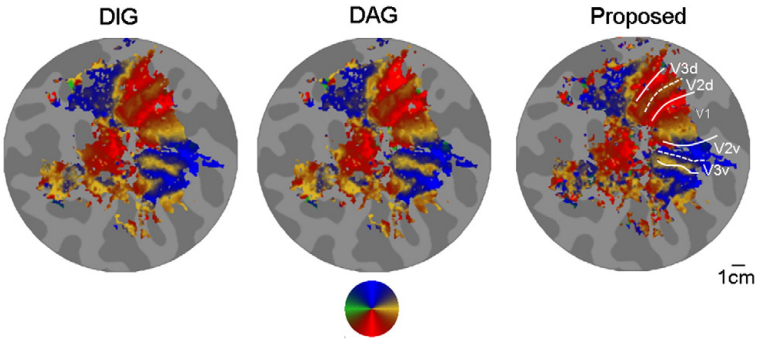

Fig. 7. Polar angle maps of the 3 different methods in the left hemisphere of a subject are similar to each other.

manifests in the topography as a suppression or disappearance of the crossing bar patterns near the pRF central region (Fig. 9A). This suppression particularly occurs when negative BOLD responses (NBR) are observed (Fig. 9A). For instance, when the bar aperture moved from the left to the right, the bar pattern faded away before reaching the positive peak (left panel of Fig. 9A). Correspondingly, a negative dip was observed before the main positive BOLD response (see the first red circle in Fig. 9A). To illustrate how surround suppression is related to the NBR, a *hypothetical*[2] pRF model with surround suppression was considered by using the difference of two Gaussians (DoG) (Fig. 9B). This choice was based on the assumption that NBRs can be explained by convolving the response from the surround of the pRF (e.g., −0.3G (6,0,5,4,0) in Fig. 9B) with the HRF under the linear assumption (Zuiderbaan et al., 2012). Using this *hypothetical* model, an estimate of the BOLD signal was generated by using the stimulus protocol applied in our experiment and the canonical HRF. The proposed method was then applied to estimate the pRF topography (Fig. 9C). In this topography crossing bar patterns disappeared near the pRF central region (Fig. 9C) because of the surround inhibition introduced in the generating model (panel B). As expected, the DoG model yielded negative dips in the BOLD signal immediately before or after the main BOLD peaks caused by stimulation of the pRF central region (Fig. 9C). These results closely match the actual BOLD response and the actual pRF topography of the voxel shown in Fig. 9A. Then we modeled the pRF from the topography shown in Fig. 9C using one single Gaussian (i.e. ignoring surround suppression), and predicted the BOLD responses. The predicted BOLD signal (Fig. 9C, green curve) did not show strong negative dips (Fig. 9C). This exercise confirmed that the observed negative dips can be interpreted as an effect of surround suppression, which a single Gaussian model does not capture. The proposed method can therefore be used to model pRFs with center surround structure.

A question arises whether the improved performance of the method we propose could be due to the existence of the inhibitory surround. This might be because the proposed method uses a thresholding step to separate the pRF central region from the full pRF topography (that includes the surround) before fitting, which the DIG and the DAG methods could not do. In order to investigate whether this is the case, we also compared the proposed method to the direct-fit difference of isotropic Gaussians (DDoIG) model (Harvey and Dumoulin, 2011; Zuiderbaan et al., 2012). The DDoIG model models the surround suppression as an additive negative isotropic Gaussian and can therefore take into account the symmetric aspects of surround suppression while modeling the pRF center. For this comparison, we used only isotropic Gaussians to build the pRF center and surround model in the direct-fit method, following the approach of (Harvey and Dumoulin, 2011; Zuiderbaan et al., 2012). In fact, anisotropy in the pRF center has been revealed in our study through direct observation of the topographies; it has not been assumed in previous studies (Harvey and Dumoulin, 2011; Zuiderbaan et al., 2012). Moreover, given the present computing power of PCs, it is impractical to introduce anisotropic Gaussians for the pRF center and surround in the direct-fit method as the computation time increases dramatically.

It is important to note that there are also other reasons not to model the surround in this study. Specifically, although the pRF topography from the proposed method reveals the presence of surround suppression for some voxels (Fig. 10), the surround suppression generated by our stimulation protocol was generally weak, making it thus difficult to 1) separate surround suppression from noise artifacts, and to 2) dissociate the late dip of the hemodynamic response function (i.e., the negative gamma function of Eq. (4) following an early strong excitatory response) from the weak negative BOLD response of surround suppression. Furthermore, the extent of suppression might be asymmetric (like the center) along different directions than the pRF center and partially depends on the regularization parameter λ_1 of Eq. (7). Furthermore, a recent study by (Goense et al., 2012) reported a larger nonlinearity in the negative BOLD response than in the positive one, which further hinders the estimation of the surround. Therefore, we examined whether the estimate of the pRF center derived from the DDoIG model (Harvey and Dumoulin, 2011; Zuiderbaan et al., 2012), could outperform the estimate of the pRF center model derived from the proposed method.

The difference in explained variance between the proposed and the DDoIG method for pRF center modeling (Fig. 10) is smaller than the one between the proposed, and the DIG and DAG methods (Fig. 3). This suggests that inclusion of the surround suppression in the pRF modeling improves the estimate of the pRF center (Supplementary Fig. 5). However, as we demonstrate in Fig. 10, despite introduction of the surround suppression in the direct-fit method, the direct-fit method could not outperform the proposed method in modeling the pRF center. Specifically, our method resulted in equal or higher explained variances compared to the DDOIG method for all thresholds tested: EV-diff > 0.1 with $p > 0.5$ at thr = 0 (whole stimulus space), and EV-diff > 0.1 with $p < 0.05$ at thr = 0.3 and p < 1e-10 at thr = 0.5, 0.7; one-tailed t-test. In addition, the DDoIG methods still had the problem of erroneous mapping of the pRF centers into high eccentricities beyond the stimulus space (Supplementary Figs. 2–4). This implies that a) constraining the pRF central region and b) capturing the anisotropy of the pRF as indicated by the pRF topography is required to model the pRF center more accurately.

For the pRF size in relationship to eccentricity, the DDoIG method provided a similar result to the ones of the DIG, the DAG, and the proposed method (Supplementary Fig. 6).

[2] The use of term "hypothetical DoG" was decided because even though the negative BOLD response is a solid concept, we do not really know whether its shape conforms to the DoG model we used, which assumes the surround represents a negatively shaped Gaussian centered at the peak of the response.

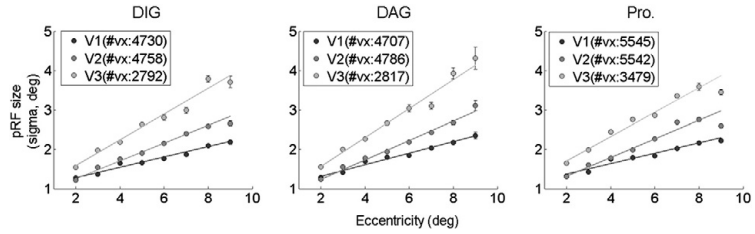

Fig. 8. Relationship between pRF size and eccentricity for DIG, DAG and the proposed method. Mean pRF size is plotted against visual field eccentricity in areas V1-3 of the left hemisphere of all 4 subjects. The plots include voxels with explained variance above 0.4 and eccentricity within 2–9°. Error bars represent the standard error of the mean.

Discussion

Here, we propose a new method for estimating population receptive field (pRF) parameters, such as retinotopic location and spatial structure, in vivo by fMRI. Our method allows us to reconstruct and visualize the visual field topography of the pRF, and has several advantages over previously proposed methods (Dumoulin and Wandell, 2008; Engel et al., 1994; Harvey and Dumoulin, 2011; Zuiderbaan et al., 2012). First, our approach enables us to observe the pRF shape before fitting, allowing us to choose an appropriate model that fits the structure of the data. Separate fits can be made for the pRF center region and the surround, facilitating the extraction of information about the latter. In addition, the proposed method is computationally more efficient than the direct fitting method. The direct fitting method (Dumoulin and Wandell, 2008; Harvey and Dumoulin, 2011; Zuiderbaan et al., 2012) requires searching over very large model-parameter spaces by assessing the

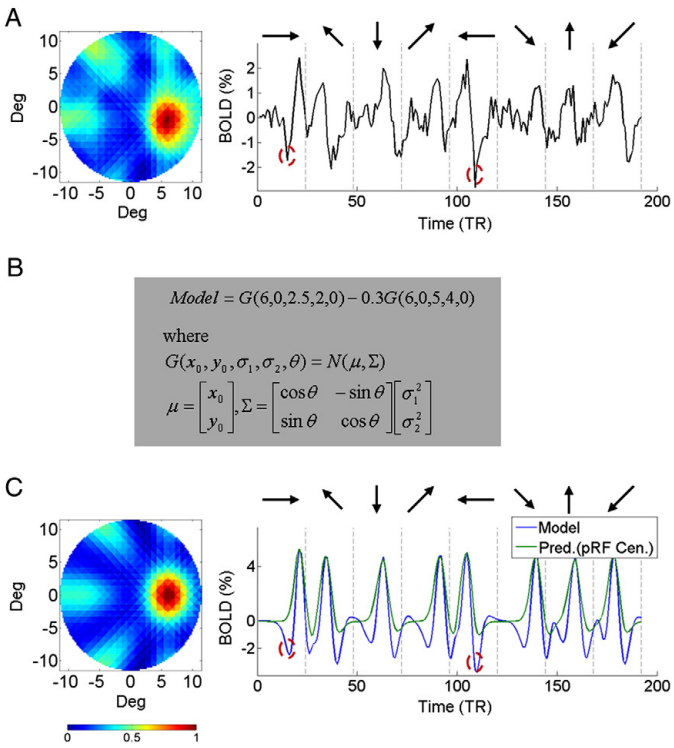

Fig. 9. Surround suppression can be indentified in the pRF topography. (A) PRF topography and BOLD signal response arising at a voxel. In the topography, bar patterns fade away near the pRF center as a sign of inhibition. The BOLD signal trace demonstrates the presence of occasional strong negative dips before and after BOLD peaks. This negative dips (e.g., red circles) matches the spatial locations where the bar patterns fade away. Normalized pRF weights are plotted in the range between [0 and 1]. (B) To illustrate how the features observed in (A) arise we modeled a pRF center with surround inhibition as a difference of Gaussians with pre-specified parameters (center location, μ, and covariance matrix, Σ). To incorporate surround suppression in the pRF center model G(6,0,2.5,2,0), a Gaussian with twice the sigmas of the center model and scaled by 0.3 was subtracted from the center model. This model was then used to estimate the BOLD signal response in panel (C) Estimated BOLD signal response generated from the hypothetical 'Model' in Figure B and the corresponding pRF topography estimated with the proposed method. Similar to the pattern seen in the actual voxel plotted in (A), stimulation with a longitudinal bar aperture leads to crossing bar patterns as the bar moves across the pRF center. As in (A) bar patterns are seen to disappear near the pRF central region because of surround suppression. The right column shows estimated BOLD time series (blue) generated from the 'Model' in panel B and the prediction (green) generated by using solely a pRF center model. The pRF center model is estimated only from the pRF central region segregated from the full topography (see Material and methods section). For comparison, the dc value of the prediction signal is matched to that of the BOLD signal. While the BOLD signal from the 'Model' in B has negative dips before and after the peaks evoked by stimulation of the pRF center region (red circles; similar to Figure A), its prediction using solely the pRF center model does not.

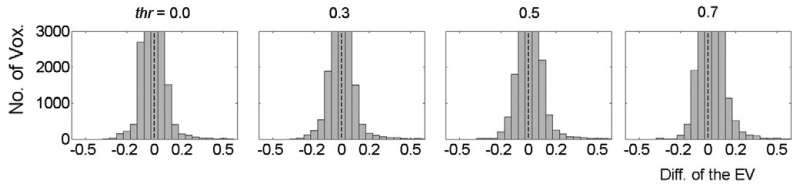

Fig. 10. Histograms of the voxel-by-voxel difference in mean explained variance between the proposed and the direct-fit difference of isotropic Gaussians (DDoIG) methods obtained by cross validation (see methods). The figure conventions match those used in Fig. 3. Significant differences are seen above a threshold of 0.3, and significance increases as threshold increases: EV-diff > 0.1 with $p > 0.5$ (non-significant) at thr = 0 (whole stimulus space), $p < 0.05$ at thr = 0.3, $p < 1e-10$ at thr = 0.5, 0.7; one-tailed t-test.

explained variance of a model with each candidate set of parameters and selecting the best one. This means that the computation time exponentially increases with the number of parameters limiting the application of this approach to a variety of models with few parameters. In contrast, the proposed method uses the pRF topography as a starting point, which already constrains the space of search for possible parameters (e.g., the peak location in the topography constrains the range of possible locations of the pRF center, while the spread of the pRF center in the topography constrains the standard deviation of the Gaussian model) making it possible to estimate a model with more parameters in less time. In addition, even though the direct fitting method tries to reduce the computation time by sparsely-sampling voxels in the first stage of parameter estimation, this method still requires model evaluation in all sampled voxels to select visually responsive voxels, and is prone to missing some visually responsive voxels (see Appendix A). The proposed method is more efficient in computation time by selecting visually responsive voxels from the explained variance, which is obtained from the pRF topography via a matrix–vector multiplication.

The method we propose results in a pRF center model that explains a higher proportion of the variance both in lower eccentricities (Supplementary Fig. 1), i.e. away from the stimulus presentation border and in all eccentricities (Fig. 3). This is in part because we restrict the stimulus space to be modeled by thresholding the pRF topography prior to applying a model fit to its center. This makes the final modeling step less susceptible to noise contamination and surround suppression presence. In contrast, the DIG and DAG methods minimize the residual between the actual BOLD signal and the prediction of the pRF-center model over the full stimulus space, and is more susceptible to noise and the surround suppression.

Moreover the DIG (Dumoulin and Wandell, 2008; Levin et al., 2010; Winawer et al., 2010; Zuiderbaan et al., 2012), DAG, and DDoIG methods provide less reliable eccentric maps, especially near the border of the stimulus presentation space. Fig. 4 shows that for direct-fit methods the minimum residual can sometimes be obtained with model parameters distant to the true ones, providing less reliable eccentricity maps. By contrast, the receptive field estimation method we propose here reflects relatively more accurate eccentricity of the pRF centers, because it is based on calculating and thresholding the pRF topography prior to performing the final model fitting. This difference is particularly clear near the stimulus space border (see Figs. 4 and 5). The erroneous mis-localization of the pRF centers near the stimulus space border by the direct-fit methods leads to a strong non-physiological bias in the eccentricity map, which persists even after removing voxels with low explained variances (Fig. 5). This is manifested by the large number of pRF centers estimated to lie at very high eccentricities, i.e. >5° beyond the stimulus space border (see Fig. 5 and Supplementary Fig. 3). This non-physiological mapping of pRF centers to distant eccentricities happens because the direct-fit methods minimize the residual over the whole stimulus space and are prone to mislocalization error as explained in Fig. 6C. The proposed method also sometimes mislocalizes pRF centers that lie near the stimulus space border. However, resulting errors are generally much smaller, i.e. on the order of the pRF radius, and error number drops rapidly for voxels with high explained variances (see Fig. 5). On the other hand, polar-angle maps were similar for the three methods, as pRF center locations computed with the two approaches mainly differ along the radial direction (see Figs. 6 and 7).

Our discussion here is limited to the estimation of the pRF center. It is generally difficult to measure surround suppression accurately because surround suppression is relatively weak and requires integration over a large area of the visual field. It is therefore susceptible to contamination by noise for the usual bar stimulation paradigms employed. Nonetheless, the proposed method is useful for inspecting whether the pRF of a voxel contains surround suppression by visualizing the pRF topography. We modeled receptive fields with surround suppression as a difference of Gaussian (Fig. 9) and then tested whether the model predicted characteristics of surround suppression observed in empirical data. The pRF topography and BOLD responses from the model matched those observed from empirical data closely by showing negative BOLD regions (NBRs) and the disappearance of bar patterns around the pRF centers in the topography (Fig. 9). A previous study showed that stimulation evokes neuronal depolarization of the central stimulated region and hyperpolarization of surrounding areas, and the NBR in the surround was associated with arteriolar vasoconstriction and neuronal inhibition there (Devor et al., 2007; Shmuel et al., 2006). These results point to the need for a more systematic study of the structure of pRF surrounds, but this will likely require new stimulation paradigms and lies beyond the scope of the current study.

We also compared the performance of our method against direct-fit difference of isotropic Gaussians (DDoIG). Even that model, which takes into account the surround suppression, did not outperform the proposed method for modeling the pRF center (Fig. 10). Importantly, adding the surround suppression did not solve the problem of erroneously mapping pRF centers into higher eccentricities, often extending far beyond the stimulus presentation space (see Supplementary Figs. 2–4). This may in part be because the DDoIG method uses concentric isotropic Gaussians to fit the center and the surround, which may lie to the mislocalization of the pRF center. Unfortunately, comparing a direct-fit anisotropic DoG model to the method we proposed was not feasible at this time, because in direct-fit methods computation time increases exponentially with the number of parameters.

Classical retinotopic mapping strategies, including the present study, estimate receptive fields by using generic flickering checkboard stimuli modulated over a spatio-temporal frequency range known to activate well receptive field centers. The neural activity is then modeled by considering stimulated areas as on-fields and other areas as off-fields. This approach leaves unexplored how the structure of the pRF depends on the properties of the visual stimulus. This is an important direction to pursue in the future. Recent fMRI studies confirm that different pRF responses can arise from specific properties of the visual stimulus. For example, Sasaki and colleagues showed a radial bias in the orientation selectivity of voxels in human and primate visual cortex (Freeman et al., 2011; Sasaki et al., 2006). There is an ongoing debate whether it is this global radial bias versus orientation preference patterns irregularly distributed over multiple voxels that lead to the success of visual stimulus orientation decoding via the BOLD signal (Freeman et al., 2011; Harrison and Tong, 2009; Kamitani and Tong, 2005; Mannion et al., 2009; Sasaki et al., 2006). Be that as it may, assuming orientation

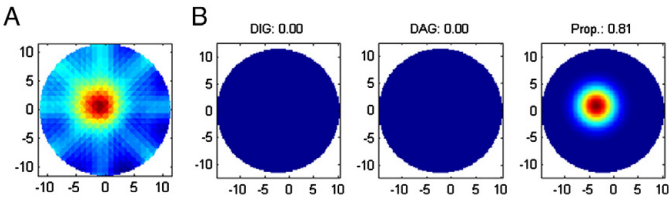

Fig. 11. PRF topography and computed models for a voxel missed by the direct-fit methods. (A) PRF Topography from a voxel missed from the direct-fit methods. Note this voxel has a robust receptive field center. (B) The three different models (DIG, DAG, and proposed) for the pRF of the selected voxel, and the explained variance of each model, respectively. In this case, because of the optimization algorithm (see main text) DIG and DAG miss the pRF completely. In contrast, the proposed method derives a robust pRF model that matches well the topography seen in (A) and has explained variance ~0.81.

information is embedded in multiple scales, it is possible that using different orientations as the bar background pattern might provoke different BOLD responses and presumably influence the derived properties of pRFs (e.g., different pRF shapes may result from gratings oriented perpendicularly vs. parallel to the bar sweep direction). These results reinforce the need to start using stimuli with specific properties in order to investigate more thoroughly the properties of pRFs in the visual cortex.

In summary, we demonstrated that our model successfully measures the structure of population receptive fields in vivo from the BOLD signal. By deriving the pRF topography as a first step our method is able to guide population receptive field modeling better than other existing methods. In addition, the proposed method is more efficient in terms of computation time. We have shown that the proposed method outperforms the direct-fit pRF estimation models. This improvement is particularly evident near the border of the stimulus presentation space, where direct methods lead to considerable pRF center mislocalization in the radial direction. Because the proposed method is subject to fewer biases than the more commonly applied direct Gaussian models, we anticipate that it will be particularly useful for monitoring how visual pRFs change with different types of visual stimulation, as a function of adaptation, or as a function of cortical reorganization in patients with injuries of the visual pathway.

Acknowledgments

This work was supported by the Max-Planck Society, the DFG, the PLASTICISE project of the 7th Framework Programme of the European Commission, Contract no. HEALTH-F2-2009-223524 (GAK, NKL), as well as an NIH award (NEI RO1- EY019272), a Howard Hughes Medical Institute Early Career Award, and a DoD (W81XWH-08-2-0146) award to SMS.

Conflict of interest

There is no conflict of interest.

Appendix A. Direct-fit methods occasionally miss visually responsive voxels

The direct-fit method proposed by Dumoulin and Wandell (2008) adopts the following two-stage process: In the first stage, spatial smoothing of the fMRI data along the cortical surface is performed and then voxels are sparsely sampled for pRF estimation in order to save computation time. For the selected voxels, pRF model parameters are estimated by computing and optimizing the explained variance of the pRF model. Then, model parameters are reconstructed for all voxels by interpolating from the sampled voxels along the cortical sheet. Then, at the second stage, a finer optimization process is performed only for the raw BOLD signal time-series that have explained variance above a certain threshold.

When model parameters are interpolated from sampled voxels with low signal-to-noise ratio (SNR), voxels with high SNR that lie near a sampled voxel with low SNR can be potentially excluded in the second fine optimization. In contrast, the proposed method uses explained variances estimated from the topography and therefore does not miss voxels with good SNR. Fig. 11 shows such an example in which direct-fit methods miss a good signal, while the proposed method does not. Our performance comparison (Figs. 3 and 10, and Supplementary Fig. 1) was conservative in that we excluded all voxels which the direct-fit methods missed (i.e. about 5% of compared voxels for which direct-fit methods set the estimated variance below threshold, to zero) while the proposed method accepted ($EV > 0.2$).

Appendix B. Supplementary data

Supplementary data to this article can be found online at http://dx.doi.org/10.1016/j.neuroimage.2013.05.026.

References

Birn, R.M., Saad, Z.S., Bandettini, P.A., 2001. Spatial heterogeneity of the nonlinear dynamics in the FMRI BOLD response. Neuroimage 14, 817–826.
Boynton, G.M., Engel, S.A., Glover, G.H., Heeger, D.J., 1996. Linear systems analysis of functional magnetic resonance imaging in human V1. J. Neurosci. 16, 4207–4221.
Brainard, D.H., 1997. The psychophysics toolbox. Spat. Vis. 10, 433–436.
Burkhalter, A., Van Essen, D.C., 1986. Processing of color, form and disparity information in visual areas VP and V2 of ventral extrastriate cortex in the macaque monkey. J. Neurosci. 6, 2327–2351.
Daniel, P.M., Whitteridge, D., 1961. The representation of the visual field on the cerebral cortex in monkeys. J. Physiol. 159, 203–221.
Devor, A., Tian, P., Nishimura, N., Teng, I.C., Hillman, E.M., Narayanan, S.N., Ulbert, I., Boas, D.A., Kleinfeld, D., Dale, A.M., 2007. Suppressed neuronal activity and concurrent arteriolar vasoconstriction may explain negative blood oxygenation level-dependent signal. J. Neurosci. 27, 4452–4459.
DeYoe, E.A., Carman, G.J., Bandettini, P., Glickman, S., Wieser, J., Cox, R., Miller, D., Neitz, J., 1996. Mapping striate and extrastriate visual areas in human cerebral cortex. Proc. Natl. Acad. Sci. U.S.A. 93, 2382–2386.
Dougherty, R.F., Koch, V.M., Brewer, A.A., Fischer, B., Modersitzki, J., Wandell, B.A., 2003. Visual field representations and locations of visual areas V1/2/3 in human visual cortex. J. Vis. 3, 586–598.
Dumoulin, S.O., Wandell, B.A., 2008. Population receptive field estimates in human visual cortex. Neuroimage 39, 647–660.
Engel, S.A., Rumelhart, D.E., Wandell, B.A., Lee, A.T., Glover, G.H., Chichilnisky, E.J., Shadlen, M.N., 1994. fMRI of human visual cortex. Nature 369, 525.
Engel, S.A., Glover, G.H., Wandell, B.A., 1997. Retinotopic organization in human visual cortex and the spatial precision of functional MRI. Cereb. Cortex 7, 181–192.
Felleman, D.J., Van Essen, D.C., 1987. Receptive field properties of neurons in area V3 of macaque monkey extrastriate cortex. J. Neurophysiol. 57, 889–920.
Freeman, J., Brouwer, G.J., Heeger, D.J., Merriam, E.P., 2011. Orientation decoding depends on maps, not columns. J. Neurosci. 31, 4792–4804.
Friston, K.J., Holmes, A.P., Poline, J.B., Grasby, P.J., Williams, S.C., Frackowiak, R.S., Turner, R., 1995. Analysis of fMRI time-series revisited. Neuroimage 2, 45–53.
Friston, K.J., Fletcher, P., Josephs, O., Holmes, A., Rugg, M.D., Turner, R., 1998. Event-related fMRI: characterizing differential responses. Neuroimage 7, 30–40.
Gattass, R., Gross, C.G., Sandell, J.H., 1981. Visual topography of V2 in the macaque. J. Comp. Neurol. 201, 519–539.
Gattass, R., Sousa, A.P., Rosa, M.G., 1987. Visual topography of V1 in the Cebus monkey. J. Comp. Neurol. 259, 529–548.
Glover, G.H., 1999. Deconvolution of impulse response in event-related BOLD fMRI. Neuroimage 9, 416–429.

Goense, J., Merkle, H., Logothetis, N.K., 2012. High-resolution fMRI reveals laminar differences in neurovascular coupling between positive and negative BOLD responses. Neuron 76, 629–639.
Hansen, K.A., David, S.V., Gallant, J.L., 2004. Parametric reverse correlation reveals spatial linearity of retinotopic human V1 BOLD response. Neuroimage 23, 233–241.
Harrison, S.A., Tong, F., 2009. Decoding reveals the contents of visual working memory in early visual areas. Nature 458, 632–635.
Harvey, B.M., Dumoulin, S.O., 2011. The relationship between cortical magnification factor and population receptive field size in human visual cortex: constancies in cortical architecture. J. Neurosci. 31, 13604–13612.
Hastie, T., Tibshirani, R., Friedman, J.H., 2001. The Elements of Statistical Learning: Data Mining, Inference, and Prediction. Springer, New York.
Haykin, S.S., 1999. Neural Networks: A Comprehensive Foundation, 2nd ed. Prentice Hall, Upper Saddle River, N.J.
Hoerl, A.E., 1970. Ridge regression. Biometrics 26, 603.
Hubel, D.H., Wiesel, T.N., 1974. Uniformity of monkey striate cortex: a parallel relationship between field size, scatter, and magnification factor. J. Comp. Neurol. 158, 295–305.
Jain, R.K., 1985. Ridge regression and its application to medical data. Comput. Biomed. Res. 18, 363–368.
Kamitani, Y., Tong, F., 2005. Decoding the visual and subjective contents of the human brain. Nat. Neurosci. 8, 679–685.
Levin, N., Dumoulin, S.O., Winawer, J., Dougherty, R.F., Wandell, B.A., 2010. Cortical maps and white matter tracts following long period of visual deprivation and retinal image restoration. Neuron 65, 21–31.
Maes, F., Collignon, A., Vandermeulen, D., Marchal, G., Suetens, P., 1997. Multimodality image registration by maximization of mutual information. IEEE Trans. Med. Imaging 16, 187–198.
Mannion, D.J., McDonald, J.S., Clifford, C.W., 2009. Discrimination of the local orientation structure of spiral glass patterns early in human visual cortex. Neuroimage 46, 511–515.
Nestares, O., Heeger, D.J., 2000. Robust multiresolution alignment of MRI brain volumes. Magn. Reson. Med. 43, 705–715.
Newsome, W.T., Maunsell, J.H., Van Essen, D.C., 1986. Ventral posterior visual area of the macaque: visual topography and areal boundaries. J. Comp. Neurol. 252, 139–153.
Ringach, D.L., 2004. Mapping receptive fields in primary visual cortex. J. Physiol. 558, 717–728.
Sasaki, Y., Rajimehr, R., Kim, B.W., Ekstrom, L.B., Vanduffel, W., Tootell, R.B., 2006. The radial bias: a different slant on visual orientation sensitivity in human and nonhuman primates. Neuron 51, 661–670.
Sereno, M.I., Dale, A.M., Reppas, J.B., Kwong, K.K., Belliveau, J.W., Brady, T.J., Rosen, B.R., Tootell, R.B., 1995. Borders of multiple visual areas in humans revealed by functional magnetic resonance imaging. Science 268, 889–893.
Shmuel, A., Augath, M., Oeltermann, A., Logothetis, N.K., 2006. Negative functional MRI response correlates with decreases in neuronal activity in monkey visual area V1. Nat. Neurosci. 9, 569–577.
Simoncelli, E.P., Paninski, L., Pillow, J., Schwartz, O., 2004. Characterization of neural responses with stochastic stimuli, Cognitive Neurosciences IiiThird edition. 327–338.
Teo, P.C., Sapiro, G., Wandell, B.A., 1997. Creating connected representations of cortical gray matter for functional MRI visualization. IEEE Trans. Med. Imaging 16, 852–863.
Tibshirani, R., 1996. Regression shrinkage and selection via the Lasso. J. R. Stat. Soc. B Methodol. 58, 267–288.
Tibshirani, R., 2011. Regression shrinkage and selection via the lasso: a retrospective. J. R. Stat. Soc. B Stat. Methodol. 73, 273–282.
Wandell, B.A., Dumoulin, S.O., Brewer, A.A., 2007. Visual field maps in human cortex. Neuron 56, 366–383.
Winawer, J., Horiguchi, H., Sayres, R.A., Amano, K., Wandell, B.A., 2010. Mapping hV4 and ventral occipital cortex: the venous eclipse. J. Vis. 10, 1.
Worsley, K.J., Friston, K.J., 1995. Analysis of fMRI time-series revisited—again. Neuroimage 2, 173–181.
Worsley, K.J., Liao, C.H., Aston, J., Petre, V., Duncan, G.H., Morales, F., Evans, A.C., 2002. A general statistical analysis for fMRI data. Neuroimage 15, 1–15.
Zou, H., Hastie, T., 2005. Regularization and variable selection via the elastic net. J. R. Stat. Soc. B Stat. Methodol. 67, 301–320.
Zuiderbaan, W., Harvey, B.M., Dumoulin, S.O., 2012. Modeling center-surround configurations in population receptive fields using fMRI. J. Vis. 12.

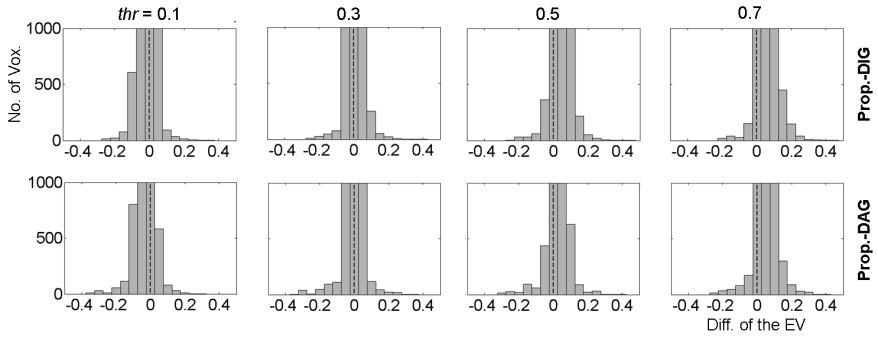

Supplementary Fig. 1. Histograms of the differences in mean explained variance between methods: the proposed vs. the direct-fit isotropic Gaussian (DIG), and the proposed vs. the direct-fit anisotropic Gaussian (DAG). The mean explained variances were obtained by cross validation (see methods). This comparison was performed in the voxels whose pRF center from both methods resides within the stimulus space. The black vertical broken lines indicate an EV difference of 0, and the Y-axis (number of voxels) is truncated above 1000 for ease of visualization. The figure conventions match those in Fig. 3. Both comparisons (i.e., Prop. vs DIG, and Prop. vs DAG) show the larger differences with the greater thresholds (EV-diff>0.01 with $p>0.5$ at thr = 0.1, and EV-diff>0.01 with $p<1e^{-10}$ for thr = 0.3, 0.5, 0.7; one-tailed t-test).

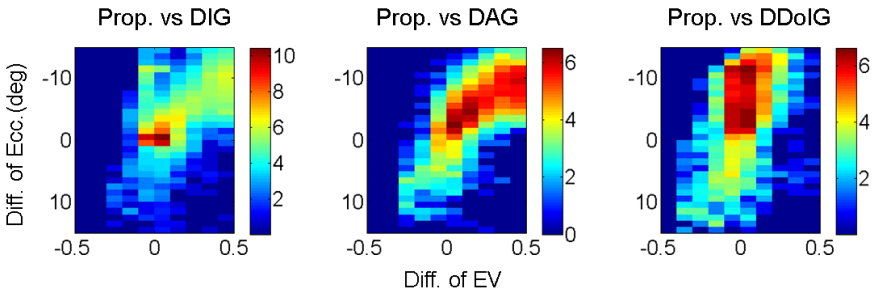

Supplementary Fig. 2. Comparison of the difference in pRF-center eccentricity and explained variance between the proposed method and direct-fit methods (DIG, DAG, DDoIG). Number of voxels from all 4 subjects is represented by a logarithmic color map. The X- axis plots the difference of explained variances, and the Y-axis the difference of pRF-center eccentricity estimates obtained by the proposed method versus a direct-fit method. In these plots, voxels at high eccentricities (>11.25 degrees) for at least one method, and with explained variance greater than 0.4 for both methods are included. For the selected voxels, explained variances are obtained taking into account only the pRF-center area, which is defined by thresholding the normalized pRF models with threshold = 0.5 (see Figs. 3 and 10). Note that the proposed method explains on average a higher proportion of the variance (positive X values). In contrast the direct-fit method gives rise to higher eccentricity estimates (negative Y values), which are erroneous. All comparisons show that direct-fit methods map pRF centers

into higher eccentricities than the proposed method without improving the explained variance significantly.

.

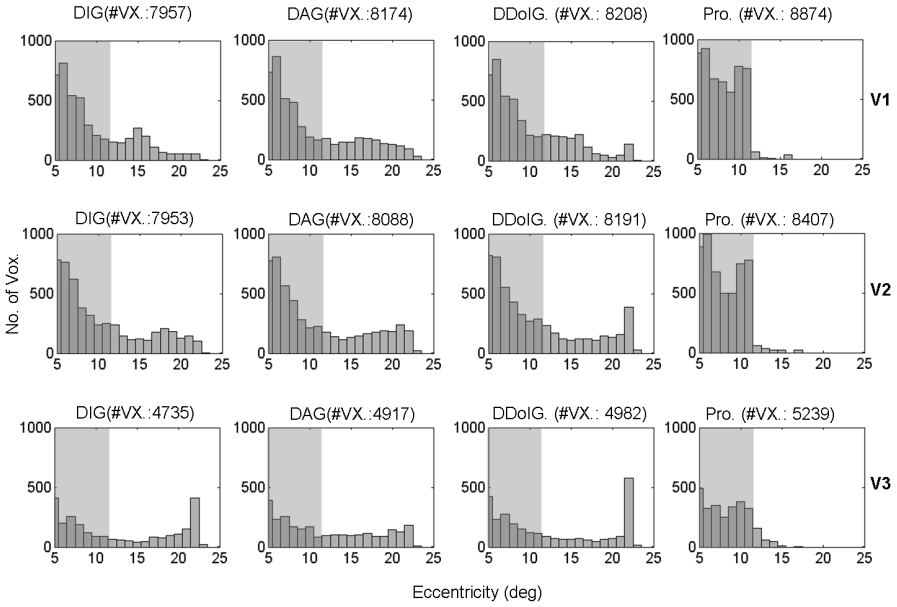

Supplementary Fig. 3. Histogram of eccentricity in left visual field maps V1-3 derived by 4 different methods (DIG, DAG, DDoIG, and the proposed). Histograms of the voxels with explained variance above 0.4 are shown. This distribution was obtained from all 4 subjects. Here, DDoIG indicates the direct-fit difference of isotropic Gaussians model (Zuiderbaan et al.,2012). Each row shows the distribution derived from area V1, V2, V3 respectively. Other figure conventions match those in Fig. 6. #VX: number of voxels from all four subjects.

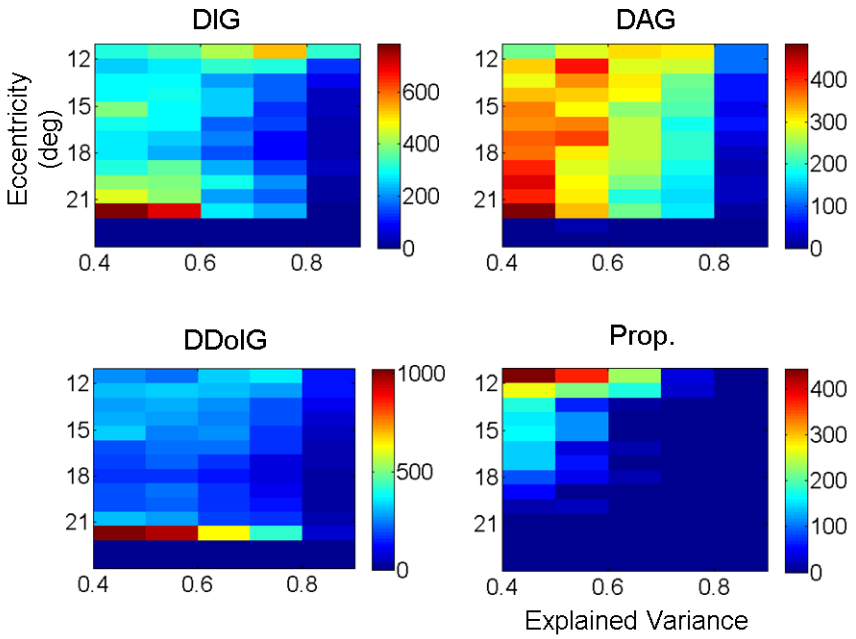

Supplementary Fig. 4. Distribution of voxels with explained variance > 0.4 and eccentricities beyond the stimulus presentation space (Ecc>11.25deg). These data were collected from all 4 subjects. All the direct-fit methods (DIG, DAG, and DDoIG) show voxels lying far outside the stimulus space with high explained variances and lead a strong peak in the highest eccentricity ~22 deg as shown in Fig. 6. In addition, even for explained variance > 0.6, the distribution is almost uniform, which indicates that explained variance is independent of eccentricity. However, the proposed method showed that the number of voxels decreases with increases of eccentricity and explained variance.

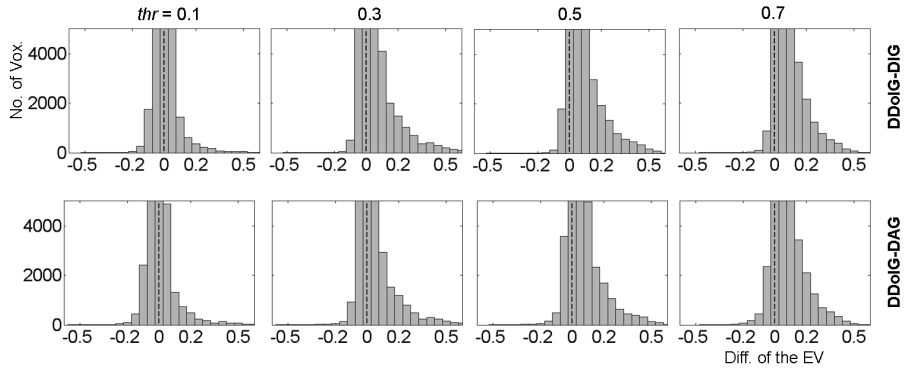

Supplementary Fig. 5. Histograms of the differences in mean explained variance between the direct-fit methods: the direct-fit difference of isotropic Gaussians (DDoIG) vs the direct-fit isotropic Gaussian (DIG), and the DDoIG vs the direct-fit anisotropic Gaussian (DAG). The mean explained variances obtained by cross validation (see methods). This comparison was performed in the voxels whose pRF center from both methods resides within the stimulus space. The black vertical broken lines indicate an EV difference of 0, and the Y-axis (number of voxels) is truncated above 5000 for ease of visualization. The figure conventions match those in Fig. 3. Both comparisons (i.e., DDoIG vs DIG, and DDoIG vs DAG) show the larger differences with the greater thresholds (EV-diff> 0.01 with $p<1e^{-10}$ for thr = 0.1, 0.3, 0.5, 0.7; one-tailed t-test).

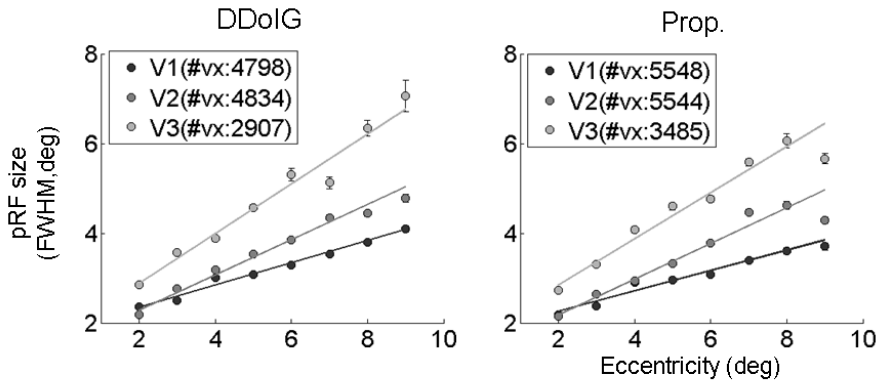

Supplementary Fig. 6. The relationship between pRF size and eccentricity for the DDoIG method. Mean pRF size (Full width at half-maximum; FWHM) is plotted against visual field eccentricity in areas V1-3 of the left hemisphere of all 4 subjects. The plots include voxels with explained variance above 0.4 and eccentricity within 1-9 degrees. Error bars represent the standard error of the mean. For comparison to the DDoIG method, pRF sizes obtained with the proposed method are also plotted in the FWHM.

A.3 "Topographical estimation of visual population receptive fields by fMRI"

Video Article

Topographical Estimation of Visual Population Receptive Fields by fMRI

Sangkyun Lee[1], Amalia Papanikolaou[2], Georgios A. Keliris[2,3], Stelios M. Smirnakis[1]

[1]Department of Neuroscience and Neurology, Baylor College of Medicine

[2]Max Planck Institute for Biological Cybernetics

[3]Bernstein Center for Computational Neuroscience

Correspondence to: Sangkyun Lee at lee.sangkyun@gmail.com

URL: http://www.jove.com/video/51811
DOI: doi:10.3791/51811

Keywords: Behavior, Issue 96, population receptive field, vision, functional magnetic resonance imaging, retinotopy

Date Published: 2/3/2015

Citation: Lee, S., Papanikolaou, A., Keliris, G.A., Smirnakis, S.M. Topographical Estimation of Visual Population Receptive Fields by fMRI. *J. Vis. Exp.* (96), e51811, doi:10.3791/51811 (2015).

Abstract

Visual cortex is retinotopically organized so that neighboring populations of cells map to neighboring parts of the visual field. Functional magnetic resonance imaging allows us to estimate voxel-based population receptive fields (pRF), *i.e.*, the part of the visual field that activates the cells within each voxel. Prior, direct, pRF estimation methods[1] suffer from certain limitations: 1) the pRF model is chosen a-priori and may not fully capture the actual pRF shape, and 2) pRF centers are prone to mislocalization near the border of the stimulus space. Here a new topographical pRF estimation method[2] is proposed that largely circumvents these limitations. A linear model is used to predict the Blood Oxygen Level-Dependent (BOLD) signal by convolving the linear response of the pRF to the visual stimulus with the canonical hemodynamic response function. PRF topography is represented as a weight vector whose components represent the strength of the aggregate response of voxel neurons to stimuli presented at different visual field locations. The resulting linear equations can be solved for the pRF weight vector using ridge regression[3], yielding the pRF topography. A pRF model that is matched to the estimated topography can then be chosen post-hoc, thereby improving the estimates of pRF parameters such as pRF-center location, pRF orientation, size, *etc*. Having the pRF topography available also allows the visual verification of pRF parameter estimates allowing the extraction of various pRF properties without having to make a-priori assumptions about the pRF structure. This approach promises to be particularly useful for investigating the pRF organization of patients with disorders of the visual system.

Video Link

The video component of this article can be found at http://www.jove.com/video/51811/

Introduction

Functional magnetic resonance imaging (fMRI) measures non-invasively the functional organization of visual cortex at a macroscopic scale (typically on the order of millimeters). Early fMRI retinotopy studies used a coherence measure between stimulus location and elicited BOLD responses[4-7]. These studies typically did not estimate population receptive field size. Later, Dumoulin and Wandell[1] proposed a method to overcome such a limitation by explicitly modeling the pRF location and size, using a linear function of this model to predict the BOLD response. However, one limitation of this pioneering method is that the parametric pRF model has to be chosen a-priori, and may lead to erroneous pRF estimates if it turns out not to be appropriate**.**

To overcome limitations of the parametric pRF-model method, new methods have been developed recently. These methods directly predict the BOLD response to the stimulus by reconstructing the pRF topography. A method[8] proposed by Greene and colleagues reconstructs the pRF topography by back-projecting the BOLD responses to the individual 1D stimulus spaces and building the pRF topography in the 2D stimulus space like a typical computer tomography technique. On the other hand, the method[2] proposed by us directly estimates the 2D pRF topography by using linear regression and applying a regularization technique. In this method, the pRF topography is represented as a set of weights which is multiplied by the stimulus to estimate the neuronal population response of a given voxel. Then, the final Blood Oxygen Level-Dependent (BOLD) response evoked by the stimulus is estimated by convolving the neuronal population response and the canonical hemodynamic response function. In order to solve the under-constrained linear system, additionally, ridge regression regularization is used to enforce sparseness (see **Figure 1** below). The regularization technique suppresses noise and artifacts and thus allows our method to estimate the pRF topography more robustly.

The topographical methods do not force the pRF shape to have a certain parametric shape, and therefore can uncover the actual pRF structure. An appropriate parametric model can then be chosen based on the pRF topography. For example, the pRF topography can be used to separate the pRF center and surround, and then the subsequent pRF center modeling can be more accurate by minimizing the influence of surround suppression as well as the influence of other potential artifacts arising in areas distant to the pRF center. We have recently performed a quantitative comparison between our method and several other methods that directly (*i.e.* before estimating the topography) fit isotropic Gaussian[1], anisotropic Gaussian, and difference of isotropic Gaussians to the pRF[9]. It was found that the topography-based method outperformed these methods with respect to pRF center modeling by achieving higher explained variance of the BOLD signal time series.

Accurate estimation of pRF properties in various areas reveals how they cover the visual field and is important for investigating the functional organization of the visual cortex particularly as it relates to visual perception. Properties such as how pRF size changes with eccentricity[1,10] and pRF center surround organization[9] are well studied in the human literature. The proposed method for estimating the pRF topography results in more accurate pRF parameter modeling and is more likely to reveal unknown regularities, not easily modeled a-priori in the direct parametric models. This approach will be especially suitable for studying pRF organization in patients with visual pathway lesions, for whom pRF structure is not necessarily predictable a-priori. Below is described how to estimate the pRF topography and how to use the topography to model the pRF center.

Protocol

1. Data Acquisition

1. Prepare a stimulus protocol that is effective in eliciting a reliable retinotopic visual response as previously described in Dumoulin and Wandell[1] and Lee *et al.*[2]. However, other well established paradigms are also applicable depending on the specific experimental question to be addressed.
2. Present bar stimuli drifting across the screen sequentially along 8 directions of space, in steps of 45 degrees. Ensure that the motion is in synchrony with scanner frame acquisition (TR ~2 sec) so that the bar moves a step once an fMRI frame starts and stays at the new location until the frame ends.
3. To measure a correct baseline signal, add epochs without bar stimulation[1].
    1. Define a field of view (10 to 15° radius) in visual angle over which the stimulus is presented. Present moving or flickering checkerboard patterns (checker size = 0.94 x 0.94 deg^2, pattern update rate = 250 msec/pattern) within the bar to elicit strong visual responses.
    2. Input the following specific parameters: 8 evenly spaced directions of motion, bar width equal to 1.875 deg, and bars move by half the bar width per frame (2 sec). Additional details can be found in Lee *et al.*[2].
    3. Generate a spot (~0.25°) in the screen center on which the subject's eyes fixate during the experiment. Change color of the spot randomly in time.
4. Scan the brain of a subject in an MRI scanner using a typical echo-planar-imaging (EPI) scan that has 192 frames duration (24 frames in each direction of motion). Repeat the scans 4-8 times to increase signal-to-noise ratio.
5. Set parameters for the EPI sequence as follows: TR = 2 sec, TE = 40 msec, matrix size = 64 x 64, 28 slices, voxel size = 3 x 3 x 3 mm^3, flip angle = 90°, Alternatively, apply sequences with a finer resolution (*e.g.*, 2 x 2 x 2 mm^3) or a short TR (*e.g.*, 1-1.5 sec) covering only the visual cortex[2].
6. Track eye movements with an eyetracker system during functional scans to ensure fixation is maintained to within 1-1.5° of the fixation point.
   NOTE: Here, a head-coordinate based eyetracker in a goggle system is used, but other suitable eyetracker systems can be used instead.
7. Instruct the subjects to fixate the spot on the screen center generated in step 1.3.2. To ensure the subjects are fixating, instruct them to report the color changes of the fixation spot.
8. Obtain anatomical scans, at 1 x 1 x 1 mm^3 resolution (*e.g.*, T1-MPRAGE; TR = 1,900 msec, TE = 2.26 msec, TI = 900 msec, flip angle = 9°, 176 partitions).
   NOTE: These anatomical scans will be used for segmentation as well as for aligning the functional images to the anatomy both within and across scans. For better alignment between functional (EPI) images and the anatomy, obtain also an inplane anatomy scan, with resolution identical to the EPI, using T1-weighted fast spoiled gradient echo (SPGR) sequence[1].

2. Data Pre-processing

NOTE: Prior to estimating pRF properties, several typical fMRI data pre-processing steps are needed, such as head motion correction and alignment of functional volumes to the anatomical scan. In this article, all pre-processing, estimation, analysis and presentation of results obtained are performed using the open source MATLAB-based software toolbox VISTA LAB available on the VISTA software site. http://white.stanford.edu/newlm/index.php/Main_Page.

1. Load the anatomical scan into MATLAB and prepare a volume anatomy using a function called createVolAnat.
2. Segment Gray matter, White matter, and CSF using the function "ItkGray".
3. Prepare functional data by converting DICOM (*i.e.*, raw MRI file format for Siemens) files into NIFTI (*i.e.*, standard functional MRI file format) files, and load data into VISTA using a function called mrInit.
4. Correct head-motion and align functional images to the anatomy loaded in step 2.1 using rxAlign based on an affine matrix transformation.
5. Average functional motion-corrected scans for improving signal-to-noise ratio by clicking mrVISTA Analysis TimeSeries Average tSeries. Exclude from averaging scans during which eye movements deviates from fixation more than 1-1.5°. If signals from different runs have different dc-drifts, average functional scans after removing the dc-drifts.
6. Calculate the mapping coordinates between functional scans and Gray matter and identify corresponding Gray-matter voxels in the functional scans by selecting the following menus: mrVISTA Window Open Gray 3-View Window. Assign BOLD signals in the Gray matter voxels by interpolation, choosing one of the options available in mrVISTA.

3. Estimation of pRF Topography and Parametric Modeling

1. Download the code files through the following link: https://sites.google.com/site/leesangkyun/prf/codes.zip, extract the compressed file and place them in a preferred location of the local computer. Add the path of the folder in MATLAB.
2. Set the stimulus parameters used in the experiment by selecting the following menus: mrVISTA Analysis Retinotopic Model Set Parameters. Specify the following parameters such as stimulus images, the stimulus size, the canonical hemodynamic function, the frame rate of the fMRI scanner.

3. Prior to the pRF estimation, prepare the initial parameter sets (**Figure 1B**).
    1. Set the cross-validation sets in “tprf_set_params.m” from the code files. Divide timeseries into at least two subsets (one set for testing and the remaining sets for training) that are long enough for the bar to sweep the entire stimulus space. Alternatively, without averaging scans in step 2.4, validate scans by leaving out one scan for testing and using the remaining scans for training.
    2. Set a coarse parameter set (λ in **Figure 1**; λ = [10^{-2} 10^{-1} 1 10^{1} 10^{2}]) in “tprf_set_params.m”. Then, set a fine scale range ([0.1 0.3 0.5 0.7 0.9 1 3 5 7 9]) in “tprf_set_params.m”.
    NOTE: The program uses the coarse set to select the λ resulting in the highest explained variance. Then, the program searches the space around the selected λ using the fine scale range, further refining the selection of λ that yields the highest explained variance.
    3. Set a threshold (0.2) of the explained variance for visually responsive voxels in “tprf_set_params.m”.
    NOTE: This threshold is used as the reference for selection of visually responsive voxels. Alternatively, make an ROI for a non-visually responsive region (***e.g.***, by drawing a sphere with a radius of 1 cm in a non-visually responsive brain area), where the threshold can be automatically calculated.
    4. Set a set of thresholds ([0.3, 0.5, 0.7]) for defining the pRF center region in the normalized topography in “tprf_set_params.m” (***i.e.***, [0 to 1] or [-1 to 1] with epochs without bar stimulation in step 1.3.1).
    NOTE: From the set of thresholds the program provided selects the “best” threshold, *i.e.* the threshold that defines a pRF central region for which the pRF center model explains the greatest signal variance. Alternatively, choose a different set of threshold values depending on the characteristics of the topography.

4. Execute “tprf_runpRFest.m” calculate the pRF topography (**Figure 1**) and fit a 2D anisotropic Gaussian. After specifying all parameters described in this protocol, and running the code, obtain the final estimation results.

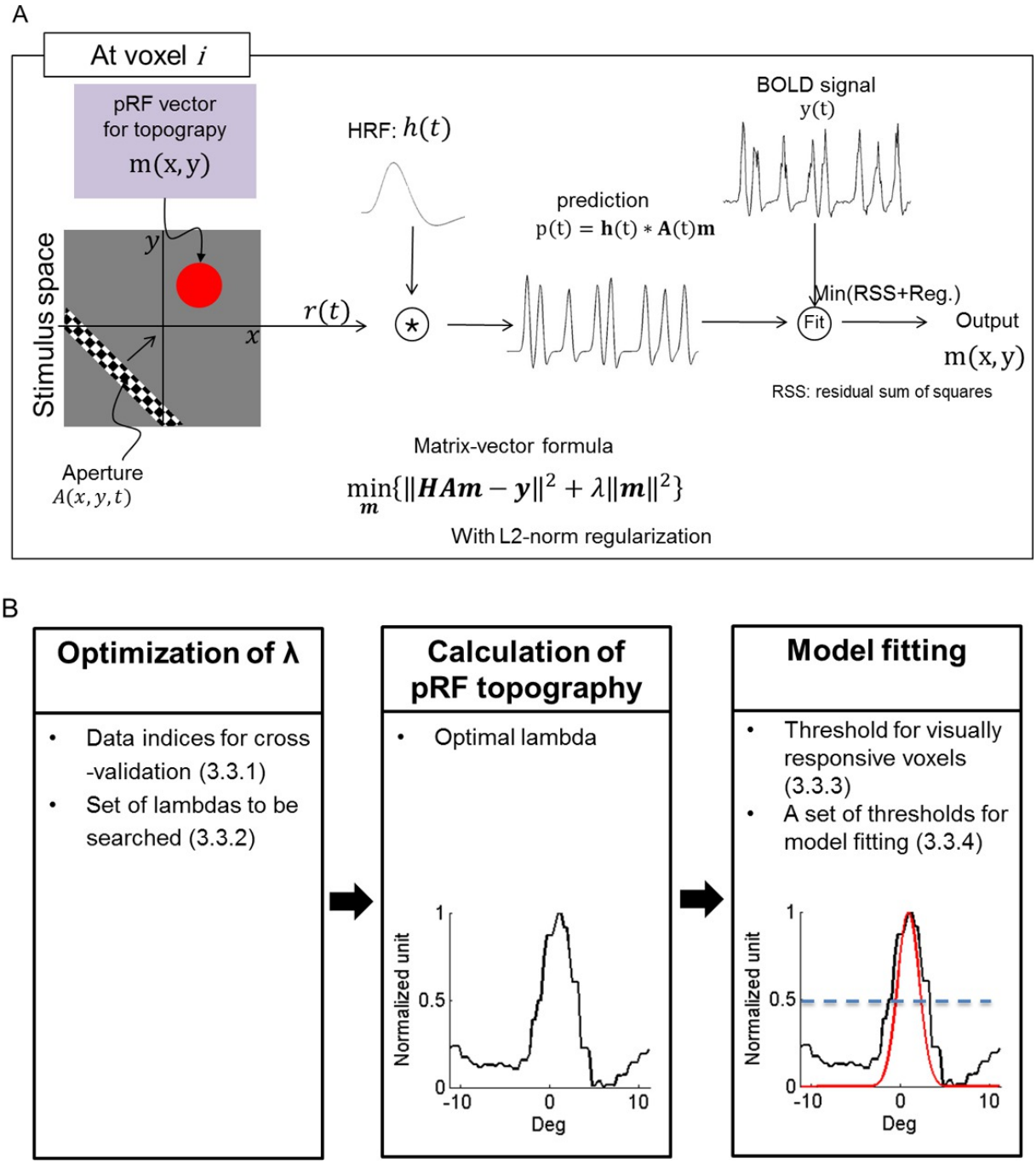

Figure 1: PRF estimation process. (A) Schematic illustration of the process followed for pRF topography estimation. ***h(t)***: hemodynamic response function, ***A(t)***: stimulus, ***m***: pRF, Reg: L2-norm regularization. **(B)** Specific steps for pRF topography estimation and pRF center modeling. The set of parameters required for the estimation is listed in each step. A one-dimensional section of topography and its model are illustrated. Under "Model Fitting", black and red curves represent the topography and its pRF center model with a center threshold of 0.5, respectively. The blue dashed line indicates a threshold for the pRF central region.

Representative Results

Accurate pRF modeling requires capturing pRF shapes correctly. Without knowing the pRF topography, the selection of circularly symmetric models used in prior studies[1,9-11] is a reasonable choice. This is because, if the local retinotopic organization is homogeneous in all directions of

visual field, a local population response could be represented as a circularly symmetric cumulative aggregate of neuronal responses. However, our observations demonstrate that this is not necessarily the case (**Figure 2**). Therefore, observation of the pRF topography can be critical for selecting an appropriate parametric function for a pRF model. This is an advantage of the pRF topography, and so the topography-based models outperform the direct-fit isotropic Gaussian models in pRF center modeling, resulting typically in higher explained variance (**Figure 2**; see Lee *et al.*[2] for additional comparisons with other models). These examples demonstrate the advantage of estimating the pRF topography prior to fitting the model.

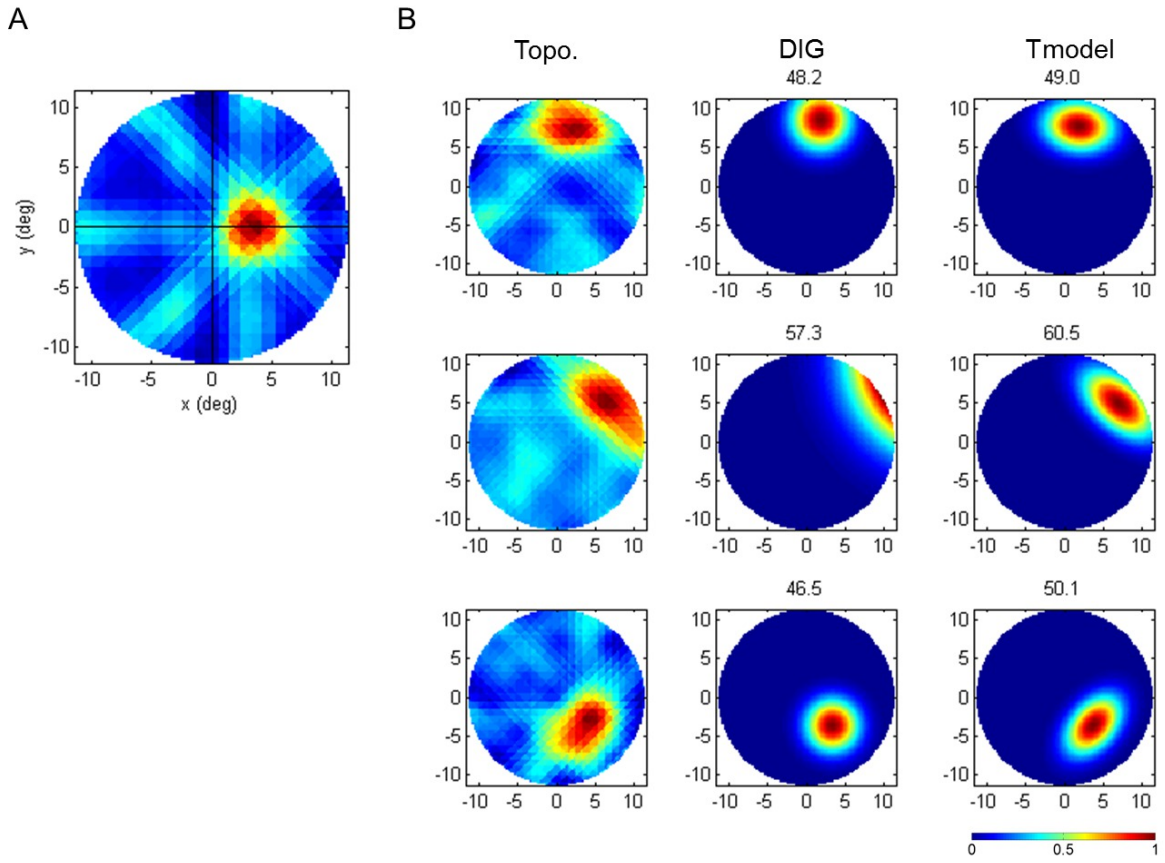

Figure 2: Examples of pRF topography estimation and fit of pRF center models. **(A)** A typical pRF topography. In the topography, red color indicates the most responsive area, which shows the pRF center lying on the middle right horizontal meridian. In the pRF topography, bar patterns across the pRF center structure with low weights are also sometimes observed. This relates to the fact that the area along the bar aperture passing through the pRF center is also stimulated simultaneously with the pRF center. They are easily eliminated in the thresholding step. **(B)** Comparison between a previous method (DIG; direct-fit isotropic Gaussian)[1] and topography-based pRF center model (T-model). The corresponding percent of explained variance is shown above each model. T-models show higher explained variance in all examples, with more accurate pRF shape capture. See Lee *et al.*[2] for more details and additional examples.

One important requirement is to ensure that the fMRI paradigm used provides good retinotopy data. Then the pRF topography method can be used to estimate retinotopic eccentricity and azimuth maps (**Figure 3**). These maps show similar basic retinotopic architecture as previous methods[1,4-7], but they are more accurate because observation of the pRF topography allows us to better separate the pRF center from the surround and from potential noise or artifacts distant to the pRF center. This, among other things, results in better estimation of the retinotopic maps at high eccentricities (a detailed account of the observed differences can be found in Lee *et al.*[2]).

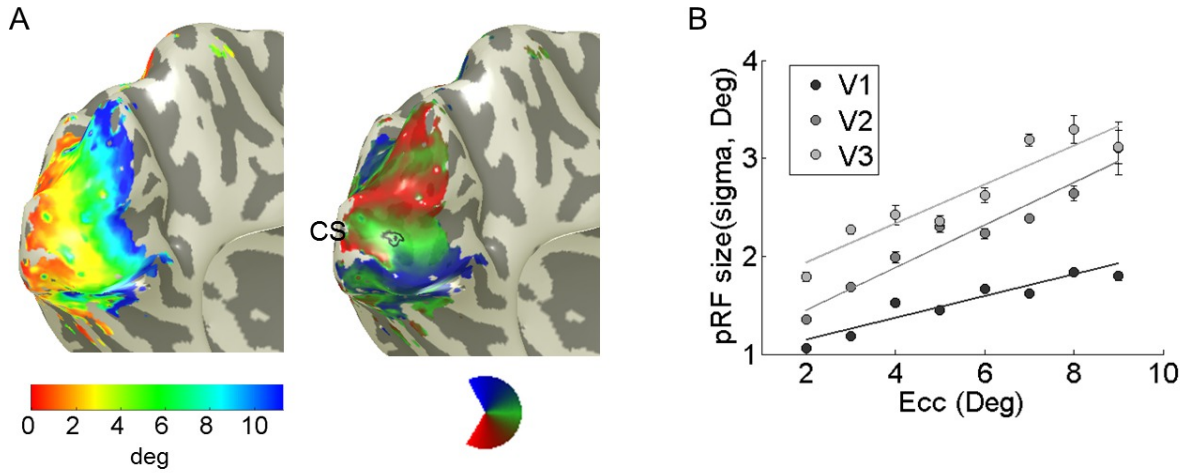

Figure 3: Retinotopic maps and pRF size. **(A)** Eccentricity and Polar angle maps in the left hemisphere of a subject. CS indicates the calcarine sulcus. In the right panel of Figure A, the black circle indicates a region-of-interest (ROI) from which the voxel whose pRF is illustrated in **Figure 4** is taken. **(B)** Relationship between pRF size and eccentricity. The pRF size increases with eccentricity in visual areas V1-3. This plot is drawn from **(A)**.

The topography-based model (T-model) method can be used to estimate various pRF properties such as pRF size, elongation, orientation, and surround suppression efficiently, without having to test many different parametric models. To aid visualization of such properties, a MATLAB function (tprf_plotpRF.m) is provided that plots the pRF topography, the corresponding pRF center model, and their fit to the raw BOLD signal (**Figure 4**). Note that in some cases, pRF properties may also be estimated directly from the topography, eliminating the need for pRF modeling.

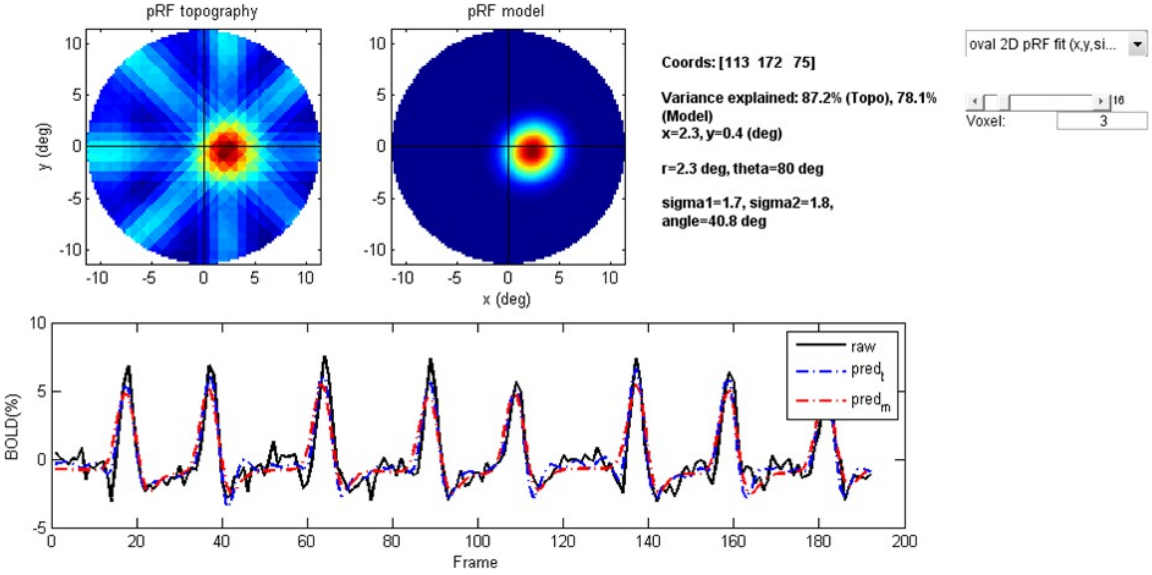

Figure 4: Demonstration of the MATLAB toolbox developed by the authors. This plot shows the pRF topography and corresponding pRF model fit of a voxel selected by a user. The illustrated voxel was selected from the ROI shown in **Figure 3A**. *raw*: actual BOLD response, $pred_t$: prediction with the pRF topography, $pred_m$: prediction with the pRF center parametric model. Please click here to view a larger version of this figure.

Discussion

This article demonstrates how to estimate the topography of visual population receptive fields in human visual cortex and how to use it to select an appropriate parametric model for the receptive field. For a successful retinotopy, an appropriate stimulation protocol and an efficient analysis method should be selected, and the subject's experimental parameters (motion and fixation) should be optimized. Bar stimuli moving sequentially across the visual field are an efficient stimulus paradigm for pRF estimation as it generates distinct BOLD responses from distinct stimulus locations. The provided method constructs the pRF topography. Since the problem of pRF estimation is generally under-determined,

a mathematical tool called ridge regression[3] is used to enforce the reasonable constraint of sparseness on the pRF weight solution. This regularization technique is very effective at estimating the pRF model when the number of observations (time points of the BOLD signal) is considerably smaller than the number of pixels covering the spatial dimension of the stimulus.

This method provides more robust estimation of the pRF center than previous methods. There are several reasons for this: 1) it first segments the pRF central region from the pRF topography and then fits an appropriate model, avoiding potential biases that may influence pRF model fits in direct models (*i.e.* surround suppression or noise artifacts far from the pRF center). 2) Having the ability to inspect the topography visually gives one the opportunity to validate the performance of the final model fit uncovering systematic errors, as well as 3) the possibility to detect features of the pRF structure that may otherwise go undetected. 4) By constraining the fitting area, this model is less likely to map the pRF inside the border of stimulus presentation incorrectly compared to direct fit models (see **Figure 2B**). Nonetheless, a user need be aware that the proposed method also has limitations for accurately capturing pRF shape near the stimulus border. This is due to the fact that near the border the bar stimuli activate partial receptive fields belonging to voxels whose pRF center would ordinarily be outside the stimulus presentation region. Any receptive field mapping method would be subject to this problem and show a relative peak at the border unless it can perfectly extrapolate from the part of the receptive field center that is mapped to the whole. Having said that, our method is more accurate than direct-fitting methods[1,9], which tend to markedly overestimate the distance to the center of pRFs that lie near the stimulus presentation border (see Figures 5 and 6 of Lee *et al.*[2] for more detail).

As discussed, to construct a robust pRF topography depends on the free regularization parameter, λ (**Figure 1)**, which can be optimized separately of individual voxels, or as a common parameter across all voxels. The regularization parameter influences pRF topography by adjusting the extent of fitting (over-fitting or under-fitting) to the data. While a small λ leads to noisy pRF topographies (*i.e.*, over-fitting) compared to the actual pRF, a large λ suppresses visual responses and thus result in more spread topographies than justified by the actual pRF size (*i.e.*, under-fitting). Selection of the optimal lambda is crucial for successful pRF estimation. We estimated λ's in different subsets of data and evaluated these estimates using a cross-validation strategy. This minimizes biases in pRF topography estimation. Potential residual biases are further reduced in the pRF center modeling step, where different topography thresholds are explored to select one that results in the highest explained variance (see Lee *et al.*[2]).

Finally, the topography approach proposed is computationally efficient. The estimation of pRF topographies over all voxels, including finding the optimal regularization parameter λ, takes only a few minutes in a PC environment. Identifying visually unresponsive voxels at this step excludes them from the more computationally demanding step of pRF-center modeling, further improving efficiency. Perhaps more importantly, investigators no longer need to test multiple different pRF models to find one that fits well, since they can be guided in choosing the appropriate model by the pRF topography.

The method demonstrated in this protocol measures population receptive field topography and uses it to guide population receptive field modeling. This approach reduces the bias present in direct population receptive field mapping methods, resulting in more robust and accurate pRF estimates. It also minimizes systematic errors and allows us to study the functional organization of the visual cortex with higher sensitivity. It is particularly applicable in the case of subjects with lesions of the visual pathways, in whom pRF structure may not be easy to anticipate a-priori.

Disclosures

The authors declare that they have no competing financial interests.

Acknowledgements

We thank the VISTA software group (Brian Wandell and associates, at Stanford).

S. S. was supported by McNair 2280403105,NEI R01-EY109272, and NEI R01-EY024019 and as HHMI Early Carrer Award. A. P. and G. K. was supported by the Max-Planck Society, G. K. was supported by the PLASTICISE project of the 7th Framework Programme of the European Commission, Contract no. HEATH-F2-2009-223524.

References

1. Dumoulin, S. O., Wandell, B. A. Population receptive field estimates in human visual cortex. *Neuroimage.* **39**, 647-660 (2008).
2. Lee, S., Papanikolaou, A., Logothetis, N. K., Smirnakis, S. M., Keliris, G. A. A new method for estimating population receptive field topography in visual cortex. *Neuroimage.* **81**, 144-157 (2013).
3. Hastie, T., Tibshirani, R., Friedman, J. H. *The elements of statistical learning : data mining, inference, and prediction.* Springer (2009).
4. Sereno, M. I., *et al.*Borders of multiple visual areas in humans revealed by functional magnetic resonance imaging. *Science.* **268**, 889-893 (1995).
5. Engel, S. A., Glover, G. H., Wandell, B. A. Retinotopic organization in human visual cortex and the spatial precision of functional MRI. *Cereb Cortex.* **7**, 181-192 (1997).
6. Engel, S. A., *et al.*fMRI of human visual cortex. *Nature.* **369**, 525 (1994).
7. DeYoe, E. A., *et al.*Mapping striate and extrastriate visual areas in human cerebral cortex. *Proc Natl Acad Sci U S A.* **93**, 2382-2386 (1996).
8. Greene, C. A., Dumoulin, S. O., Harvey, B. M., Ress, D. Measurement of population receptive fields in human early visual cortex using back-projection tomography. *J Vis.* (2014).
9. Zuiderbaan, W., Harvey, B. M., Dumoulin, S. O. Modeling center-surround configurations in population receptive fields using fMRI. *J Vis.* (2012).
10. Harvey, B. M., Dumoulin, S. O. The relationship between cortical magnification factor and population receptive field size in human visual cortex: constancies in cortical architecture. *J Neurosci.* **31**, 13604-13612 (2011).

11. Haak, K. V., Cornelissen, F. W., Morland, A. B. Population receptive field dynamics in human visual cortex. *PLoS One.* **7**, e37686 (2012).

A.4 "Nonlinear population receptive field changes in human area V5/MT+ of healthy subjects with simulated visual field scotomas" (In review)

Title: Nonlinear population receptive field changes in human area V5/MT+ of healthy subjects with simulated visual field scotomas

Author names and affiliations

Amalia Papanikolaou[a,b,d], Georgios A. Keliris[a,c,f], Sangkyun Lee[b], Nikos K. Logothetis[a,e], Stelios M. Smirnakis[b]

[a]Max Planck Institute for Biological Cybernetics, Spemannstr. 38, 72076 Tuebingen, Germany

[b]Department of Neurology, Baylor College of Medicine, Houston, TX, 77030

[c]Bio-Imaging Lab, University of Antwerp, Universiteitsplein 1, 2610 Wilrijk, Belgium

[d]Graduate School of Neural and Behavioural Sciences, International Max Planck Research School, Tuebingen, Germany

[e]Division of Imaging Science and Biomedical Engineering, University of Manchester, Manchester M13 9PT, UK

[f]Bernstein Center for Computational Neuroscience, Tuebingen, Germany

Corresponding authors:

Amalia Papanikolaou
Max Planck Institute for Biological Cybernetics
Spemannstr. 38, 72076, Tuebingen, Germany
Phone: +49 7071 601 1662
Email: amalia.papanikolaou@tuebingen.mpg.de

Georgios Keliris, PhD
Max Planck Institute for Biological Cybernetics
Spemannstr. 38, 72076, Tuebingen, Germany
Phone: +49 7071 601 695
Email: georgios.keliris@tuebingen.mpg.de

Stelios M. Smirnakis, MD, PhD
Baylor College of Medicine, Department of Neuroscience and Neurology
One Baylor Plaza, Houston, TX, 77030, USA
Tel. +1-713-798-3972
email: ssmirnakis@cns.bcm.edu

Keywords:

fMRI, hV5/MT+, reorganization, artificial scotoma

Abstract

There is extensive controversy over whether the adult visual cortex is able to reorganize following visual field loss (scotoma) as a result of retinal or cortical lesions. Functional magnetic resonance imaging (fMRI) methods provide a useful tool to study the aggregate receptive field properties and assess the capacity of the human visual cortex to reorganize following injury. However, these methods are prone to biases near the boundaries of the scotoma. Retinotopic changes resembling reorganization have been observed in the early visual cortex of normal subjects when the visual stimulus is masked to simulate retinal or cortical scotomas. It is not known how the receptive fields of higher visual areas, like hV5/MT+, are affected by partial stimulus deprivation. We measured population receptive field (pRF) responses in human area V5/MT+ of 5 healthy participants under full stimulation and compared them with responses obtained from the same area while masking the left superior quadrant of the visual field ("artificial scotoma" or AS). We found that pRF estimations in area hV5/MT+ are nonlinearly affected by the AS. Specifically, pRF centers shift towards the AS, while the pRF amplitude increases and the pRF size decreases near the AS border. The observed pRF changes do not reflect reorganization but reveal important properties of normal visual processing under different test-stimulus conditions.

Introduction

An important question is whether the adult visual cortex is able to reorganize in subjects with visual field defects (scotomas) as a result of retinal or cortical lesions. Studies in subjects suffering from macular degeneration or retinal lesions produced controversial results (Kaas et al., 1990, Heinen and Skavenski, 1991, Chino et al., 1992, Gilbert and Wiesel, 1992, Chino et al., 1995, DeAngelis et al., 1995, Schmid et al., 1996, Murakami et al., 1997, Horton and Hocking, 1998, Calford et al., 1999, Sunness et al., 2004, Baker et al., 2005, Smirnakis et al., 2005, Giannikopoulos and Eysel, 2006, Baker et al., 2008, Masuda et al., 2008, Schumacher et al., 2008, Dilks et al., 2009, Wandell and Smirnakis, 2009, Baseler et al., 2011). Similarly, studies on subjects with lesions of the primary visual cortex or the optic radiation remain inconclusive (Eysel and Schmidt-Kastner, 1991, Eysel and Schweigart, 1999, Eysel et al., 1999, Rumpel et al., 2000, Mittmann and Eysel, 2001, Barmashenko et al., 2003, Zepeda et al., 2003, Dilks et al., 2007, Yan et al., 2012, Imbrosci et al., 2013, Papanikolaou et al., 2014).

Interestingly, changes in the retinotopic maps of the early visual cortex have been observed even in normal subjects after masking the visual stimulus to simulate retinal or cortical scotomas. In particular, when the stimulus was masked to simulate a foveal scotoma, population receptive fields (pRFs) representing the scotoma shifted in locations outside the scotoma border and increased in size (Baseler et al., 2011, Haak et al., 2012a). It was suggested that these pRF changes were due to a combination of the position and size scatter of individual receptive fields within a voxel influenced by modulatory feedback signals from extrastriate visual areas (Haak et al., 2012a). However, a recent study suggests that the observed pRF

changes are an artifact of the analysis method and that pRF biases can be eliminated if the masked stimulus is incorporated in the model when estimating the pRF (Binda et al., 2013). It is important to characterize these biases in order to ensure that changes in the retinotopic organization observed in patients are not simply an artifact of model estimation in the context of incomplete stimulus presentation (artificial scotoma).

In addition, presenting a truncated visual stimulus, as is typically done in the artificial scotoma, can have nonlinear effects that can modify receptive field location and size estimates in individual neurons. This is expected to be especially prominent for receptive fields in higher areas, which cover a large portion of the visual field. Area V5/MT+ is of particular interest as it has been shown to be modulated by visual stimuli presented inside the scotoma following lesions of the primary visual cortex (V1) (Bruce et al., 1986, Rodman et al., 1989, Maunsell et al., 1990, Rodman et al., 1990, Girard et al., 1992, Barbur et al., 1993, ffytche et al., 1996, Rosa et al., 2000, Schoenfeld et al., 2002, Morland et al., 2004, Bridge et al., 2010, Schmid et al., 2010) and has been associated with the phenomenon of subconscious visual perception, called "blindsight" (Poppel et al., 1973, Weiskrantz et al., 1974). Visual field maps and population receptive field sizes have been recently characterized for the human hV5/MT+ complex in normals (Amano et al., 2009). However, it is not known how these are affected by partial stimulus presentation.

Here we used a new method, which estimates the population receptive field (pRF) topography in the visual cortex with minimal bias (Lee et al., 2013) to measure pRF changes that occur in area hV5/MT+ of five healthy subjects after masking the stimulus in the left upper quadrant of the visual field ("artificial scotoma" or AS). This simulates a homonymous quadrantanopic scotoma that occurs often as result of partial V1 or optic radiation lesions. We compared responses obtained under the AS condition with simulations obtained from a linear AS model (or LAS model). The LAS model simulates the pRFs under the AS condition based on the actual pRFs derived under the full stimulus condition (pRF_{FF}) assuming that the only effect of the AS is that it does not stimulate the corresponding part of the pRF. This provides a prediction of the expected position and shape of the residual pRFs under the AS. In other words, the LAS model provides an estimation of the pRF changes expected to occur as a result of the truncated stimulus assuming that the pRF linearly integrates the AS (pRF_{LAS}). We found pRF changes in hV5/MT+ under the AS condition (pRF_{AS}) that are significantly different than those obtained with the LAS model suggesting that the pRFs are nonlinearly affected by the truncated stimulus presented. In particular, pRF_{AS} centers shift towards the border of the AS, the pRF_{AS} amplitude increases and the pRF_{AS} size decreases near the border of the AS. In addition, we found significant errors in pRF estimation which extend inside the AS when estimating the pRF topography using the full stimulus instead of the masked stimulus. These erroneous estimates are not due simply to a methodological artifact, but are the result a significant BOLD spread that occurs inside the AS during the presentation of the truncated stimulus. It is important to understand the changes that occur in order to be able to separate them from true reorganization. We undertake this task below.

Materials and Methods

Subjects: Five healthy subjects (S1-S5, 22-65 years old, 1 female) were recruited. All subjects had normal or corrected-to-normal visual acuity. The experiments were approved by the Ethical Committee of the Medical Faculty of the University of Tuebingen.

Data acquisition and preprocessing: Functional and structural MRI experiments were performed at the Max Planck Institute for Biological Cybernetics, Tuebingen, Germany using a 3.0 Tesla high-speed echo-planar imaging device (Trio, Siemens Ltd., Erlargen, Germany) with a quadrature head coil. At least two T1-weighted anatomical volumes were acquired for each subject with a three-dimensional magnetization prepared rapid acquisition gradient echo (T1 MPRAGE scan) and averaged following alignment to increase signal to noise ratio (matrix size= 256×256, voxel size= 1×1×1 mm^3, 176 partitions, flip angle= 9°, TR= 1900 ms, TE= 2.26 ms, TI= 900 ms). Blood oxygen level dependent (BOLD) image volumes were acquired using gradient echo sequences of 28 contiguous 3 mm-thick slices covering the entire brain (repetition time [TR] = 2,000 ms, echo time [TE] = 40 ms, matrix size=64×64, voxel size=3×3×3 mm3, flip angle=90°).

At least 5 functional scans were acquired for each subject, consisting of 195 image volumes, the first 3 of which were discarded. The functional images were corrected for motion in between and within scans (Nestares and Heeger, 2000). The functional images were aligned to the high-resolution anatomical volume using a mutual information method (Maes et al., 1997) where the resampled time series values in the volume are spatially interpolated relative to the nearest functional voxels. All subsequent analysis was performed in the interpolated data. However, we took care that this does not affect the retinotopic maps obtained and the statistical comparisons that are performed, because the interpolation method we used does not distort the generated time series and the comparisons we made were between different groups of subjects rather than between different numbers of voxels. Preprocessing steps were performed in MATLAB using the mrVista toolbox (http://white.stanford.edu/software/).

Stimuli: *Full Field stimulus:* Subjects were presented with moving square-checkerboard bars (100% contrast) through MRI compatible digital goggles (VisuaStim, Resonance Technology Company, Inc, Northridge, CA, USA; 30° horizontal and 22.5° vertical field of view, 800x600 resolution, min luminance = 0.3cd/m2 and max luminance = 12.2cd/m2). The stimulus was presented within a circular aperture with a radius of 11.25° around the fixation point. The bar width was 1.875° and travelled sequentially in 8 different directions, moving by a step half of its size (0.9375°) every image volume acquisition (TR=2 seconds). Stimuli were generated using Psychtoolbox (Brainard, 1997) and an open toolbox (VISTADISP) in MATLAB (The Mathworks, Inc.). The subjects' task was to fixate a small dot in the center of the screen (radius: 0.0375°; 2 pixels) and respond to the color change by pressing a button. The color was changing randomly with a frequency of one every 6.25 seconds. An infrared eye tracker was used to record eye movements inside the scanner (iView XTM, SensoMotoric Instruments GmbH) (Fig. S4). For two of the subjects (S4-S5) the eye movements under the full field stimulus presentation were not recorded due to technical problems. However, they performed a challenging detection task at fixation and their performance was always >95% correct.

AS-stimulus: Subjects were asked to participate for a second session during which an isoluminant mask was placed in the left superior quadrant of the visual field, simulating a left upper quadrantanopia ("artificial scotoma" of AS). All other stimulus' parameters stayed the same. Eye movements were recorded for all subjects under the AS stimulus presentation (Fig. S4B).

Population receptive field topography: We used a recent method developed by Lee and colleagues which estimates the population receptive field (pRF) topography in the visual cortex (Lee et al., 2013). The pRF structure p_i at voxel i is represented by a set of weights which predicts the BOLD signal $d_i(t)$ at voxel i and time t, using the stimulus protocol $s(t)$ and the hemodynamic response function $h(t)$ as $d_i = h(t) * \left(p_i^T s(t)\right) = Kp_i$. The weight vector p is estimated by solving a linear model based on ridge regression with a bias: $J_i = \|y_i - K^+ p_i^+\|^2 + \lambda_1 \|p_i\|^2$ where $K^+ = [K\ 1^{M\times 1}], p_i^+ = [p_i\ \alpha], \alpha$ is a constant value to account for the bias and λ_1 is a free parameter to control the extent to which the least-square function is regularized. The regularization parameter λ_1 is selected after cross validation between different scans for each subject.

PRF topography estimates when subjects were scanned under the AS stimulation were derived in two ways. First, we used the actual AS stimulus as stimulus protocol to predict the BOLD signal. In this case, the lack of stimulus forces the topography weights to be ~0 within the AS area. Using the AS stimulus in the model is a good way to represent complete deprivation of input and allows to make more accurate predictions of the pRFs outside of the AS. Second, we examined the effects of using the full field stimulus as stimulus protocol to model pRFs under the AS condition. A summary of the different methodologies used to derive the pRF topography under different stimulation paradigms is presented in Fig. 1.

In contrast to direct-fit methods (Dumoulin and Wandell, 2008), the method we use does not assume a priori the pRF shape and thus is useful for studies of reorganization where the actual pRF shape cannot be anticipated. We retained only those voxels in the visual area, for which the topography explained more than 12% of the variance. This threshold was set after measuring the mean explained variance in a non-visually responsive area (6% ± 2%) and setting the value of the threshold at 3 standard deviations above the mean.

LAS-model: We compared actual pRF topography estimates derived when the AS is applied to linear expectations arising by the lack of stimulation inside the AS region. To do this, we developed a model that predicts the pRF topography under the AS condition based on the pRF topography estimated under the full stimulus condition (Fig. 1B). Briefly, the pRF topography of each voxel with variance explained above 12%, as estimated under full stimulation, is convolved with the AS stimulus. In this way the part of the pRF overlapping with the AS area is omitted. The product of the convolution is used to re-estimate the topography. The regularization parameter used to estimate the AS-prediction topography was set to be ¾ of the regularization parameter under the full stimulus condition because the stimulus space under the AS is ¾ of the stimulus space under full stimulation (Poppel et al., 1973). Using a regularization parameter same as in the full field stimulus condition did not affect the results presented here.

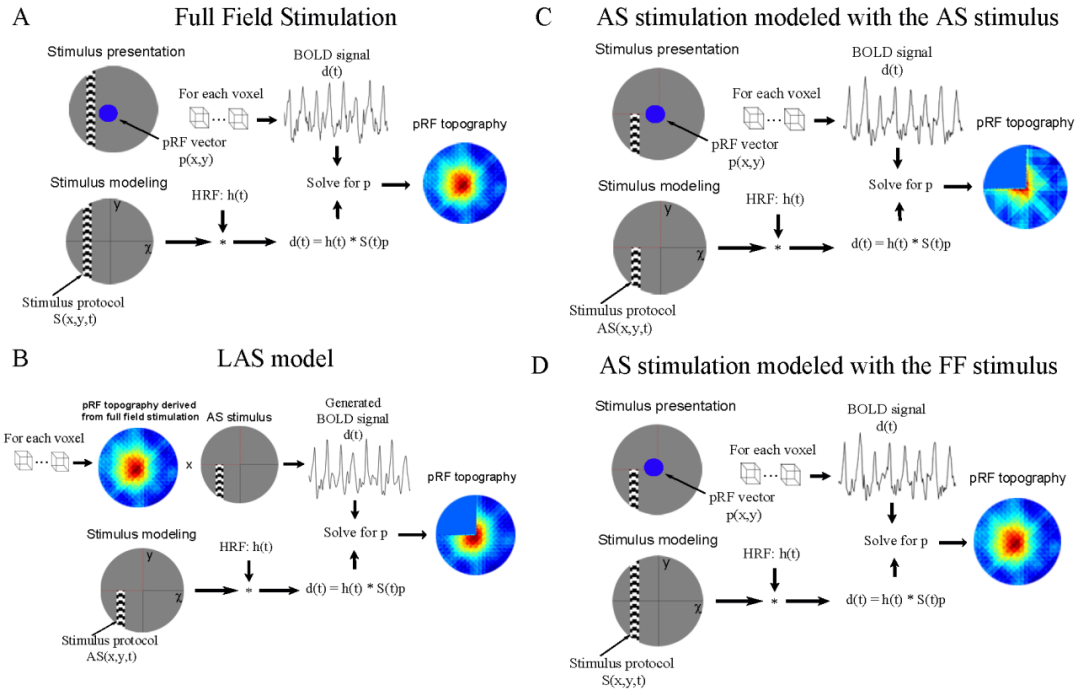

Fig. 1: PRF topography derived under different stimulation and modeling conditions. (A) A schematic illustration of the process followed to estimate the pRF topography under full field stimulation (pRF_{FF}). Subjects are presented with moving bars covering the full visual field. The BOLD signal of each voxel is predicted using the full field stimulus protocol and the hrf to derive the pRF topography as described in the methods section. **(B)** The pRF topography derived under the full field stimulation (A) is convolved with the AS stimulus to generate BOLD time series that simulate the expected BOLD signal under the AS condition assuming that the pRF linearly integrates the AS stimulus. The generated BOLD signal is then used to re-estimated the pRF topography using the AS stimulus protocol in the model (pRF_{LAS}). The border of the AS is indicated by red dashed lines. **(C)** The process followed to derive the pRF topography under AS stimulation using the AS stimulus in the model (pRF_{AS}). **(D)** The process followed to derive the pRF topography under AS stimulation using the full field stimulus in the model.

PRF center, size and amplitude estimates: Because pRFs near the border of the AS may not have a circular shape we could not fit a Gaussian model to get an estimate of the pRF center and size. Instead we used the topography directly to get eccentricity and polar angle values corresponding to the center of the pRF as well as an estimate of the pRF size.

To do so, the pRF topography of each visually responsive voxel is normalized to range between 0 and 1. A lower threshold of 0.4 is applied to the pRF topography in order to keep only the central region of the pRF. This threshold was selected after calculating the average amplitude (0.3±0.1) in non-visually responsive areas (i.e. areas of the far ipsilateral visual field) and setting the value of the threshold at 1 standard deviation above the mean. This was calculated by

averaging the pRF topography amplitude in visual field locations with eccentricity greater than 7° in the ipsilateral visual field of V1, where the stimulus can produce no response. If there are more than one disconnected peaks of activity in the topography, then we keep only the one that covers the largest area in the topography. This way small peaks of activity that may be the result of noise are discarded. The thresholded topography is then converted to a binary image by replacing all values above threshold to value 1 and all other pixels with value 0. The pRF center is estimated by finding the center of mass of the binary image (centroid of all pixels with value 1). This gives us the corresponding elevation and azimuth coordinates which can also be translated to the respective eccentricity and polar angle. We also calculated the center mass of the original image and confirmed that binarizing does not affect the results.

The pRF size is estimated as the area of the topography that lies above the 0.4 threshold. That is the number of pixels with value 1 in the binary image calculated as described above. This gives us an estimate of the area of the visual field that activates the corresponding voxel. Using different thresholds to estimate the pRF does not change the main results presented in this paper.

The pRF amplitude of each voxel is estimated as the peak amplitude of the pRF topography before normalization.

Visual Field coverage maps: The visual field coverage maps define the locations within the visual field that evoke a significant response from voxels within a region of interest (ROI) in the cortex. To estimate this we plot at each visual field location the maximum value between all pRF topographies that cover this location (color map). The pRF topography of each voxel is normalized, thresholded and all peaks of noise are discarded as described above. Using different thresholds for the pRF does not change the conclusions presented in the paper (Fig. S1). The pRF centers (estimated from the pRF topography as described above) across all voxels within the ROI are overlaid as grey dots.

Deconvolution of the BOLD signal: A deconvolution method was applied to the BOLD time series of each voxel in order to estimate the actual response of the voxel as the stimulus is presented at each visual field location. To do so, the BOLD time series of each voxel was averaged across scans to reduce the signal to noise ratio. The averaged signal was further smoothed using locally weighted linear regression (lowess method in MATLAB) in order to avoid outliers that can be amplified after deconvolution. Then a Fast Fourier transform deconvolution is applied to extract the hemodynamic response function from the data.

The baseline was calculated for each voxel as the average BOLD signal change over 5 steps of the bar when the horizontal bar was located between 7-10° in the hemifield ipsilateral to our ROI. After deconvolution and removal of the baseline, the BOLD time series is averaged over all voxels in the ROI and plotted as a function of the bar location.

Significance Tests: A two-sample Kolmogorov-Smirnov test was performed in order to compare the pRF center location and size distributions between the AS condition and the LAS-model. The significance level selected to reject the NULL hypothesis (same distributions) was estimated by comparing the distribution of each subject with the average distribution for each condition. The minimum p-value of these comparisons was then used to test for significance between the

mean distribution of the AS condition and the LAS model. We note that this is a conservative choice, and may suppress the identification of small differences.

Direct-fit pRF method: To compare with prior literature, we also derived pRF estimates using a direct-fit pRF method (Dumoulin and Wandell, 2008). In this case, the implementation of the pRF model is a circularly symmetric Gaussian receptive field in visual space, whose center and radius are estimated by fitting the BOLD signal responses to estimated responses elicited by convolving the model with the moving bar stimuli. We estimated visual field coverage maps by plotting the pRF centers across all voxels within each area (grey dots, Fig. 8a) and the relative pRF size by fitting a 2D Gaussian with peak amplitude normalized to one. The color map is estimated by plotting at each visual field location the maximum normalized pRF amplitude between all Gaussian shaped pRFs that cover this location.

Results

pRF changes in the hemisphere contralateral to the artificial scotoma

We measured pRF responses in right area hV5/MT+ of 5 subjects under full stimulation and after masking the left superior quadrant of the visual field ("artificial scotoma" or AS), thereby simulating a left upper quadrantanopia (methods).

Changes in the size and phase maps of activated area hV5/MT+

We measured visual responsiveness in area hV5/MT+ by the number of voxels whose pRF topography explains above 12% of the variance in the BOLD data. This threshold was set after calculating the mean explained variance in regions of interest that correspond to non-visually responsive voxels (6%, standard deviation 2%) and setting it at 3 standard deviations above the mean. Using this criterion, we found that only ~12% of voxels become unresponsive when the AS is applied. The mean size of area hV5/MT+ under the full stimulus condition is 1379 ± 156 mm^2 (mean ± standard error of the mean, N = 5 subjects) and decreases slightly under the AS condition to 1202 ± 144 mm^2. This is in contrast to area V1, whose visually responsive area is reduced by approximately 36% in the presence of the AS (2250 ± 356 mm^2 under the full stimulus condition versus 1420 ± 88 mm^2 under the AS condition). Since voxels in area hV5/MT+ have considerably larger pRF size than voxels in area V1 (Smith et al., 2001), more hV5/MT+ voxels can be activated by parts of the stimulus that fall outside the AS area, partially explaining this disparity. A signature of this is a shift of hV5/MT+ voxel pRF centers to reflect locations outside the AS. Accordingly, the angular map shows that a relatively small number of voxels (16%) with centers inside the superior visual field quadrant (e.g. inside the AS) become unresponsive after the AS stimulus is applied (Fig. 3A.b; magenta). The remaining voxels (84%) shift their pRF centers towards the blue color that corresponds to the lower visual field quadrant (Fig. 3A.b). PRF location shifts outside of the AS are expected if we assume we are mapping the residual part of the pRFs that falls outside of the AS.

To differentiate between pRF changes that are expected as a result of stimulating only a part of the receptive field versus unexpected pRF changes under the AS condition, we compared pRF responses obtained under the AS condition with estimates obtained from a model which

simulates the pRF topography expected under the AS condition based on the actual pRF topography derived under the full stimulus condition. To do so, the topography of each voxel in hV5/MT+ as estimated under the full stimulus condition is convolved with the AS stimulus. This way, the part of the pRF_{FF} which overlaps with the AS is omitted and does not contribute in the estimation. The output of the convolution is then used as data set to re-estimate the pRF topography (Fig. 1B). The new topography estimate is derived by using the AS stimulus in the model. This results in a prediction of the expected position and shape of the residual pRFs under the assumption that the only effect of the AS is that it does not stimulate the corresponding part of the pRF topography (as derived by the full field stimulus). This pRF estimate is referred to as the Linear Artificial Scotoma model or "LAS" (Fig. 1B; see methods), and is denoted pRF_{LAS}. We used the AS stimulus paradigm to estimate the pRF topography for both data derived from the LAS model (Fig. 1B; pRF_{LAS}) and from the actual AS stimulation condition (Fig. 1C; pRF_{AS}). We reasoned that using the AS stimulus in the model is a good way to represent complete deprivation of input as in the normal subjects with AS stimulus we use here or patients with retinal lesions. The effects of using the full-field stimulus in the model are presented in a later section.

As expected, the LAS model properly captures the residual part of a pRF_{FF} which lies outside the AS (Fig. 2b). The part of the pRF which overlaps with the AS is omitted resulting in a decrease of the pRF_{LAS} size and a shift of the pRF_{LAS} center away from the AS (red dashed circle; Fig. 2b bottom). We would expect to see the same pRF changes under the AS condition assuming that the pRF linearly integrates the AS. However, pRFs estimated under the AS condition (pRF_{AS}) appear to be smaller in size and shift closer to the border of the AS (magenta dashed circle; Fig. 2c bottom) compared with the predictions of the LAS model (pRF_{LAS}), suggesting that the truncated stimulus exerts a nonlinear effect.

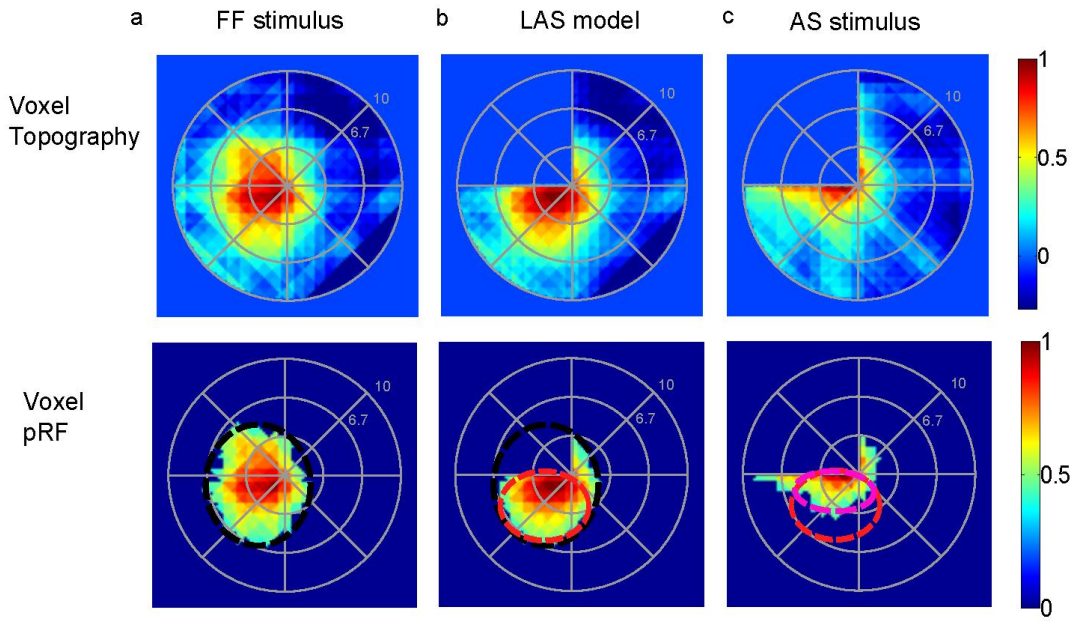

Fig. 2: pRF topographies of a voxel in right hV5/MT+ partly covered by the AS. Top row: **(a)** pRF topography of one voxel in hV5/MT+ under the full field stimulus condition (pRF_{FF}). The pRF covers locations both in the left upper and lower quadrants. **(b)** pRF topography of the same voxel under the Linear-AS model (pRF_{LAS}). In brief, from the topography of the full field stimulus pRF_{FF}, the part of the pRF falling within the AS area is omitted by convolving the pRF_{FF} with the AS stimulus. The result of the convolution is then used to re-estimate the topography using the AS stimulus at this case, deriving the pRF_{LAS}. In this case only of the part of the pRF which falls outside of the AS area is mapped. This gives us an estimate of the expected pRF topography under the AS condition, assuming linearity. **(c)** pRF topography of the same voxel under the AS condition (pRF_{AS}). The pRF_{AS} looks different than it would be expected based on the LAS model (pRF_{LAS}). The pRF_{AS} topography seems to have shifted towards the AS-border. Bottom row: The pRF topographies of the same voxel are presented under the different stimulation conditions after thresholding at 0.4 of the maximum value. By thresholding we derive only the central area of the pRF, useful for estimating the pRF center location and pRF size. The black, red, and magenta circles indicate the visual field area covered by the pRF under the full field stimulus condition, under the LAS model and under the AS condition respectively. These do not represent model fits but they are manually drawn for illustration purposes.

Topography and coverage maps

We examined how all pRFs in hV5/MT+ cover the visual field under the different stimulation conditions by plotting the visual field coverage maps from all hV5/MT+ voxels (Amano et al., 2009). These maps are estimated by deriving appropriately normalized pRFs from the topography of each voxel (Fig. S1B) and plotting the maximum pRF amplitude at each visual field location of all the pRFs that cover this location (methods). No activity is predicted in the upper visual field quadrant where the AS is placed for both the LAS model and the AS stimulation condition, since the lack of stimulus forces the topography weights to be ~0 in that area (Fig. 3B.b,c). Area hV5/MT+ under the LAS model covers the lower visual field quadrant as expected (Fig. 3B.b). The visual field coverage of hV5/MT+ under the AS-stimulus condition, however, shows a clustering of pRF centers near the border of the AS (Fig. 3B.c). This results from the fact that pRF centers under the AS condition appear to be smaller in size and shift closer to the border of the AS as shown by the topography of individual voxels (Fig. 2 and Fig. S1A-B). In addition, visual field locations in the inferior quadrant, away of the AS border, appear to be less well covered by the contralateral hV5/MT+ (Fig. 3B.c top, Fig. S1.C-D) relative to the prediction of the LAS model (Fig. 3B.b top, Fig. S1.C-D) as a result of the pRF location shift and the reduction in the pRF size. This also contrasts with the complete visual field coverage of the inferior quadrant seen in the contralateral area V1 (Fig. 3B.c_bottom) suggesting that the observed effect is the result of post-V1 processing. The shift in pRF center location under the AS condition is mainly observed for pRFs in hV5/MT+ that are partly covered by the AS and suggests a nonlinear effect of the truncated stimulus in modulating the pRF of these voxels. PRFs in area V1 are generally smaller than pRFs in area hV5/MT+ and thus less affected by the truncated stimulus.

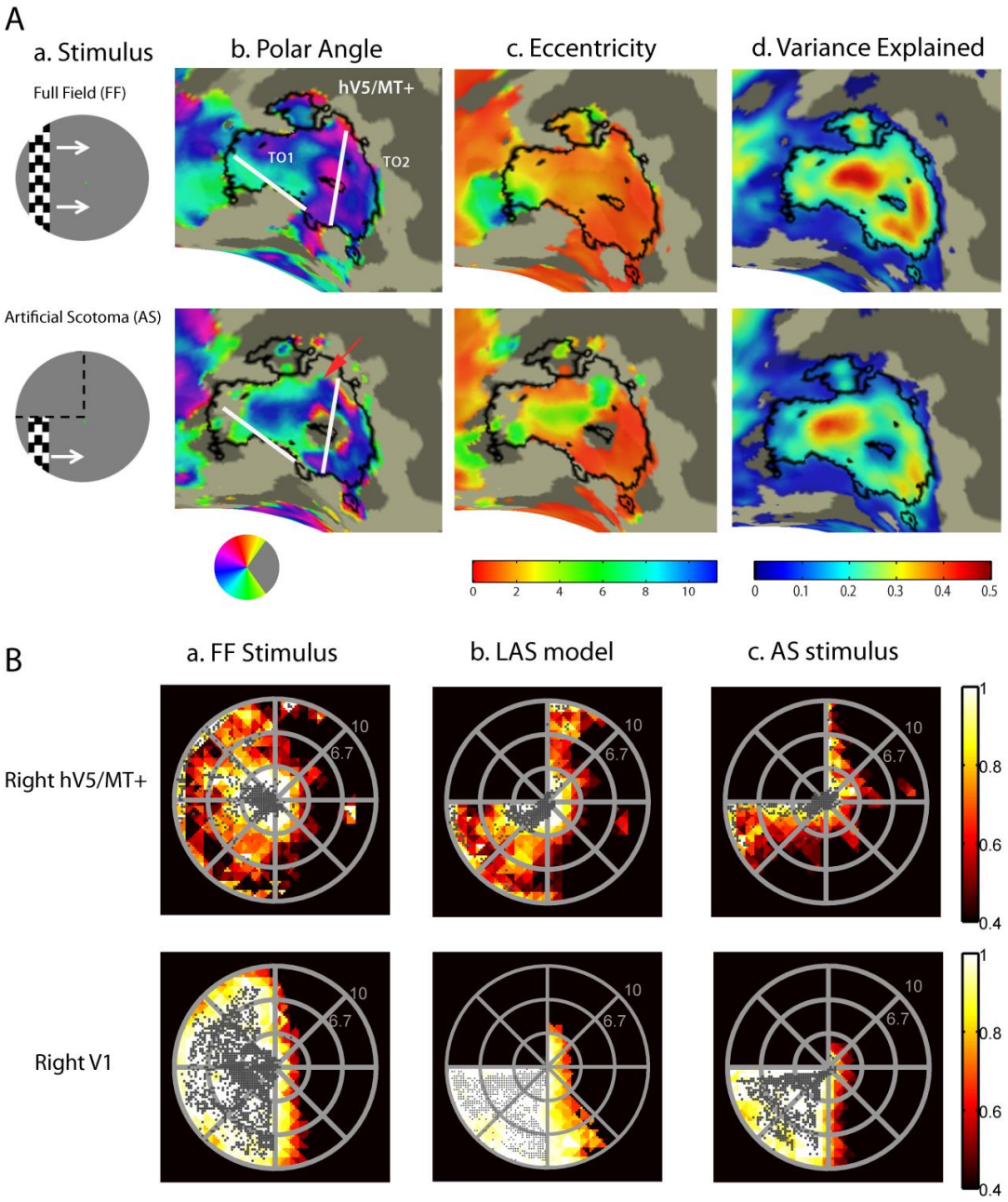

Fig. 3: Retinotopy and visual field coverage maps of area hV5/MT+. (A.a) A snapshot of the stimulus for the vertical bar excursion under the full field (FF) stimulation (top) and when and artificial scotoma (AS) is placed on the upper left quadrant (bottom). White arrows (top) indicate the bar direction of motion and black dotted lines (bottom) the location of the AS. **(A.b-d)** Polar angle (b), eccentricity (c) and variance explained (d) maps overlaid on the inflated right occipito-temporal region of a subject under the full stimulus condition (top) versus the AS condition (bottom). Angular and eccentricity color maps indicate the visual field angle and

eccentricity of the center of the pRF topography respectively, at each cortical location. Significantly activated voxels (explained variance > 12%) of area hV5/MT+ under the full stimulus condition are selected and overlaid on the maps as a black-bordered ROI. Areas TO1 and TO2 could be identified as described in (Amano et al., 2009) and are shown here on the angular maps. We use the whole area hV5/MT+ for the subsequent analysis. A small part of area hV5/MT+ with voxels devoted to the superior visual field quadrant (magenta color on the angular map; A.b top) become unresponsive under the AS stimulation condition (A.b bottom). A larger fraction of pRFs with blue/cyan color, corresponding to the lower visual field quadrant, are observed on the angular map under the AS condition compared to the full stimulus condition (red arrow). This suggests that, as expected, under the AS condition some pRFs shift their locations to the lower quadrant where stimulus is present. **(B)** ***Top:*** Visual field (VF) coverage maps of area hV5/MT+ (top) from a subject (S1) under the full stimulus condition (a) under the LAS model (b) and under the actual AS condition (c). The color map indicates the maximum pRF amplitude of the topography (after appropriately thresholding and normalizing, see methods) at each visual field location of all the pRFs that cover this location. The pRF centers across all voxels within the area of interest are overlaid as gray dots. The visual field coverage of right hV5/MT+ under the full stimulus condition (top left) largely covers the contralateral hemifield. The visual field coverage of hV5/MT+ under the AS stimulus condition (c) shows a clustering of pRF centers near the border of the AS. Note that it differs from the coverage expected based on the LAS model (b) or the visual field coverage of V1 (c bottom). This suggests that the truncated stimulus has a nonlinear effect in modulating the response of hV5/MT+ voxels, leading to pRF profiles that concentrate near the AS border. Visual field coverage maps of the remaining subjects are shown in Fig. S2. ***Bottom***: the visual field coverage of area V1 under the full stimulus condition (a) under the LAS model (b) and under the AS condition (c) is shown for comparison. We found no significant difference between the pRFs derived under the AS stimulus condition and after applying the LAS model in area V1 (Fig. S3a). Nonlinear effects of the truncated stimulus are less prominent (not seen) here, likely because of the smaller V1 receptive field size.

PRF center location and size shifts

To summarize the findings for all subjects we compared the distribution of pRF_{AS} center elevation (distance from the horizontal meridian) for subjects under the AS condition with the expected pRF_{LAS} center elevation distribution based on the LAS model, in the hV5/MT+ contralateral to AS hemisphere. As expected pRF centers that belong to the superior visual field quadrant (elevation > 0) under full stimulation, shift their location towards the lower visual field quadrant both in the case of the AS condition and the LAS model (elevation < 0, Fig. 4a right). This shift, however, is significantly different for the AS condition with pRF_{AS} centers clustering near the AS border (elevation = 0, gray bars) compared to the expected distribution based on the LAS model (white bars, Fig. 4a right; $p = 10^{-87} < 10^{-51}$, Kolmogorov-Smirnov test, significance is reported as p = a < b, where b is the value selected to reject the NULL hypothesis; see methods). PRF centers that belong in the inferior visual field quadrant (elevation < 0) under full stimulation also shift their location towards the AS-border when the AS is applied (Fig. 4a left). Note the greater clustering of pRF_{AS} centers near the AS-border (elevation = 0) for the AS condition (gray bars, Fig. 4a left) compared to the LAS model (white bars). The distributions are

significantly different ($p \approx 0 < 10^{-27}$). For both quadrants, the differences were significant not only for the aggregate distributions but also for each individual subject (Table S1). Note that there is no significant difference in the pRF center elevation distribution of the inferior quadrant between the pRFs derived under the full bar stimulation and after applying the LAS model (Fig. S3b, $p = 10^{-19} > 10^{-32}$) suggesting that the observed differences under the AS condition are not the result of a methodological error.

In addition, we observed a large decrease in pRF size in the presence of the AS. PRFs in the superior quadrant had a mean pRF size decrease of 44 ± 2.3% (mean ± standard error of the mean, N = 5 subjects), significantly larger than the expected pRF size decrease based on the LAS model (27 ± 1.9%, Fig. 4b right; $p = 10^{-4}$, two sample t-test). PRFs in the inferior quadrant also had a decrease in pRF size of 35 ± 5.4% significantly larger than the smaller decrease expected from the LAS model (14 ± 2%, Fig. 4b left; $p = 10^{-3}$, two sample t-test). A significant difference was observed between the mean of the pRF size distribution under the AS condition versus the LAS model, both for pRFs in the superior ($p = 10^{-135} < 10^{-8}$, Kolmogorov-Smirnov test) and inferior ($p \approx 0 < 10^{-32}$) quadrants (Fig. S3c).

The change in location and size of the pRFs under the AS condition was also associated with an increase of pRF amplitude near the AS-border. We measured the peak amplitude of the pRF topography as a function of distance from the AS-border averaged over all 5 subjects. We found that the pRF amplitude is significantly increased under the AS condition near the AS-border and within 1° from it compared with both the LAS model and the full stimulus condition ($p=10^{-3} < 10^{-2}$ at 1° elevation while $p = 0.32 > 10^{-2}$ at 3° elevation, two sample t-test; Fig. 4c left). The increase occurs across the whole range of eccentricities for the pRFs that are within 1° from AS-border (Fig. 4c right).

The differences between the LAS model and the AS condition cannot be explained by eye movements. Subjects were able to maintain fixation within 1.5° radius from the center of fixation for scans both under the full field stimulus condition and under the AS stimulus condition except for very occasional excursions beyond this range (Fig. 5a). The results remain unchanged after removing from the analysis the epochs where the subjects had eye deviations (>1.5°) from the fixation point. In addition, a pRF shift towards a specific direction in the visual field (AS border), would require systematic eye movements towards the opposite direction. However, the distributions of eye position with respect to the azimuth and elevation of the visual field are similar for both sessions under the full stimulus condition (LAS model) and under the AS condition (Fig. 5b) suggesting that even small deviations from the fixation point cannot explain the observed findings (Kolmogorov-Smirnov test, $p = 0.55$ for the azimuth distributions and $p = 0.77$ for the elevation distributions).

In summary, we observed a shift of the pRF centers towards the AS-border when the stimulus is excluded from the upper left quadrant of the visual field (AS-condition). The shift was associated with a relative increase in pRF amplitude near the AS-border and a decrease in pRF size. This suggests that using a truncated stimulus can reveal nonlinear aspects of receptive field summation that could be mistaken for reorganization in the appropriate context.

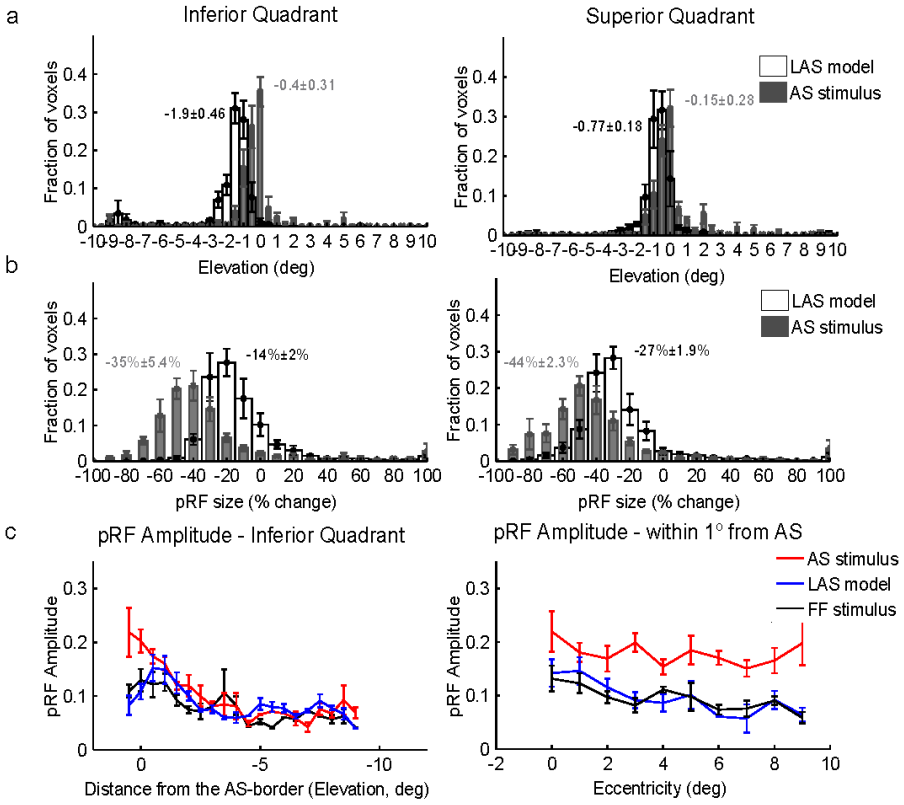

Fig. 4: PRF location, size and amplitude changes in contralateral hV5/MT+ under the AS stimulus condition. (a) Average distributions of the pRF center elevation from voxels in hV5/MT+ of 5 subjects under the AS condition (gray bars) and under the LAS model (white bars). The voxels are divided into two groups according to their pRF center location as estimated from the full field stimulus condition, one for pRFs in the inferior quadrant (left) and one for pRFs at the superior quadrant (right). PRFs originally located in the left superior quadrant (where the AS is applied; see right panel) shift towards the lower quadrant (negative values) in both the LAS model and the AS stimulus condition. The shift observed for the pRF centers under the AS condition however is smaller than expected based on the LAS model and seems to cluster more near the AS-border (elevation = 0). PRFs with centers in the inferior quadrant also shift their location towards the AS-border in the presence of the AS, in contrast to the LAS model (left panel). The mean distributions are significantly different for pRFs both in the superior ($p = 10^{-50} < 10^{-44}$) and inferior ($p = 0 < 10^{-31}$) quadrants. The mean and standard error of the mean of each distribution is indicated on top of the graphs with gray color for the AS stimulus and black color for the LAS model. **(b)** Average distributions of the percent change in pRF size for the LAS model (white bars) versus the AS stimulus condition (gray bars). The change in pRF size is calculated as the difference between the pRF size under the AS condition (or under the LAS model) and the pRF size of the same voxels under the full stimulus condition, normalized by the pRF size under the full stimulus condition (see methods). When the AS is applied we have a significantly larger decrease in pRF size than expected based on the LAS-model. This is true for voxels with pRF centers in either the superior (AS; right panel) or inferior

(left panel) quadrants. **(c)** ***Left:*** Average pRF topography amplitude in the right (contralateral to the scotoma) hV5/MT+ of 5 subjects under the full stimulus (FF) condition (black), the LAS model (blue) and the AS condition (red) as a function of distance from the AS-border (pRF elevation, left panel). The pRF amplitude is larger within one degree from the AS-border when the AS is applied compared with the LAS model and the full stimulus condition. ***Right:*** Average pRF topography amplitude of voxels in the right hV5/MT+ with pRF centers located within 1 degree from the AS-border (-1° to 0° elevation), as a function of eccentricity. The pRF amplitude is larger across the whole range of eccentricities in the AS-condition (red) compared with the LAS model (blue) and the full stimulus condition (black). For all graphs, the error bars indicate the standard error of the mean across subjects (N = 5).

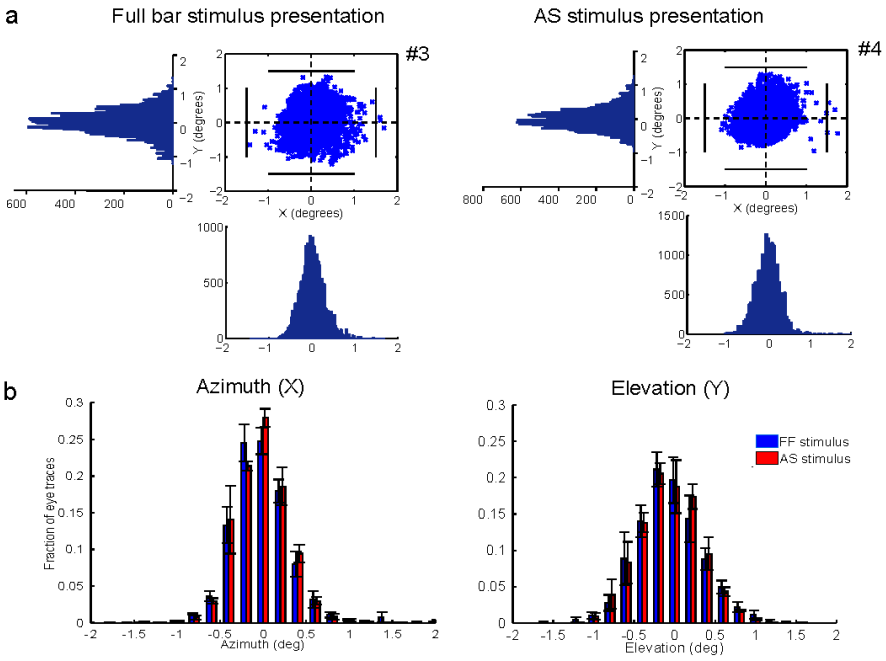

Fig. 5: Eye positions for different stimulus presentations. (a) Eye movements of one control subject (S1) under the full field stimulus presentation (left) and under the AS stimulus presentation (right). Eye positions plotted at 60Hz for one whole session (6.4 min). The number of eye deviations, defined as excursions > 1.5° from the fixation point is indicated next to the graphs with the number sign (#). The eye movements for all subjects are shown in Fig. S4. **(b)** Average fraction of eye traces with respect to the azimuth (left) and elevation (right) for the full field stimulus presentation (blue bars) and the AS stimulus presentation (red bars) for 3/5 control subjects. Two of the subjects (S4 and S5) were excluded as their eye movements under the full field stimulus presentation were not recorded. However, their eye movements were recorded under the AS assuring that the subjects were able to maintain fixation (Fig. S4B). The error bars indicate the standard error of the mean across subjects (N = 3). The distributions are

not significantly different between conditions ($p = 0.55$ for the azimuth distributions and $p = 0.77$ for the elevation distributions) suggesting that the pRF changes seen in Fig. 4 are not the result of eye movements.

pRF changes in the hemisphere ipsilateral to the artificial scotoma

Visual deprivation of one quadrant in the visual field may potentially induce changes in the location, shape and amplitude of pRFs in the ipsilateral hV5/MT+ that have ipsilateral or bilateral responses. We found that ~12% ± 7% (mean ± standard error of the mean, N = 5) of voxels become unresponsive in the ipsilateral (left) hemisphere under the AS condition (stimulus exclusion from the left upper visual field quadrant). The mean size of area hV5/MT+ in the left hemisphere was found to be 1360 ± 236 mm^2 (mean ± standard error of the mean, N = 5 subjects), falling to 1151 ± 159 mm^2 under the AS condition. As expected, the visual field coverage maps of area hV5/MT+ of the left hemisphere, both under full field stimulation or under the LAS model, span the contralateral hemifield (Fig. 6a). Surprisingly, the visual field coverage under the AS condition showed a displacement of the pRF centers towards the superior quadrant (dots in Fig. 6a right). The displacement occurred mainly for pRF centers originally located in the inferior quadrant (Fig. 6b left). The average distribution of pRF center elevation shows a significant shift of the pRF centers towards the superior quadrant (elevation > 0) under the AS condition (Fig. 6b; $p \approx 0 < 10^{-20}$). The effect was also significant for each individual subject (Table S1). No significant shift was observed for the average elevation distribution of pRFs originally located in the superior quadrant (Fig. 6b right; $p = 10^{-20} > 10^{-21}$). However, there was a significant shift in the pRF center azimuth (distance from the vertical meridian) distributions towards the vertical meridian (azimuth = 0) for both the inferior ($p = 10^{-244} < 10^{-56}$) and superior quadrants ($p = 10^{-199} < 10^{-32}$; Fig. 6c) suggesting that the pRF centers of both the superior and inferior quadrants in ipsilateral hV5/MT+ shift their location towards the vertical border of the scotoma.

There was a significant decrease in pRF_{AS} size of ~28% in both quadrants (28 ± 5% for the superior quadrant and 27 ± 5% for the inferior quadrant, $p = 10^{-5}$, two sample t-test; Fig. 6d) compared to the relatively small decrease expected from the LAS model (4.8 ± 6% for the superior quadrant and 1.3 ± 2% for the inferior quadrant).

Furthermore, we observed a significantly increased pRF amplitude under the AS condition for pRFs in the superior quadrant ($p = 10^{-3} < 10^{-2}$ at 1° elevation, two sample t-test; Fig. 6e left). PRFs under the AS scotoma in the inferior quadrant had a pRF amplitude similar to the full stimulus condition ($p = 0.3 > 10^{-2}$ at -2° elevation; Fig. 6e left). The increase in the superior quadrant occurred mainly for pRFs near the vertical meridian which is the vertical border of the AS and within 1° from AS (Fig. 6e right) similar to the increase observed in the horizontal border of the AS in the contralateral hV5/MT+ (Fig. 4c left). The mean amplitude of AS pRFs at 1° azimuth was significantly larger compared with the full field stimulus pRFs ($p = 10^{-3} < 10^{-2}$; Fig. 6e right). PRFs away from the AS vertical border did not have a significant increase in the pRF amplitude ($p = 0.48 > 10^{-2}$ at -4° azimuth; Fig. 6e right). This suggests that pRFs in ipsilateral hV5/MT+ are also subject to nonlinear influences from the truncated stimulus even though it is presented in the ipsilateral hemifield.

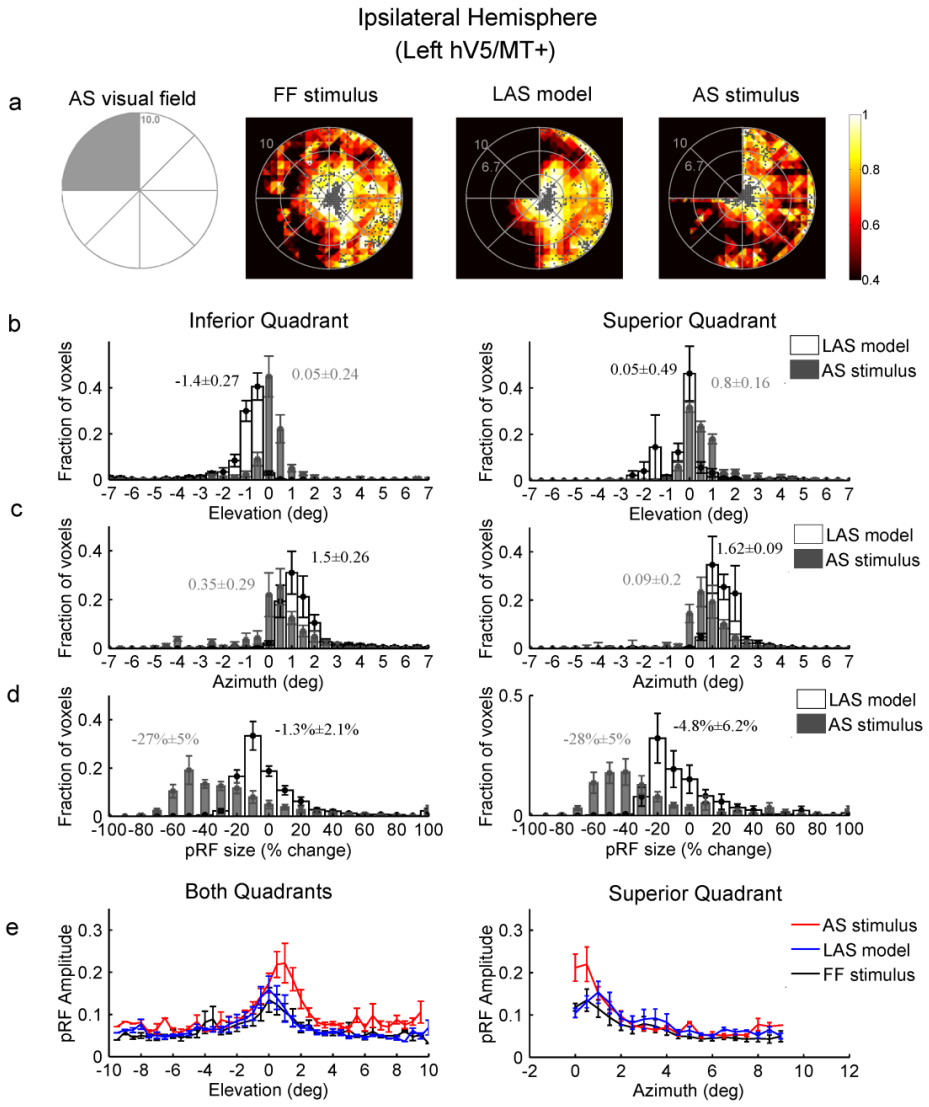

Fig. 6: PRF location, size and amplitude changes in ipsilateral hV5/MT+ under the AS condition. (a) Visual field coverage maps of area hV5/MT+ ipsilateral to the AS (left hemisphere) for a subject under the full field (FF) stimulus condition (2nd column), under the LAS model (3rd column) and under the AS condition (4th column). On the left, a sketch of the visual field indicates the location of the AS (shaded gray area). The visual field coverage maps under full field stimulation or under the LAS model, span the contralateral hemifield. The visual field coverage under the AS condition on the other hand shows a relative displacement of the pRFs towards the superior quadrant, which is the quadrant opposite from the AS. **(b)** Average pRF center elevation distribution from voxels in ipsilateral hV5/MT+ of 5 subjects under the AS condition (gray bars) and under the LAS model (white bars). As in Fig. 4a, the voxels are divided

into two groups according to their pRF center location as estimated from the full field stimulus condition, one for pRFs in the inferior quadrant (left panel) and the other for pRFs at the superior quadrant (right panel). The mean and standard error of the mean of each distribution is indicated on top of the graphs with gray color for the AS stimulus and black color for the LAS model. The pRF center elevation distribution does not change significantly in the presence of the AS for voxels in the superior quadrant (right). PRFs of the inferior quadrant, however, shift their location towards the superior quadrant in the case of the AS condition (gray bars, left) compared with the distribution of the LAS model. **(c)** Same as in b for the pRF center azimuth. The pRF center azimuth distributions significantly shift towards the vertical meridian under the AS condition for both the inferior and superior quadrants. **(d)** Average percent change of the pRF size (as described in Fig. 4b) for 5 subjects under the LAS model (white bars) and the AS stimulus condition (gray bars) separately plotted for voxels located in the inferior quadrant (left panel) and the superior quadrant (right panel). The pRF size of left (ipsilateral) hV5/MT+ under the AS condition is decreased more than expected based on the LAS model (white bars). **(e)** ***Left:*** average pRF amplitude of the pRF topographies in left hV5/MT+ of 5 subjects under the full stimulus condition (black), under the LAS-prediction condition (blue) and under the AS condition (red) as a function of pRF elevation. The pRF amplitude is larger under the AS condition for pRFs located in the superior quadrant (elevation > 0). Right, average pRF amplitude of voxels in left hV5/MT+ with pRF center locations in the superior quadrant as a function of pRF azimuth. The pRF amplitude is larger within 1° from the vertical border of the AS (azimuth = 0) in the AS stimulus case (red) compared with the LAS-prediction (blue) and the full stimulus condition (black). For all graphs, the error bars indicate the standard error of the mean across subjects (N = 5).

In summary, the results so far demonstrate a displacement of pRF center location of voxels in area hV5/MT+ when an AS is used in the upper left quadrant of the visual field. The observed displacement is towards the AS border compared to LAS model prediction, suggesting that significant nonlinearities influence the pRF estimation when using the truncated stimulus. A further signature of these nonlinearities is an increase in pRF amplitude observed near the horizontal border of the AS (Fig. 4c left). PRF center shifts are not restricted to the hemisphere contralateral to the AS, but are also observed in the hemisphere ipsilateral to the AS. In this case, pRFs shift towards the quadrant contralateral to the AS (right superior quadrant), and the pRF amplitude increases particularly near the vertical meridian (vertical border of the AS). The more striking finding is a significant decrease in average pRF size observed in area hV5/MT+ area of both hemispheres. Notably pRF size under the AS condition is significantly smaller than the pRF size expected from the LAS model, further supporting the influence of nonlinear interactions in pRF estimation when using the truncated stimulus.

Biases in pRF estimation depend on the stimulus condition used for modeling

For all aforementioned results, our method uses the AS stimulus to estimate the pRF topography under the AS condition (Fig. 1C). As a result, pRF weights outside the stimulus space, i.e. inside the AS area, cannot be estimated. This is appropriate for studies of normal subjects with AS stimuli like here as well as in studies of patients with dense retinal lesions since the input never reaches the brain. However, a question in studies of patients with visual cortical

lesions is whether activity arises from the interior of the visual field scotoma. Typically, retinotopic mapping in patients is performed using a full stimulus (bar, wedge or ring), which overlaps the area of the scotoma (Dilks et al., 2007, Baseler et al., 2011, Papanikolaou et al., 2014). In this case, modeling both sets of responses using the full stimulus condition might be more appropriate for comparing patients and AS subjects. Thus we also examined whether pRF biases occur in subjects stimulated with the AS stimulus when their pRF topographies are modeled using the full stimulus (Fig. 1D).

As expected, we found no pRF centers within the AS area when we used the full stimulus to estimate the pRFs from the data generated by the LAS model (Fig. 7a, left). However, the visual field coverage maps of the right hV5/MT+ under the AS condition cover most of the area of the AS itself (Fig. 7a, right). PRFs lie well within the area of the AS, well beyond the eye movements' range (Fig. 5). In patients, such pRFs could be erroneously interpreted as arising from stimuli presented in the interior of the scotoma. However, in the case of normal subjects stimulated with the AS stimulus there is in fact no stimulus presented inside the AS, and thus the observed pRF topographies are the result of an artifact, in the sense that they do not represent the weights by which the voxel would integrate a stimulus that falls in the AS. Our method fits well the fMRI BOLD signal (Fig. 7b) suggesting they do not simply represent a mistake in fitting. To understand how this signal arises, we computed the average neural responses (estimated by the deconvolved BOLD signal change) of all significantly activated voxels in hV5/MT+ separately for different bar directions of motion (see Fig. 7c, methods). The BOLD signal response of each voxel was calculated as a difference from the baseline, defined as the signal elicited when the vertical bar is in the furthest part of the visual field contralateral to the scotoma (ipsilateral to the hV5/MT+ considered). This location is expected to produce little if any activity to area hV5/MT+ contralateral to the scotoma. This procedure sets the baseline of each voxel to zero.

When a horizontal bar is moving from the top (AS location) to the bottom (stimulated) visual field quadrant, the average BOLD signal in the right hemisphere is initially at baseline (zero) as there is no stimulus presented within the AS (blue bars, Fig. 7c). Activity greater than baseline starts to be elicited when the bar is near 2° from the horizontal meridian (AS border), commensurate with the size of the subject's fixation eye movements. In contrast, when the horizontal bar is moving in the opposite direction, from the bottom (stimulated) to the top (AS) visual field quadrant, the BOLD signal spreads further into the superior quadrant (positive elevations) where no stimulus was presented (white bars, Fig. 7c). The BOLD signal seen within the AS in this case is likely to be the result of increased hemodynamic spread resulting from the fact that the bar comes from the inferior (seeing) to the superior (blind) quadrant. This activates hV5/MT+ likely eliciting a hemodynamic wave that persists beyond the entry of the bar to the region of the scotoma. Similar spread occurs for other bar directions as long as the part of the stimulus moves from lower (seeing) to higher (non-seeing) visual field locations. It is also possible that this effect may be in part due to neural activity related to stimulus anticipation. However, what argues against this is that there is minimal to no shift in the BOLD signal profile elicited in the right hV5/MT+ when the bar moves from left to right versus right to left (Fig. S5a). In this case the bar is moving from the contralateral (left) to the ipsilateral (right) visual field or vice versa, crossing different hemispheres and vascular territories, so vascular spread should not occur. In accordance to this the BOLD signal shift should essentially disappear for the left to right bar transitions, as is shown to happen in Fig. S5a. It is difficult to

imagine why this would happen if the dominant underlying mechanism for the shift were to be neural anticipation. The discrepancy in the BOLD time series within the AS area for the different bar directions is in part the cause of the pRF coverage observed within the AS when fitting the data using the full stimulus model. Note that although BOLD differences between bar directions occur also in early visual areas with small receptive fields (such as area V1, Fig. S5b), the effect is smaller (~2°) and affect visual field coverage estimates less (Fig. S5b).

Therefore, a different approach is needed for comparing responses between patients and AS subjects when using the drifting bar stimulus. One solution would be if one fits the BOLD time series of each voxel separately for each bar direction and model the boundaries of the pRF by marking the visual field locations where the BOLD signal rises above baseline for each direction. This would allow us to observe directly the spread of BOLD activity in each direction, taking into account asymmetries that may arise.

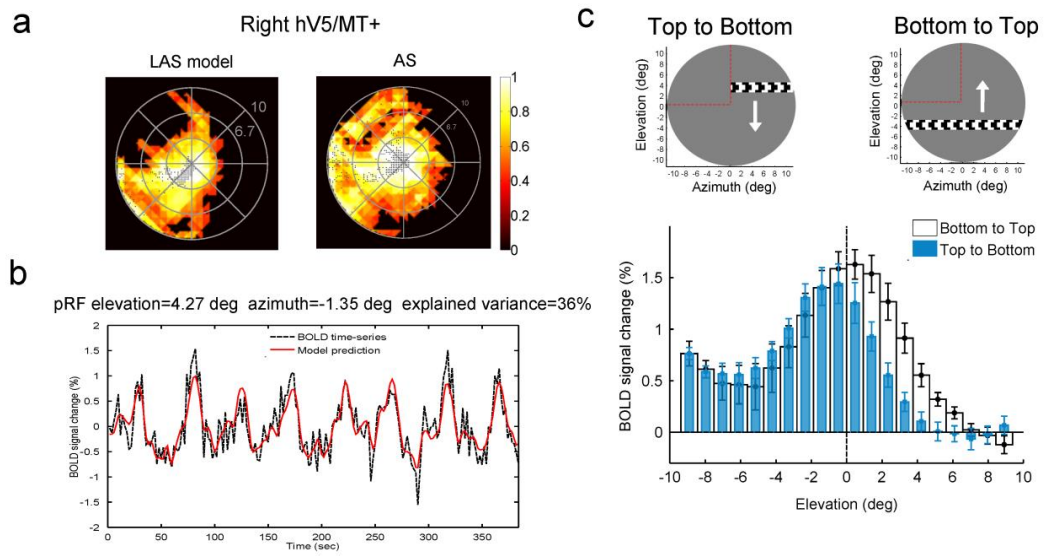

Fig. 7: PRF biases under the AS condition. (a) Visual field coverage of the right hV5/MT+ in one subject under the LAS model (left) and under the AS condition (right) assuming the full bar stimulus for modeling the pRFs (Fig. 1D). The map covers significantly the area of the AS at the upper left quadrant of the visual field under the AS condition in contrast to the LAS model. **(b)** The BOLD time series of a voxel with pRF center located well within the area of the AS (elevation = 4.27°, azimuth = -1.35°). The model predicts 36% of the variance in the data suggesting that the pRF prediction is not a fitting artifact. **(c)** The average BOLD signal change from all voxels in the right hV5/MT+ as a horizontal bar is moving from the top (elevation > 0; AS) to the bottom of the visual field (elevation < 0; seeing quadrant; blue bars) and vice versa (white bars). On top, a snapshot of the orientation of the bar, the direction of motion (white arrow) and the AS location (marked with red dashed lines, for illustration purposes). Before averaging, the BOLD time series of each voxel is deconvolved to adjust for the hemodynamic response function and the baseline is subtracted. The baseline is defined as the signal value

when the vertical bar is located in the far ipsilesional part of the visual field, which should produce little or no visual modulation in the region examined (see methods). This procedure sets the baseline of each voxel to zero. When the bar is moving from the top to the bottom of the visual field (blue bars), the average BOLD signal change when the bar is in the superior quadrant (location of the AS; elevation > 0) drops to baseline values compared with the average signal under the full field stimulus condition. Activity starts when the bar is near 2° from the horizontal meridian (AS border), commensurate with the subject's fixation eye movements. On the other hand, when the bar moves from the bottom to the top of the visual field (white bars), activity spreads beyond the horizontal border of the AS (elevation = 0) well within the superior quadrant corresponding to the AS. The error bars indicate the standard error of the mean across subjects (N = 5).

Comparison to direct-fit methods

We compared results obtained with our method with a method that fits directly a 2-dimensional Gaussian pRF model to predict the fMRI time-series (Dumoulin and Wandell, 2008). This method has been previously applied to characterize pRF changes in the early visual cortex of healthy participants with artificial scotomas (Baseler et al., 2011, Haak et al., 2012a, Binda et al., 2013). The direct-fit model can extrapolate estimates of the pRF that fall outside the stimulus space (i.e. inside the AS) by applying a Gaussian fit to the tail of the pRF that lies inside the stimulus space (Binda et al., 2013). As a result, when the direct-fit method is used to estimate the pRFs, the visual field coverage maps of the right hV5/MT+ cover the area of the AS both under the LAS model and under the AS condition (Fig. 8a). The visual field coverage maps cover the area of the AS whether we incorporate the AS stimulus in the model or we use the full field stimulus (Fig. S6A). Whether this extrapolation is justified is an open question. Nevertheless, even with this method we did observe differences between the AS condition and the LAS model. In particular, pRF centers originally located in the inferior quadrant (under the full field stimulus condition) shift within the AS (superior quadrant, elevation>0) under the AS condition compared to pRFs estimated using the LAS model which retain their location within the inferior quadrant as expected (Fig. 8b, left). The distributions are significantly different ($p = 10^{-215} < 10^{-19}$). PRFs originally located in the superior quadrant retain their location within the AS (elevation>0) for both the LAS model and the AS condition (Fig. 8b, right). In this case, the pRF elevation distribution under the AS condition appears to be significantly shifted, with more voxels lying within the AS compared to the LAS model ($p = 10^{-51} < 10^{-30}$). In addition, the pRF centers found within the AS have increased amplitude compared to both the LAS model and the full field stimulus condition (Fig. 8c). These findings are comparable with those observed using our method confirming that the pRFs are nonlinearly affected by the truncated stimulus. Contrary to our method though, we did not observe a clear pattern for the pRF size when using the direct-fit method. Most pRFs under the LAS model had no change in the pRF size compared with the full field stimulus condition, while some pRFs had increased size (Fig. 8d). PRFs under the AS condition on the other hand shows large variability, many voxels showing markedly decreased or increased pRF size (Fig. 8d), sometimes almost triple the size of the original pRF under the full field stimulus condition (pRF change of 180%). We have previously shown that direct-fit methods are subject to potentially large errors in extrapolating the pRF structure and center when it lies outside the stimulus presentation space (Lee et al., 2013). For example, for a pRF located near the edge of the AS, the direct-fit method could potentially fail to capture the

actual pRF center and size (Fig. 8e). This is because direct-fit methods use the visible (residual) portion of the pRF that falls outside of the AS to extrapolate how the pRF should look like inside the AS. This might result in a correct prediction where the pRFs under the AS condition match with those under the full field stimulus condition, as in (Binda et al., 2013). However, in other cases the extrapolated pRFs within the AS may differ from the pRFs under the full field stimulus condition as a result of a fitting error (Fig. 8e), nonlinearity or both (Fig. S6B). Our method only captures the portion of the pRF topography that lies within the stimulus presentation space and thus results in more veridical estimates in this case.

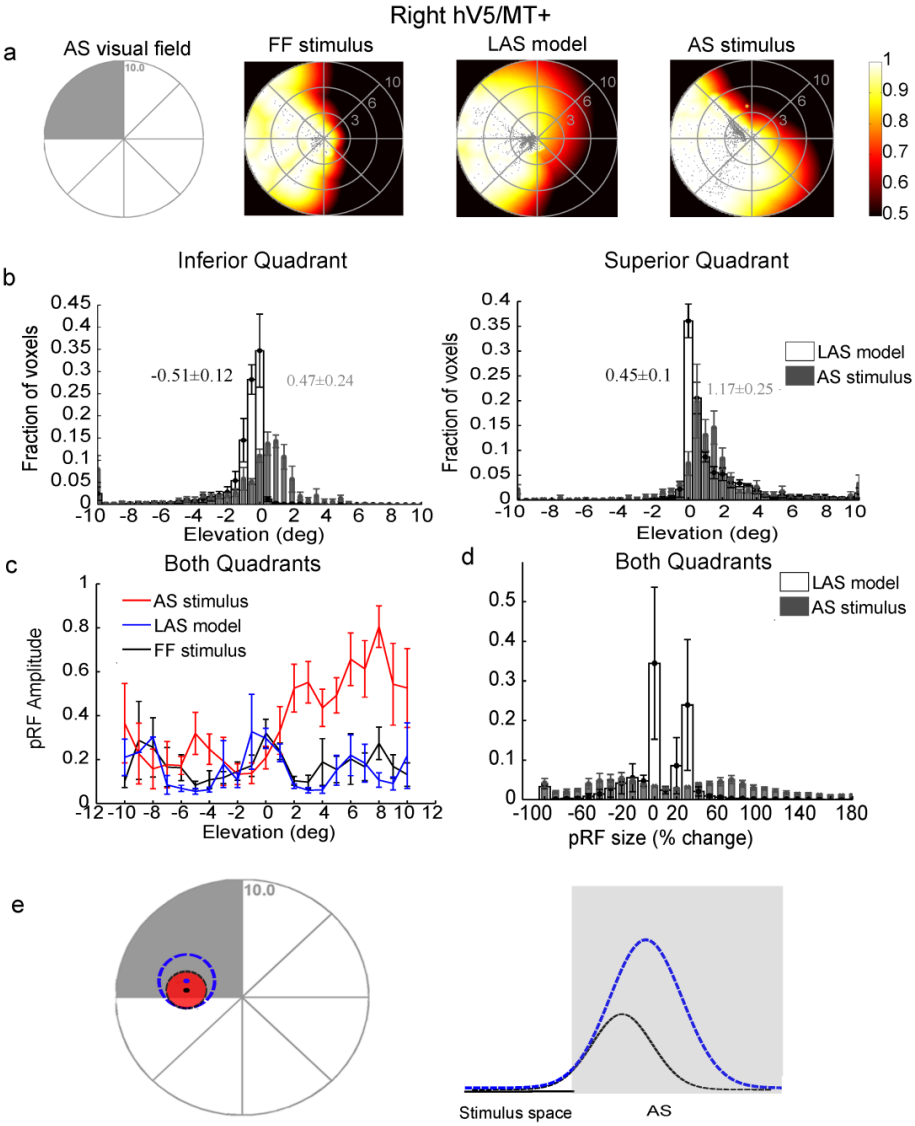

Fig. 8: PRF changes in contralateral hV5/MT+ under the AS condition using a direct-fit method. (a) Visual field coverage maps of area hV5/MT+ contralateral to the AS (right hemisphere) for a subject under the full field (FF) stimulus condition (2nd column), under the LAS model (3rd column) and under the AS condition (4th column). On the left, a sketch of the visual field indicates the location of the AS (shaded gray area). The visual field coverage maps extend significantly within the area of the AS at the upper left quadrant of the visual field both under the LAS model and under the AS condition. **(b)** Average pRF center elevation distribution from voxels in right hV5/MT+ of 5 subjects under the AS condition (gray bars) and under the LAS model (white bars). As in Fig. 4a, the voxels are divided into two groups according to their pRF center location as estimated from the full field stimulus condition, one for pRFs in the inferior quadrant (left panel) and the other for pRFs at the superior quadrant (right panel). The mean and standard error of the mean of each distribution is indicated on top of the graphs with gray color for the AS stimulus and black color for the LAS model. The pRF center elevation distributions are significantly shifted within the AS under the AS condition for both voxels in the inferior (left) and superior quadrants (right) compared with the distributions of the LAS model. **(c)** Average pRF amplitude of the pRFs in right hV5/MT+ of 5 subjects under the full stimulus condition (black), under the LAS model (blue) and under the AS condition (red) as a function of pRF elevation. The pRF amplitude is larger under the AS condition for pRFs located in the superior quadrant (elevation > 0). **(d)** Average percent change of the pRF size (as described in Fig. 4b) for 5 subjects under the LAS model (white bars) and the AS stimulus condition (gray bars) plotted for all voxels in right hV5/MT+. For all graphs, the error bars indicate the standard error of the mean across subjects (N = 5). **(e)** Schematic illustration of a pRF located at the edge of the AS. The light gray represents the area of the AS. The red circle represents the true pRF. The black and the blue dashed lines represent different model fits. The black and blue dots denote the corresponding pRF centers. The direct-fit model extrapolates estimates of the pRF that fall outside the stimulus space (inside the AS) by applying a Gaussian fit to the tail of the pRF that lies inside the stimulus space. This approach however may potentially result in erroneous model fits. For example, see the black versus the blue curves in the right panel, which both fit the part of the stimulus space outside the AS very well, but result in markedly different pRFs. These methods are therefore prone to errors in capturing the actual pRF shape near stimulus presentation borders (such as the border of the AS) (Lee et al., 2013), potentially resulting, for example, in an enlarged and mislocalized pRF (blue dashed line).

Discussion

Nonlinear pRF changes in hV5/MT+ under an "Artificial Scotoma" condition

Population receptive field (pRF) measurements provide a way to gauge the degree of reorganization after injury in human visual areas (Baseler et al., 2011, Papanikolaou et al., 2014). Because fMRI voxels contain more than 10^6 neurons (Leuba and Garey, 1989), pRF estimates depend both on the size of individual neuron receptive fields and on their scatter within each voxel. When different subsets of neurons within a voxel get activated, pRF estimates may change. For example, if only a subset of the neuronal population is activated in the case of the artificial scotoma, the pRF estimate will change (Baseler et al., 2011, Haak et al., 2012a, Haak et al., 2012b, Binda et al., 2013) without reflecting cortical reorganization. In

addition, presenting a truncated visual stimulus can have nonlinear effects that can modify receptive field location and size estimates in individual neurons. It is important to understand how such changes manifest in pRF estimation to be able to separate them from true reorganization. Here, we measured pRF changes that occur in area hV5/MT+ of five normal subjects after masking the stimulus in the upper left quadrant of the visual field ("artificial scotoma" or AS), thereby simulating a quadrantanopic scotoma.

The results show that most of the pRFs in the superior quadrant (AS) remain responsive and shift their location outside the boundaries of the AS (inferior quadrant). One possible reason for this might be that we can only map the part of the pRF that extends outside of the AS area, where stimulus is presented (Wandell and Smirnakis, 2009). However, this does not appear to be the whole story. Interestingly, pRF centers cluster at the AS border under the AS condition whereas they are expected to lie further within the inferior quadrant based on the prediction of the linear AS model (Fig. 4a). In addition, pRFs located in the inferior quadrant (outside the AS), which are expected to have minimal change, also shift towards the AS border (Fig. 4a). This is accompanied by a significant reduction in the pRF size of hV5/MT+ voxels (Fig. 4b) as well as an increase in the amplitude of pRFs that occurs within 1° of the horizontal AS border (Fig. 4c). Notably, similar pRF changes were observed in the hV5/MT+ complex of the hemisphere ipsilateral to the AS (Fig. 6), except in this case pRF centers also shift towards the vertical border of the AS. These changes suggest that nonlinear processes contribute to the BOLD response elicited by the truncated stimulus presented in the case of the artificial scotoma (AS). They may for example be the result of decreased inhibition close to the AS border resulting in disproportional increase of the pRF amplitude compared to the amplitude expected when using the full bar stimulus. Importantly, these deviations from linearity occurring in hV5/MT+ pRF estimation under the AS condition do not reflect true reorganization, but rather properties of normal visual processing under different test-stimulus conditions.

Comparison with Prior Studies

Previous studies have found ectopic pRFs in locations of the early visual cortex (areas V1-V3) that correspond to the AS (Baseler et al., 2011, Haak et al., 2012a, Haak et al., 2012b). In particular, Haak et al. found that, in the presence of a foveal artificial scotoma, pRFs at the center of the visual field shifted to more peripheral locations and increased in size (Haak et al., 2012a). Here we show that a shift of pRFs originally located inside the AS to locations outside of the AS, but not an increase in pRF size, can be partially explained by the LAS model, which models what is expected when stimulating only the part of the pRF_{FF} that does not fall inside the artificial scotoma. However, we also show that pRF shifts under the AS condition differ from shifts predicted by the LAS model suggesting that nonlinear processes contribute to the BOLD response elicited by the AS stimulus. In particular, pRFs cluster more at the border of the AS and the pRF size is decreased compared to the LAS model. In addition, we show a shift of the pRF centers originally located outside of the AS towards the AS border and an increase in the pRF amplitude near the AS border, which have not been previously reported.

Although these findings differ from those of Haak et al. (Haak et al., 2012a), we note that the pRF shifts reported by Haak et al. are found in the early visual cortex (area V1), while our results reflect pRF changes in hV5/MT+. However, we have not observed pRF shifts in area V1 under the AS condition in the magnitude reported by Haak et al. (Haak et al., 2012a). It is important to

note that Haak et al. used a direct-fit method for pRF estimation, and this may be the source of a bias near a stimulus presentation border, such as the border of AS (Lee et al., 2013). This bias can potentially lead to significant mislocalization of the pRF center as well as erroneous estimation of the pRF size (see Fig. 8 for an illustration). It is therefore possible that the pRF changes observed in (Haak et al., 2012a) may reflect a bias as a result the pRF method used. The method we used here (Lee et al., 2013) is considerably more robust to such a bias. Another possibility is that the differences between the study of Haak et al. and ours originate from the fact that a different AS stimulus is used. Haak et al. used a large foveal scotoma while we used a scotoma covering one quadrant. It is possible that stimulating only the periphery may affect pRF responses in the central visual field, an effect that might be hidden in our case since we stimulate both peripheral and central locations in the seeing quadrant. .

Another study (Binda et al., 2013) adopted an approach more similar to ours, and compared responses obtained under the AS condition with simulated responses computed using pRFs estimated from the full-field stimulus condition (similar to the LAS model). They found that when a multifocal stimulus presentation is used, pRF shifts in the AS condition can be largely predicted by the simulations. This agrees with our estimations in early visual cortex (area V1; Fig. 3B) but not in area hV5/MT+, where we show that pRFs under the AS condition differ from pRFs obtained using the LAS model. Binda et al. did not study responses in higher visual cortex where receptive fields cover a large portion of the visual field and thus they are likely to be more susceptible to the presence of a truncated stimulus.

Interestingly, when using a moving bar stimulus presentation, Binda et al. found pRF shifts under the AS condition that are different than those obtained from the model predictions (i.e. LAS model) suggesting that the pattern of visual stimulation (multifocal versus moving bar stimulation) may play a critical role in the conclusions that can be drawn. However, we do not believe that the effects we observed here represent simply an artifact of the stimulus presentation paradigm. First, we did not observe this effect in early visual areas. Specifically, we saw no significant difference between pRF estimates obtained by LAS versus the true AS condition in area V1 under our moving bar stimulation paradigm (Fig. S3a). Second, the main question is whether some of the nonlinearities we observe may be the result of differences in hemodynamic effects induced by the moving bar stimulus presentation in the AS versus the LAS stimulus condition (Fig. 7). Although there is a differential spread of the BOLD signal depending on bar stimulus direction (see next section), this does not fully explain the findings presented here. For example, it cannot explain the shift of the pRFs that are located outside of the AS towards the scotoma border, nor the increase in the pRF amplitude near the AS border. Note also that artifacts related to potential hemodynamic spread inside the area of the AS are minimized by our use of the AS-stimulus model for pRF estimation, which effectively restricts pRF weight estimation outside the AS, in the part of the visual field that was actually visually stimulated.

PRF estimates in hV5/MT+ depend strongly on whether the full bar or the truncated (AS) bar stimulus model is used for estimation

PRF estimation in the presence of an artificial scotoma represents an important control in most studies of patients suffering from visual field defects (Dilks et al., 2007, Baseler et al., 2011, Papanikolaou et al., 2014). However, it is an open question whether the appropriate stimulus

model to use for pRF estimation is a truncated bar versus a full bar stimulus. We found significant differences in hV5/MT+ pRFs estimated when using the truncated bar (AS stimulus) versus the full bar stimulus model. Note that in both cases the actual stimulus presentation is done with the AS stimulus. Specifically, visual field coverage maps of the contralateral area hV5/MT+ covered most of the AS area when pRFs were estimated using the full bar model compared to the truncated bar model, which showed minimal coverage (Fig. 7a versus Fig. 3B). This has important implications regarding the interpretation of pRF topographies. In general, nonzero pRF weights that correspond to the region of the AS should not be straightforwardly interpreted as direct pRF measurements, since no visual stimulus was actually presented there. Rather they represent a form of extrapolation from responses arising outside the AS, which are subject to the assumptions underlying the pRF model. To avoid the interpretation difficulties this entails, our analysis primarily focused on comparing pRF weights estimated outside the AS region, derived under the truncated bar stimulus model (Figs. Fig**. 3**-Fig**. 6**). This ensures that conclusions drawn are not subject to potential extrapolation errors.

We derived pRF estimates under the full bar stimulus model to make a link with existing literature (Fig. 7). Differences in the pRF estimation when applying two different stimulus models (full bar versus truncated bar) to the same actual stimulation condition (AS) have been reported before in the early visual cortex of subjects with artificial scotomas (Binda et al., 2013). However, the reported effect was largely opposite to what we observe here. Binda et al. report that when the full bar stimulus model is used to estimate pRF location, pRFs originally inside the artificial scotoma (AS) region shift outside the AS boundaries. On the other hand, when the AS stimulus model is used, pRFs are found within the AS area. The difference between Binda et al. and our study can be partially explained by the different approach we used to estimate pRFs. Our method, uses a linear topography estimation approach to estimate the pRF structure (Lee et al., 2013) and, *when the AS-model is applied*, it appropriately cannot cover areas outside the stimulus presentation space. Binda et al. use a direct-fit method, which can extrapolate pRF weights that fall outside the stimulus space, i.e. inside the AS, by fitting the tail of the pRF that lies inside the stimulus space (Fig. 8). This extrapolation is easier to perform when the AS-model (truncated bar) is applied, resulting in significant pRF coverage inside the scotoma in this case. Our method instead yields significant pRF coverage inside the scotoma, when we apply the *full bar stimulus* condition (Fig. 7). The lesson here is that the particular type of extrapolation accomplished depends strongly on the pRF model used, and resulting pRF estimates should be considered with caution, pending empirical validation.

Comparison with the direct method of pRF estimation

To ensure that the effects we report are not the result of the method of pRF estimation we used, we repeated our analysis using the direct method of pRF estimation (Dumoulin and Wandell, 2008) to estimate responses in hV5/MT+. We found that our main conclusions remain valid (Fig. 8) confirming that the pRFs are nonlinearly affected by the truncated stimulus.

We note that direct estimation methods can lead to biased estimates for pRFs that lie close to a stimulus presentation boundary (Lee et al., 2013) (Fig. 8e) and should be used with caution in subjects with sharp visual field scotoma boundaries. For example, when we used the direct-fit method to estimate pRFs in area hV5/MT+ we found that visual field coverage maps covered the area of the AS, whether we use the truncated bar (AS-model) or the full bar stimulus model

(Fig. 8a, Fig. S6A). One interpretation of these extrapolated pRF topographies that extend inside the AS is that they represent the actual pRF profiles that would have been obtained had the artificial scotoma not been there (Binda et al., 2013). However, this does not occur in our case as both the pRF center elevation and size distributions obtained under the AS condition differ from those obtained under the full field stimulus condition (Fig. S6B). Since errors in parameter estimation can arise easily by extrapolating partial data fitting of this nature (see fig. 8e), careful validation of results obtained is required. Here we concentrated on modeling the part of the receptive field that lies outside the artificial scotoma, in order to minimize potential for error.

Directional asymmetry of the BOLD response elicited by the bar stimulus at the border of AS

In our case, activity observed within the AS area appears to be in part the result of asymmetric BOLD responses occurring when the bar stimulus moves from seeing to non-seeing locations of the visual field (Fig. 7c). One possibility is that BOLD signal responses differ within the AS because the brain generates an expectation of the upcoming stimulus (Kastner et al., 1999, Ghose and Bearl, 2010) or because of filling-in phenomena (Meng et al., 2005). Anticipation of the upcoming stimulus may in part explain the BOLD spread within the AS area, however, it is unlikely to be the whole explanation here. Effects of stimulus expectation should be apparent also when the bar is moving from the contralateral to the ipsilateral visual hemifield. Although there is a small BOLD spread when the vertical bar moves from the contralateral to the ipsilateral visual hemifield that could be the result of anticipation (Fig. S5a), the effect does not occur in the same magnitude as when the horizontal bar enters the scotoma (Fig. 7c), suggesting that the BOLD spread within the AS area is likely the result of persistent hemodynamic activity which cannot occur across hemispheres. Moreover, the type of stimulus we use (moving bar truncated in the area of the AS) is not conducive to filling-in phenomena (De Weerd et al., 1998) effectively ruling out this possibility.

Such asymmetric differences in the BOLD signal may potentially be avoided by changing stimulus design, for example by having the bar stimulus positions interleaved randomly rather than presented sequentially, as Binda et al. suggest (Binda et al., 2013). However, the ability of such stimuli to activate hV5/MT+ and yield reliable pRF estimates in higher areas warrants further investigation (Binda et al., 2013). An alternative approach is to calculate directly the boundaries of the pRF from the BOLD time series of each voxel separately for each direction of motion of the visual stimulus (bar). For example, one could identify the visual field location where the BOLD activity starts to rise above baseline separately for each bar direction. In this way, hysteresis phenomena also become apparent and can be taken into account or investigated as needed. This approach has some similarity to classical receptive field mapping methods (Hubel and Wiesel, 1962)), although the time scales involved are of course much different.

Conclusions

We have shown that pRF estimates in area hV5/MT+ are nonlinearly affected by a truncated stimulus presented (AS) in order to simulate a quadrantanopic visual field scotoma. This was signified by a shift of the pRF centers towards the border of the AS, a decrease in pRF size and an increase in pRF amplitude near the AS border. In addition, we found erroneous pRF estimates inside the area corresponding to the AS, when we used the full bar stimulus model

for predicting the pRF topography when the actual stimulus presented included the AS. These biases are not the result of a trivial methodological artifact but appear to originate from asymmetric BOLD responses occurring when the stimulus moves from seeing to non-seeing locations of the visual field. We argue that these responses are not simply neural anticipatory responses but likely contain a significant hemodynamic component. Distinguishing pRF changes that occur as the result of true reorganization versus different test-stimulus presentation conditions is an important task that needs to be undertaken when studying the organization of visual cortex in patients with visual field deficits. The purpose of this work was to point out some of the issues involved.

Acknowledgements

This work was supported by National Eye Institute R01 (EY024019) to SMS, the Deutsche Forschungsgemeinschaft, the Plasticise Consortium (Project HEALTH-F2-2009-223524) and the Max Planck Society.

References

Amano K, Wandell BA, Dumoulin SO (2009) Visual field maps, population receptive field sizes, and visual field coverage in the human MT+ complex. J Neurophysiol 102:2704-2718.

Baker CI, Dilks DD, Peli E, Kanwisher N (2008) Reorganization of visual processing in macular degeneration: replication and clues about the role of foveal loss. Vision Res 48:1910-1919.

Baker CI, Peli E, Knouf N, Kanwisher NG (2005) Reorganization of visual processing in macular degeneration. J Neurosci 25:614-618.

Barbur JL, Watson JD, Frackowiak RS, Zeki S (1993) Conscious visual perception without V1. Brain : a journal of neurology 116 (Pt 6):1293-1302.

Barmashenko G, Eysel UT, Mittmann T (2003) Changes in intracellular calcium transients and LTP in the surround of visual cortex lesions in rats. Brain Res 990:120-128.

Baseler HA, Gouws A, Haak KV, Racey C, Crossland MD, Tufail A, Rubin GS, Cornelissen FW, Morland AB (2011) Large-scale remapping of visual cortex is absent in adult humans with macular degeneration. Nat Neurosci 14:649-655.

Binda P, Thomas JM, Boynton GM, Fine I (2013) Minimizing biases in estimating the reorganization of human visual areas with BOLD retinotopic mapping. Journal of vision 13:13.

Brainard DH (1997) The Psychophysics Toolbox. Spat Vis 10:433-436.

Bridge H, Hicks SL, Xie J, Okell TW, Mannan S, Alexander I, Cowey A, Kennard C (2010) Visual activation of extra-striate cortex in the absence of V1 activation. Neuropsychologia 48:4148-4154.

Bruce CJ, Desimone R, Gross CG (1986) Both striate cortex and superior colliculus contribute to visual properties of neurons in superior temporal polysensory area of macaque monkey. Journal of neurophysiology 55:1057-1075.

Calford MB, Schmid LM, Rosa MG (1999) Monocular focal retinal lesions induce short-term topographic plasticity in adult cat visual cortex. Proc Biol Sci 266:499-507.

Chino YM, Kaas JH, Smith EL, 3rd, Langston AL, Cheng H (1992) Rapid reorganization of cortical maps in adult cats following restricted deafferentation in retina. Vision Res 32:789-796.

Chino YM, Smith EL, 3rd, Kaas JH, Sasaki Y, Cheng H (1995) Receptive-field properties of deafferentated visual cortical neurons after topographic map reorganization in adult cats. J Neurosci 15:2417-2433.

De Weerd P, Desimone R, Ungerleider LG (1998) Perceptual filling-in: a parametric study. Vision research 38:2721-2734.

DeAngelis GC, Anzai A, Ohzawa I, Freeman RD (1995) Receptive field structure in the visual cortex: does selective stimulation induce plasticity? Proc Natl Acad Sci U S A 92:9682-9686.

Dilks DD, Baker CI, Peli E, Kanwisher N (2009) Reorganization of visual processing in macular degeneration is not specific to the "preferred retinal locus". J Neurosci 29:2768-2773.

Dilks DD, Serences JT, Rosenau BJ, Yantis S, McCloskey M (2007) Human adult cortical reorganization and consequent visual distortion. J Neurosci 27:9585-9594.

Eysel UT, Schmidt-Kastner R (1991) Neuronal dysfunction at the border of focal lesions in cat visual cortex. Neurosci Lett 131:45-48.

Eysel UT, Schweigart G (1999) Increased receptive field size in the surround of chronic lesions in the adult cat visual cortex. Cereb Cortex 9:101-109.

Eysel UT, Schweigart G, Mittmann T, Eyding D, Qu Y, Vandesande F, Orban G, Arckens L (1999) Reorganization in the visual cortex after retinal and cortical damage. Restor Neurol Neurosci 15:153-164.

ffytche DH, Guy CN, Zeki S (1996) Motion specific responses from a blind hemifield. Brain : a journal of neurology 119 (Pt 6):1971-1982.

Ghose GM, Bearl DW (2010) Attention directed by expectations enhances receptive fields in cortical area MT. Vision research 50:441-451.

Giannikopoulos DV, Eysel UT (2006) Dynamics and specificity of cortical map reorganization after retinal lesions. Proc Natl Acad Sci U S A 103:10805-10810.

Gilbert CD, Wiesel TN (1992) Receptive field dynamics in adult primary visual cortex. Nature 356:150-152.

Girard P, Salin PA, Bullier J (1992) Response selectivity of neurons in area MT of the macaque monkey during reversible inactivation of area V1. Journal of neurophysiology 67:1437-1446.

Haak KV, Cornelissen FW, Morland AB (2012a) Population receptive field dynamics in human visual cortex. PLoS One 7:e37686.

Haak KV, Langers DR, Renken R, van Dijk P, Borgstein J, Cornelissen FW (2012b) Abnormal visual field maps in human cortex: A mini-review and a case report. Cortex.

Heinen SJ, Skavenski AA (1991) Recovery of visual responses in foveal V1 neurons following bilateral foveal lesions in adult monkey. Exp Brain Res 83:670-674.

Horton JC, Hocking DR (1998) Monocular core zones and binocular border strips in primate striate cortex revealed by the contrasting effects of enucleation, eyelid suture, and retinal laser lesions on cytochrome oxidase activity. J Neurosci 18:5433-5455.

Hubel DH, Wiesel TN (1962) Receptive fields, binocular interaction and functional architecture in the cat's visual cortex. The Journal of physiology 160:106-154.

Imbrosci B, Neubacher U, White R, Eysel UT, Mittmann T (2013) Shift from phasic to tonic GABAergic transmission following laser-lesions in the rat visual cortex. Pflugers Arch 465:879-893.

Kaas JH, Krubitzer LA, Chino YM, Langston AL, Polley EH, Blair N (1990) Reorganization of retinotopic cortical maps in adult mammals after lesions of the retina. Science 248:229-231.

Kastner S, Pinsk MA, De Weerd P, Desimone R, Ungerleider LG (1999) Increased activity in human visual cortex during directed attention in the absence of visual stimulation. Neuron 22:751-761.

Lee S, Papanikolaou A, Logothetis NK, Smirnakis SM, Keliris GA (2013) A new method for estimating population receptive field topography in visual cortex. Neuroimage 81C:144-157.

Leuba G, Garey LJ (1989) Comparison of neuronal and glial numerical density in primary and secondary visual cortex of man. Experimental brain research 77:31-38.

Maes F, Collignon A, Vandermeulen D, Marchal G, Suetens P (1997) Multimodality image registration by maximization of mutual information. IEEE Trans Med Imaging 16:187-198.

Masuda Y, Dumoulin SO, Nakadomari S, Wandell BA (2008) V1 projection zone signals in human macular degeneration depend on task, not stimulus. Cereb Cortex 18:2483-2493.

Maunsell JH, Nealey TA, DePriest DD (1990) Magnocellular and parvocellular contributions to responses in the middle temporal visual area (MT) of the macaque monkey. The Journal of neuroscience : the official journal of the Society for Neuroscience 10:3323-3334.

Meng M, Remus DA, Tong F (2005) Filling-in of visual phantoms in the human brain. Nature neuroscience 8:1248-1254.

Mittmann T, Eysel UT (2001) Increased synaptic plasticity in the surround of visual cortex lesions in rats. Neuroreport 12:3341-3347.

Morland AB, Le S, Carroll E, Hoffmann MB, Pambakian A (2004) The role of spared calcarine cortex and lateral occipital cortex in the responses of human hemianopes to visual motion. J Cogn Neurosci 16:204-218.

Murakami I, Komatsu H, Kinoshita M (1997) Perceptual filling-in at the scotoma following a monocular retinal lesion in the monkey. Vis Neurosci 14:89-101.

Nestares O, Heeger DJ (2000) Robust multiresolution alignment of MRI brain volumes. Magn Reson Med 43:705-715.

Papanikolaou A, Keliris GA, Papageorgiou TD, Shao Y, Krapp E, Papageorgiou E, Stingl K, Bruckmann A, Schiefer U, Logothetis NK, Smirnakis SM (2014) Population receptive field analysis of the primary visual cortex complements perimetry in patients with homonymous visual field defects. Proceedings of the National Academy of Sciences of the United States of America 111:E1656-1665.

Poppel E, Held R, Frost D (1973) Leter: Residual visual function after brain wounds involving the central visual pathways in man. Nature 243:295-296.

Rodman HR, Gross CG, Albright TD (1989) Afferent basis of visual response properties in area MT of the macaque. I. Effects of striate cortex removal. The Journal of neuroscience : the official journal of the Society for Neuroscience 9:2033-2050.

Rodman HR, Gross CG, Albright TD (1990) Afferent basis of visual response properties in area MT of the macaque. II. Effects of superior colliculus removal. The Journal of neuroscience : the official journal of the Society for Neuroscience 10:1154-1164.

Rosa MG, Tweedale R, Elston GN (2000) Visual responses of neurons in the middle temporal area of new world monkeys after lesions of striate cortex. The Journal of neuroscience : the official journal of the Society for Neuroscience 20:5552-5563.

Rumpel S, Hoffmann H, Hatt H, Gottmann K, Mittmann T, Eysel UT (2000) Lesion-induced changes in NMDA receptor subunit mRNA expression in rat visual cortex. Neuroreport 11:4021-4025.

Schmid LM, Rosa MG, Calford MB, Ambler JS (1996) Visuotopic reorganization in the primary visual cortex of adult cats following monocular and binocular retinal lesions. Cereb Cortex 6:388-405.

Schmid MC, Mrowka SW, Turchi J, Saunders RC, Wilke M, Peters AJ, Ye FQ, Leopold DA (2010) Blindsight depends on the lateral geniculate nucleus. Nature 466:373-377.

Schoenfeld MA, Noesselt T, Poggel D, Tempelmann C, Hopf JM, Woldorff MG, Heinze HJ, Hillyard SA (2002) Analysis of pathways mediating preserved vision after striate cortex lesions. Ann Neurol 52:814-824.

Schumacher EH, Jacko JA, Primo SA, Main KL, Moloney KP, Kinzel EN, Ginn J (2008) Reorganization of visual processing is related to eccentric viewing in patients with macular degeneration. Restor Neurol Neurosci 26:391-402.

Smirnakis SM, Brewer AA, Schmid MC, Tolias AS, Schuz A, Augath M, Inhoffen W, Wandell BA, Logothetis NK (2005) Lack of long-term cortical reorganization after macaque retinal lesions. Nature 435:300-307.

Smith AT, Singh KD, Williams AL, Greenlee MW (2001) Estimating receptive field size from fMRI data in human striate and extrastriate visual cortex. Cereb Cortex 11:1182-1190.

Sunness JS, Liu T, Yantis S (2004) Retinotopic mapping of the visual cortex using functional magnetic resonance imaging in a patient with central scotomas from atrophic macular degeneration. Ophthalmology 111:1595-1598.

Wandell BA, Smirnakis SM (2009) Plasticity and stability of visual field maps in adult primary visual cortex. Nat Rev Neurosci 10:873-884.

Weiskrantz L, Warrington EK, Sanders MD, Marshall J (1974) Visual capacity in the hemianopic field following a restricted occipital ablation. Brain 97:709-728.

Yan L, Imbrosci B, Zhang W, Neubacher U, Hatt H, Eysel UT, Mittmann T (2012) Changes in NMDA-receptor function in the first week following laser-induced lesions in rat visual cortex. Cerebral cortex 22:2392-2403.

Zepeda A, Vaca L, Arias C, Sengpiel F (2003) Reorganization of visual cortical maps after focal ischemic lesions. J Cereb Blood Flow Metab 23:811-820.

Supplementary Material

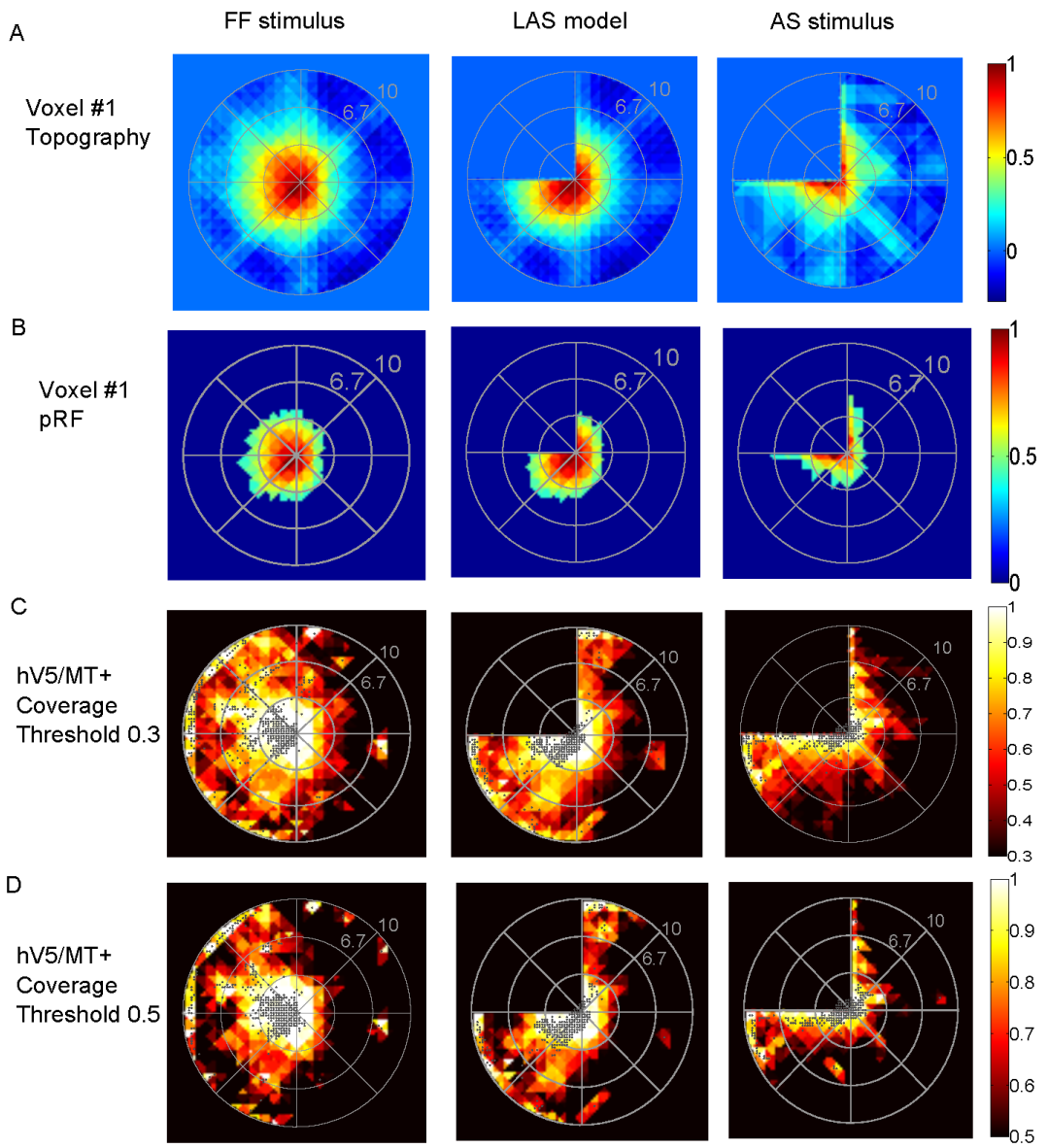

Fig. S1: (A) Left, pRF topography of one voxel in hV5/MT+ under the full field stimulus condition (pRF_{FF}). The pRF covers locations both in the left upper and lower quadrants. Middle, pRF topography of the same voxel under the Linear-AS model (pRF_{LAS}, see methods). In brief, from the topography of the full field stimulus pRF_{FF}, the part of the pRF falling within the AS area is omitted by convolving the pRF_{FF} with

the AS stimulus. The result of the convolution is then used to re-estimate the topography, deriving the pRF_{LAS}. In this case only of the part of the pRF which falls outside of the AS area is mapped. This gives us an estimate of the expected pRF topography under the AS condition, assuming linearity. Right, pRF topography of the same voxel under the AS condition (pRF_{AS}). The pRF_{AS} looks different than it would be expected based on the LAS model (pRF_{LAS}). The pRF_{AS} topography seems to have shifted towards the AS-border. **(B)** The pRF topographies of the same voxel presented in (A) under the different stimulation conditions after thresholding at 0.4 of the maximum value. By thresholding we derive only the central area of the pRF, useful for estimating the pRF center location and pRF size (see methods). **(C-D)** The visual field coverage maps of hV5/MT+ from one control subject under the full field stimulus condition (left), under the LAS model (middle) and under the AS condition (right) when the threshold used to estimate the central pRF is 0.3 of the maximum (C) and 0.5 of the maximum (D). The main observations presented in the Fig. 2, hold across different thresholds.

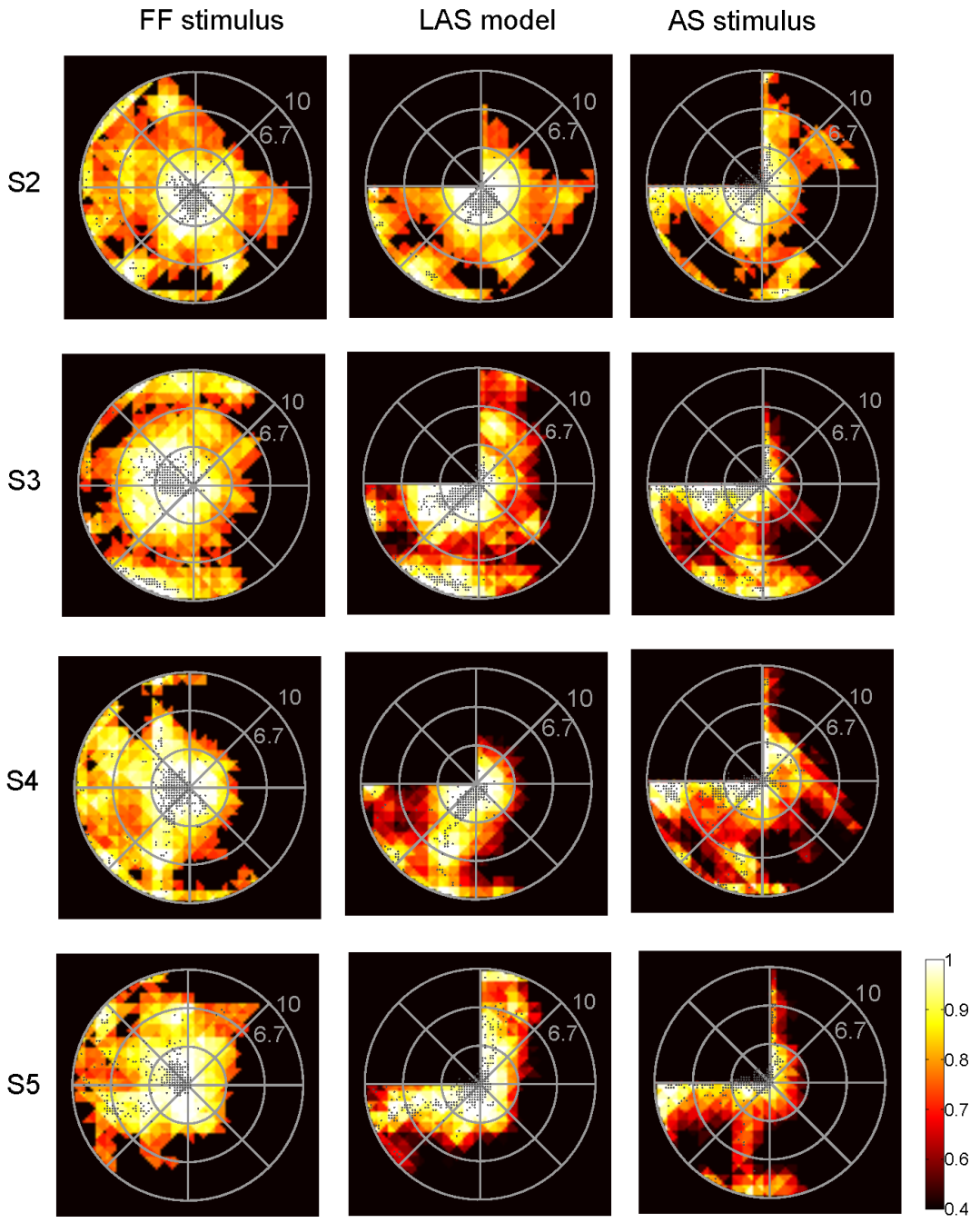

Fig. S2: Visual field coverage maps of subjects S2, S3, S4, S5. The visual field coverage maps of right hV5/MT+ from the remaining four subjects under the full field stimulus condition (left), under the LAS model (middle) and under the AS condition (right).

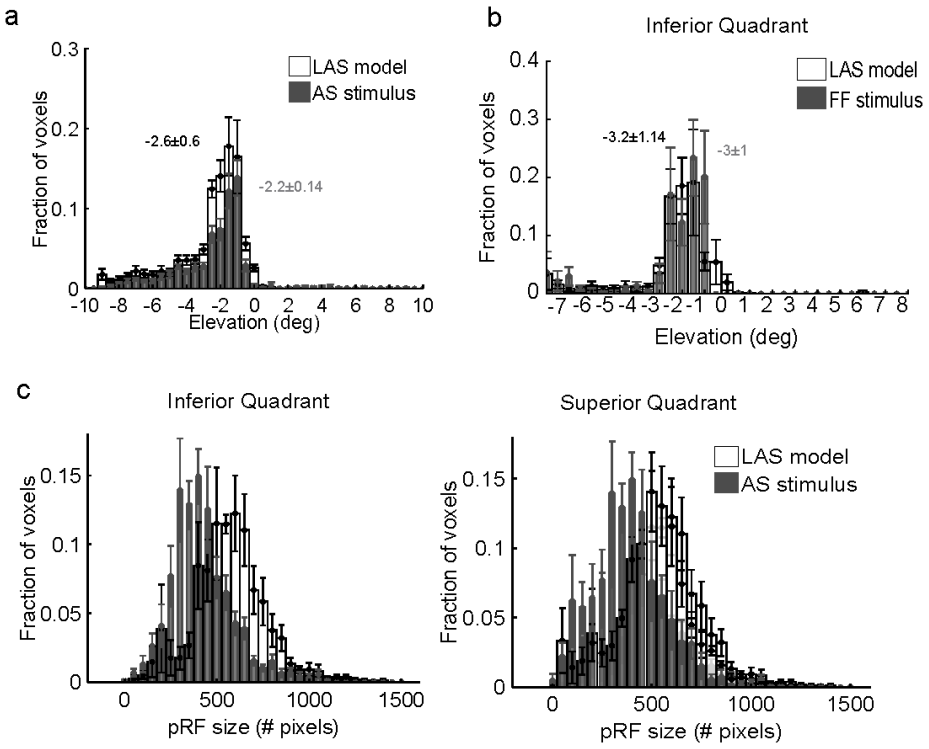

Fig. S3: (a) Average distributions of the pRF center elevation from voxels in area V1 under the AS stimulus condition (gray bars) and under the LAS model (white bars) for all subjects. The mean and standard error of the mean of each distribution is indicated on top of the graphs with gray color for the AS stimulus and black color for the LAS model. There are no significant differences between the two distributions ($p = 10^{-17} > 10^{-57}$). **(b)** Average distributions of the pRF center elevation from voxels in hV5/MT+ corresponding to the inferior quadrant under the full field stimulus condition (white bars) and under the LAS model (gray bars) for all subjects. There are no significant differences between the two distributions ($p = 10^{-19} > 10^{-32}$) suggesting that the LAS model is a good estimator of the residual pRFs expected under the AS condition. **(c)** Average distributions of the pRF size (surface area size of the pRF topography that showed activity above threshold) from voxels in hV5/MT+ corresponding to the inferior (left) and superior (right) quadrants under the LAS model (white bars) and under the AS condition (gray bars) for all subjects. For all graphs, the error bars indicate the standard error of the mean across subjects (N=5).

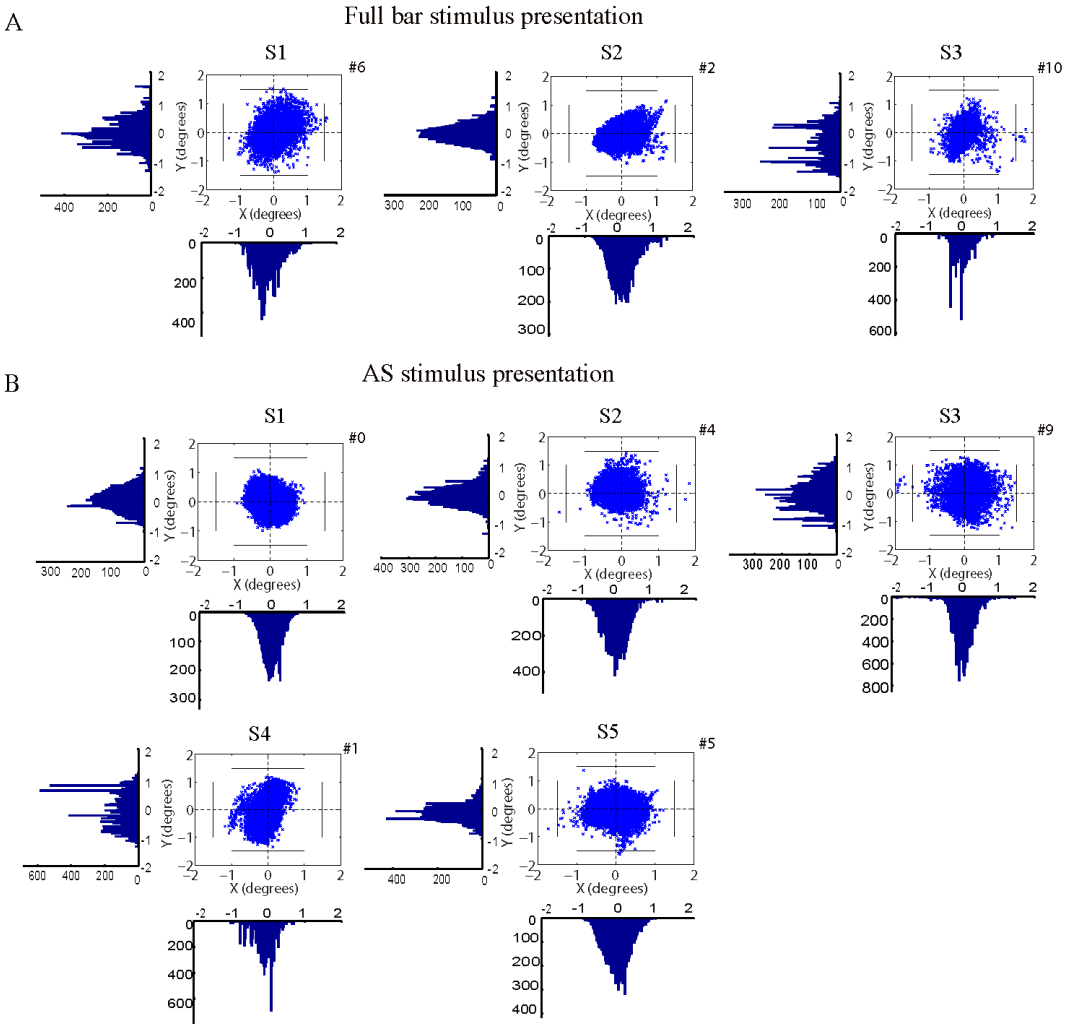

Fig. S4: Eye movements for all subjects under the full field stimulus presentation **(A)** and under the AS stimulus presentation **(B)**. Eye positions plotted at 60Hz for one whole session (6.4 min). The number of eye deviations, defined as excursions > 1.5° from the fixation point is indicated next to the graphs with the number sign (#).

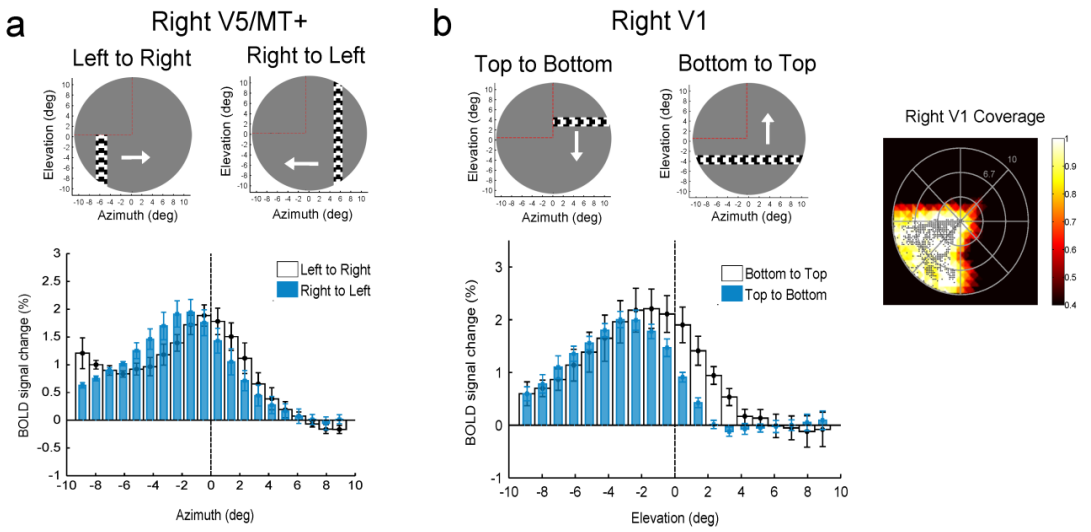

Fig. S5: Average BOLD signal change under the AS condition. (a) The average BOLD signal change from all voxels in the right V5/MT+ as a vertical bar is moving from the left (azimuth < 0; contralateral hemifield/AS) to the right of the visual field (azimuth > 0; ipsilateral hemifield) (white bars) compared to the average signal change as the vertical bar is moving from the left (ipsilateral) to the right (contralateral) of the visual field (blue bars). The error bars indicate the standard error of the mean across control subjects (N=5). On top, a snapshot of the orientation of the bar and direction of motion (white arrow). **(b)** Left, the average BOLD signal change from all voxels in the right V1 as a horizontal bar is moving from the top (elevation > 0; AS) to the bottom of the visual field (elevation < 0; seeing quadrant) (blue bars) compared to the average signal change as the horizontal bar is moving from the bottom to the top of the visual field (white bars). Right, visual field coverage of the right area V1 in one subject under the AS condition assuming the full bar stimulus for modeling the pRFs.

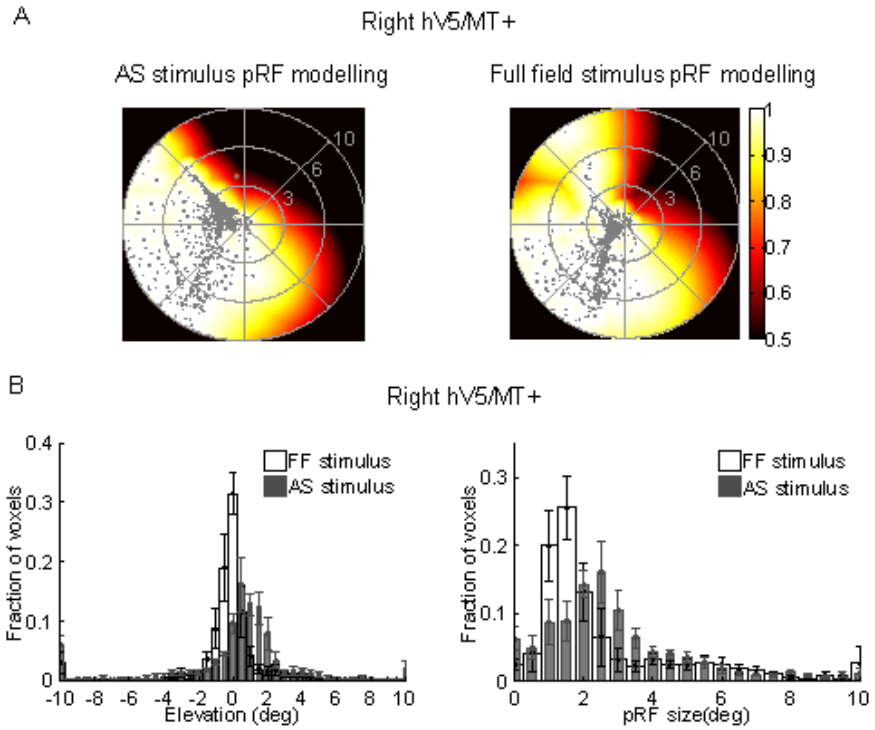

Fig. S6: (A) Visual field coverage maps of area hV5/MT+ contralateral to the AS (right hemisphere) for a subject under AS condition using a direct-fit method (Dumoulin and Wandell, 2008). On the left, the AS stimulus is used in the pRF estimation while on the right, the full field stimulus is used. In both cases the actual stimulus presentation is done with the AS stimulus. The visual field coverage maps extend significantly within the area of the AS at the upper left quadrant of the visual field whether we use the truncated bar (AS-model) or the full bar stimulus model. **(B)** Average distributions of the pRF center elevation (left) and pRF size (right) for voxels in right hV5/MT+ of 5 subjects under the AS condition (gray bars) and under full field stimulation (white bars). PRF estimates are obtained using a direct-fit method (Dumoulin and Wandell, 2008). PRF distributions obtained under the AS condition differ significantly from those obtained under the full field stimulus condition for both the pRF center elevation ($p = 10^{-214} < 10^{-157}$, Kolmogorov-Smirnov test) and pRF size ($p = 10^{-214} < 10^{-157}$).

Table S1: Kolmogorov-Smirnov significance tests between the pRF center distributions of each control subject (S1-S5) under the AS condition and under the LAS model prediction for each visual field quadrant. Right= right hemisphere, Left= left hemisphere, IQ= inferior quadrant, SQ= superior quadrant. Significance is reported as p= a < b, where b is the value selected to reject the NULL hypothesis. b is estimated by comparing the distribution of each subject with all the other subjects for the same condition (AS or LAS). The minimum p-value of these comparisons was then used to test for significance between the distribution of the AS condition and the LAS model for each subject.

	S1	**S2**	**S3**	**S4**	**S5**
Elevation					
Right IQ	$10^{-201} < 10^{-10}$	$0 < 10^{-13}$	$10^{-64} < 0.05$	$10^{-56} < 10^{-43}$	$10^{-22} < 10^{-3}$
Right SQ	$10^{-29} < 10^{-4}$	$10^{-3} < 0.3$	$10^{-30} < 10^{-14}$	$10^{-39} < 10^{-2}$	$10^{-27} < 10^{-20}$
Left IQ	$10^{-122} < 10^{-20}$	$10^{-318} < 10^{-38}$	$10^{-92} < 10^{-6}$	$10^{-101} < 10^{-22}$	$10^{-118} < 10^{-11}$
Left SQ	$10^{-10} < 10^{-6}$	$10^{-7} > 10^{-9}$	$10^{-2} > 10^{-3}$	$10^{-9} > 10^{-21}$	$10^{-3} > 10^{-4}$
Azimuth					
Left IQ	$10^{-45} < 10^{-15}$	$10^{-195} < 10^{-37}$	$10^{-86} < 10^{-64}$	$10^{-12} > 10^{-35}$	$10^{-53} > 10^{-56}$
Left SQ	$10^{-156} < 10^{-14}$	$10^{-5} < 10^{-3}$	$10^{-45} < 10^{-32}$	$10^{-12} > 10^{-32}$	$10^{-32} < 10^{-7}$

A.5 "Organization of area hV5/MT+ in subjects with homonymous visual field defects" (Study under preparation)

Title: Organization of Area hV5/MT+ in Subjects with Homonymous Visual Field Defects

Short title: hV5/MT+ organization in quadrantanopic patients

Author names and affiliations

Amalia Papanikolaou[a,d], Georgios A. Keliris[a,f], Sangkyun Lee[b], T. Dorina Papageorgiou[b], Ulrich Schiefer[c,h], Nikos K. Logothetis[a,e], Stelios M. Smirnakis[b]

[a]Max Planck Institute for Biological Cybernetics, Spemannstr. 38, 72076 Tuebingen, Germany

[b]Department of Neuroscience and Neurology, Baylor College of Medicine, Houston, TX, 77030

[c]Center for Ophthalmology, University of Tuebingen, Tuebingen, Germany

[d]Graduate School of Neural and Behavioural Sciences, International Max Planck Research School, Tuebingen, Germany

[e]Division of Imaging Science and Biomedical Engineering, University of Manchester, Manchester M13 9PT, UK

[f]Bernstein Center for Computational Neuroscience, Tuebingen, Germany

[h]Competence Center Vision Research, Study Course "Ophthalmic Optics & Audiology", Faculty of Optics & Mechatronics, University of Applied Sciences, Aalen, Germany

Corresponding authors:

Amalia Papanikolaou
Max Planck Institute for Biological Cybernetics
Spemannstr. 38, 72076, Tuebingen, Germany
Phone: +49 7071 601 1662
Email: amalia.papanikolaou@tuebingen.mpg.de

Georgios Keliris, PhD
Max Planck Institute for Biological Cybernetics
Spemannstr. 38, 72076, Tuebingen, Germany
Phone: +49 7071 601 695
Email: georgios.keliris@tuebingen.mpg.de

Stelios M. Smirnakis, MD, PhD
Baylor College of Medicine, Department of Neuroscience and Neurology
One Baylor Plaza, Houston, TX, 77030, USA
Tel. +1-713-798-3972
email: ssmirnakis@cns.bcm.edu

Keywords:

fMRI, hV5/MT+, Cortical blindness, reorganization, blindsight

Abstract

Damage to the primary visual cortex (V1) leads to a scotoma in the retinotopically corresponding part of the visual field. Nonetheless, a small amount of residual visual sensitivity persists within the blind field. This residual capacity has been linked to activity observed in the middle temporal area complex (V5/MT+). However, it remains unknown whether the organization of area hV5/MT+ changes following V1 lesions. We measured population receptive fields in area hV5/MT+ of five patients with homonymous quadrantanopia as a result of V1+ lesions. Interestingly, we found responses in hV5/MT+ arising inside the scotoma for all patients and identified two possible sources of activation. 1) Responses might originate from a spared part of area V1 corresponding to the scotoma, but surprisingly they do not guarantee visual perception. 2) Responses independent of area V1 input suggesting the existence of functional V1-bypassing pathways.

Introduction

Partial lesions of the primary visual cortex (area V1) or its inputs lead to a scotoma in the contralateral visual hemifield, the extent of which corresponds retinotopically to the region affected. However, some patients retain a small amount of residual visual sensitivity within their blind field (Poppel et al., 1973, Weiskrantz et al., 1974). This residual performance, originally termed “blindsight”, suggests that there are alternate pathways to transmit information from the retina to cortex, which effectively bypass area V1.

Blindsight has been associated with activity observed in the middle temporal area (V5/MT) following V1 lesions. Experiments in macaque and New World marmoset monkeys showed that a significant proportion of V5/MT cells remain visually responsive in the absence of area V1 input (Bruce et al., 1986, Rodman et al., 1989, Maunsell et al., 1990, Rodman et al., 1990, Girard et al., 1992, Rosa et al., 2000, Schmid et al., 2010). In addition, Rosa et al. (Rosa et al., 2000) showed that many area MT neurons have ectopic receptive fields responding to the visual field surrounding the scotoma, suggesting reorganization. In contrast, experiments on New World owl monkeys showed that V5/MT depends entirely on V1 for visual activation (Kaas and Krubitzer, 1992, Krubitzer and Kaas, 1992, Collins et al., 2003, Collins et al., 2005). The basis of this discrepancy is not yet understood.

Visually driven activity was observed in human complex hV5/MT+ when moving stimuli were presented inside the blind visual field of a well-studied patient (G.Y.) with extensive area V1 injury (Barbur et al., 1993, ffytche et al., 1996, Morland et al., 2004). Visual-motion related activity in hV5/MT+ was also observed in a patient with homonymous hemianopia and Riddoch syndrome (Schoenfeld et al., 2002) and a patient with bilateral damage to the gray matter of V1 (Bridge et al., 2010). However, it is not known how the organization of area hV5/MT+ changes following chronic deprivation of V1 input.

Here we studied the organization of hV5/MT+ area in 5 patients with partial or complete quadrantanopia due to partial lesions of area V1 or the optic radiation. To do so, we developed a new method, which models the boundaries of population receptive fields (pRF) directly from the BOLD signal of each voxel in the visual cortex. This method was developed after we found significant errors in the pRF estimation in area hV5/MT+ of healthy subjects with simulated visual field scotomas (Papanikolaou et al., 2015) using existing pRF mapping methods (Dumoulin and Wandell, 2008, Lee et al., 2013).

Using this approach, we found that hV5/MT+ of the ipsilesional hemisphere does respond to stimuli presented within the scotoma. In 4/5 patients, it is possible that these responses originate from a spared, activated, part of area V1 that corresponds to the dense region of the scotoma, but they apparently do not contribute to visual awareness as judged by standard methods of visual field perimetry (methods). In 2/5 patients (one

patient showed both patterns) hV5/MT+ responses arise despite lack of significant corresponding V1 activation suggesting the existence of functional V1-bypassing pathways.

Results

Mapping the pRF boundaries separately for each direction of motion of the visual stimulus

Differences in the retinotopic maps of normal subjects have been observed when the visual stimulus is masked to simulate retinal or cortical scotomas compared to when the full visual field is stimulated (Haak et al., 2012a, Haak et al., 2012b, Binda et al., 2013). These biases are important to know in order to ensure that changes in retinotopic organization seen in patients are not simply an artifact of model estimation caused by incomplete stimulus presentation due to the presence of the visual field scotoma. We have recently shown that responses in area hV5/MT+ are nonlinearly affected after masking the upper left quadrant of the visual field in healthy subjects simulating an upper left quadrantanopia (artificial scotoma or AS) (Papanikolaou et al., 2015). In addition, we found erroneous pRF estimates inside the area corresponding to the AS, when we used the full bar stimulus model for estimating the pRFs when the actual stimulus presented included the AS. These biases occurred for both direct-fit methods (Dumoulin and Wandell, 2008) and topography based methods (Lee et al., 2013) and were not the result of a trivial methodological artifact but originated from asymmetric BOLD responses occurring when the bar stimulus moved from seeing to non-seeing locations of the visual field (Fig. 8 in Papanikolaou et al, 2015).

In patients retinotopic mapping is performed using a full stimulus (in this case a drifting checkerboard bar), which overlaps the area of the scotoma. Thus a different approach is needed for comparing responses between patients and AS subjects when using the drifting bar stimulus. We developed a method, which calculates directly the boundaries of the pRF from the BOLD time series of each voxel separately for each direction of motion of the visual stimulus. This was done by identifying the visual field locations where the BOLD activity starts to rise above baseline separately for each bar direction, in the spirit of classical methods of receptive field mapping (see methods). In this way, hysteresis phenomena in the BOLD signal can be directly observed and taken into account, and biases in pRF estimation can be eliminated. A schematic representation of method is shown in Fig. 1.

We used this method for estimating pRF responses in spared area hV5/MT+ of patients with V1+ or optic radiation lesions that resulted in dense contralateral scotomas, as described below.

Patients: Anatomical lesion and visual field defects

We examined 5 patients, P1-5, with complete or partial dense quadrantanopic defects. Each patient's lesion and consequent visual field defect is presented in detail in Table 1. The anatomical location of the lesion and patient retinotopic maps are presented in Fig. 2.

In brief, patients P1, P3, P4 have lesions which extend from the part of V1 inferior to the calcarine sulcus to extrastriate ventral visual areas, resulting in superior quadrantanopic defects (Fig. 3A.b,d,e). P2 has a superior quadrantanopia (Fig. 3A.c) following a temporal optic radiation lesion. P5 has a relatively smaller lesion, which involves part of the foveal ventral V1 and ventral extrastriate areas V2 and V3 resulting in a partial but dense quadrantanopic defect (Fig. 3A.f). Patients' P1, P2, P3 and P4 V1 organization has been described in more detail before (Papanikolaou et al., 2014).

Table 1: Patient data. Patient identification (ID), side of brain lesion (Hemisphere), visual areas affected by the lesion (Areas), type of homonymous visual field defect (LUQ: Left Upper Quadrantanopia, RUQ: Right Upper Quadrantanopia) and time span between brain lesion and examination (Δt). P1 has a left superior

quadrantanopic defect following a lesion of the right inferior calcarine cortex. The lesion extends from the part of V1 inferior to the calcarine sulcus to extrastriate cortex corresponding to the ventral visual areas V2 and V3. P2 has a superior quadrantic defect of the right visual field following a temporal optic radiation infarct of the left hemisphere. This deafferents a significant portion of V1 by cutting its input, while the gray matter of it remains intact. Patient P3 has a homonymous superior quadrantic defect of the right visual field following a lesion of the left V1 inferior to the calcarine sulcus and extrastriate cortex corresponding to ventral visual areas V2, V3 and V4. P4 has a lesion of the left inferior calcarine cortex, which involves ventral striate area V1, ventral extrastriate areas V2, V3 and V4, and extends to the dorsal area V1 where it spares a small part of the dorsal periphery. This has created a homonymous superior quadrantic defect of the right visual field. P5 has a lesion in the right hemisphere, which involves part of the foveal ventral V1 and ventral extrastriate areas V2 and V3, resulting in a partial quadrantanopic defect of the left visual field.

Patient ID	Hemisphere	Visual Areas	Visual Field Defect	Δt (years)
P1	Right	V1v, V2v, V3v	LUQ	7
P2	Left	Temporal optic radiation	RUQ	10
P3	Left	V1v, V2v, V3v, V4	RUQ	0,5
P4	Left	V1d (partially), V1v, V2v, V3v, V4,	RUQ	7
P5	Right	V1v (foveal), V2v, V3v	Partial LUQ	7

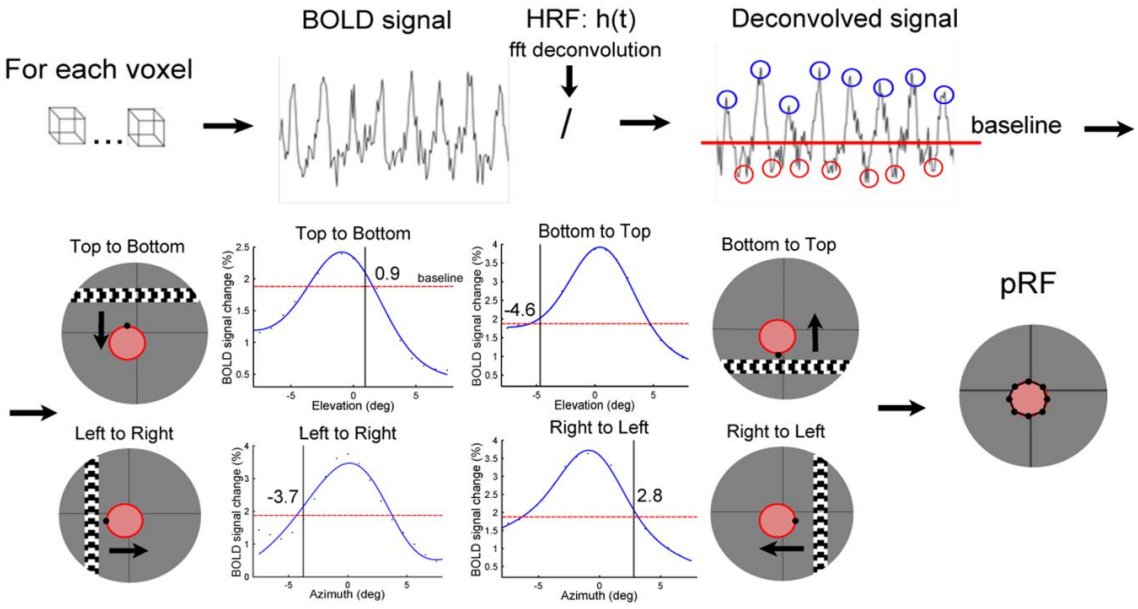

Fig. 1: Schematic illustration of the pRF mapping method. We estimated the boundaries of the pRF directly from the BOLD time series of each voxel in the visual cortex by marking the location in the visual field when BOLD activity starts to rise above a baseline threshold separately for each bar direction. For each voxel, a Fourier deconvolution method (fft deconvolution) is applied to the BOLD time series in order to estimate the actual response of the voxel as the stimulus is presented at each visual field location (see methods). Then a

baseline threshold (top right, red line) is calculated from the deconvolved signal as the 1/3 distance between the average of the local minima (red circles) and the local maxima (blue circles) of the BOLD signal. The BOLD signal is then separated for each bar direction and a two-term Gaussian model is fit to the data. An example of four out of the eight directions are shown (BOLD signal change as a function of the visual field location of the bar; bottom left). The blue line represents the fitted model and the red dotted line the baseline threshold. The pRF is estimated by marking the location in the visual space at the time when the fitted signal rises above baseline for each bar direction (black line). This forms an octagon (since there are 8 different bar directions) in visual space which represents the pRF (bottom right).

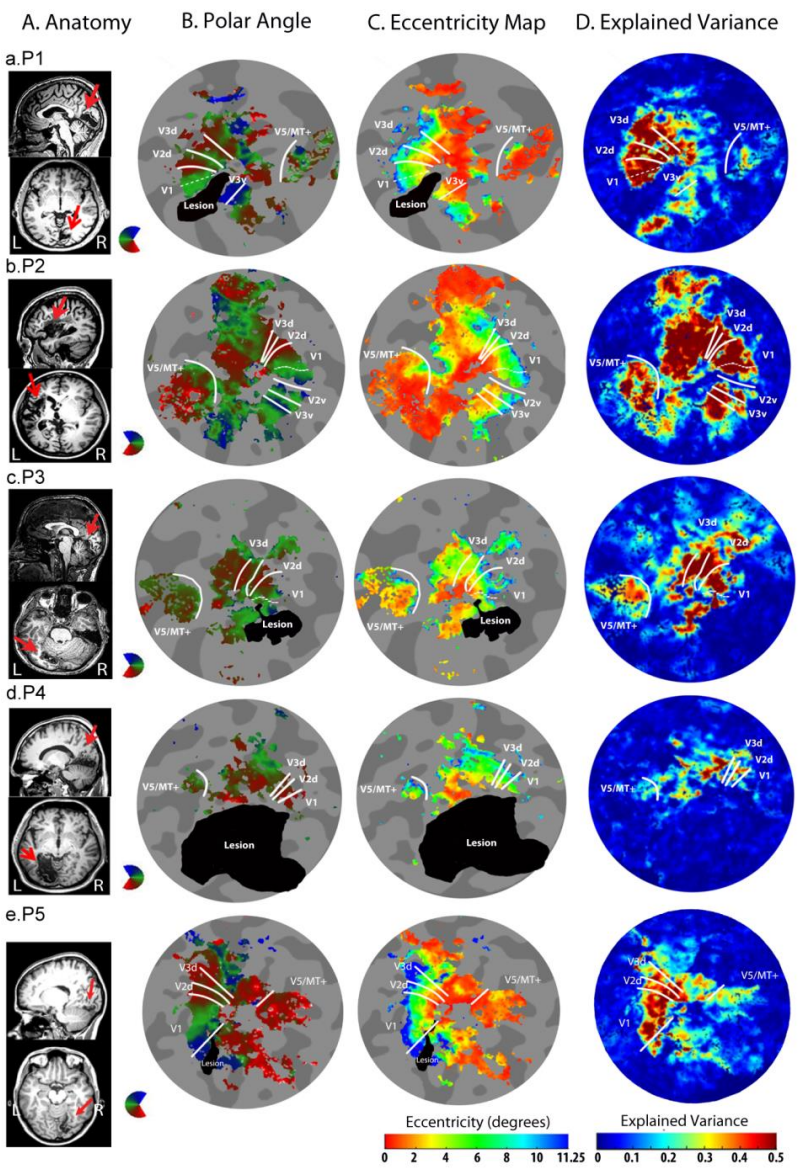

Fig. 2: Anatomical location of the lesion and retinotopic mapping for each patient. (A) Anatomical location of the lesion. A sagittal (top) and an axial (bottom) slice illustrates each patient's anatomical lesion (a red arrow points to the lesion). **(B-D)** Retinotopic mapping of each patient. The polar angle, eccentricity and variance explained maps are overlaid on the flattened occipital lobe of the lesioned hemisphere. The lesioned area is colored black. White contour lines indicate borders between visual areas. Patients P1, P2, P3 and P4 have been presented before in (Papanikolaou et al., 2014). The figure has been modified with permission to include the retinotopy maps of the new patient P5.

hV5/MT+ responses following partial V1+ lesions

Visual field coverage density maps

We compared hV5/MT+ coverage density maps with the same maps obtained from the spared portion of area V1 and with visual perimetry maps defining the perceptual scotoma. The maps represent the number of pRFs that cover each visual field location (methods). All patients showed activity in hV5/MT+ that extended well beyond the border of the scotoma into the superior (anopic) visual field quadrant (Fig. 3B.b-f). Raw BOLD responses from voxels in hV5/MT+ confirm that activity arises from stimulus presented within the visual field scotoma (Fig. 4). We identified two possible source mechanisms for this activation (see below).

Visual field regions overlapping with the patients' scotoma covered by both hV5/MT+ and V1:

For patients P1, P2, P3 and P5, visual field locations overlapping with the patients' perceptual scotoma in hV5/MT+ are also covered by V1 (Fig. 3B-C.b,c,d,f; red arrows) suggesting that hV5/MT+ responses arise from the spared part of area V1. Surprisingly however, these patients still have a dense visual field defect corresponding to these locations (Fig. 3A.b,c,d,f).

In principle, the lack of a percept may happen because: i) retinotopically corresponding extrastriate areas are injured, or ii) the activity generated may be too weak, too asynchronous, or too disorganized to elicit a percept. For patients P1, P3 and P5 the lesion includes extrastriate visual areas V2v and V3v (Fig. 2). Therefore the visual field deficit of these patients may be due to damage in these extrastriate areas. Nevertheless, visual information reaches area hV5/MT+ suggesting that the V1 to hV5/MT+ projection is largely spared.

Patient P2, however, has an optic radiation lesion and thus the pathways from V1 to higher visual areas are intact (Fig. 2). Therefore the visual field deficit of these patients cannot be due to damage in these extrastriate areas. Ventral areas V2 and V3 also showed responses that overlap with this patient's scotoma (

Fig. **5**), further supporting the viewpoint that extrastriate cortex remains functional in this case. In this case, option (ii) may dominate. We previously found (Papanikolaou et al., 2014), that the mean amplitude of area V1 pRF centers that fall inside the scotoma is significantly lower (0.77±0.09) than the mean amplitude of pRF centers that fall in the inferior (seeing) quadrant for this patient (1.06±0.05 stdev). The same holds in hV5/MT+ (mean pRF amplitude within the scotoma is 0.83±0.02 compared with 0.92±0.05 in the inferior/seeing quadrant). Note however, that the observed decrease is modest in both area V1 and hV5/MT+. This suggests that although it is possible that the decrease in the level of visually driven activity may contribute to the loss of visual perception, it is unlikely by itself to be the sole story (see next section).

Visual field areas overlapping with the patients' scotoma that are covered by hV5/MT+ but not V1:

The visual field coverage density maps of hV5/MT+ in patients P4, P1, cover parts of the visual field scotoma that are not covered by the spared part of area V1 (Fig. 3B-C.e,b; green arrows). In fact, the corresponding part of area V1 is anatomically lesioned (Fig. 2) suggesting that hV5/MT+ activity arises via pathways that bypass area V1, i.e. through the SC and pulvinar (Rodman et al., 1990) or through the LGN (Maunsell et al., 1990, Schmid et al., 2009, Schmid et al., 2010). However, input from these pathways is apparently not sufficiently strong or sufficiently organized to mediate conscious vision. Indeed, the mean amplitude of hV5/MT+ pRFs with center within the scotoma of patient P4 is smaller than the mean hV5/MT+ pRF amplitude in the healthy hemisphere (ratio: 0.67±0.1). However, weak modulation may contribute to the loss of vision, but cannot explain it: the inferior (seeing) quadrant outside the visual field scotoma has pRFs with similar mean amplitude (ratio: 0.68±0.1), without obvious visual field deficit. It is also evident that in normal subjects a modest decrease in the contrast of the stimulus may induce similar levels of activity in area hV5/MT+ or other extrastriate areas without compromising visual perception. A reasonable hypothesis is then that either i) activity in other extrastriate areas important for visual perception is sufficiently compromised to abolish the

visual percept, or ii) the activity seen in V1 and hV5/MT+ is abnormal at a finer scale not reflected in the BOLD signal, even though it impedes the formation of a visual percept.

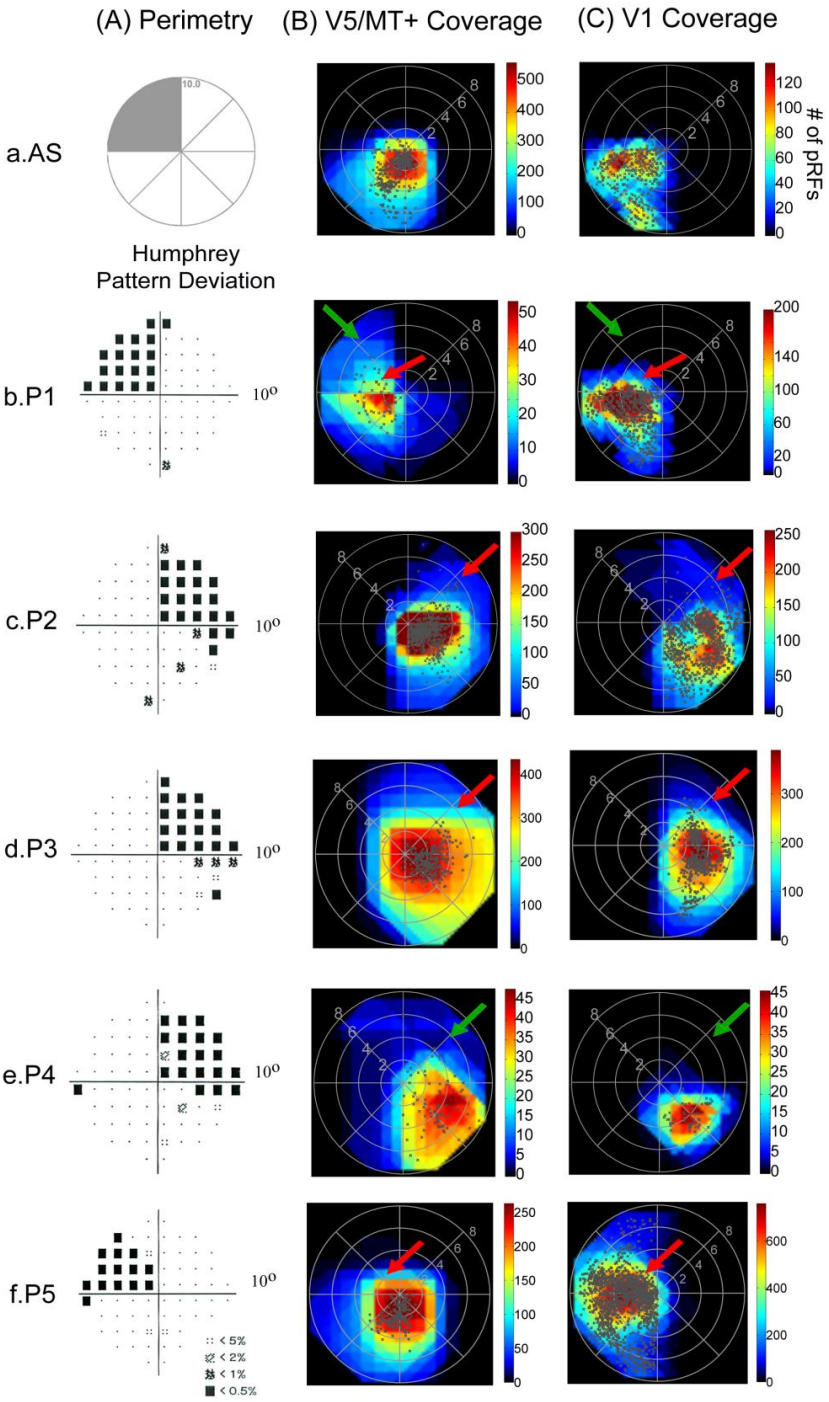

Fig. 3: Visual field coverage density maps of area hV5/MT+ and V1 of the lesioned hemisphere. (A) Pattern deviation probability plots of the 10-degree Humphrey type (10-2) visual field test for all patients. The small black dots show the locations in the visual field that are normal, while the black squares indicate a visual field defect on a $p < 0.5\%$ level according to the pattern probability plot (this means that less than 0.5% of normal subjects would be expected to have such a low sensitivity at this visual field location). Pattern deviation numeric plots for all patients had visual sensitivity < -20dB (absolute visual field scotoma) at all visual field locations within the affected quadrants. The perceptual scotoma was verified as well by a kinetic perimetry test (Octopus 101; methods). For simplicity only the Humphrey perimetries are presented here, since the kinetic perimetries agreed with the defect seen by Humphrey perimetry in the central visual field. **(B)** Visual field coverage density maps of area hV5/MT+ and **(C)** the spared part of area V1 of the lesioned hemisphere for each patient. The color map indicates the number (#) of pRFs that cover each visual field location. The pRF centers from all voxels

within each area are plotted as grey dots. Two main patterns of activity have been observed between patients. Patients P1, P2, P3, and P5 have visual field regions overlapping with the patients' scotoma that are covered by both hV5/MT+ and V1 (red arrows). Apparently this activity is not always sufficient to mediate conscious vision suggesting it is either too disorganized to elicit a percept or that damage to other areas is responsible for the visual deficit. On the other hand, patients P1, and P4 have visual field areas overlapping with the patients' scotoma that are covered by V5/MT+ but not V1 (green arrows) suggesting the existence of functional V1-bypassing pathways. Activity in hV5/MT+ alone is also not sufficient to elicit a percept.

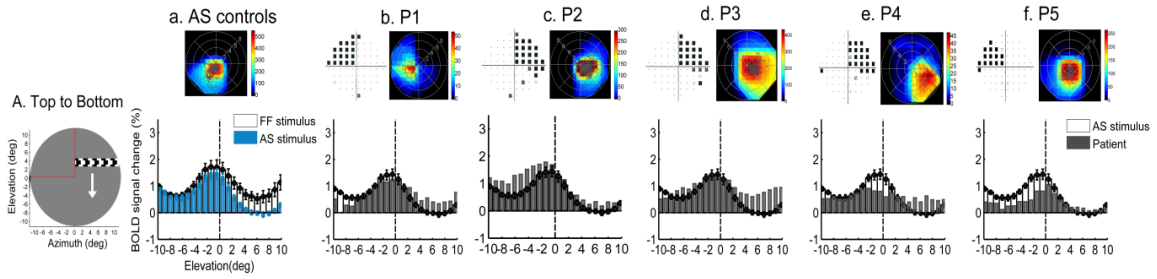

Fig. 4: **Average BOLD signal change in hV5/MT+.** The average BOLD signal change from all voxels in the right hV5/MT+ in controls and the hV5/MT+ of the lesioned hemisphere in patients (right hemisphere for P1 and P5, left hemisphere for P2, P3 and P4) as a horizontal bar is moving from the top (elevation>0; AS/scotoma) to the bottom of the visual field (elevation<0; seeing quadrant). Before averaging, the BOLD time series of each voxel is deconvolved to remove the hemodynamic response function (see methods) and the baseline is removed. The baseline here is defined as the signal value when the vertical bar is located in the far ipsilesional part of the visual field, which should produce little or no visual modulation in the region examined. This is calculated as the average BOLD signal change over 5 steps of the bar when the horizontal bar was located between 7-10° in the hemifield ipsilateral to our ROI. This procedure sets the baseline of each voxel to zero. **(a)** The average signal of the AS controls (blue bars) is compared with the full field stimulus condition (white bars). When the AS is applied, the average BOLD signal change when the bar is in the superior quadrant (location of the AS; elevation>0) drops to baseline values compared with the average signal under the full field stimulus condition. Activity starts when the bar is near 2° from the horizontal meridian (AS border), commensurate with the subject's fixation eye movements. **(b-f)** The average signal of the patients (gray bars) compared with the AS controls (white bars). For all patients, activity starts when the stimulus is located well within the perceptual scotoma (elevation>3°) in contrast to the AS controls. This suggests that, for the patients, hV5/MT+ activity in the lesioned hemisphere can either originate from stimulus positions located within the scotoma, or from the contralateral hemisphere via callosal connections. The error bars indicate the standard error of the mean across control subjects (N=5). The left column shows a snapshot of the orientation of the bar (orange color) and direction of motion (white arrow). On top, we plot instances of the visual field perimetry and visual field coverage density maps as presented in Fig. 3.

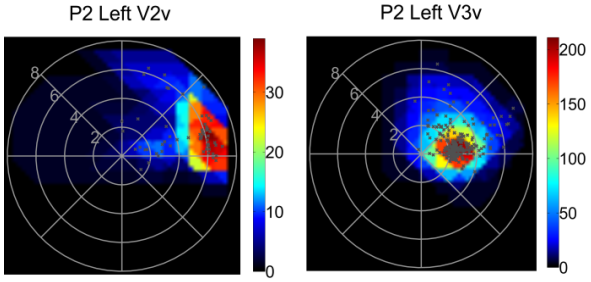

Fig. 5: **Visual field coverage density maps of ventral areas V2 and V3 of patient P2.** The visual field coverage density maps of areas V2v (left) and V3v (right) from the left hemisphere of patient P2. The color map indicates the number of pRF that cover

each visual field location. The pRF centers across all voxels within each area are plotted with grey dots.

It is important to note that the overlap between visual field coverage maps and the scotoma seen on perimetry cannot be explained by eye movements. Subjects were able to maintain fixation within 1.5° radius from the center of fixation except for very occasional excursions beyond this range (Fig. 6). The results remain unchanged after removing from the analysis the epochs where the subjects had eye deviations (>1.5°) from the fixation point. Patient's P3 eye movements were not recorded, but he performed a challenging detection task at fixation and his performance was maintained >80% correct.

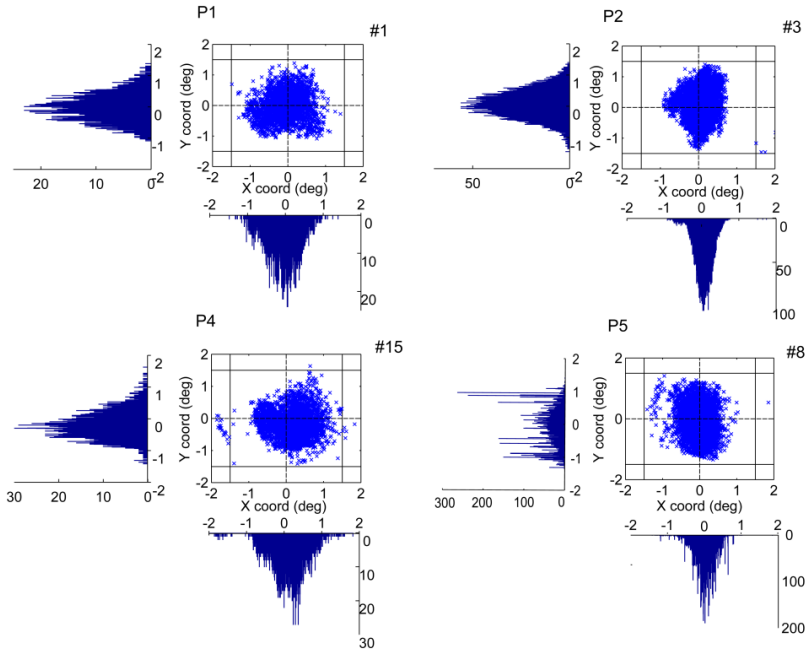

Fig. 6: **Eye movements for patients P1, P2, P4 and P5.** Eye positions are plotted at 60Hz for each subject for one whole session (6.4 min). The number of eye deviations, defined as excursions > 1.5^0 from the fixation point is indicated next to the graphs with the number sign (#).

In summary, we have identified responses in hV5/MT+ that cover the patients' scotoma. For some patients such hV5/MT+ responses appear to be mediated by spared V1 to hV5/MT+ projections while, for others, by V1-bypassing pathways. Unfortunately, visually driven BOLD activity observed in hV5/MT+ is not sufficient to mediate conscious vision. Perhaps more surprisingly, visually driven activity in corresponding regions of V1 and early extrastriate areas including hV5/MT+ does not guarantee visual perception in some subjects. This suggests that the fine coordination of visual activity patterns across visual areas may be an important determinant of whether visual perception persists following lesions of the visual system.

Discussion

We measured area hV5/MT+ responses in five patients (P1-5) with chronic post-chiasmatic lesions resulting in dense homonymous visual field quadrantanopia. We studied how area hV5/MT+ covers the visual field following V1+ lesions and how this corresponds to the perimetric scotoma.

One important question is whether there are responses in hV5/MT+ to stimuli presented within the scotoma and what pathways these responses arise from. For all patients, visual field coverage density maps of hV5/MT+ overlap with areas of the perimetric scotoma (Fig. 3). This is consistent with reports of V5/MT activity after V1 lesions in monkeys (Bruce et al., 1986, Rodman et al., 1989, Girard et al., 1992, Rosa et al., 2000, Schmid et al., 2010) and humans (Barbur et al., 1993, ffytche et al., 1996, Schoenfeld et al., 2002, Morland et al., 2004, Bridge et al., 2010). We identified two possible mechanisms for this activity.

Responses arising from the spared part of area V1. For 4/5 patients (P1-3, P5) there were visual field regions overlapping with the patients' perceptual scotoma that were covered by both area hV5/MT+ and area V1. Area hV5/MT+ activity corresponding to such regions likely arises from the spared part of area V1 (Fig. 3). We showed previously that pRF maps in spared V1 may overlap significantly with dense regions of the perimetric scotoma without contributing to visual awareness (Papanikolaou et al., 2014), and postulated that lesions downstream of V1 input may be responsible. Here we show that even though pRF maps of both area V1 and hV5/MT+ cover the same region of the scotoma, this does not guarantee that visual awareness will be present there (Fig. 3). Patients P1, P3 and P5 have a cortical lesion that involves ventral areas V2 and V3 suggesting that the visual field deficit in the superior quadrant of these patients may be due to loss of activity in these areas. This however cannot explain the visual field deficit of patient P2, who has an optic radiation lesion that spares projection pathways of area V1 as well as extrastriate areas. Therefore the coverage maps of P2's extrastriate areas are largely intact (

Fig. **5**). Nevertheless, this subject has a dense quadrantanopia (Fig. 3A.c). One possible explanation may be that the level of activity elicited by visual stimulation in this patient is not sufficient to support useful vision. However, the mean amplitude of pRFs covering the scotoma in subject P2 is decreased by only ~27% compared to "seeing" locations, both in area V1 and hV5/MT+. It is unlikely that this could be the sole cause for the perceptual defect, since: 1) such decreases are routine when presenting stimuli of low contrast without affecting visual perception, 2) similarly low pRF amplitudes sometimes occur in seeing locations (area hV5/MT+ of patient P4). These observations suggest that the BOLD signal amplitude of the pRF maps, a surrogate measure of visual modulation strength, is not necessarily a good indicator of residual visual perceptual capacity. Instead, disrupted or poorly synchronized organization of visual processing as a result of the optic radiation lesion is likely to play a significant role.

Responses arising from V1-bypassing pathways. For 2/5 patients (P1 and P4) there are visual field regions covered by area hV5/MT+ that are not covered by V1. In fact, the part of V1 corresponding to these areas of the visual field is anatomically lesioned Fig. 2. Since activity in these locations arises from stimulus presented within the scotoma (Fig. 4), this strongly suggests that there are V1-bypassing pathways capable of activating area hV5/MT+ in these patients. Activity in these pathways is also not sufficient to reduce the size of the scotoma in visual field perimetry however.

In contrast to prior reports (Barbur et al., 1993, Zeki and Bartels, 1999) our results suggest that activation of hV5/MT+ alone is not sufficient for visual awareness. Other studies have pointed out the importance of feedback projections from V5/MT to V1 (Cowey and Walsh, 2000, Pascual-Leone and Walsh, 2001, Silvanto et al., 2005) supporting the idea that V1 is critical for conscious perception. Here we showed that V1 and hV5/MT+ can be simultaneously active, presumably because feedforward projections from V1 to hV5/MT+ remain intact, but this is not necessarily a sufficient condition for conscious perception. It is unlikely that the lesion has selectively damaged the feedback connections from hV5/MT+ to V1 while sparing feedforward connections. Our results suggest two possibilities that can contribute to the loss of visual perception: 1) extrastriate visual areas V2/V3 play an important role in visual awareness (Horton and Hoyt, 1991, Merigan et al., 1993, Slotnick and Moo, 2003, Salminen-Vaparanta et al., 2012) and their injury contributes significantly to the loss of visual perception. 2) Activity across visual areas becomes too asynchronous or disorganized for awareness to arise (Pollen, 1999).

Conclusions

We found that pRF maps of ipsi-lesional area hV5/MT+ overlap significantly with regions of the dense perimetric scotoma. In some cases these regions are covered by both V1 and hV5/MT+ while in others they are covered only by hV5/MT+ suggesting the existence of functional V1 bypassing pathways. Apparently, hV5/MT+ activation, even if accompanied by activity in corresponding parts of V1 cannot guarantee visual perception. It would be interesting to characterize whether different regions of the scotoma have different capacity for recovery based on their profile of coverage by spared visual areas. If this turns out to be the case, characterizing the changes occurring in extrastriate visual areas following V1 lesions could help us develop better strategies for visual rehabilitation.

Materials and Methods

Subjects: *Patients*. Five adult subjects (27-64 years old, 3 females) with visual cortical lesions participated in our study. Four of the patients were recruited at the Center for Ophthalmology of the University Clinic in Tuebingen and one at the Center for Advanced MR Imaging (CAMRI) of the Baylor College of Medicine (BCM). Four of the participants suffered from homonymous visual field deficits as a result of ischemic or hemorrhagic stroke 7-10 years before they enrolled in our study. One patient however, sustained an ischemic stroke 0.5 years prior to study recruitment (Table 1). The extent and location of the injury was confirmed by MRI anatomical acquisition (see below).

Controls. Five healthy subjects (22-65 years old, 4 females) were recruited as controls. All subjects, patients and controls, had normal or corrected-to-normal visual acuity. The experiments were approved by the Ethical Committee of the Medical Faculty of the University of Tuebingen, and the IRB committee of the Baylor College of Medicine.

Perimetric visual field tests: All patients underwent a Humphrey type (10-2) visual field test (Beck et al., 1985, Trope and Britton, 1987), with a background luminance level of 10 cd/m². We present the Humphrey pattern deviation plots for all patients in Fig. 3. The small black dots show the locations in the visual field that are normal, while the black squares indicate defective locations ($P < 0.5\%$ indicates that the pattern deviation value for that test location will be found in less than 0.5% of normal subjects). Pattern deviation numeric plots for all patients had visual sensitivity <-20dB (absolute visual field scotoma) at all visual field locations within the affected quadrants. Black square locations outside the affected quadrants showed visual sensitivity <-10dB (mostly still <-20dB). Patients P1, P2, P4 and P5 underwent additionally a binocular semi-automated 90° kinetic perimetry obtained with the OCTOPUS 101-perimeter (HAAG-STREIT, Koeniz, Switzerland) (Hardiess et al., 2010) which verified scotoma.

Data acquisition and preprocessing: Functional and structural MRI experiments were performed at the Max Planck Institute for Biological Cybernetics, Tuebingen, Germany and at the CAMRI of BCM, using a 3.0 Tesla high-speed echo-planar imaging device (Trio, Siemens Ltd., Erlargen, Germany) with a quadrature head coil. At least two T1-weighted anatomical volumes were acquired for each subject with a three-dimensional magnetization prepared rapid acquisition gradient echo (T1 MPRAGE scan) and averaged following alignment to increase signal to noise ratio (matrix size= 256×256, voxel size= 1×1×1 mm^3, 176 partitions, flip angle= 9°, TR= 1900 ms, TE= 2.26 ms, TI= 900 ms). At Tuebingen, blood oxygen level dependent (BOLD) image volumes were acquired using gradient echo sequences of 28 contiguous 3 mm-thick slices covering the entire brain (repetition time [TR] = 2,000 ms, echo time [TE] = 40 ms, matrix size=64×64, voxel size=3×3×3 mm3, flip angle=90°). Functional image (echo planar) acquisition at BCM consisted of 29, 3.6mm-thick slices covering the entire brain (TR = 2,000 ms, TE = 30 ms, matrix size=64×64, voxel size = 3.46×3.46×3.6 mm 3, flip angle=90°; 200 volumes).

At least 5 functional scans were acquired for each subject, consisting of 195 image volumes, the first 3 of which were discarded. The functional images were corrected for motion in between and within scans (Nestares and Heeger, 2000). Subsequently, fMRI data were averaged across scans. The functional images were aligned to the high-resolution anatomical volume using a mutual information method (Maes et al., 1997) where the resampled time series values in the volume are spatially interpolated relative to the nearest functional voxels. Preprocessing steps were performed in MATLAB using the mrVista toolbox (http://white.stanford.edu/software/).

Stimuli: Subjects were presented with moving square-checkerboard bars (100% contrast) through MRI compatible digital goggles (VisuaStim, Resonance Technology Company, Inc, Northridge, CA, USA; 30° horizontal and 22.5° vertical field of view, 800x600 resolution, min luminance = 0.3cd/m2 and max luminance = 12.2cd/m2). The stimulus was presented within a circular aperture with a radius of 11.25° around the fixation point. The bar width was 1.875° and travelled sequentially in 8 different directions, moving by a step half of its size (0.9375°) every image volume acquisition (TR=2 seconds). Stimuli were generated using Psychtoolbox (Brainard, 1997) and an open toolbox (VISTADISP) in MATLAB (The Mathworks, Inc.). The subjects' task was to fixated a small dot in the center of the screen (radius: 0.0375°; 2 pixels) and respond to the color change by pressing a button. The color was changing randomly with a frequency of one every 6.25 seconds. An infrared eye tracker was used to record eye movements (iView XTM, SensoMotoric Instruments GmbH). The eye movement traces of patients P1, P2, P4 and P5 are shown in Fig. S3. One patient (P3) was not eyetracked. However, his accuracy at the fixation task was always more than 80% suggesting that the subject could maintain fixation.

Control subjects were asked to participate for a second session during which an isoluminant mask was placed in the left superior quadrant of the visual field, simulating a left upper quadrantanopia ("artificial scotoma" of AS). All other stimulus' parameters stayed the same.

Population receptive field mapping: We estimated the boundaries of the pRF directly from the BOLD time series of each voxel in the visual cortex. The pRF boundaries were identified by marking the location in the visual field where the BOLD activity starts to rise above baseline separately for each bar direction. The following steps were taken in order to estimate this: 1) A deconvolution method was applied to the BOLD time series of each voxel in order to estimate the actual response of the voxel as the stimulus is presented at each visual field location. To do so, the BOLD time series of each voxel were averaged across scans to reduce the signal to noise ratio. The averaged signal was further smoothed using locally weighted linear regression (lowess method in MATLAB) in order to avoid outliers that can be amplified after deconvolution. Then a Fourier deconvolution is applied to remove the hemodynamic response function from the data. 2) A baseline was calculated from the deconvolved signal of each voxel. The local maximum and minimum peaks of the deconvolved BOLD time series were calculated using function *findpeaks* (MATLAB). A minimum peak distance was set according to the stimulus duration for each bar direction. This way, only the local peaks that correspond to each bar direction are identified. The baseline is then estimated as the 1/3 distance between the average of the minimum and maximum peaks. This threshold was set after calculating the noise in non-visually responsive locations. 3) The BOLD signal of each voxel was then separated for each bar direction and a two-term Gaussian model was fit to the data. The pRF boundaries were estimated by marking the location in the visual space at the time the fitted signal rises above baseline for each bar direction. This forms an octagon (since there are 8 different bar directions) in visual space, which represents the pRF (see Fig. 1).

The pRF center is estimated as the center of the octagon. The pRF amplitude of each voxel is estimated as the mean peak amplitude of the fitted Gaussian for each bar direction. The average pRF amplitude of an area in the lesioned hemisphere is normalized by the average pRF amplitude from the same area on the contra-lesional hemisphere.

Visual field coverage density maps: The visual field coverage density maps define the locations within the visual field that that are covered by the pRFs of voxels within a region of interest (ROI) in the cortex. To estimate this we plot at each visual field location the number of the pRFs that cover this location (color map). The pRF centers (estimated as described above) across all voxels within the ROI are overlaid as grey dots.

References

Barbur JL, Watson JD, Frackowiak RS, Zeki S (1993) Conscious visual perception without V1. Brain : a journal of neurology 116 (Pt 6):1293-1302.

Beck RW, Bergstrom TJ, Lichter PR (1985) A clinical comparison of visual field testing with a new automated perimeter, the Humphrey Field Analyzer, and the Goldmann perimeter. Ophthalmology 92:77-82.

Binda P, Thomas JM, Boynton GM, Fine I (2013) Minimizing biases in estimating the reorganization of human visual areas with BOLD retinotopic mapping. Journal of vision 13:13.

Brainard DH (1997) The Psychophysics Toolbox. Spat Vis 10:433-436.

Bridge H, Hicks SL, Xie J, Okell TW, Mannan S, Alexander I, Cowey A, Kennard C (2010) Visual activation of extra-striate cortex in the absence of V1 activation. Neuropsychologia 48:4148-4154.

Bruce CJ, Desimone R, Gross CG (1986) Both striate cortex and superior colliculus contribute to visual properties of neurons in superior temporal polysensory area of macaque monkey. Journal of neurophysiology 55:1057-1075.

Collins CE, Lyon DC, Kaas JH (2003) Responses of neurons in the middle temporal visual area after long-standing lesions of the primary visual cortex in adult new world monkeys. The Journal of neuroscience : the official journal of the Society for Neuroscience 23:2251-2264.

Collins CE, Xu X, Khaytin I, Kaskan PM, Casagrande VA, Kaas JH (2005) Optical imaging of visually evoked responses in the middle temporal area after deactivation of primary visual cortex in adult primates. Proceedings of the National Academy of Sciences of the United States of America 102:5594-5599.

Cowey A, Walsh V (2000) Magnetically induced phosphenes in sighted, blind and blindsighted observers. Neuroreport 11:3269-3273.

Dumoulin SO, Wandell BA (2008) Population receptive field estimates in human visual cortex. Neuroimage 39:647-660.

ffytche DH, Guy CN, Zeki S (1996) Motion specific responses from a blind hemifield. Brain : a journal of neurology 119 (Pt 6):1971-1982.

Girard P, Salin PA, Bullier J (1992) Response selectivity of neurons in area MT of the macaque monkey during reversible inactivation of area V1. Journal of neurophysiology 67:1437-1446.

Haak KV, Cornelissen FW, Morland AB (2012a) Population receptive field dynamics in human visual cortex. PLoS One 7:e37686.

Haak KV, Langers DR, Renken R, van Dijk P, Borgstein J, Cornelissen FW (2012b) Abnormal visual field maps in human cortex: A mini-review and a case report. Cortex.

Horton JC, Hoyt WF (1991) Quadrantic visual field defects. A hallmark of lesions in extrastriate (V2/V3) cortex. Brain 114 (Pt 4):1703-1718.

Kaas JH, Krubitzer LA (1992) Area 17 lesions deactivate area MT in owl monkeys. Vis Neurosci 9:399-407.

Krubitzer LA, Kaas JH (1992) The somatosensory thalamus of monkeys: cortical connections and a redefinition of nuclei in marmosets. The Journal of comparative neurology 319:123-140.

Lee S, Papanikolaou A, Logothetis NK, Smirnakis SM, Keliris GA (2013) A new method for estimating population receptive field topography in visual cortex. Neuroimage 81:144-157.

Maes F, Collignon A, Vandermeulen D, Marchal G, Suetens P (1997) Multimodality image registration by maximization of mutual information. IEEE Trans Med Imaging 16:187-198.

Maunsell JH, Nealey TA, DePriest DD (1990) Magnocellular and parvocellular contributions to responses in the middle temporal visual area (MT) of the macaque monkey. The Journal of neuroscience : the official journal of the Society for Neuroscience 10:3323-3334.

Merigan WH, Nealey TA, Maunsell JH (1993) Visual effects of lesions of cortical area V2 in macaques. The Journal of neuroscience : the official journal of the Society for Neuroscience 13:3180-3191.

Morland AB, Le S, Carroll E, Hoffmann MB, Pambakian A (2004) The role of spared calcarine cortex and lateral occipital cortex in the responses of human hemianopes to visual motion. J Cogn Neurosci 16:204-218.

Nestares O, Heeger DJ (2000) Robust multiresolution alignment of MRI brain volumes. Magn Reson Med 43:705-715.

Papanikolaou A, Keliris GA, Lee S, Logothetis NK, Smirnakis SM (2015) Nonlinear population receptive field changes in human area V5/MT+ of healthy subjects with simulated visual field scotomas.

Papanikolaou A, Keliris GA, Papageorgiou TD, Shao Y, Krapp E, Papageorgiou E, Stingl K, Bruckmann A, Schiefer U, Logothetis NK, Smirnakis SM (2014) Population receptive field analysis of the primary visual cortex complements perimetry in patients with homonymous visual field defects. Proceedings of the National Academy of Sciences of the United States of America 111:E1656-1665.

Pascual-Leone A, Walsh V (2001) Fast backprojections from the motion to the primary visual area necessary for visual awareness. Science 292:510-512.

Pollen DA (1999) On the neural correlates of visual perception. Cerebral cortex 9:4-19.

Poppel E, Held R, Frost D (1973) Leter: Residual visual function after brain wounds involving the central visual pathways in man. Nature 243:295-296.

Rodman HR, Gross CG, Albright TD (1989) Afferent basis of visual response properties in area MT of the macaque. I. Effects of striate cortex removal. The Journal of neuroscience : the official journal of the Society for Neuroscience 9:2033-2050.

Rodman HR, Gross CG, Albright TD (1990) Afferent basis of visual response properties in area MT of the macaque. II. Effects of superior colliculus removal. The Journal of neuroscience : the official journal of the Society for Neuroscience 10:1154-1164.

Rosa MG, Tweedale R, Elston GN (2000) Visual responses of neurons in the middle temporal area of new world monkeys after lesions of striate cortex. The Journal of neuroscience : the official journal of the Society for Neuroscience 20:5552-5563.

Salminen-Vaparanta N, Koivisto M, Noreika V, Vanni S, Revonsuo A (2012) Neuronavigated transcranial magnetic stimulation suggests that area V2 is necessary for visual awareness. Neuropsychologia 50:1621-1627.

Schmid MC, Mrowka SW, Turchi J, Saunders RC, Wilke M, Peters AJ, Ye FQ, Leopold DA (2010) Blindsight depends on the lateral geniculate nucleus. Nature 466:373-377.

Schmid MC, Panagiotaropoulos T, Augath MA, Logothetis NK, Smirnakis SM (2009) Visually driven activation in macaque areas V2 and V3 without input from the primary visual cortex. PLoS One 4:e5527.

Schoenfeld MA, Noesselt T, Poggel D, Tempelmann C, Hopf JM, Woldorff MG, Heinze HJ, Hillyard SA (2002) Analysis of pathways mediating preserved vision after striate cortex lesions. Ann Neurol 52:814-824.

Silvanto J, Lavie N, Walsh V (2005) Double dissociation of V1 and V5/MT activity in visual awareness. Cerebral cortex 15:1736-1741.

Slotnick SD, Moo LR (2003) Retinotopic mapping reveals extrastriate cortical basis of homonymous quadrantanopia. Neuroreport 14:1209-1213.

Trope GE, Britton R (1987) A comparison of Goldmann and Humphrey automated perimetry in patients with glaucoma. Br J Ophthalmol 71:489-493.

Weiskrantz L, Warrington EK, Sanders MD, Marshall J (1974) Visual capacity in the hemianopic field following a restricted occipital ablation. Brain 97:709-728.

Zeki S, Bartels A (1999) Toward a theory of visual consciousness. Conscious Cogn 8:225-259.

A.6 "A Systematic Approach to Visual System Rehabilitation - Population Receptive Field Analysis and Real-time Functional Magnetic Resonance Imaging Neurofeedback Methods"

Chapter 14

A Systematic Approach to Visual System Neurorehabilitation — Population Receptive Field Analysis and Real-time Functional Magnetic Resonance Imaging Neurofeedback Methods

T. Dorina Papageorgiou, Amalia Papanikolaou and Stelios M. Smirnakis

Additional information is available at the end of the chapter

http://dx.doi.org/10.5772/57000

1. Introduction: Is visual rehabilitation inside a cortical scotoma possible, in principle?

Visual information transmission flows from the retinal ganglion cells to the lateral geniculate nucleus and then to the primary visual cortex (V1), the chief cortical relay of visual information and in turn, to "higher" extrastriate areas. Beyond area V1, visual processing is distributed across multiple interconnected brain areas, the precise role of which and their interactions are not yet, completely understood. To add to the dynamic complexity of the system, feedback from higher areas and modulation by top-down processes, such as attention are often critical in the formation of visual percepts (Deco and Lee; 2004; Olhausen, 2003; Kastner and Ungerleider, 2000; Mumford, 1994; Hubel and Weisel, 1977).

Impairment of visual function can occur at any point along the visual pathway from the eye to the cortex. We focus our discussion here on V1 lesions, which result in dense contralateral visual field defects known as "scotomas". Scotomas as a consequence of area V1 lesions often involve the contralateral half of the visual field resulting in hemianopia, or a contralateral visual field quadrant the consequence of which is quadrantanopia. V1 lesions are the most prevalent injury of the visual cortex, often occurring as a result of posterior cerebral artery (PCA) stroke, hemorrhage, or traumatic brain injury (TBI) (Pambakian and Kennard, 1997; Zhang et al., 2006; Ajina and Kennard, 2012). Twenty to thirty percent of stroke survivors experience visual disability (Taylor, 1997; Gilhotra et al., 2002; Giorgi et al., 2009), while the

incidence of significant visual perceptual impairment in TBI victims exceeds 50% in some studies (McKenna et al., 2006; Lew et al., 2007; Elisevich et al., 1984). The loss of visual perception inside a large scotoma can significantly affect the patient's ability to perform daily tasks, navigate in unknown environments, and function independently (Ajina and Kennard, 2012; Rizzo and Robin, 1996; Riggs, et al., 2007). Visual rehabilitation is clearly necessary for the daily living function of these patients. The literature describing visual rehabilitation efforts is extensive and doing justice to it all is beyond the scope of this chapter. We should mention at the outset that we will not discuss, the large literature on practicing eye movement strategies or, using prisms to remap the unseen onto the seen part of the visual field. Instead, we focus on novel approaches that aim to enhance perception inside the visual field scotoma.

To date, no established method exists to rehabilitate visual perception in adult patients with lesions of the primary visual cortex. The lack of effective methods for rehabilitation has led to the general perception that the adult visual cortex has decreased capacity to compensate after injury. This engenders diminished hope that successful strategies can be established to promote the recovery of visual perception after cortical injury. This is partly justified, as several attempts claiming to have achieved significant results have failed. The most notable recent example is an effort by Nova Vision claiming that a rehabilitative paradigm based on a "saccade-to-target" task could significantly shrink dense visual field scotomas (Kasten et al.; 1998, 1999; 2000, 2001, 2006; Poggel et al., 2001, 2004, 2006; Sabel et al., 2000, 2004; Werth and Moehrenschlager, 1999; Zihl and VonCramon, 1979; Zihl and Von Carmon, 1985; Jobke et al., 2009). Albeit early psychophysical training methods and Nova Vision studies were seen as promising (Kerkhoff et al., 1992; Kerkhoff et al., 1994; Julkunen, 2003; Kasten et al., 1995; 1998a, b, 1999; 2000, 2001; Poggel et al., 2001, 2004, 2006; Sabel et al., 2000, 2004; Werth and Moehrenschlager, 1999; Zihl and VonCramon, 1979; Zihl, 1990), later studies implementing rigorous eye movement controls failed to find a reduction in the visual field scotoma in patients with V1 lesions (Reinhard et al., 2005; Horton, 2005a; Horton, 2005b; Pleger et al., 2003).

Although these efforts are disappointing, the rehabilitation of scotomas resulting from V1 injuries is not altogether a cause without hope (Kasten et al., 1998; Huxlin et al., 2009; Schmid et al., 2010; Poggel et al., 2010; Sahraie et al., 2010; Schmid et al., 2009; Alexander and Cowey, 2009). On one hand, patchy injuries to area V1 or its inputs in the optic radiation seem to be amenable to rehabilitation, as training can help recruit and strengthen surviving connections. In support of this, Sabel and colleagues (Kasten et al., 1999) showed that ~74% of patients with partial optic nerve involvement showed significant recovery with training, compared to 29% of patients with post-chiasmatic lesions. This is likely the result of increased recruitment of partially-lesioned fiber pathways or islands of residual vision (Fendrich et al., 1992). On the other hand, recent evidence suggests that even when lesions to area V1 or, its proximal inputs are dense, it may be possible to some extent to functionally bypass the area of the injury:

First, there exist anatomical pathways that bypass the area of V1 injury (fig. 1). One such pathway projects from the retina to the koniocellular (intercalated) layers of the lateral geniculate nucleus directly, or to the superior colliculus and from there to extrastriate cortex. This pathway originates in the retinal Pγ class of ganglion cells, which comprises ~10% of the total ganglion cell number is particularly dense near the fovea (Henry and Reid, 2000), and is

http://dx.doi.org/10.5772/57000

known to survive retrograde degeneration following V1 lesions (Cowey and Stoerig, 1989). Another V1-bypassing pathway projects from the retina to the pulvinar directly or via the superior colliculus and from there to the extrastriate visual areas. Notably, although parvocellular and magnocellular projections to the lateral geniculate nucleus and beyond markedly atrophy following striate cortical lesions (Vanburen, 1963; Mihailovic et alo., 1971), superior collicular (Dineen et al., 1982) and pulvinar (Cowey, 1974) projections remain unchanged.

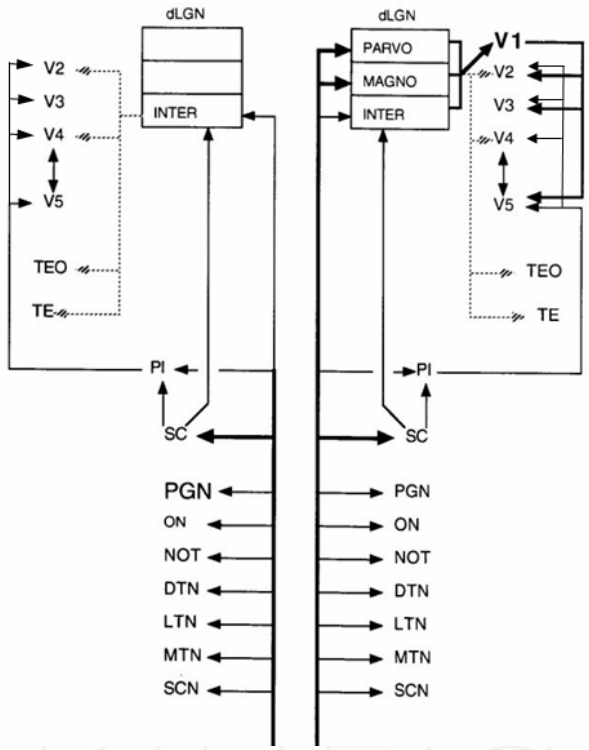

Figure 1. Overview of relevant anatomical visual pathways (Modified with permission from Stoerig and Cowey, 1997): Possible extra-geniculostriate pathways contributing to blindsight behavior, and residual extrastriate cortex activity, adapted from Stoerig and Cowey (Stoerig and Cowey, 1997). This diagram shows known retinofugal inputs, and some of the subsequent projections. On the right, the pathways are shown with intact V1. On the left V1 has been lesioned. Two pathways stand out as potentially mediating the residual activity observed in extrastriate cortex (Rodman et al., 1989; Schmid et al., 2009; Schmid et al., 2010), as well as related aspects of blindsight behavior: **1)** The koniocellular pathway (dotted lines) from the K (intercalated) layers of the thalamus directly to areas V2, V3, V4, V5/MT. This pathway originates in the retinal Pγ class of ganglion cells, comprising ~10% of total ganglion cells, survives retrograde degeneration following V1 lesions, and is particularly dense near the fovea (Cowey and Stoerig, 1989; Henry and Reid, 2000). This pathway receives both direct retinal and superior collicular input. **2)** The projection from the inferior pulvinar to V2, V3, V4, V5/MT, which also receives direct input from the retina, as well as input from the retinotectal (superior colliculus) pathway. PGN: pre-geniculate nucleus, ON: olivary nucleus, NOT: nucleus of optic tract, MTN, LTN, DTN: medial, lateral, dorsal terminal accessory optic nuclei, SCN: suprachiasmatic nucleus, SC: superior colliculus, PI: inferior pulvinar.

Second, these pathways have been shown to be functional under certain conditions. Lesions of area V1 or its post-chiasmatic afferents deprive the extrastriate visual cortex of its main input and result in a dense contralateral visual field scotoma, in which conscious visual perception is thought to be irreversibly lost (Cowey and Stoerig, 1991; Stoerig and Barth, 2001). Remarkably, despite the absence of a conscious visual percept, a capacity to process certain attributes of the visual stimulus persists inside the scotoma, the phenomenon known as "blindsight" (Kluver, 1936; Poppel et al., 1973; Weiskrantz, 1974). The blindsight phenomenon implies that at least some extra-geniculo-striate retinofugal pathways (Cowey, 2010; Schmid et al., 2010; Weiskrantz, 2004; Schoenfeld et al, 2002; Moore et al., 2001; Goebel et al., 2001; Stoerig and Cowey, 1997; Moore et al., 1995; Cowey and Stoerig, 1991; Girard et al., 1991; Pasik and Pasik, 1971) can functionally bypass area V1. This is corroborated by experiments in humans and primates, which have directly demonstrated that extrastriate areas can be modulated by the visual stimulus in the absence of V1 input (Rodman et al., 1989; Baseler et al., 1999; Goebel et al., 2001; Schmid et al., 2009; Schmid et al., 2010). For example, Rodman and Gross demonstrated that area V5/MT can be directly activated through the pathway bypassing area V1 via the superior colliculus (Rodman et al., 1989; Rodman et al., 1990), while Schmid et al. (Schmid et al., 2009; Schmid et al., 2010) showed that early extrastriate areas V2, V3 can be visually modulated by the LGN in the absence of V1 input. Schmid et al. further elucidated that transiently inactivating LGN in V1 lesioned animals not only abolishes visual modulation in areas V2, V3 but also, returns the monkey's blindsight performance to chance. Unfortunately, the V1-bypassing pathways that mediate the blindsight phenomenon are weak and of limited practical value. The potential of these pathways to induce recovery remains unrealized. This underscores the need to examine the mechanisms underlying the recovery reported in recent studies (Huxlin et al., 2008; Huxlin et al., 2009; Sahraie et al., 2006) in order to understand how to develop effective rehabilitative paradigms. It remains to be examined whether novel neuro-rehabilitative training algorithms can strengthen V1-bypassing pathways to derive practical benefit.

Third, training can improve performance inside the scotoma of subjects with area V1 lesions. Behavioral training in healthy subjects can improve visual performance by inducing plasticity and reorganization in the physiology of visual networks (Karni and Sagi, 1991; Liu et al., 2000; Yang and Maunsell, 2004; Ahissar and Hochstein, 1997). Perceptual learning is retinotopically specific, suggesting it involves a use-dependent synaptic enhancement induced by pre-and postsynaptic activity (Brown et al., 1988). Studies in humans (Pleger et al., 2003; Taub et al., 2002; Weiller, C. 1998; Lindberg et al., 2003, Takeuchi et al., 2005) and animals (Rudolph et al., 1994; Rudolph and Pasternak, 1999; Rudolph and Delay, 1993, Fabre-Thorpe et al., 1994; Friel et al., 2000; Huxlin and Pasternak, 2004) with V1 lesions, as well as behavioral studies of "blindsight" (Chokron et al., 2008; Stoerig and Cowey, 1997; Sahraie et al., 2006; Overgaard, 2011) suggest that visual performance in the scotoma can also improve with training (Raninen et al., 2007; Henriksson et al., 2007). More recently, Huxlin et al. (2006)-following their work on cats-trained V1+lesioned patients to perform a two-alternative forced choice random dot kinematogram (RDK) direction of motion

http://dx.doi.org/10.5772/57000

discrimination task in their blind hemifield (Huxlin et al., 2009). *Remarkably, direction of motion discrimination thresholds recovered from chance to normal at trained locations (Huxlin et al., 2009).* Eye movements were strictly controlled, and there were no obvious artifacts that could confound the findings. Recovery was retinotopically specific, but could be extended by training consecutively adjacent locations that lay progressively deeper inside the scotoma, inducing recovery up to ~20° from the scotoma border in one subject. Furthermore, recovery in this task appeared to carry some practical significance, as the subjects' ability to dodge basketballs "thrown" at them from the blind hemifield in a virtual reality environment, improved (Iorizzo et al., 2011). These findings sparked renewed interest in studying visual rehabilitation strategies. This is encouraging, but it is necessary to note that visual rehabilitation results appear more variable across the literature (see table 1, in a recent review by Sabel et al. (Sabel et al., 2011), and (Horton, 2005a; Horton, 2005b) for a critical review of the field). Three important questions remain to be answered regarding scotomas resulting from V1 lesions: i) can visual rehabilitative training result in improved visual performance of practical significance? ii) what is the underlying mechanism of recovery? and 3) what is the optimal method for visual rehabilitative training?

In summary, even though visual rehabilitation following area V1+lesions is a difficult problem, it is not a hopeless endeavor. Anatomical pathways bypassing the area of the lesion exist, and they have been demonstrated to be functional in certain situations. Although early trials have been inconclusive, a recent report by Huxlin et al. (Huxlin et al., 2009), suggests that some recovery is possible, at least in the domain of visual motion perception. Further studies are needed: (i) to independently corroborate the results of Huxlin et al. (Huxlin et al., 2009); (ii) to understand what visual attributes and types of lesions are amenable to recovery; and (iii) to study the mechanism of recovery. *It is important to note that we do not expect even successful rehabilitation methods to restore vision to pre-lesion levels.* For one, the quality of the restored visual percept will most likely differ from normal. The reason is that, following V1 lesions, the magnocellular and parvocellular pathways largely degenerate (fig. 1), shifting the balance towards the koniocellular pathway, which is spared. Nevertheless, successful visual rehabilitation can train patients to use the qualitatively and quantitatively different form of visual perception mediated by appropriately strengthened V1-bypassing pathways. The design of such a neuro-rehabilitative approach will confer considerable practical significance.

2. Using fMRI to functionally characterize and classify cortical lesions and corresponding scotomas

To design effective visual rehabilitation strategies for cortical scotomas, we have to grapple with the issue of lesion variability. Cortical lesions differ from individual to individual, and this impacts whether or not the resulting scotoma is amenable to rehabilitation. Consequently, some patients show good recovery following visual rehabilitative training (Kasten et al.,

1998; Huxlin, 2009) and others no recovery at all (Reinhard et al., 2005; Horton et al., 2005a; Horton et al., 2005b; and our personal observation). It remains unclear what criteria one may use to select patients more likely to recover. Scotomas are mapped using visual field perimetry to determine the part of the visual field where visual perception is impaired. A problem faced in studies of visual rehabilitation is that patients often have heterogeneous lesions, even though the extent and density of their perceptual visual scotomas, measured by perimetry, match. Conversely, the anatomical characterization of the lesion is not always a reliable indication of the properties or, the extent of the resulting scotoma. Consequently, neither visual field perimetry maps nor, purely anatomical information are sufficient indicators of the capacity for rehabilitation.

A measure of the ability of visual stimuli presented inside the scotoma to elicit perceptually sub-threshold activity in spared visual cortex would add valuable information. Functional magnetic resonance imaging (fMRI) can be used to identify which sectors of the visual field scotoma remain able to transmit visual information to spared regions of the visual cortex (fig. 3), downstream from the lesion. This can help to classify functionally different types of lesions that yield similar scotomas, and to identify regions of the scotoma that elicit different patterns of functional activation and may therefore, have different capacity for rehabilitation. The underlying hypothesis is that parts of the scotoma that can still convey visual information to higher areas, bypassing the cortical lesion, will be more amenable to rehabilitation. Moreover, the extrastriate areas that become activated may reveal clues about the attributes of the visual stimulus that will be more amenable to rehabilitation.

We propose to apply state-of-the-art fMRI methods to characterize voxel by voxel, how population receptive fields (pRF; Wandell et al., 2007; Dumoulin and Wandell, 2008; Amano et al., 2009; Lee et al., 2013) in spared visual areas are organized to cover the visual field following cortical visual pathway injuries (see figs. 2, and 3) (Baseler et al., 2011). The pRF of a voxel refers to the region of visual space that elicits a visually-induced modulation of the BOLD (Blood-Oxygen-Level-Dependent) signal in that voxel. Various pRF models have been proposed in the literature (Dumoulin and Wandell, 2008; Zuiderbaan et al., 2012; Lee et al., 2013). The simplest and most commonly used is a circularly symmetric, 2D Gaussian model with center (x,y) and radius (σ) (Dumoulin and Wandell, 2008). The BOLD time series predicted by this model is derived by convolving the pRF model with the stimulus sequence and the BOLD hemodynamic response function (HRF; Boynton et al., 1996; Worsley et al., 2002). The pRF's parameters are then estimated by fitting the BOLD signal predicted by the model to the actual BOLD signal measurement obtained from each voxel.

Early methods of retinotopic mapping, such as ring and wedge stimuli (DeYoe et al., 1996; Dougherty et al., 2003; Engel et al., 1994; Sereno et al., 1995), as well as moving bar stimuli (Wandell et al., 2007), which traverse the visual field in different directions can usually provide robust pRF estimates (see fig. 2) rendering them useful for studying cortical reorganization. One limitation of direct-fit pRF estimation methods is that these can result in estimation biases at the scotoma border (Lee et al., 2013). Recently, a 2-step pRF estimation method based on first estimating the pRF topography, thresholding it, and then fitting an appropriate pRF model

http://dx.doi.org/10.5772/57000

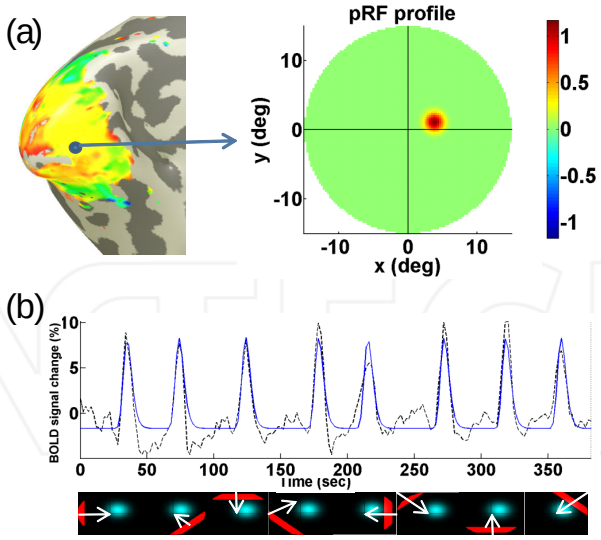

Figure 2. The population receptive field (pRF) model. This model estimates the region of the visual field that elicits a response in a small region (voxel) of the visual cortex. One implementation of the pRF model is a circularly symmetric Gaussian receptive field in visual space whose center and radius are estimated by fitting the BOLD signal responses to the estimated responses elicited by convolving the model with the moving bar stimulus and the hemodynamic response. (**a**) shows the estimated position and size of the pRF in the visual field of a voxel located in V1. (**b**) shows the BOLD time-series (dashed line) and the model prediction (solid line) from the same voxel. The model explains a large amount of variance in the time course data. Below, we illustrate the position and direction of motion of the stimulus bar that elicited the peaks in the BOLD signal.

has been introduced to largely circumvent this problem (Lee et al., 2013). This is the preferred method to use near the scotoma border.

2.1. Visual field coverage maps can potentially help to guide neurorehabilitation strategies

Population receptive field analysis can measure the residual capacity of areas controlling vision to process visual information following V1+injuries. Plotting the pRFs from all voxels of a given area together as a color map reveals the "visual field coverage map" of that area. This represents the part of the visual field that can visually modulate the area. Note that visual field coverage maps of extrastriate areas often overlap with the area of the dense perceptual scotoma, measured by visual field perimetry. This is illustrated in the second panel of figure 3 for the human middle temporal cortex (hV5/MT+), an area important for visual motion perception (Zeki et al., 2004; ffytche et al., 2000; Zeki and ffytche et al., 1998). Note that the pRF maps of many hV5/MT+voxels lie inside the perceptual scotoma (left upper quadrant in fig. 3). In fact, in this specific case (fig. 3), they cover the whole extent of the scotoma. This implies that hV5/MT+is activated by visual stimuli presented in the left upper quadrant even though the subject does not perceive these stimuli. This suggests that there is a functional V1-bypassing pathway to area hV5/MT+that may promote recovery, if appropriately rehabilitated. There-

fore, a promising rehabilitation strategy is to strengthen this pathway. It is likely, that it will be easier to rehabilitate visual motion perception inside parts of the scotoma that are covered by the pRF maps of area hV5/MT+. It is also, likely that rehabilitation will be even easier in parts of the scotoma that are also covered by the pRF maps of spared, earlier, visual areas. The third panel of fig. 3 illustrates the visual field coverage map of the spared portion of area V1. Note, that this extends above the horizontal meridian to partly overlap with the area of the scotoma. This defines two regions where visual rehabilitation may be different, according to the above hypothesis. The region of the scotoma indicated by the green arrow is represented in the coverage maps of both area hV5/MT+and the spared area V1, and is expected to have higher potential for rehabilitation. The region of the scotoma indicated by the blue arrow is represented only in the coverage map of area hV5/MT+and is expected to present a more difficult challenge for rehabilitation. Visual field coverage maps (Amano et al., 2009) obtained by fMRI are an important adjunct to perimetric maps as they often provide complementary information (personal observation) and will likely be useful in tailoring therapy to appropriate visual field locations.

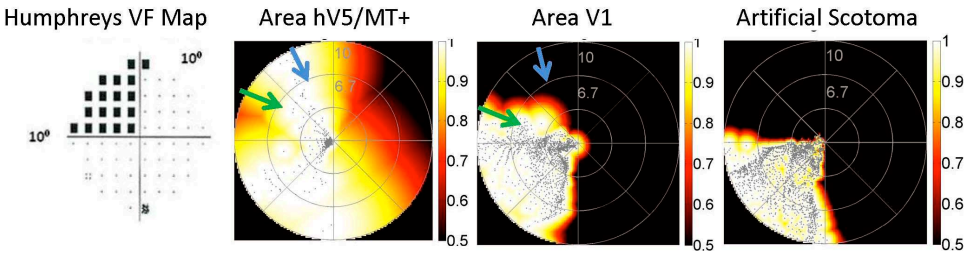

Figure 3. Visual Field Coverage Maps of spared visual areas with significant overlap with the region of the scotoma, define visual field locations that may be more amenable to rehabilitation. Humphreys VF Map panel: Humphreys 10-2 visual field map, illustrating that the subject had a dense left upper quadrantanopia. Area hV5/MT± panel: The visual field coverage map (Amano et al., 2009) of the right hV5/MT+shows visual field locations that evoke significant activity from hV5/MT+of the lesioned hemisphere. At each visual field location, the highest pRF value of all pRFs that cover this location is plotted. PRF normalization limits the range of values between 0-1. Large values indicate significant visual modulation. Note, that although the subject is blind in the left upper quadrant, the subject's hV5/MT+responds to stimuli presented in the left upper quadrant. A potential advantage of using visual field coverage maps is that therapy can be individualized to each patient's appropriate visual field locations, which are not necessarily predictable from perimetric maps. Area V1 Panel: Visual field coverage map of the spared right area V1 extends above the left horizontal meridian into the dense area of the scotoma seen in the Humphreys map. This activity may be induced in orthotopic voxels that survive and are partially active following the V1 lesion (Kasten et al., 1998), or in anatomically ectopic V1 voxels that belong to the upper occipital lobe, which would ordinarily have had receptive fields in the left lower visual field quadrant. Note, that this area does not cover the entire quadrant, as is the case of the coverage map in area hV5/MT+. This mismatch will likely have implications for rehabilitation. For example, it may be easier to rehabilitate regions of the scotoma where the visual field coverage maps of spared V1 and hV5/MT± are congruent (green arrow), as opposed to incongruent (blue arrow). Control with AS (artificial scotoma) Panel: Visual field coverage map from the entire area V1 of a normal subject with an "artificial scotoma" simulating left upper quadrantanopia. By artificial scotoma we mean an area of the stimulus being excluded, in order to simulate the patient's scotoma. Note, that the visual field coverage map in this control case is as expected, i.e. it does not encroach into the left upper quadrant.

http://dx.doi.org/10.5772/57000

2.2. Quantitative pRF measurements provide a useful biomarker for gauging the effect of neurorehabilitation strategies

Fig. 4 illustrates that pRF measurements in area hV5/MT+ipsilateral to a chronic V1+lesion differ from those in the normal hemisphere. Specifically, pRFs in hV5/MT+voxels of the lesioned hemisphere are smaller on average, and pRF-centers cluster near the vertical meridian (x=0; fig. 4C). Training may further change the pRF topography. Changes in the pRF topography before and after training can be a potentially useful biomarker for evaluating different rehabilitation paradigms before perceptual recovery becomes evident. Applying this approach systematically can help to formulate new hypotheses guiding future neuro-rehabilitation attempts. One hypothesis is that following visual motion rehabilitation training the sensitivity to motion stimuli of hV5/MT+ will increase, which will positively correlate with behavioral recovery. Alternatively, attentional networks or, other "higher" areas that receive input from hV5/MT+may reorganize to process visual motion information more effectively. Analyzing pRF maps obtained from visually responsive areas before and after training, will allow us to investigate the above hypotheses and to adopt appropriate rehabilitation strategies.

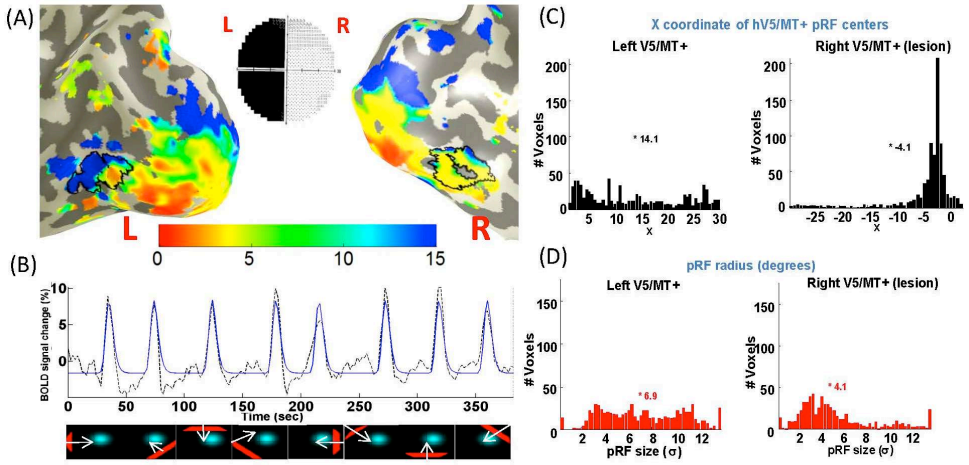

Figure 4. *hV5/MT±* pRF mapping in a hemianopic patient: (A) Inflated occipital lobe of the normal (left) and lesioned (right) hemisphere with hV5/MT+outlined on the eccentricity map. Mid-inset is a 30-2 Humphrey perimeter showing dense left hemianopia. (B) Illustrates the method used to calculate pRF parameters (same as in fig. 2). The pRF model parameters are optimized to fit the BOLD signal, voxel by voxel. Note the close fit between the BOLD time-series (dashed line) and the pRF model prediction (solid line). The position and direction of motion of the stimulus bar that elicited each response is illustrated (bottom). (C) The X coordinate of the pRF centers in hV5/MT+of the normal (left) hemisphere is evenly distributed while in the lesioned (right) hemisphere it clusters near the vertical meridian (x=0). Note however, that the pRF centers still lie within the scotoma (negative X values). (D): Distribution of pRF radii of hV5/MT+voxels in the intact (left) and in the lesioned (right) hemisphere. The distribution of pRF radii shifts to smaller values in area hV5/MT+of the lesioned hemisphere. This may be because ipsilesional hV5/MT+voxels are driven by a V1-bypassing pathway that drives visual periphery less effectively.

In summary, pRF measurements:

1. Classify subregions of the perimetric scotoma depending on how they are covered by spared visual areas; different regions will likely have different potential for rehabilitation.
2. Allow us to study the mechanism by which rehabilitation strategies improve visual performance.
3. Serve as quantitative biomarkers to evaluate the effects of training before perceptual recovery becomes evident, accelerating the pursuit of a rational strategy for visual rehabilitation.

Other methods of analysis can be applied here, but we do not have the space to do them justice. We mention briefly the promise of recent developments in effective connectivity analysis (Fuji et al., 2009; Stilla et al., 2008; Hinrichs et al., 2006) and diffusion tensor imaging (Wedeen et al., 2012; Yeatman et al., 2012; Van den Stock et al., 2011; Sherbondy et al., 2008; Fields, 2008; Okada et al., 2007; Schoth et al., 2006; Kikuta et al., 2006; Dougherty et al., 2005; Taoka et al., 2005; de Gelder et al., 2005; Reinges et al., 2004; Morris et al., 2001) for studying inter-area pathways that survive post-lesion, and whether they can become stronger by training. Population receptive field and effective connectivity analysis can be used to explore visual system reorganization and recovery following injury, and to generate concrete hypotheses on how to enhance and accelerate recovery of visual function by the application of cutting-edge rehabilitative strategies.

3. How to approach visual neurorehabilitation?

To date, we have little understanding of how the visual cortex reorganizes after injury, and no proven effective treatment strategies to rehabilitate the recovery of visual perception in the affected portion of the visual field in V1-lesioned patients. Understanding how to manipulate the brain's capacity for plasticity is an important step in the long-term effort to design treatments aiming to enhance the ability of the nervous system to recover after injury. To make progress along this front, we need to: i) study the mechanisms by which the adult brain adapts and reorganizes after injury; and ii) devise approaches that will allow us to manipulate the process of reorganization to induce visual recovery.

The network of visual areas can be viewed as a heavily interconnected circuit subject to a series of hierarchy rules. Early areas usually process sensory information initially, by passing it on to higher areas, and in turn, extract "higher" order features and control the flow of information through feedback loops. Increased performance following training can therefore be the result of changes that occur in early areas (Schoups et al., 2001; Yotsumoto et al., 2008; Censor and Sagi, 2009; Karni and Sagi, 2008), or the result of changes that occur in "higher" visual areas and attentional networks (Law and Gold, 2008; Yang and Maunsell, 2004; Lewis et al., 2009). Area V1 injuries, interrupt the cardinal feed-forward pathway but, as discussed above, visually driven information can still activate surviving extrastriate areas through bypassing routes (Cowey, 1974; Dineen et al., 1982; Rodman et al., 1989; Cowey and Stoerig, 1997; Baseler et al.,

http://dx.doi.org/10.5772/57000

1999; Goebel et al., 2001; Schmid et al., 2009; Schmid et al., 2010). The pattern of activity elicited in surviving visual areas interacts with higher "centers" in frontal, parietal and temporal areas but, in the absence of V1 input, fails to generate a strong visual percept. We suggest here two general, non-mutually exclusive approaches to visual rehabilitation:

"Bottom-up" approach: Visual rehabilitation strengthens V1-bypassing pathways to increase the response elicited in surviving extrastriate areas.

"Top-down" approach: Visual rehabilitation reorganizes higher "centers" to learn to process the modulated patterns of activity elicited in extrastriate areas by V1-bypassing inputs.

Non-invasive approaches to visual rehabilitation aim to enhance these pathways by recruiting the mechanisms of plasticity the brain uses for learning. Various behavioral approaches have been used. They usually involve performing a visual task that directs attention to a sub-threshold stimulus, requires a choice, and then provides feedback about correct and incorrect choices (see fig. 5). Although such methods are effective for perceptual learning in general (Yotsumoto et al., 2008; Law and Gold, 2008; Yang and Maunsell, 2004), in the domain of rehabilitation of a dense perceptual scotoma results have been at best variable (Huxlin et al., 2009; Raninen et al., 2007 Sahraie, et al., 2006; Reinhard et al., 2005; Horton et al., 2005a; Horton et al., 2005b; Pleger et al., 2003). The most notable exception has been a recent well-controlled report by Huxlin and co-workers (Huxlin et al., 2009), which demonstrated strong recovery of direction of visual motion perception inside the scotoma of 5 hemianopic subjects (Huxlin et al., 2009; Huxlin, 2006). Two other groups independently, Sahraie et al. and Raninen et al., report that visual sensitivity can improve with training in humans with homonymous scotomas (Sahraie, 2006; Henriksson et al., 2007; Raninen et al., 2007). Encouraging results were also obtained by Pleger and co-workers, who showed that visual cortex reorganization was possible via daily visual stimulation training over a period of 6 months in 3 subjects with partial cortical blindness (Pleger et al., 2003). Although these are encouraging reports, the issue remains far from settled (Horton et al., 2005a; Horton et al., 2005b). Additional studies corroborating recent results and probing the mechanism of recovery are clearly needed to guide the implementation of new, more effective rehabilitation strategies. In what follows, we discuss the promise and challenges of a new visual rehabilitation approach, which aims to use "real time" fMRI neurofeedback to train subjects to promote plasticity in V1-bypassing pathways relevant to recovery.

4. Introduction to real-time functional Magnetic Resonance Imaging neurofeedback approaches

Less than two decades ago, the real-time functional magnetic resonance (rt-fMRI) method has been introduced (Cox, 1995) in the field of neuro-rehabilitation, which extracts the BOLD (Blood-Oxygen-Level-Dependent) signal from the subject's brain in real-time and uses it to provide feedback to the subject. Since the BOLD signal reflects neural activity this approach is called real-time fMRI neurofeedback (rt-fMRI nFb). Multiple studies have shown that rt-fMRI nFb, can train subjects to modulate the magnitude and spatial extent of the activity

elicited in various cortical and subcortical areas (Berman et al., 2011; Bray et al., 2007; Caria et al., 2007; Caria et al., 2010; Chiew et al., 2012; deCharms et al., 2004; deCharms et al., 2005; Frank et al., 2012; Haller et al., 2010; Hamilton et al., 2011; Hinds et al., 2011; Johnson et al., 2012; Johnson et al., 2011; Johnson et al; 2010; Lee et al., 2012; Li et al., 2012; McCaig et al., 2011; Papageorgiou et al., 2009a; Papageorgiou et al., 2009b; Papageorgiou et al., 2013; Posse et al., 2003; Rota et al., 2009; Ruiz et al., 2013; Scharnowski et al., 2012; Shibata et al., 2011; Subramanian et al., 2011; Sulzer et al., 2013; Veit et al., 2012; Weiskopf et al., 2007; Weiskopf et al., 2004; Weiskopf et al., 2003; Yoo and Jolesz, 2002; Yoo et al., 2008; Zotev et al., 2011). The goal of this approach is to train subjects to control the pattern of their brain activity in a way that promotes a desired behavior. It can also be used to boost the neural capacity for learning and plasticity (Shibata et al., 2012; Scharnowski et al., 2012; Shibata et al., 2011; Weiskopf et al., 2004; deCharms et al., 2004; deCharms et al., 2005). If this is applied effectively, it could serve as a useful tool to promote neuro-rehabilitation.

The ability of rt-fMRI nFb to induce a behavioral change was first shown by Weiskopf et al. (Weiskopf et al., 2003) and deCharms et al. (deCharms et al., 2005). In the deCharms et al. study, chronic-pain patients were coached to decrease their pain by learning to control the BOLD signal intensity of the rostral anterior cingulate cortex (rACC), a region known to be involved in pain perception (Apkarian et al., 2005; Peyron et al., 2000). After training, subjects were able to voluntarily increase or decrease the rACC BOLD signal intensity, which was correlated with an increased or decreased level of pain, respectively; i.e., a 50% decrease in the rACC activity of chronic pain subjects corresponded approximately to a 64% decrease in their pain. This effect was specific to rtfMRI nFb training applied to rACC; i.e., no effect was seen after similar training conducted without rtfMRI NFb or, after sham rtfMRI nFb training derived from the activity of another subject's rACC.

Similar results have been obtained in other cortical and subcortical domains (Posse et al., 2003; Lee et al., 2011; Hamilton et al., 2011; Ruiz et al., 2013). A recent study showed that healthy volunteers were able to volitionally regulate the activity of their insula when given rt-fMRI nFb (Lee et al., 2011). Posse and his team (Posse et al., 2003) trained subjects to upregulate their amygdala, an area whose level of activity is associated with sad affect and depression (Wang et al., 2012; Anand et al., 2007; Liu et al., 2011). Amygdala upregulation induced by rt-fMRI feedback was positively correlated with self-ratings of sadness across repeated fMRI sessions (Posse et al., 2003). Conversely, Hamilton et al. used rt-fMRI nFb to train subjects to downregulate subgenual ACC and posterior cingulate cortex, resulting in positive mood induction (Hamilton et al., 2011). Sham rt-fMRI nFb showed no effect. Ruiz et al. showed that schizophrenic patients can be trained by rt-fMRI nFb to voluntarily control their anterior insula bilaterally (Ruiz et al., 2013). The effect of bilateral anterior insula activation is reflected on their ability to recognize face emotion, a known deficit in schizophrenia. These findings collectively, suggest that: *1) rt-fMRI nFb can be used to train subjects to voluntarily control specific areas; 2) changes in the activity of certain areas can be associated with significant behavioral changes; 3) rt-fMRI nFb training can achieve stronger behavioral results than similar training without nFb; and 4) rt-fMRI training can induce reorganization that can outlast the period of the training inside the magnet and even induce visual perceptual learning (Shibata et al. 2011).*

http://dx.doi.org/10.5772/57000

Shibata et al. in a seminal study used rt-fMRI nFb to induce perceptual learning (Shibata et al., 2011). Rt-fMRI nFb methods were used to enable subjects to induce activity patterns in their early visual cortex corresponding to one particular orientation. Initially, the subjects performed an orientation discrimination task and a decoder of area V1/V2 activity was constructed to classify a pattern of the measured fMRI signals into one of three orientations. Once the decoder was constructed, each subject participated in a 5 to 10-day rt-fMRI nFb stage, during which they learned to induce patterns of activity in areas V1/V2 corresponding to the target orientation. During this stage, subjects were instructed to maximize the signal delivered to them via feedback, but were not told how to induce the desired patterns of activity that would result in increased activity. Subjects did not know what was to be learned. Using this strategy they were able to induce visual perceptual learning specific to the target orientation in areas V1/V2. Learning occurred as a function of the subject's ability to elicit the particular pattern of activation corresponding to the target orientation in early visual areas. Remarkably, subjects were able to generate this pattern simply by being given the instruction to maximize feedback, without being aware that the pattern to be elicited was related to orientation. This demonstrated that the rt-fMRI nFb method can be used to induce highly specific activity patterns within a brain region and that repeatedly eliciting the desired pattern of activity is sufficient to induce plasticity in early visual areas. *These findings suggest that rt-fMRI nFb training can be used to induce targeted and individualized plasticity in the visual system.*

The studies described above (Ruiz et al., 2013; Linden et al., 2012; Subramanian et al., 2011; Shibata et al., 2011; Lee et al., 2011; Hamilton et al., 2011; deCharms et al., 2004; Posse et al., 2003) show that manipulating the activity in select brain areas can induce plasticity. Modified paradigms can also be designed to increase plasticity along specific pathways, by co-activating input and recipient neuronal populations. For example, a projection from area A to recipient area B in the brain can increase or, decrease in strength, depending on the relative activity between input projections from A and recipient neurons in B. Rt-fMRI nFb does not have the temporal resolution necessary to precisely implement Hebbian mechanisms of plasticity. Nevertheless it can be used to train the subject to voluntarily manipulate the activity level of select neuronal populations in area B while their input from A is presented. The hypothesis is that "top-down" activation of area B enhanced by nFb judiciously paired with "bottom-up" presentation of inputs that activate A, can increase the strength of the projection A->B either by their interaction or additive effect. Below, we discuss an example outlining how this proposal might work for the rehabilitation of visual motion perception following area V1 lesions (see also fig. 5).

Area hV5/MT+is associated with global coherent visual motion perception. The goal is to use rt-fMRI nFb methods to strengthen the neural pathways bypassing the V1 lesion and project to area hV5/MT+in order to improve visual motion perception of random dot kinematogram (RDK) stimuli (see fig. 5). The first step is to train the subject to voluntarily upregulate their hV5/MT+activity. To do this, we ask the subject to practice mental imagery of fully coherent visual motion stimuli in their blind hemifield, moving in the direction of the anticipated stimulus. During mental imagery, the subject receives rt-fMRI nFb proportional to the activity in their hV5/MT+via a visual interface at fixation (red arrow in fig. 5). Subjects are trained to

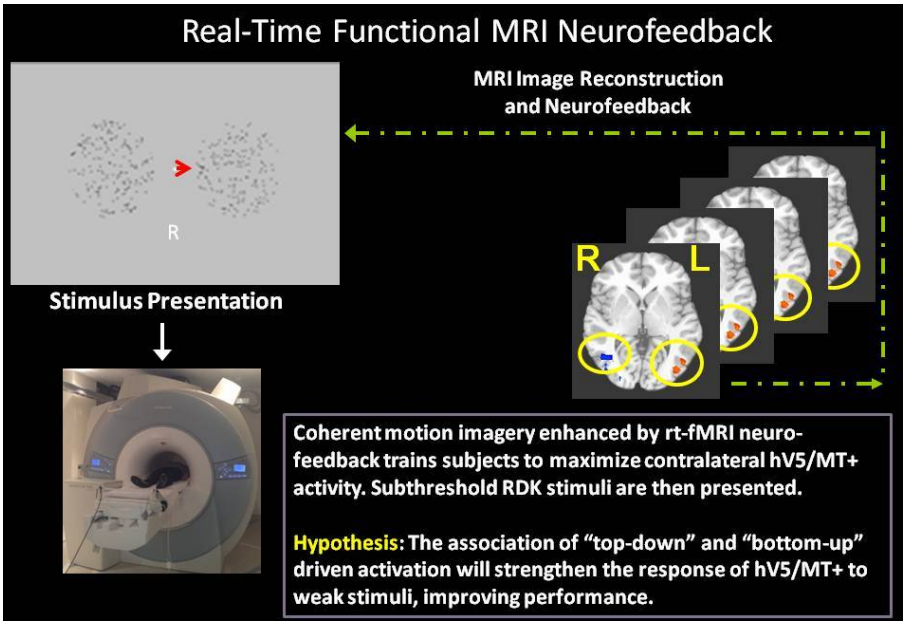

Figure 5. Rt-fMRI nFb paradigm for neurorehabiliation of visual motion perception: The subject lies supine inside the scanner, while s/he is presented with a 0% coherent RDK stimulus. Brain volumes are acquired every 2sec (TR). hV5/MT+(circled) is selected as our ROI. Turbo Brain Voyager software (Brain Innovation) is used to deliver nFb. The BOLD signal in hV5/MT+is estimated in real time (every TR), normalized, and "fed" back, via the length of a horizontal arrow at fixation, to train the subject to upregulate area hV5/MT+. Subjects are instructed to attend to the RDK they are cued towards, either right (R) or left (L) and imagine that it is coherent (when in fact it is not). This increases the level of activity in the contralateral hV5/MT+: (i) superimposing coherent motion via imagery on the right RDK increases left hV5/MT+activity, which is color-coded in red; (ii) superimposing coherent motion via imagery on the left RDK increases right hV5/MT+activity, which is color-coded in blue. The subject uses the length of the arrow to determine the degree of effort and success of his/her strategy. *When the rt-fMRI nFb driven, "top-down," hV5/MT+activation crosses a threshold, sub-threshold RDK stimuli are presented. The association between "top-down" and "bottom-up" activation will engage Hebbian-like learning mechanisms aiming to strengthen the response of hV5/MT+to sub-threshold stimuli.* The hypothesis is that once these pathways are strengthened, the presentation of sub-threshold stimuli will elicit enough activity in area hV5/MT+to improve performance in the direction of motion discrimination task. We note that *hV5/MT+can be upregulated via rt-fMRI nFb enhanced imagery even when it has lost its V1 input.* Once the subject learns how to upregulate hV5/MT+inside the magnet over the period of training, we hypothesize that s/he will also be able to transfer this learned voluntary ability during training outside the MRI environment.

maximize ipsi-lesional hV5/MT+activity using the imagery task. This nFb mediated, "top-down" increase in hV5/MT+activity will then be paired with the presentation of visual motion stimuli that are invisible (sub-threshold) to subjects with V1+lesions. We hypothesize that, by repeatedly presenting sub-threshold visual motion stimuli while hV5/MT+is activated in a "top-down" fashion by nFb, we will engage Hebbian-like association learning mechanisms (Hebb, 1946; Rebesco and Miller, 2011; Gallistel and Matzel, 2013). These mechanisms will promote plasticity in the surviving, V1-bypassing pathways that become activated by the stimulus presentation and project to area hV5/MT+. In other words, we hypothesize that after nFb training, regions of area hV5/MT+deprived of V1 input will respond more strongly to

http://dx.doi.org/10.5772/57000

visual stimuli presented inside the scotoma, improving performance. If successful, this strategy will induce a "neural bypass" of V1 function with respect to visual motion perception.

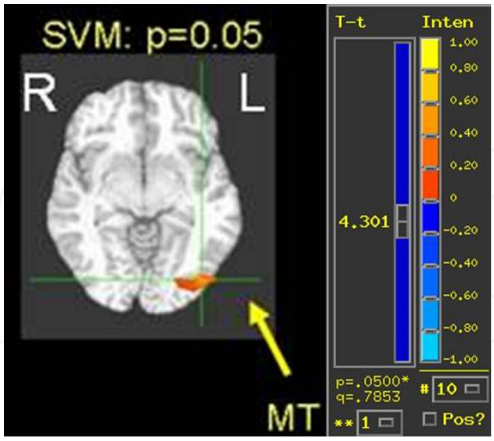

Figure 6. *The support vector machine (SVM) algorithm defines area hV5/MT+when it is trained on coherent motion RDKs*. Subjects fixated while two RDKs were presented simultaneously on symmetric locations in the right (red color-coded activation) and left (blue color-coded activation) visual hemifields. The RDK presented in the left visual field was always kept at 0% coherence (no global motion direction), while the RDK in the right visual field alternated between 0% coherence and 100% coherence. A support vector machine algorithm was trained on the whole brain to classify when the coherent RDK (right visual field/red-color coded activation) was presented. The color map indicates the region that was important in classifying the presentation of a 100% coherent versus a 0% coherent RDK in the right visual field. As expected, the area underlined by the green crosshairs corresponds to area hV5/MT+. Five subjects tested gave consistent results (3dANOVA2 performed in AFNI, p=0.05).

One advantage that rt-fMRI nFb methods have over behavioral feedback approaches is that specific brain pathways or areas can be selectively trained. It is then, feasible to train targeted components of the neural circuit that are likely to contribute to recovery. One example, is strengthening neural pathways that bypass the region of injury to promote recovery. Thus far, we have been discussing a univariate rt-fMRI nFb approach, where the nFb provided is proportional to the activity of a specific region of interest (in the above example, area hV5/MT +) or, pattern of activity (Shibata et al., 2011). An alternative to the univariate nFb method is the multivariate classification approach (Papageorgiou et al., 2013; Papageorgiou et al., 2009; LaConte et al., 2007; Mourao-Miranda et al., 2005). In this approach, a classification algorithm, usually, the support vector machine (Vapnik, 1995) is trained on a set of relevant data in order to identify the brain networks that are involved in a specific computation (task). This is akin to the localizer that is used to identify the region of interest in the univariate approach. In fact, in the case of presentation of RDK stimuli, the multivariate SVM approach picks out chiefly area hV5/MT+, as expected (see fig. 6 below). However, in other cases, this approach may reveal different patterns of activity than expected, helping to formulate new hypotheses about the networks that might contribute to rehabilitation. Once the parameters of the classification algorithm are trained, the algorithm can be used to provide neuro-feedback to the subject in

separate sessions. This approach may be effective in cases where the pathways that need to be modulated to induce recovery are not known a-priori.

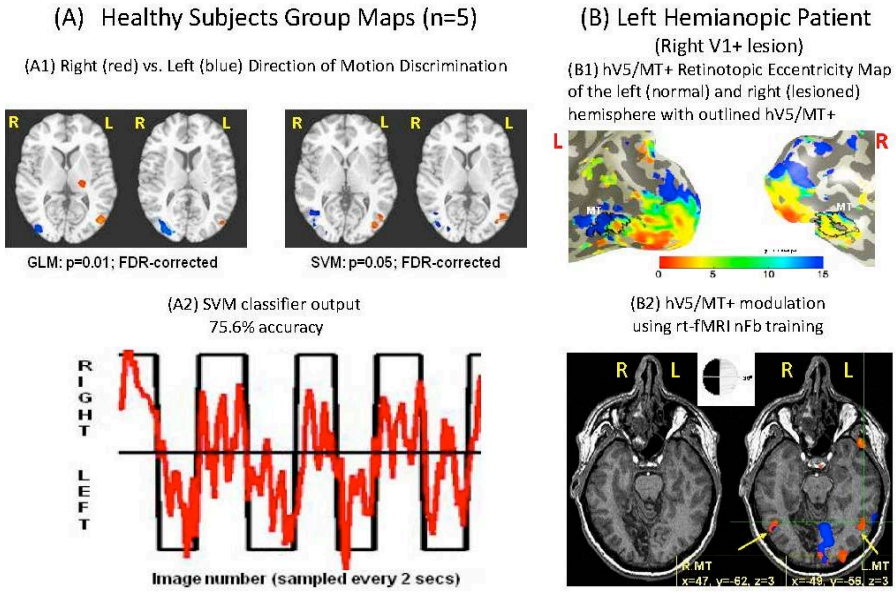

Figure 7. *Rt-fMRI nFb can be used to selectively upregulate hV5/MT+in a top-down manner during a mental imagery task.* In the absence of a coherent moving stimulus, subjects (n=5) were able to use imagery of coherent motion to selectively upregulate hV5/MT+via rt-fMRI nFb training. (**A**) Non-coherent RDKs were presented symmetrically in the Left (L) and the (R) hemifield and subjects were cued to imagine that the Lor the R RDK contained coherent motion. The level of contralateral hV5/MT+activity was delivered via the length of an arrow at the fixation point. (**A1**) Red/blue regions correspond to voxels upregulated when the subject is instructed to imagine coherent motion in the right/left visual field, respectively. Similar results are obtained when using a standard GLM (left panel), versus plotting the weight vector of the support vector machine (SVM) algorithm that classifies whether subjects imagined coherent motion to the left versus the right hemifield (right panel). The regions identified correspond to area hV5/MT+in both hemispheres (color red, blue). *Therefore, subjects can be trained via rt-fMRI nFb to modulate their hV5/MT+activity even in the absence of a coherently moving stimulus;* (**A2**) Output (red curve) of a support vector machine classifier indicating the side of the visual field where the subject imagined coherent motion. The correct choice indicated by the black curve; the prediction of the classifier by the red curve. Positive values indicate the subject was instructed to imagine coherent motion on the right, negative on the left. Note that area hV5/MT+activity can predict the subject's perceptual state. (**B1**) Eccentricity maps of a subject with left hemianopia illustrating that area hV5/MT+(outlined) of the lesioned (right) hemisphrere can be visually driven. Only the posterior lateral aspect of the two inflated hemispheres is presented. (**B2**) Illustrates that *hV5/MT+can also be upregulated via rt-fMRI nFb training in a V1+lesioned patient.* **Left Panel**: Right (R) PCA lesion, resulting in left (L) hemianopia (inset). **Right Panel**: Red color-coded areas represent the activity elicited by the subject's coherent motion imagery in the left (hemianopic) visual field, while blue color-coded area represents non-coherent motion presentation, as generated by GLM. Left hemianopic visual field imagery of coherent motion activated hV5/MT+bilaterally. Preliminary data for implementing the proposal we outlined above are encouraging as they suggest that ipsilesional hV5/MT+activity: (1) conveys information about the stimulus (**B1**), and (2) can be upregulated using rt-fmri nFb imagery in V1+lesioned patients (**B2**).

In summary, emerging strategies based on rt-fMRI nFb hold considerable promise, as they can be: 1) used to enhance plasticity in a number of systems (Berman et al., 2011; Bray et al., 2007;

http://dx.doi.org/10.5772/57000

Caria et al., 2010; deCharms et al., 2004; Haller et al., 2010; Johnson et al., 2012; Johnston et al., 2010; Lee et al., 2012; Li et al., 2012; McCaig et al., 2011; Papageorgiou et al., 2013; Posse et al., 2003; Ruiz et al., 2013; Subramanian et al., 2011; Sulzer et al., 2013; Veit al., 2012; Yoo and Jolesz, 2002; Yoo et al., 2008; Zotev et al., 2011) including in the visual system of healthy participants (Scharnowski et al., 2012; Shibata et al., 2011); 2) superior to normal behavioral methods (deCharms et al., 2005); 3) tailored to induce perceptual learning (plasticity) in a highly specific fashion (Shibata et al., 2011); 4) used to identify pathways relevant to recovery via multivariate computational methods; and 5) used to induce long-lasting learning effects reported to persist outside the magnet, after the end of training (Ruiz et al., 2013; Sulzer et al., 2013). In the long-term, rtfMRI nFb methods promise to induce cortical plasticity that is efficient, robust and targeted for each patient. Lessons learned are likely to apply beyond the visual system to disorders of motor function, cognition, speech, language and emotion.

5. Challenges and future considerations using rt-fMRI nFb for visual neurorehabilitation

Many challenges need to be overcome in order to study the efficacy of rt-fMRI nFb methods in visual rehabilitation. Primarily, we need to develop effective rt-fMRI nFb paradigms in subjects with V1 lesions. The challenge is to implement rt-fMRI nFb training protocols to strengthen specific pathways that are hypothesized to play a role in visual performance. It is important to understand which visual pathways are more amenable to rehabilitation and what is the best rt-fMRI nFb paradigm to use. This requires elucidating which factors are "necessary and sufficient variables for learning" (Weiskopf, 2012). The answers to these questions will in general depend on the specifics of the visual function that requires rehabilitation, as well as on other factors such as the subject's motivation.

Quantifying the degree of induced reorganization using population receptive field (pRF) methods is complementary to behavioral performance measures and represents a valuable neuroimaging biomarker for studying the mechanism of recovery induced by nFb rehabilitation methods. Information obtained will then, allow us to refine future rehabilitative approaches. Several different pathways may be able to contribute to recovery. For example, in the case of the visual motion rehabilitation example, the focus was on strengthening "bottom-up" pathways to enhance the response of the ipsilesional area hV5/MT+to the visual motion stimulus. One can hypothesize other strategies that focus instead on reorganizing higher areas, such as frontal eye fields (FEF), supplementary eye fields (SEF) areas involved in the generation of visual motion percepts downstream of hV5/MT+by "reading out" the weak activity that persists in extrastriate cortex following V1+lesions. Or, one can focus on strategies that reorganize attentional networks, such as middle frontal gyrus (mFG), intraparietal sulcus (IPS), superior parietal lobule (SPL), and anterior cingulate cortex (ACC) that enhance the weakened responses elicited in surviving areas following V1+lesions.

There are important technical challenges. One criticism is that rt-fMRI nFb approaches are impractical because they require large amounts of magnet time. Although this may have some truth in it, preliminary studies reveal that time spent inside the magnet is much less than what

pure behavioral methods, require. Deciding how many rt-fMRI nFb sessions are needed to induce plasticity is a question that still needs to be answered. Preliminary evidence suggests that as few as 5-10 sessions can be sufficient to induce a strong perceptual learning effect in normal subjects (Shibata et al., 2011, and unpublished data of ours), but this will need to be validated specifically in patients with V1 lesions. Healthy participants and patients undergoing rt-fMRI nFb training sessions inside the magnet can learn to voluntarily elicit the desired pattern of activity. Subjects can then, gradually learn to implement this process outside the magnet, transferring their experience from rt-fMRI nFb sessions to ordinary behavioral sessions. We do not have adequate evidence yet, to determine under what conditions training accomplished inside the rt-fMRI environment can be transferred outside the magnet, but there is reason to be hopeful (Ruiz et al., 2013; Sulzer et al., 2013). The clinical applicability of rt-fMRI nFb training will become significantly broader if it becomes feasible to decouple the patient's training sessions from the rt-fMRI nFb environment. Another important question is how long the effects of rt-fMRI nFb training are expected to last and whether this depends on the number of rt-fMRI nFb sessions used for training. Here too, there is reason for optimism given the results of Shibata et al. who managed to induce perceptual learning within 5 sessions of rtfMRI nFb (Shibata et al., 2011).

Many important challenges remain. However, it is now possible to lay the foundation of a systematic approach to visual rehabilitation using novel rt-fMRI nFb methods guided by pRF analysis of spared visual areas. This approach promises to teach us a lot about the visual system's capacity for plasticity after injury, and offers hope that effective, and robust visual rehabilitation methods, such as the novel rt-fMRI nFb approach will be used in the field of visual neuro-rehabilitation.

6. Conclusion

Neurorehabiliation of visual loss that occurs as a result of primary visual cortex injury is a difficult problem. To date, we have little understanding of the plasticity and reorganization mechanisms operating in the adult visual system following V1 injury. Consequently, no reliable method exists to effectively rehabilitate V1-lesioned patients who experience loss of visual perception in the contralateral hemifield (Horton, 2005a; Horton, 2005b; Pambakian and Kennard, 1997). Interestingly, recent results have shown that visually driven activity persists in extrastriate cortex following chronic area V1+lesions (Schmid, 2010; Schmid, 2009; Rodman, 1989; Rodman, 1990; Baseler, 1999), and that it is possible in some cases to rehabilitate visual motion perception (Das, 2010; Huxlin, 2009; Raninen et al., 2007; Henriksson et al., 2007; Sahraie et al., 2010). This confirms the existence of functional pathways that bypass the V1+lesion, providing direct input to spared extrastriate cortex. Such pathways are generally too weak to result in practical benefit. However, appropriate training strategies may be able to strengthen them sufficiently to induce recovery.

Real-time fMRI neuro-feedback strategies allow subjects to voluntarily modulate activity in certain brain areas or, neural pathways. These methods can be used to promote plasticity (Shibata et al., 2011). For example, we hypothesize that rt-fMRI nFb may be used to strengthen pathways that bypass the region of V1 injury to transmit visual motion information to area

http://dx.doi.org/10.5772/57000

hV5/MT+. One paradigm that could, in theory, be used to accomplish this is the following: Subjects are trained by rt-fMRI nFb to voluntarily upregulate their hV5/MT+activity. Whenever hV5/MT+activity crosses a pre-set threshold, sub-threshold visual stimuli are presented. Repeated pairing of the "top-down" nFb-driven activation with the "bottom-up" stimulus-driven activation will engage Hebbian-like, association learning mechanisms, strengthening the response of hV5/MT+to visual motion stimuli. Visual motion stimuli that were previously sub-threshold may then, rise above threshold following training, improving performance.

Rehabilitating dense visual field scotomas requires adopting a systematic approach. Plasticity changes induced by new rehabilitation strategies should be mapped and their mechanism studied. We have presented evidence that pRF analysis is an excellent tool for this purpose, quantifying changes and providing rich data for formulating hypotheses about what regions of the visual field may be more amenable to rehabilitation and what pathways contribute to recovery.

We conclude that, even though rt-fMRI nFb methods are currently in their infancy, they hold considerable promise for inducing plasticity in targeted pathways promoting successful rehabilitation. Although here, we have focused on the visual system, principles discussed apply to the neuro-rehabilitation of several other domains of brain function, such as motor control, language, speech (Papageorgiou et al., 2009a; Papageorgiou et al., 2009b; Papageorgiou et al., 2013), emotion and cognition.

Acknowledgements

Part of the work that is presented here was supported by: (i) a McNair Foundation award, a McNair Medical Institute (MMI) award and a Fight for Sight Grant to T.D. Papageorgiou; and (ii) an NEI RO1 (EY019272), DoD (W81XWH-08-2-0146), and an HHMI Early Career Award to S. M. Smirnakis.

Author details

T. Dorina Papageorgiou[1,2], Amalia Papanikolaou[4] and Stelios M. Smirnakis[1,3,4]

1 Department of Neurology, Baylor College of Medicine, Houston, Texas, USA

2 Department of Physical Medicine and Rehabilitation, Baylor College of Medicine, Houston, Texas, USA

3 Deparment of Neuroscience, Baylor College of Medicine, Houston, Texas, USA

4 Departments of MaxPlanck Institute for Biological Cybernetics, Tuebingen, Germany

References

[1] Ahissar, M. and S. Hochstein (1997). "Task difficulty and the specificity of perceptual learning." *Nature* 387(6631): 401-6.

[2] Ajina, S. and C. Kennard (2012). "Rehabilitation of damage to the visual brain." *Rev Neurol (Paris)* 168(10): 754-61.

[3] Alexander, I. and A. Cowey (2009). "The cortical basis of global motion detection in blindsight." *Exp Brain Res* 192(3): 407-11.

[4] Amano, K., B. A. Wandell, et al. (2009). "Visual field maps, population receptive field sizes, and visual field coverage in the human MT+ complex." *J Neurophysiol* 102(5): 2704-18.

[5] Anand, A., Y. Li, et al. (2007). "Reciprocal effects of antidepressant treatment on activity and connectivity of the mood regulating circuit: an FMRI study." *J Neuropsychiatry Clin Neurosci* 19(3): 274-82.

[6] Apkarian, A. V., M. C. Bushnell, et al. (2005). "Human brain mechanisms of pain perception and regulation in health and disease." *Eur J Pain* 9(4): 463-84.

[7] Baseler, H. A., A. Gouws, et al. (2011). "Large-scale remapping of visual cortex is absent in adult humans with macular degeneration." *Nat Neurosci* 14(5): 649-55.

[8] Baseler, H. A., A. B. Morland, et al. (1999). "Topographic organization of human visual areas in the absence of input from primary cortex." *J Neurosci* 19(7): 2619-27.

[9] Berman, B. D., S. G. Horovitz, et al. (2012). "Self-modulation of primary motor cortex activity with motor and motor imagery tasks using real-time fMRI-based neurofeedback." *Neuroimage* 59(2): 917-25.

[10] Boynton, G. M., S. A. Engel, et al. (1996). "Linear systems analysis of functional magnetic resonance imaging in human V1." *J Neurosci* 16(13): 4207-21.

[11] Bray, S., S. Shimojo, et al. (2007). "Direct instrumental conditioning of neural activity using functional magnetic resonance imaging-derived reward feedback." *J Neurosci* 27(28): 7498-507.

[12] Brown, T. H., P. F. Chapman, et al. (1988). "Long-term synaptic potentiation." *Science* 242(4879): 724-8.

[13] Caria, A., R. Sitaram, et al. (2010). "Volitional control of anterior insula activity modulates the response to aversive stimuli. A real-time functional magnetic resonance imaging study." *Biol Psychiatry* 68(5): 425-32.

[14] Caria, A., R. Veit, et al. (2007). "Regulation of anterior insular cortex activity using real-time fMRI." *Neuroimage* 35(3): 1238-46.

http://dx.doi.org/10.5772/57000

[15] Censor, N. and D. Sagi (2009). "Global resistance to local perceptual adaptation in texture discrimination." *Vision Res* 49(21): 2550-6.

[16] Chiew, M., S. M. LaConte, et al. (2012). "Investigation of fMRI neurofeedback of differential primary motor cortex activity using kinesthetic motor imagery." *Neuroimage* 61(1): 21-31.

[17] Chokron, S., C. Perez, et al. (2008). "From blindsight to sight: cognitive rehabilitation of visual field defects." *Restor Neurol Neurosci* 26(4-5): 305-20.

[18] Corbetta, M. and G. L. Shulman (2002). "Control of goal-directed and stimulus-driven attention in the brain." *Nat Rev Neurosci* 3(3): 201-15.

[19] Cowey, A. (2010). "Visual system: how does blindsight arise?" *Curr Biol* 20(17): R702-4.

[20] Cowey, A. (1974). "Atrophy of retinal ganglion cells after removal of striate cortex in a rhesus monkey." *Perception* 3(3): 257-60.

[21] Cowey, A. and P. Stoerig (1997). Blindsight in man and monkey. Brain 120(Pt 3): 535-59.

[22] Cowey, A. and P. Stoerig (1989). "Projection patterns of surviving neurons in the dorsal lateral geniculate nucleus following discrete lesions of striate cortex: implications for residual vision." *Exp Brain Res* 75(3): 631-8.

[23] Cowey, A. and P. Stoerig (1991). "The neurobiology of blindsight." *Trends Neurosci* 14(4): 140-5.

[24] Cox, R. W. (1996). "AFNI: software for analysis and visualization of functional magnetic resonance neuroimages." *Comput Biomed Res* 29(3): 162-73.

[25] Das, A. and K. R. Huxlin (2010). "New approaches to visual rehabilitation for cortical blindness: outcomes and putative mechanisms." *Neuroscientist* 16(4): 374-87.

[26] de Gelder, B., J. S. Morris, et al. (2005). "Unconscious fear influences emotional awareness of faces and voices." *Proc Natl Acad Sci U S A* 102(51): 18682-7.

[27] deCharms, R. C., K. Christoff, et al. (2004). "Learned regulation of spatially localized brain activation using real-time fMRI." *Neuroimage* 21(1): 436-43.

[28] deCharms, R. C., F. Maeda, et al. (2005). "Control over brain activation and pain learned by using real-time functional MRI." *Proc Natl Acad Sci U S A* 102(51): 18626-31.

[29] Deco, G. and T. S. Lee (2004). "The role of early visual cortex in visual integration: a neural model of recurrent interaction." *Eur J Neurosci* 20(4): 1089-100.

[30] DeYoe, E. A., G. J. Carman, et al. (1996). "Mapping striate and extrastriate visual areas in human cerebral cortex." *Proc Natl Acad Sci U S A* 93(6): 2382-6.

[31] Dineen, J., A. Hendrickson, et al. (1982). "Alterations of retinal inputs following striate cortex removal in adult monkey." *Exp Brain Res* 47(3): 446-56.

[32] Dougherty, R. F., M. Ben-Shachar, et al. (2005). "Functional organization of human occipital-callosal fiber tracts." *Proc Natl Acad Sci U S A* 102(20): 7350-5.

[33] Dougherty RF, V.M. Koch, et al. (2003). "Visual field representations and locations of visual areas V1/2/3 in human visual cortex." J Vis. 3(10):586-98.

[34] Dumoulin, S. O. and B. A. Wandell (2008). "Population receptive field estimates in human visual cortex." *Neuroimage* 39(2): 647-60.

[35] Elisevich, K. V., R. M. Ford, et al. (1984). "Visual abnormalities with multiple trauma." *Surg Neurol* 22(6): 565-75.

[36] Engel, S. A., D. E. Rumelhart, et al. (1994). "fMRI of human visual cortex." *Nature* 369(6481): 525.

[37] Fabre-Thorpe, M., F. Levesque, et al. (1994). "Preservation of pointing accuracy toward moving targets after extensive visual cortical ablations in cats." *Cortex* 30(4): 585-601.

[38] Fendrich, R., C. M. Wessinger, et al. (1992). "Residual vision in a scotoma: implications for blindsight." *Science* 258(5087): 1489-91.

[39] ffytche, D.H., A. Howseman, et al. (2000). Human area V5 and motion in the ipsilateral visual field. Eur J Neurosci. 12(8):3015-25.

[40] Fields, R. D. (2008). "White matter in learning, cognition and psychiatric disorders." *Trends Neurosci* 31(7): 361-70.

[41] Frank, S., S. Lee, et al. (2012). "The obese brain athlete: self-regulation of the anterior insula in adiposity." *PLoS One* 7(8): e42570.

[42] Friel, K. M., A. A. Heddings, et al. (2000). "Effects of postlesion experience on behavioral recovery and neurophysiologic reorganization after cortical injury in primates." *Neurorehabil Neural Repair* 14(3): 187-98.

[43] Fujii, T., H. C. Tanabe, et al. (2009). "An investigation of cross-modal plasticity of effective connectivity in the blind by dynamic causal modeling of functional MRI data." *Neurosci Res* 65(2): 175-86.

[44] Gall, C., B. Steger, et al. (2013). "Evaluation of two treatment outcome prediction models for restoration of visual fields in patients with postchiasmatic visual pathway lesions." *Neuropsychologia*.

[45] Gallistel, C. R. and L. D. Matzel (2013). "The neuroscience of learning: beyond the Hebbian synapse." *Annu Rev Psychol* 64: 169-200.

[46] Gilhotra, J. S., P. Mitchell, et al. (2002). "Homonymous visual field defects and stroke in an older population." *Stroke* 33(10): 2417-20.

[47] Giorgi, R. G., R. L. Woods, et al. (2009). "Clinical and laboratory evaluation of peripheral prism glasses for hemianopia." *Optom Vis Sci* 86(5): 492-502.

[48] Girard, P., P. A. Salin, et al. (1991). "Visual activity in areas V3a and V3 during reversible inactivation of area V1 in the macaque monkey." *J Neurophysiol* 66(5): 1493-503.

[49] Goebel, R., L. Muckli, et al. (2001). "Sustained extrastriate cortical activation without visual awareness revealed by fMRI studies of hemianopic patients." *Vision Res* 41(10-11): 1459-74.

[50] Haller, S., N. Birbaumer, et al. (2010). "Real-time fMRI feedback training may improve chronic tinnitus." *Eur Radiol* 20(3): 696-703.

[51] Hamilton, J. P., G. H. Glover, et al. (2011). "Modulation of subgenual anterior cingulate cortex activity with real-time neurofeedback." *Hum Brain Mapp* 32(1): 22-31.

[52] Hebb, D.O. (1949). Distinction in coherent neural network between resting and working brain states. *The organization of behavior*. New York: Wiley & Sons.

[53] Henriksson, L., A. Raninen, et al. (2007). "Training-induced cortical representation of a hemianopic hemifield." *J Neurol Neurosurg Psychiatry* 78(1): 74-81.

[54] Henry, S.H. R.C. Reid (2000). The koniocellular pathway in primate vision. *Annual Review of Neuroscience* 23: 127-153.

[55] Hinds, O., S. Ghosh, et al. (2011). "Computing moment-to-moment BOLD activation for real-time neurofeedback." *Neuroimage* 54(1): 361-8.

[56] Hinrichs, H., H. J. Heinze, et al. (2006). "Causal visual interactions as revealed by an information theoretic measure and fMRI." *Neuroimage* 31(3): 1051-60.

[57] Hopfinger, J. B., M. H. Buonocore, et al. (2000). "The neural mechanisms of top-down attentional control." *Nat Neurosci* 3(3): 284-91.

[58] Horton, J. C. (2005a). "Disappointing results from Nova Vision's visual restoration therapy." *Br J Ophthalmol* 89(1): 1-2.

[59] Horton, J. C. (2005b). "Vision restoration therapy: confounded by eye movements." *Br J Ophthalmol* 89(7): 792-4.

[60] Hua, T., P. Bao, et al. (2010). "Perceptual learning improves contrast sensitivity of V1 neurons in cats." *Curr Biol* 20(10): 887-94.

[61] Hubel, D. H. and Wiesel, T. N. (1977). Ferrier Lecture: Functional Architecture of Macaque Monkey Visual Cortex, Proceedings of the Royal Society of London. Series B, Biological Sciences, Vol. 198, No. 1130 (May 19, 1977), pp. 1-59 Published by: The Royal Society Stable URL: http://www.jstor.org/stable/77245.

[62] Huxlin, K. R., J. M. Williams, et al. (2008a). "A neurochemical signature of visual recovery after extrastriate cortical damage in the adult cat." *J Comp Neurol* 508(1): 45-61.

[63] Huxlin, K. R. (2008b). "Perceptual plasticity in damaged adult visual systems." *Vision Res* 48(20): 2154-66.

[64] Huxlin, K. R., T. Martin, et al. (2009). "Perceptual relearning of complex visual motion after V1 damage in humans." *J Neurosci* 29(13): 3981-91.

[65] Huxlin, K. R. and T. Pasternak (2004). "Training-induced recovery of visual motion perception after extrastriate cortical damage in the adult cat." *Cereb Cortex* 14(1): 81-90.

[66] Huxlin, K. Plasticity of Visual Perception After Permanent Damage to the Adult Visual Cortex. in "Visual Field restoration Therapy Symposium"— Nanos Annual Meeting. 2006. Tuscon, AZ.

[67] Iorizzo, D. B., M. E. Riley, et al. (2011). "Differential impact of partial cortical blindness on gaze strategies when sitting and walking - an immersive virtual reality study." *Vision Res* 51(10): 1173-84.

[68] Jobke, S., E. Kasten, et al. (2009). "Vision restoration through extrastriate stimulation in patients with visual field defects: a double-blind and randomized experimental study." *Neurorehabil Neural Repair* 23(3): 246-55.

[69] Johnson, K. A., K. Hartwell, et al. (2012). "Intermittent "real-time" fMRI feedback is superior to continuous presentation for a motor imagery task: a pilot study." *J Neuroimaging* 22(1): 58-66.

[70] Johnston, S., D. E. Linden, et al. (2011). "Upregulation of emotion areas through neurofeedback with a focus on positive mood." *Cogn Affect Behav Neurosci* 11(1): 44-51.

[71] Johnston, S. J., S. G. Boehm, et al. (2010). "Neurofeedback: A promising tool for the self-regulation of emotion networks." *Neuroimage* 49(1): 1066-72.

[72] Julkunen, L., O. Tenovuo, et al. (2003). "Rehabilitation of chronic post-stroke visual field defect with computer-assisted training: a clinical and neurophysiological study." *Restor Neurol Neurosci* 21(1-2): 19-28.

[73] Karni, A. and D. Sagi (1991). "Where practice makes perfect in texture discrimination: evidence for primary visual cortex plasticity." *Proc Natl Acad Sci U S A* 88(11): 4966-70.

[74] Kasten, E., U. Bunzenthal, et al. (2007). "Vision restoration therapy does not benefit from costimulation: A pilot study." *J Clin Exp Neuropsychol* 29(6): 569-84.

[75] Kasten, E., U. Bunzenthal, et al. (2006). "Visual field recovery after vision restoration therapy (VRT) is independent of eye movements: an eye tracker study." *Behav Brain Res* 175(1): 18-26.

[76] Kasten, E., E. Muller-Oehring, et al. (2001). "Stability of visual field enlargements following computer-based restitution training — results of a follow-up." *J Clin Exp Neuropsychol* 23(3): 297-305.

[77] Kasten, E., D. A. Poggel, et al. (1999). "Restoration of vision II: residual functions and training-induced visual field enlargement in brain-damaged patients." *Restor Neurol Neurosci* 15(2-3): 273-87.

[78] Kasten, E., D. A. Poggel, et al. (2000). "Computer-based training of stimulus detection improves color and simple pattern recognition in the defective field of hemianopic subjects." *J Cogn Neurosci* 12(6): 1001-12.

[79] Kasten, E. and B. A. Sabel (1995). "Visual field enlargement after computer training in brain-damaged patients with homonymous deficits: an open pilot trial." *Restor Neurol Neurosci* 8(3): 113-27.

[80] Kasten, E., S. Wuest, et al. (1998a). "Residual vision in transition zones in patients with cerebral blindness." *J Clin Exp Neuropsychol* 20(5): 581-98.

[81] Kasten, E., S. Wust, et al. (1998b). "Computer-based training for the treatment of partial blindness." *Nat Med* 4(9): 1083-7.

[82] Kastner, S. and L. G. Ungerleider (2000). "Mechanisms of visual attention in the human cortex." *Annu Rev Neurosci* 23: 315-41.

[83] Kerkhoff, G., U. Munssinger, et al. (1992). "Rehabilitation of homonymous scotomata in patients with postgeniculate damage of the visual system: saccadic compensation training." *Restor Neurol Neurosci* 4(4): 245-54.

[84] Kerkhoff, G., U. Munssinger, et al. (1994). "Neurovisual rehabilitation in cerebral blindness." *Arch Neurol* 51(5): 474-81.

[85] Kikuta, K., Y. Takagi, et al. (2006). "Early experience with 3-T magnetic resonance tractography in the surgery of cerebral arteriovenous malformations in and around the visual pathway." *Neurosurgery* 58(2): 331-7; discussion 331-7.

[86] Kluver, H. (1936). An analysis of the effects of the removal of the occipital lobes in monkeys, *J Psychol*, 2: 49- 61.

[87] LaConte, S. M., S. J. Peltier, et al. (2007). "Real-time fMRI using brain-state classification." *Hum Brain Mapp* 28(10): 1033-44.

[88] Law, C. T. and J. I. Gold (2008). "Neural correlates of perceptual learning in a sensory-motor, but not a sensory, cortical area." *Nat Neurosci* 11(4): 505-13.

[89] Lee, S., A. Papanikolaou, et al. (2013). "A new method for estimating population receptive field topography in visual cortex." *Neuroimage* 81: 144-57.

[90] Lee, S., S. Ruiz, et al. (2011). "Detection of cerebral reorganization induced by real-time fMRI feedback training of insula activation: a multivariate investigation." *Neurorehabil Neural Repair* 25(3): 259-67.

[91] Lew, H. L., J. H. Poole, et al. (2007). "Program development and defining characteristics of returning military in a VA Polytrauma Network Site." *J Rehabil Res Dev* 44(7): 1027-34.

[92] Lewis, C. M., A. Baldassarre, et al. (2009). "Learning sculpts the spontaneous activity of the resting human brain." *Proc Natl Acad Sci U S A* 106(41): 17558-63.

[93] Li, X., K. J. Hartwell, et al. (2012). "Volitional reduction of anterior cingulate cortex activity produces decreased cue craving in smoking cessation: a preliminary real-time fMRI study." *Addict Biol* 18(4): 739-48.

[94] Lindberg, P., H. Forssberg, et al. (2003). "[Rehabilitation after stroke. Imaging techniques show how the cortical reorganization is affected by training]." *Lakartidningen* 100(51-52): 4289-92.

[95] Linden DE, Habes I, et al. (2012). Real-time self-regulation of emotion networks in patients with depression. PLoS One 7(6):e38115.

[96] Liu, Z. and D. Weinshall (2000). "Mechanisms of generalization in perceptual learning." *Vision Res* 40(1): 97- 109.

[97] Liu X, Zhu XH, Chen W. (2011). Distinction in coherent neural network between resting and working brain states. Brain Connect 1(5):377-88. doi: 10.1089/brain.2011.0044.

[98] Marshall, R. S., J. J. Ferrera, et al. (2008). "Brain activity associated with stimulation therapy of the visual borderzone in hemianopic stroke patients." *Neurorehabil Neural Repair* 22(2): 136-44.

[99] McCaig, R. G., M. Dixon, et al. (2011). "Improved modulation of rostrolateral prefrontal cortex using real-time fMRI training and meta-cognitive awareness." *Neuroimage* 55(3): 1298-305.

[100] McKenna, K., D. M. Cooke, et al. (2006). "The incidence of visual perceptual impairment in patients with severe traumatic brain injury." *Brain Inj* 20(5): 507-18.

[101] Mihailovic LT, Cupic D, Dekleva N. (1971). Changes in the numbers of neurons and glial cells in the lateral geniculate nucleus of the monkey during retrograde cell degeneration. *J Comp Neurol* 142: 223-9.

[102] Moore, T., H. R. Rodman, et al. (2001). "Direction of motion discrimination after early lesions of striate cortex (V1) of the macaque monkey." *Proc Natl Acad Sci U S A* 98(1): 325-30.

[103] Moore, T., H. R. Rodman, et al. (1995). "Localization of visual stimuli after striate cortex damage in monkeys: parallels with human blindsight." *Proc Natl Acad Sci U S A* 92(18): 8215-8.

[104] Morris, J. S., B. DeGelder, et al. (2001). "Differential extrageniculostriate and amygdala responses to presentation of emotional faces in a cortically blind field." *Brain* 124(Pt 6): 1241-52.

[105] Mourao-Miranda, J., A. L. Bokde, et al. (2005). "Classifying brain states and determining the discriminating activation patterns: Support Vector Machine on functional MRI data." *Neuroimage* 28(4): 980-95.

[106] Mumford, D. (1994). Neuronal architectures for pattern theoretic problems. In: *Large Scale Neuronal Theories of the Brain*, Koch C, Davis, JL, eds., MIT Press, pp. 125-152.

[107] Okada, T., Y. Miki, et al. (2007). "Diffusion tensor fiber tractography for arteriovenous malformations: quantitative analyses to evaluate the corticospinal tract and optic radiation." *AJNR Am J Neuroradiol* 28(6): 1107-13.

[108] Olshausen, B.A. Principles of Image Representation in Visual Cortex. In: *The Visual Neurosciences*, L.M. Chalupa, J.S. Werner, Eds. MIT Press, 2003: 1603-1615.

[109] Overgaard, M. (2011). "Visual experience and blindsight: a methodological review." *Exp Brain Res* 209(4): 473-9.

[110] Pambakian, A.L. and C. Kennard (1997). Can visual function be restored in patients with homonymous hemianopia? Br J Ophthalmol (4): p. 324-8.

[111] Papageorgiou, T. D., W. A. Curtis, et al. (2009a). "Neurofeedback of two motor functions using supervised learning-based real-time functional magnetic resonance imaging." *Conf Proc IEEE Eng Med Biol Soc* 2009: 5377-80.

[112] Papageorgiou, T.D., M. McHenry, J.L. Lisinski, J.P. White, and S.M. LaConte (2009b). Speech rate control using supervised learning-based rea-time fMRI. 15th Annual Meeting of the Organization for Human Brain Mapping, San Franscisco. *Neuroimage*, 47: p. 97.

[113] Papageorgiou, T.D., LaConte, S.M., Lisinski, J.L., Peng, X., and Smirnakis, S.M, Classification Accuracy and Spatial Networks on Motion Coherence using Real-time fMRI. Hum Brain Mapp, Barcelona, 2010.

[114] Papageorgiou, T. D., J. M. Lisinski, et al. (2013). "Brain-computer interfaces increase whole-brain signal to noise." *Proc Natl Acad Sci U S A* 110(33): 13630-5.

[115] Papanikolaou, A., G.A. Keliris, T.D. Papageorgiou, Y. Shao, E. Krapp, E. Papageorgiou, K. Stingl, A. Bruckmann, U. Schiefer, N.K. Logothetis, and S.M. Smirnakis (2014). Population receptive field analysis of the primary visual cortex complements perimetry in patients with homonymous visual field defects. *Proc Natl Acad Sci U S A* 111(16):E1656-65.

[116] Pasik, T. and P. Pasik (1971). "The visual world of monkeys deprived of striate cortex: effective stimulus parameters and the importance of the accessory optic system." *Vision Res* Suppl 3: 419-35.

[117] Pessoa, L., S. Kastner, et al. (2003). "Neuroimaging studies of attention: from modulation of sensory processing to top-down control." *J Neurosci* 23(10): 3990-8.

[118] Peyron, R., B. Laurent, et al. (2000). "Functional imaging of brain responses to pain. A review and meta-analysis (2000)." *Neurophysiol Clin* 30(5): 263-88.

[119] Pleger, B., A. F. Foerster, et al. (2003). "Functional magnetic resonance imaging mirrors recovery of visual perception after repetitive tachistoscopic stimulation in patients with partial cortical blindness." *Neurosci Lett* 335(3): 192-6.

[120] Plow, E. B., S. N. Obretenova, et al. (2011). "Combining visual rehabilitative training and noninvasive brain stimulation to enhance visual function in patients with hemianopia: a comparative case study." *PM R* 3(9): 825-35.

[121] Poggel, D. A., E. Kasten, et al. (2006). "Improving residual vision by attentional cueing in patients with brain lesions." *Brain Res* 1097(1): 142-8.

[122] Poggel, D. A., E. Kasten, et al. (2001). "Unusual spontaneous and training induced visual field recovery in a patient with a gunshot lesion." *J Neurol Neurosurg Psychiatry* 70(2): 236-9.

[123] Poggel, D. A., E. Kasten, et al. (2004). "Attentional cueing improves vision restoration therapy in patients with visual field defects." *Neurology* 63(11): 2069-76.

[124] Poggel, D. A., I. Mueller, et al. (2010). "Subjective and objective outcome measures of computer-based vision restoration training." *NeuroRehabilitation* 27(2): 173-87.

[125] Poppel, E., R. Held, et al. (1973). "Leter: Residual visual function after brain wounds involving the central visual pathways in man." *Nature* 243(5405): 295-6.

[126] Posse, S., D. Fitzgerald, et al. (2003). "Real-time fMRI of temporolimbic regions detects amygdala activation during single-trial self-induced sadness." *Neuroimage* 18(3): 760-8.

[127] Raninen, A., S. Vanni, et al. (2007). "Temporal sensitivity in a hemianopic visual field can be improved by long-term training using flicker stimulation." *J Neurol Neurosurg Psychiatry* 78(1): 66-73.

[128] Rebesco, J. M. and L. E. Miller (2011). "Stimulus-driven changes in sensorimotor behavior and neuronal functional connectivity application to brain-machine interfaces and neurorehabilitation." *Prog Brain Res* 192: 83-102.

[129] Reinges, M. H., T. Krings, et al. (2004). "Functional and diffusion-weighted magnetic resonance imaging for visualization of the postthalamic visual fiber tracts and the visual cortex." *Minim Invasive Neurosurg* 47(3): 160-4.

[130] Reinhard, J., A. Schreiber, et al. (2005). "Does visual restitution training change absolute homonymous visual field defects? A fundus controlled study." *Br J Ophthalmol* 89(1): 30-5.

[131] Riggs, R. V., K. Andrews, et al. (2007). "Visual deficit interventions in adult stroke and brain injury: a systematic review." *Am J Phys Med Rehabil* 86(10): 853-60.

[132] Rizzo, M. and D. A. Robin (1996). "Bilateral effects of unilateral visual cortex lesions in human." *Brain* 119(Pt 3): 951-63.

[133] Rodman, H. R., C. G. Gross, et al. (1989). "Afferent basis of visual response properties in area MT of the macaque. I. Effects of striate cortex removal." *J Neurosci* 9(6): 2033-50.

[134] Rodman, H. R., C. G. Gross, et al. (1990). "Afferent basis of visual response properties in area MT of the macaque. II. Effects of superior colliculus removal." *J Neurosci* 10(4): 1154-64.

[135] Rota, G., R. Sitaram, et al. (2009). "Self-regulation of regional cortical activity using real-time fMRI: the right inferior frontal gyrus and linguistic processing." *Hum Brain Mapp* 30(5): 1605-14.

[136] Rudolph, K. and T. Pasternak (1999). "Transient and permanent deficits in motion perception after lesions of cortical areas MT and MST in the macaque monkey." *Cereb Cortex* 9(1): 90-100.

[137] Rudolph, K. K., V. P. Ferrera, et al. (1994). "A reduction in the number of directionally selective neurons extends the spatial limit for global motion perception." *Vision Res* 34(24): 3241-51.

[138] Rudolph, T. M. and E. R. Delay (1993). "Recovery of a temporally based visual discrimination after visual cortex lesion in the rat." *Behav Brain Res* 53(1-2): 189-99.

[139] Ruiz, S., K. Buyukturkoglu, et al. (2013). "Real-time fMRI brain computer interfaces: Self-regulation of single brain regions to networks." *Biol Psychol*.

[140] Sabel, B. A., P. Henrich-Noack, et al. (2011). "Vision restoration after brain and retina damage: the "residual vision activation theory"." *Prog Brain Res* 192: 199-262.

[141] Sabel, B. A. and E. Kasten (2000). "Restoration of vision by training of residual functions." *Curr Opin Ophthalmol* 11(6): 430-6.

[142] Sabel, B. A., S. Kenkel, et al. (2004). "Vision restoration therapy (VRT) efficacy as assessed by comparative perimetric analysis and subjective questionnaires." *Restor Neurol Neurosci* 22(6): 399-420.

[143] Sahraie, A., M. J. Macleod, et al. (2010). "Improved detection following Neuro-Eye Therapy in patients with post-geniculate brain damage." *Exp Brain Res* 206(1): 25-34.

[144] Sahraie, A., C. T. Trevethan, et al. (2006). "Increased sensitivity after repeated stimulation of residual spatial channels in blindsight." *Proc Natl Acad Sci U S A* 103(40): 14971-6.

[145] Schmid, M. C., S. W. Mrowka, et al. (2010). "Blindsight depends on the lateral geniculate nucleus." *Nature* 466(7304): 373-7.

[146] Schmid, M. C., T. Panagiotaropoulos, et al. (2009). "Visually driven activation in macaque areas V2 and V3 without input from the primary visual cortex." *PLoS One* 4(5): e5527.

[147] Schoenfeld, M. A., H. J. Heinze, et al. (2002). "Unmasking motion-processing activity in human brain area V5/MT+ mediated by pathways that bypass primary visual cortex." *Neuroimage* 17(2): 769-79.

[148] Schoth, F., U. Burgel, et al. (2006). "Diffusion tensor imaging in acquired blind humans." *Neurosci Lett* 398(3): 178-82.

[149] Schoups, A., R. Vogels, et al. (2001). "Practising orientation identification improves orientation coding in V1 neurons." *Nature* 412(6846): 549-53.

[150] Sereno, M. I., A. M. Dale, et al. (1995). "Borders of multiple visual areas in humans revealed by functional magnetic resonance imaging." *Science* 268(5212): 889-93.

[151] Scharnowski, F., C. Hutton, et al. (2012). "Improving visual perception through neurofeedback." *J Neurosci* 32(49): 17830-41.

[152] Sherbondy, A. J., R. F. Dougherty, et al. (2008). "Identifying the human optic radiation using diffusion imaging and fiber tractography." *J Vis* 8(10): 12 1-11.

[153] Shibata K, L.H. Chang, (2012). Decoding reveals plasticity in V3A as a result of motion perceptual learning. PLoS One. 7(8):e44003.

[154] Shibata, K., T. Watanabe, et al. (2011). "Perceptual learning incepted by decoded fMRI neurofeedback without stimulus presentation." *Science* 334(6061): 1413-5.

[155] Stilla, R., R. Hanna, et al. (2008). "Neural processing underlying tactile microspatial discrimination in the blind: a functional magnetic resonance imaging study." *J Vis* 8(10): 13 1-19.

[156] Stoerig, P. and E. Barth (2001). "Low-level phenomenal vision despite unilateral destruction of primary visual cortex." *Conscious Cogn* 10(4): 574-87.

[157] Subramanian, L., J. V. Hindle, et al. (2011). "Real-time functional magnetic resonance imaging neurofeedback for treatment of Parkinson's disease." *J Neurosci* 31(45): 16309-17.

[158] Sulzer, J., R. Sitaram, et al. (2013). "Neurofeedback-mediated self-regulation of the dopaminergic midbrain." *Neuroimage* 83C: 817-825.

[159] Stoerig, P. and A. Cowey (1997). "Blindsight in man and monkey." *Brain* 120 (Pt 3): 535-59.

[160] Takeuchi, N., T. Chuma, et al. (2005). "Repetitive transcranial magnetic stimulation of contralesional primary motor cortex improves hand function after stroke." *Stroke* 36(12): 2681-6.

[161] Taoka, T., M. Sakamoto, et al. (2005). "Diffusion tensor imaging in cases with visual field defect after anterior temporal lobectomy." *AJNR Am J Neuroradiol* 26(4): 797-803.

[162] Taub, E., G. Uswatte, et al. (2002). "New treatments in neurorehabilitation founded on basic research." *Nat Rev Neurosci* 3(3): 228-36.

[163] Taylor, T. N. (1997). "The medical economics of stroke." *Drugs* 54 Suppl 3: 51-7; discussion 57-8.

[164] Van den Stock, J., M. Tamietto, et al. (2011). "Cortico-subcortical visual, somatosensory, and motor activations for perceiving dynamic whole-body emotional expressions with and without striate cortex (V1)." *Proc Natl Acad Sci U S A* 108(39): 16188-93.

[165] Vanburen, J. M. (1963). "Trans-Synaptic Retrograde Degeneration in the Visual System of Primates." *J Neurol Neurosurg Psychiatry* 26: 402-9.

[166] Vapnik, N. (1995). The nature of statistical learning theory. Springer.

[167] Veit, R., V. Singh, et al. (2012). "Using real-time fMRI to learn voluntary regulation of the anterior insula in the presence of threat-related stimuli." *Soc Cogn Affect Neurosci* 7(6): 623-34.

[168] Wandell, B. A., S. O. Dumoulin, et al. (2007). "Visual field maps in human cortex." *Neuron* 56(2): 366-83.

[169] Wang, L., W. Dai, et al. (2012). "Amplitude of low-frequency oscillations in first-episode, treatment-naive patients with major depressive disorder: a resting-state functional MRI study." *PLoS One* 7(10): e48658.

[170] Wedeen, V. J., D. L. Rosene, et al. (2012). "The geometric structure of the brain fiber pathways." *Science* 335(6076): 1628-34.

[171] Weiller, C. (1998). "Imaging recovery from stroke." *Exp Brain Res* 123(1-2): 13-7.

[172] Weiskopf, N. (2012). "Real-time fMRI and its application to neurofeedback." *Neuroimage* 62(2): 682-92.

[173] Weiskopf, N., R. Sitaram, et al. (2007). "Real-time functional magnetic resonance imaging: methods and applications." *Magn Reson Imaging* 25(6): 989-1003.

[174] Weiskopf, N., F. Sharnowski, et al., (2004). Self-regulation of local brain activity using real-time functional magnetic resonance imaging (fMRI). *J Physiol Paris*, 98(4-6): p. 357-73.

[175] Weiskopf, N., R. Veit, et al. (2003). "Physiological self-regulation of regional brain activity using real-time functional magnetic resonance imaging (fMRI): methodology and exemplary data." *Neuroimage* 19(3): 577-86.

[176] Weiskrantz, L. (2004). "Roots of blindsight." *Prog Brain Res* 144: 229-41.

[177] Weiskrantz, L., E. K. Warrington, et al. (1974). "Visual capacity in the hemianopic field following a restricted occipital ablation." *Brain* 97(4): 709-28.

[178] Werth, R. and M. Moehrenschlager (1999). "The development of visual functions in cerebrally blind children during a systematic visual field training." *Restor Neurol Neurosci* 15(2-3): 229-41.

[179] Worsley, K. J., C. H. Liao, et al. (2002). "A general statistical analysis for fMRI data." *Neuroimage* 15(1): 1-15.

[180] Yang, T. and J. H. Maunsell (2004). "The effect of perceptual learning on neuronal responses in monkey visual area V4." *J Neurosci* 24(7): 1617-26.

[181] Yeatman, J. D., R. F. Dougherty, et al. (2012). "Tract profiles of white matter properties: automating fiber-tract quantification." *PLoS One* 7(11): e49790.

[182] Yoo, S. S. and F. A. Jolesz (2002). "Functional MRI for neurofeedback: feasibility study on a hand motor task." *Neuroreport* 13(11): 1377-81.

[183] Yoo, S. S., J. H. Lee, et al. (2008). "Neurofeedback fMRI-mediated learning and consolidation of regional brain activation during motor imagery." *Int J Imaging Syst Technol* 18(1): 69-78.

[184] Yotsumoto, Y., T. Watanabe, et al. (2008). "Different dynamics of performance and brain activation in the time course of perceptual learning." *Neuron* 57(6): 827-33.

[185] Zeki, S. (2004) Thirty years of a very special visual area, area V5. J. Physiol. 557, 1–2.

[186] Zeki S., and D.H. ffytche (1998). The Riddoch syndrome: insights into the neurobiology of conscious vision. *Brain* 121(Pt 1):25-45.

[187] Zhang, X., S. Kedar, et al. (2006). "Natural history of homonymous hemianopia." *Neurology* 66(6): 901-5.

[188] Zihl, J. and D. von Cramon (1979). "Restitution of visual function in patients with cerebral blindness." *J Neurol Neurosurg Psychiatry* 42(4): 312-22.

[189] Zihl, J. and D. von Cramon (1985). "Visual field recovery from scotoma in patients with postgeniculate damage. A review of 55 cases." Brain 108 (Pt 2): 335-65.

[190] Zotev, V., F. Krueger, et al. (2011). "Self-regulation of amygdala activation using real-time FMRI neurofeedback." PLoS One 6(9): e24522.

[191] Zuiderbaan, W., B. M. Harvey, et al. (2012). "Modeling center-surround configurations in population receptive fields using fMRI." J Vis 12(3): 10.